

CONSTITUTIVE MODELING OF CROSS-LINKED POLYMERS DURING AGING

By

Seyedamir Bahrololoumi Tabatabaei

A DISSERTATION

Submitted to
Michigan State University
in partial fulfillment of the requirements
for the degree of

Civil Engineering - Doctor of Philosophy
Mechanical Engineering - Dual Major

2024

ABSTRACT

Due to unique features such as high stretchability, chemical toleration, wear resistance, anti-slipping, and durability; industrial applications of cross-linked polymers have been growing through the past decades. Their practical function can cover a broad range of applications from insensitive to sensitive industries such as automotive, medical, mining, and petroleum. In most such cases, the polymeric components are simultaneously exposed to mechanical loads as well as environmental elements like humidity and oxygen. This affair can considerably reduce the nominal service life of the polymers and cause irreversible damage to their functionality. In the literature, this chemical/physical phenomenon is generally regarded as the *aging* mechanism, which is classified into different subcategories based on the source of aging. Thermo-oxidation, hydrolysis, and hygrothermal are some of the main types of chemical aging in which oxygen, temperature, and water play major roles in the deterioration of polymer matrix.

Such classes can be either the result of individual aging elements or due to combined synergized effects of the above-mentioned environmental factors. Any type of aging can induce irreversible damage to the polymer matrix, which results in the reduction of materials' nominal service life. While predicting any of these types of aging is of great interest to researchers in the last few years, there is still a long way to find a comprehensive model which can consider the synergized effects of chemical aging.

Here, multi-physics models are devised to describe the solo and combined long-term effects of different environmental elements on the constitutive behavior of cross-linked polymers. These models are relevant for all decay mechanisms formed by the occurrence of two simultaneous micro-mechanisms; (i) formation/reduction of the cross-links, and (ii) chain scission. We modeled each sub-mechanism through a linear kinetic equation which is then coupled into the modular network concept to allow the calculation of synergies and parallel damage accumulation through multiple sources. In this respect, hydrolytic aging is considered to be induced by chain scission and reduction of the cross-link, while thermal aging is considered a superposition of two competing effects of cross-link formation and chain scission. Besides, hygrothermal damage can be regarded as a race

among three micro-structural phenomena; i) chain scission due to the presence of temperature, ii) reduction of cross-links attributed to the attendance of water, and iii) formation of cross-links as a consequence of oxygen reactions.

These proposed models are micro-mechanically based and are mainly relevant to thin samples due to our underlying assumption of homogeneous diffusion of oxygen and water throughout the matrix. These models have been validated against extensive data sets obtained from experiments we specifically designed for concept validation. In view of their interpretation, precision, and deep insight, it provides insight into the nature of damage accumulation. The model is a good choice for advanced implementation in FE applications.

Copyright by
SEYEDAMIR BAHROLOLOUMI TABATABAEI
2024

"In respectful dedication to the cherished memory of my esteemed family members: my beloved wife, Gelareh, whose unwavering love has consistently fortified me; my father, Majid, a guiding light and and my mother, Saeedeh, whose unwavering support has shaped my path. It remains deeply regrettable that my father, who selflessly invested in my future, couldn't witness its fulfillment due to the tragic impact of COVID-19."

ACKNOWLEDGEMENTS

As I began penning this acknowledgment, I encountered the immense challenge of expressing adequate gratitude for the myriad forms of assistance, support, and understanding offered by numerous individuals throughout the journey of crafting this dissertation. The fear of inadvertently overlooking or inadequately representing someone's invaluable contributions loomed large. It is undeniable that an extensive community has played an integral role in guiding me toward completing this work, and the individuals mentioned herein are just a fraction of this supportive network.

First and foremost, I extend my heartfelt gratitude to my esteemed advisers, Dr. Roozbeh Dargazany and Dr. Thomas Pence. Your guidance and belief in my capabilities have been instrumental in nurturing my growth as an independent researcher.

I wish to express profound appreciation to my esteemed committee members, Dr. Nizar Lajnef, Dr. Sara Roccabianca, and Prof. Rafael Auras. Their wealth of expertise, combined with the privilege of learning from their classes, significantly contributed to shaping my intellectual evolution throughout my graduate studies.

I am sincerely thankful to my invaluable colleagues and friends within the High-Performance Materials (HPM) group, notably Vahid Morovati, Mamoon Shaafaey, Hamid Mohammadi, Aref Ghaderi, Yang Chen, Sharif Alazhary, and Ramin Akbari. Their collaborative spirit and insightful discussions have been invaluable contributions to this endeavor.

I am profoundly indebted to Dr. Manoochehr Najmi for his unwavering guidance and invaluable advice, which have been pivotal throughout my journey. Additionally, I extend heartfelt gratitude to my mother-in-law, Fariba. While the list of friends is extensive, I am immensely grateful to each of you for transforming my journey into a joyous and supportive experience, akin to a second family away from home. I extend my sincerest wishes for success in all your future endeavors.

The successful completion of this dissertation owes immeasurably to my beloved wife, Gelareh Najmi, my best friend. Her unwavering support, enduring patience, and selfless sacrifices during my trials, absences, moments of frustration, and impatience are beyond commendation.

TABLE OF CONTENTS

| | |
|---|------------|
| CHAPTER 1 Introduction | 1 |
| CHAPTER 2 Fundamentals of Continuum Mechanics and Non-linear Finite Element Method | 3 |
| CHAPTER 3 A Multi physics Constitutive Model to Predict Hydrolytic Aging in Quasi static Behaviour of Thin Cross linked Polymers | 21 |
| CHAPTER 4 A Physically Based Model for Thermo-Oxidative and Hydrolytic Aging of Elastomers | 53 |
| CHAPTER 5 A Multi Physics Approach on Modeling of Hygrothermal Aging and its Effects on Constitutive Behavior of Cross linked Polymers | 79 |
| CHAPTER 6 Thermal Aging Coupled with Cyclic Fatigue in Cross-linked Polymers: Constitutive Modeling & FE Implementation | 113 |
| CHAPTER 7 Summary and Future Works | 139 |
| BIBLIOGRAPHY | 141 |

CHAPTER 1

Introduction

1.1 Motivation

Cross-linked polymers have become ubiquitous throughout the world due to their excellent properties such as high extensibility, strength, abrasion and chemical resistance, and durability [1, 2]. They are widely used in different industries such as automotive, transportation, power distribution, and aerospace. In view of their demanding applications, rubber-like components should be reliably designed to be subjected to a high number of cyclic loading in harsh environments. However, their reliability considerably decreases over time due to a process known as *aging*. This process usually causes a significant change in the properties of rubber-like materials over their service life [3, 4]. To this end, reliable lifetime estimation of products made by cross-linked polymers can be extremely challenging, especially for products that are exposed to multiple damages.

The aging process can happen due to an individual or combined effects of different environmental factors such as humidity, temperature, and radiation [5, 6]. These environmental factors facilitate degradation mechanisms. These mechanisms can be categorized into those with major impacts such as hygro-thermal [7, 8], hydrolysis [9, 10], thermo-oxidation [11, 6, 12], and those with the less severe impact such as chemical corrosion [13], and ozone cracking [14]. While these mechanisms potentially can significantly reduce the service life of an elastomeric component, the latter group is not that prevalent in nature. Although predicting the individual contribution of different mechanisms has been the center of attention in the literature, there is still a long way to go in modeling aging mechanisms.

Usually, polymers are used in applications where in situ testing is expensive due to inaccessibility. Therefore, predictive models are needed to prevent the catastrophic failure of the structures

because of aging. Subsequently, a computationally simple yet precise model that can predict the mechanical properties of cross-linked polymers during aging is in high demand. Albeit their popularity, theoretical efforts for both thermo-oxidative aging and hydrolysis are limited. These efforts can be categorized into two different approaches, phenomenological and micro-mechanical. Phenomenological approaches use a mathematical model, usually without a physical meaning, to describe the changes in material properties based on a thermodynamic framework [15, 16]. Though phenomenological models can accurately model the behavior, they do not offer any insight into the relationship between model parameters and real material ones. On the other hand, micro-mechanical models are based on physical motivation. They developed from statistical mechanics of polymer structure and physics of polymer chain network. Consequently, their parameters do have physical meaning [17]. The lack of a proper micro-mechanical model for modeling elastomer constitutive behavior prompted us to begin this research. The main goal of this research is to develop a micro-mechanical model that can accurately explain the elastic and inelastic responses of elastomers in various aging environments.

CHAPTER 2

Fundamentals of Continuum Mechanics and Non-linear Finite Element

Method

The constitutive modeling of elastomers involves nonlinear continuum mechanical quantities, which describe the behavior of materials undergoing a large deformation. Thus, a basic foundation on continuum mechanics, including fundamental geometric mappings and basic stress measures of a solid body undergoing large deformations, is briefly discussed in this chapter. For a comprehensive description and understanding of the topic, the reader can refer to continuum mechanics reference materials such as [2].

2.1 Some Notes on Continuum Mechanics

In continuum mechanics theory, it is assumed that an object fully occupies the space with its substances. Physical properties of a solid or fluid medium are related through mathematical tensor measures. These measures are independent of their observed coordinate system in general. However, they can be represented in different coordinate systems. In this section, the relation of various mechanical measurements is briefly reviewed.

2.1.1 Deformation gradient

A continuum body B_{t_0} in a 3D Euclidean space at time t_0 , in which any arbitrary point P_0 with respect to an arbitrary basis can be represented by $\mathbf{X} \in \mathbb{E}^3$. As the body deforms in the space, the medium occupies its current configuration at B_t . Given that the geometrical mapping of the body from B_{t_0} to B_t is one-to-one, any point from the initial configuration, P_0 , uniquely maps to its new configuration coordinate, P , with an arbitrary basis of $\mathbf{x} \in \mathbb{E}^3$.

The geometrical mapping of the regions of the body from current configuration B_{t_0} to the reference configurations B_t in any arbitrary coordinate system, e^i ($i = 1, 2, 3$), can represent the position of point P and P_0 by

$$\mathbf{x} = \hat{\mathbf{x}}(\theta^1, \theta^2, \theta^3, t), \quad \mathbf{X} = \hat{\mathbf{X}}(\theta^1, \theta^2, \theta^3) = \hat{\mathbf{x}}(\theta^1, \theta^2, \theta^3, t_0). \quad i = 1, 2, 3, \quad (2.1)$$

Therefore, the displacement vector, \mathbf{u} , of point P can be written as

$$\mathbf{u} = \hat{\mathbf{u}}(\theta^1, \theta^2, \theta^3, t) = \mathbf{x} - \mathbf{X} \quad (2.2)$$

Given a Euclidean space with a set of orthonormal (Cartesian) basis vectors, say \mathbf{e}_i ($i = 1, 2, 3$), one can express each point of the body as

$$\begin{aligned} \mathbf{X} &= X^i \mathbf{e}_i, & X^j &= \mathbf{X} \cdot \mathbf{e}_j, & j &= 1, 2, 3, \\ \mathbf{u} &= u^i \mathbf{e}_i, & u^j &= \mathbf{u} \cdot \mathbf{e}_j, & j &= 1, 2, 3, \\ \mathbf{x} &= x^i \mathbf{e}_i, & x^j &= \mathbf{x} \cdot \mathbf{e}_j = X^j + u^j, & j &= 1, 2, 3, \end{aligned} \quad (2.3)$$

where the Einstein notation, summation over repeated indices, is applied. Deformation can be related to the tangent vectors of the coordinate lines in each of the configurations. Tangent vectors of sufficiently differentiable \mathbf{X} and \mathbf{x} can be written as

$$\mathbf{G}_i = \frac{\partial \mathbf{X}}{\partial \theta^i}, \quad \mathbf{g}_i = \frac{\partial \mathbf{x}}{\partial \theta^i}, \quad i = 1, 2, 3, \quad (2.4)$$

The relative motion of an arbitrary point with respect to its adjacent point can be calculated in a direction \mathbf{a} through the directional derivative as

$$\left. \frac{d}{ds} \hat{\mathbf{x}}(\mathbf{X} + s\mathbf{a}, t) \right|_{s=0} = \lim_{\Delta s \rightarrow 0} \frac{\hat{\mathbf{x}}(\mathbf{X} + \Delta s\mathbf{a}, t) - \hat{\mathbf{x}}(\mathbf{X}, t)}{\Delta s} = (\text{Grad } \mathbf{x}) \mathbf{a}. \quad (2.5)$$

Therefore, second-order deformation gradient tensor, $(\text{Grad } \mathbf{x})$, can be written by a linear mapping

of vector \mathbf{a} into vector $\left. \frac{d}{ds} \hat{\mathbf{x}}(\mathbf{X} + s\mathbf{a}, t) \right|_{s=0}$ as

$$\mathbf{F} = \text{Grad } \mathbf{x} = \frac{d\hat{\mathbf{x}}}{d\mathbf{X}}. \quad (2.6)$$

where, $d\mathbf{X}$ is a infinitesimal element before deformation and $d\hat{\mathbf{x}}$ is the same element on the body after deformation. This tensor plays a pivotal role in deformation kinematics, which can describe the relative motion of material elements during deformation. Therefore, one has the relation of infinitesimal elements in reference and current configurations as

$$d\mathbf{x} = \mathbf{F}d\mathbf{X}, \quad d\mathbf{X} = \mathbf{F}^{-1}d\mathbf{x}. \quad (2.7)$$

Moreover, the change of volume and surface elements can be related to the deformation gradient tensor through these relations. To this end, a volume in the reference configuration of three non-co-planar vectors, $d\mathbf{X}_1$, $d\mathbf{X}_2$ and $d\mathbf{X}_3$, can be defined as

$$dV_0 = [d\mathbf{X}_1 d\mathbf{X}_2 d\mathbf{X}_3] = (d\mathbf{X}_1 \times d\mathbf{X}_2) \cdot d\mathbf{X}_3. \quad (2.8)$$

Using Eq. 2.7, each of these vectors deforms in the current configuration to

$$d\mathbf{x}_1 = \mathbf{F}d\mathbf{X}_1, \quad d\mathbf{x}_2 = \mathbf{F}d\mathbf{X}_2, \quad d\mathbf{x}_3 = \mathbf{F}d\mathbf{X}_3. \quad (2.9)$$

Thus, the volume of the element in the current configuration can be written as

$$dV = [d\mathbf{x}_1 d\mathbf{x}_2 d\mathbf{x}_3] = (d\mathbf{x}_1 \times d\mathbf{x}_2) \cdot d\mathbf{x}_3 = JdV_0,$$

where

$$J = \frac{dV}{dV_0} = |\mathbf{F}^i_j| = \det \mathbf{F} > 0. \quad (2.10)$$

In addition, by defining the surface element of reference and current state as $d\mathbf{A}_0 = d\mathbf{X}_1 \times d\mathbf{X}_2$

and $d\mathbf{A} = d\mathbf{x}_1 \times d\mathbf{x}_2$, the relation of the surface areas can be calculated by substituting Eq. 2.9 into $dV_0 = JdV$ as

$$d\mathbf{A} = J\mathbf{F}^{-T}d\mathbf{A}_0. \quad (2.11)$$

where $dA = |d\mathbf{A}|$ and $dA_0 = |d\mathbf{A}_0|$ are the surface areas in the current and reference configuration, respectively. An element length in reference and current states can be calculated similarly as

$$\begin{aligned} \|d\mathbf{x}\|^2 &= d\mathbf{x} \cdot d\mathbf{x} = d\mathbf{X} (\mathbf{F}^T \mathbf{F}) d\mathbf{X} = d\mathbf{X} \mathbf{C} d\mathbf{X}, \\ \|d\mathbf{X}\|^2 &= d\mathbf{X} \cdot d\mathbf{X} = d\mathbf{x} (\mathbf{F}^{-T} \mathbf{F}^{-1}) d\mathbf{x} = d\mathbf{x} \mathbf{b}^{-1} d\mathbf{x}, \end{aligned} \quad (2.12)$$

where $\mathbf{C} = \mathbf{F}^T \mathbf{F}$ and $\mathbf{b} = \mathbf{F} \mathbf{F}^T$ are the right and left Cauchy-Green tensors, respectively. The change in the length of a linear element, the stretch of a material element, is defined as the ratio of the deformed to the referenced length of the material element. Deformation changes the length of an element $d\mathbf{X}$ in direction \mathbf{N} in initial state to $d\mathbf{x}$ in direction \mathbf{n} in the current state as

$$\begin{aligned} \lambda(\mathbf{N}) &= \frac{dx}{dX} = \sqrt{\frac{\|d\mathbf{x}\|^2}{\|d\mathbf{X}\|^2}} = \sqrt{\frac{d\mathbf{X} \mathbf{N} \mathbf{C} \mathbf{N} d\mathbf{X}}{dX^2}} \\ &= (\mathbf{N} \mathbf{C} \mathbf{N})^{\frac{1}{2}}, \end{aligned} \quad (2.13)$$

and

$$\lambda(\mathbf{n}) = (\mathbf{n} \mathbf{b}^{-1} \mathbf{n})^{-\frac{1}{2}}. \quad (2.14)$$

Another measure of the change in element length during deformation can be written as

$$\begin{aligned} \|d\mathbf{x}\|^2 - \|d\mathbf{X}\|^2 &= 2d\mathbf{X} \mathbf{E} d\mathbf{X} \\ &= 2d\mathbf{x} \mathbf{e} d\mathbf{x} \end{aligned} \quad (2.15)$$

where $\mathbf{E} = \frac{1}{2}(\mathbf{C} - \mathbf{I}) = \frac{1}{2}(\mathbf{F}^T \mathbf{F} - \mathbf{I})$ called the Green-Lagrange strain tensor and $\mathbf{e} = \frac{1}{2}(\mathbf{I} - \mathbf{b}^{-1}) = \frac{1}{2}(\mathbf{I} - \mathbf{F}^{-T} \mathbf{F}^{-1})$ is Almansi strain tensor.

2.1.2 Deformation rate

The material velocity gradient can be defined as similar to the deformation gradient by

$$\mathbf{L} = \text{Grad} \dot{\mathbf{x}} = \frac{\partial}{\partial \mathbf{X}} \left[\frac{\partial \mathbf{x}(\mathbf{X}, t)}{\partial t} \right] = \frac{\partial}{\partial t} \left(\frac{\partial \mathbf{x}}{\partial \mathbf{X}} \right) = \dot{\mathbf{F}}. \quad (2.16)$$

The spatial velocity gradient, the derivative of a spatial velocity field \mathbf{v} with respect to the current configuration, can be written as

$$\mathbf{l} = \text{grad} \dot{\mathbf{x}} = \frac{\partial \mathbf{v}}{\partial \mathbf{X}} \frac{\partial \mathbf{X}}{\partial \mathbf{x}} = \dot{\mathbf{F}} \mathbf{F}^{-1}. \quad (2.17)$$

The spatial gradient of velocity can be decomposed to a symmetric part $\mathbf{d} = \frac{1}{2}(\mathbf{l} + \mathbf{l}^T)$ and a skew-symmetric part $\mathbf{w} = -\mathbf{w}^T = \frac{1}{2}(\mathbf{l} - \mathbf{l}^T)$. The symmetric part is called the deformation rate

$$\mathbf{d} = \frac{1}{2}(\mathbf{l} + \mathbf{l}^T) = \frac{1}{2}(\dot{\mathbf{F}} \mathbf{F}^{-1} + \mathbf{F}^{-T} \dot{\mathbf{F}}^T) = \frac{1}{2} \mathbf{F}^{-T} \dot{\mathbf{C}} \mathbf{F}^{-1}. \quad (2.18)$$

In addition, the skew+symmetric part is referred to spin (vorticity) tensor

$$\mathbf{w} = -\mathbf{w}^T = \frac{1}{2}(\mathbf{l} - \mathbf{l}^T) = \frac{1}{2}(\dot{\mathbf{F}} \mathbf{F}^{-1} - \mathbf{F}^{-T} \dot{\mathbf{F}}^T). \quad (2.19)$$

The rate of Green-Lagrange strain tensor $\dot{\mathbf{E}}$ can be written as

$$\dot{\mathbf{E}} = \frac{1}{2} \dot{\mathbf{C}} = \frac{1}{2} \mathbf{F}^T \mathbf{d} \mathbf{F}. \quad (2.20)$$

The rate of the volume change can be calculated by the time derivative of the determinant of the deformation gradient as

$$\dot{J} = \frac{\partial \det \mathbf{F}}{\partial t} = J \text{tr} \mathbf{d} \quad (2.21)$$

2.1.3 Stress measures

The stress is defined by traction force vector $d\mathbf{F}_s$ per unit of area, which is defined as the neighboring continuum points of the body dA . The stress in each arbitrary point P_0 and P in reference and its counterpart in the current configuration is defined based on infinitesimal areas dA and da around them with the unit vectors of N and n normal to them, respectively. Thus, the relation of the traction force and stress can be written as

$$d\mathbf{F}_s = \mathbf{T}dA = \mathbf{t}da, \quad (2.22)$$

where the vectors \mathbf{T} and \mathbf{t} are the traction force in reference and deformed configurations, respectively. Therefore, second-order tensors $\boldsymbol{\sigma}$ and \mathbf{P} can be expressed based on the Cauchy's stress theorem as

$$\mathbf{t} = \boldsymbol{\sigma}\mathbf{n} \quad \mathbf{T} = \mathbf{P}\mathbf{N}, \quad (2.23)$$

where $\boldsymbol{\sigma}$ represents the Cauchy stress tensor related to force on the body surface in the current configuration and \mathbf{P} is the first Piola-Kirchhoff stress second-order tensor defined based on the surface area in the initial configuration. The first Piola-Kirchhoff stress and Cauchy stress tensor can be related through Nanson's formula 2.11 and 2.23 as

$$d\mathbf{F} = \mathbf{t}dA = \boldsymbol{\sigma}dA = J\boldsymbol{\sigma}\mathbf{F}^{-T}da. \quad (2.24)$$

The second Piola-Kirchhoff stress tensors \mathbf{S} can be calculated by pulling back the force vector df_s in the current state to the reference configuration. Similarly, another spatial stress measure, the Kirchhoff stress tensor $\boldsymbol{\tau}$, can be calculated and converted to other measures as the following set of equations

$$\mathbf{P} = J\boldsymbol{\sigma}\mathbf{F}^{-T} = \boldsymbol{\tau}\mathbf{F}^{-T} = \mathbf{F}\mathbf{S}, \quad \mathbf{S} = J\mathbf{F}^{-1}\boldsymbol{\sigma}\mathbf{F}^{-T}, \quad \boldsymbol{\tau} = J\boldsymbol{\sigma} \quad (2.25)$$

Note that nominal/first Piola-Kirchhoff stress is not a symmetric tensor due to its two-point coordinate systems.

2.1.4 Balance principles

For a body B with volume V , mass M , and boundary surface A in the current state, the rate of change of the linear momentum is directly proportional to the force applied on the body, which can be defined by

$$\int_M \mathbf{v} dM = \int_V \rho \dot{\mathbf{x}} dV,$$

where ρ is the density and $v = \dot{\mathbf{x}}$ is the velocity vector of a particle. The momentum can be calculated by summation of a body force and a surface force as

$$\frac{d}{dt} \int_V \rho \dot{\mathbf{x}} dV = \int_V \mathbf{f} dV + \int_A \mathbf{t} dA. \quad (2.26)$$

The surface forces can be obtained through the Cauchy theorem (2.23) and the divergence theorem

$$\int_A \mathbf{t} dA = \int_A \boldsymbol{\sigma} \mathbf{n} dA = \int_V \operatorname{div} \boldsymbol{\sigma} dV. \quad (2.27)$$

By substituting Eq. 2.27 into Eq. 2.26, the balance equation is then

$$\int_V (\operatorname{div} \boldsymbol{\sigma} + \mathbf{f} - \rho \ddot{\mathbf{x}}) dV = 0. \quad (2.28)$$

For any arbitrary point of the body, one can rewrite Eq. 2.28 as

$$\operatorname{div} \boldsymbol{\sigma} + \mathbf{f} = \rho \ddot{\mathbf{x}}. \quad (2.29)$$

In order to calculate the balance of mechanical energy, one can multiply Eq. 2.29 with the velocity vector \mathbf{v} as

$$\mathbf{v} \cdot \operatorname{div} \boldsymbol{\sigma} + \mathbf{v} \cdot \mathbf{f} = \rho \mathbf{v} \cdot \ddot{\mathbf{x}}. \quad (2.30)$$

Eq. 2.30 can be further simplified considering the symmetry of the Cauchy stress tensor as

$$\mathbf{v} \cdot \operatorname{div} \boldsymbol{\sigma} = \operatorname{div}(\mathbf{v} \boldsymbol{\sigma}) - \boldsymbol{\sigma} : \operatorname{grad} \mathbf{v} = \operatorname{div}(\mathbf{v} \boldsymbol{\sigma}) - \boldsymbol{\sigma} : \mathbf{d}, \quad (2.31)$$

which gives

$$\operatorname{div}(\mathbf{v} \boldsymbol{\sigma}) - \boldsymbol{\sigma} : \mathbf{d} + \mathbf{v} \cdot \mathbf{f} = \rho \frac{d}{dt} \left(\frac{1}{2} \mathbf{v} \cdot \mathbf{v} \right). \quad (2.32)$$

Integrating Eq. 2.32 over the volume of the body and considering Eq. 2.27 yield to

$$\frac{d}{dt} \int_M \left(\frac{1}{2} \mathbf{v} \cdot \mathbf{v} \right) dM + \int_V (\boldsymbol{\sigma} : \mathbf{d}) dV = \int_A (\mathbf{v} \cdot \mathbf{t}) dA + \int_V (\mathbf{v} \cdot \mathbf{f}) dV. \quad (2.33)$$

The balance of mechanical energy can be rewritten by taking into account the physical meaning of each term in the Eq. 2.33 as

$$\dot{K} + \mathcal{W} = \mathcal{P}, \quad (2.34)$$

where \mathcal{P} , \dot{K} , and \mathcal{W} refer to the power of external forces, the stress power, and the changes in the kinetic energy, respectively. The power of external forces can be written as

$$\mathcal{P} = \int_A (\mathbf{v} \cdot \mathbf{t}) dA + \int_V (\mathbf{v} \cdot \mathbf{f}) dV. \quad (2.35)$$

The kinetic energy and the stress power of the system is then formulated by

$$\begin{aligned} K &= \int_V \left(\rho \frac{1}{2} \mathbf{v} \cdot \mathbf{v} \right) dV, \\ \mathcal{W} &= \int_V (\boldsymbol{\sigma} : \mathbf{d}) dV. \end{aligned} \quad (2.36)$$

Note that the stress power can be calculated through other strain-stress measures and each of the stress measures $\boldsymbol{\sigma}$, \mathbf{P} , and \mathbf{S} are conjugate with deformation measures \mathbf{d} , $\dot{\mathbf{F}}$, and $\dot{\mathbf{E}}$, respectively. For instance, the stress power can be calculated using the first Piola-Kirchhoff stress and deformation gradient as

$$\mathcal{W} = \int_{V_0} (\mathbf{P} : \dot{\mathbf{F}}) dV_0 = \int_V J^{-1} (\mathbf{P} : \dot{\mathbf{F}}) dV. \quad (2.37)$$

Thus, the stress power can also be obtained from

$$(\mathbf{P} : \dot{\mathbf{F}}) = (\boldsymbol{\sigma} : \mathbf{d}) = (\mathbf{S} : \dot{\mathbf{E}}) = \left(\mathbf{S} : \frac{1}{2} \dot{\mathbf{C}} \right). \quad (2.38)$$

In addition, the total energy dissipation due to the deformation \mathcal{D} can be obtained

$$\mathcal{D} = \mathcal{W} - \int_{V_0} \dot{\Psi} dV_0 \quad (2.39)$$

where $\dot{\Psi}$ refers to the rate of stored energy per unit volume in the reference state.

2.1.5 Thermo-elasticity

The relations between mechanical and thermal energy is called thermo-elasticity, which can be derived using the first and second laws of thermodynamics. The 1st law of thermodynamics is the conservation of energy, which is formulated as

$$dU = dQ + dW. \quad (2.40)$$

where dU , dQ , and dW are the changes in the internal energy of the system, the heat absorbed by the system, and the work done on the system. The U and W can be expressed as

$$U = \int_V \rho \mathcal{U} dV, \quad \mathcal{W} = \frac{dW}{dt} \quad (2.41)$$

where \mathcal{U} is the internal energy density. According to the second law, the changes in the entropy of a reversible process (elastic deformation), dS at absolute temperature T is formulated as

$$dS = \frac{dQ}{T}. \quad (2.42)$$

Moreover, the change in the Helmholtz energy \mathfrak{A} is defined as

$$d\mathfrak{A} = dU - SdT - TdS. \quad (2.43)$$

At a constant temperature, the change in Helmholtz energy is equal to the change in the work done on the system $dW = d\mathfrak{A}$. In the small displacement dl of solid-like structures, dW due to force f can be written by

$$dW = fdl - p_h dV, \quad (2.44)$$

where p_h and dV denote the hydro-static pressure and the volume change. In the case of incompressible material like elastomers, dV can be neglected. So, the force of an isothermal process can be obtained using Eq. 2.43 and Eq. 2.44 as

$$f = \frac{dU}{dl} - T \frac{dS}{dl}. \quad (2.45)$$

The first part of Eq. 2.45 represents the energetic interactions of a single molecule or the volume change of the body [18]. However, experimental evidences suggest that the contribution of energetic force in the total force is negligible in moderate and large deformations of elastomers. Thus, the force of the system can be approximated only by entropy component as

$$f = -T \frac{dS}{dl}. \quad (2.46)$$

For an entropic material, the Helmholtz free energy required to perturb the entropy of the system is

$$d\mathfrak{A} = -TdS. \quad (2.47)$$

2.2 Thermodynamic Consistency

According to the second law of thermodynamic that is used in continuum mechanics, elastic energy of the system mainly increases due to the decrease in entropy, which is known as Clausius-Duhem inequality

$$\mathcal{D} \geq 0. \quad (2.48)$$

The constitutive model is thermodynamically consistent if and only if Clausius-Duhem inequality is satisfied on all points of body at any time. In other words, the energy balance should be satisfied during a thermodynamical deformation process. The energy balance can be rewritten by substituting Eq. 2.40 to Eq. 2.34 as

$$\dot{K} - P = \frac{d}{dt}(U - Q) = \dot{U} - \dot{Q}, \quad (2.49)$$

where the thermal power \dot{Q} is defined as

$$\dot{Q} = \int_V \rho \mathcal{Q} dV - \int_A \rho \mathbf{q} \cdot \mathbf{n} dA. \quad (2.50)$$

In Eq. 2.50, \mathcal{Q} and \mathbf{q} are the transferred heat and the surface heat flux per unit of mass, respectively.

Moreover, Eq. 2.49 can be rewritten as

$$\boldsymbol{\sigma} : \mathbf{l} = \rho \dot{\mathfrak{A}} - \rho \mathcal{Q} + \text{div } \mathbf{q}. \quad (2.51)$$

Therefore, Clausius-Duhem inequality can be obtained by

$$\rho \mathcal{D} = \rho T \dot{\mathcal{S}} - (\rho \mathcal{Q} - \operatorname{div} \mathbf{q}) \geq 0, \quad (2.52)$$

where \mathcal{S} is the entropy density. Clausius-Duhem inequality can be further simplified by substitution of the energy balance law (2.51) and mass conservation ($\rho_0 = J\rho$) as

$$\mathcal{D} = T \dot{\mathcal{S}} - \left(\dot{\mathcal{U}} - \frac{1}{\rho_0} \mathbf{P} : \dot{\mathbf{F}} \right) \geq 0. \quad (2.53)$$

considering the stored energy density per unit of reference volume $\Psi = \hat{\Psi}(\mathbf{F}, T, \mathbf{\Omega})$ as a function of set of internal variables $\mathbf{\Omega}$. In most of the constitutive models, the internal variables have been adopted to describe the history dependent dissipative effects. Note that all the quantities of the Clausius-Duhem inequality, such as \mathcal{S} , \mathbf{q} , and \mathbf{P} should be functions of internal variables. For a more comprehensive review of thermo-elasticity, the reader is referred to [19, 20]. Substituting the Helmholtz free energy $\Psi = \rho_0(\mathcal{U} - T\mathcal{S})$ into Eq. 2.53 results in

$$\rho J \mathcal{D} = -\dot{\Psi} - \rho J S \dot{T} + \mathbf{P} : \dot{\mathbf{F}} \geq 0 \quad (2.54)$$

where $\dot{\Psi}(\mathbf{F}, T, \mathbf{\Omega})$ can be obtained as

$$\dot{\Psi} = \frac{\partial \Psi}{\partial \mathbf{F}} : \dot{\mathbf{F}} + \frac{\partial \Psi}{\partial T} \dot{T} + \frac{\partial \Psi}{\partial \mathbf{\Omega}} \cdot \dot{\mathbf{\Omega}}. \quad (2.55)$$

Eq. 2.54 can be rewritten considering Eq. 2.55 as

$$\rho J \mathcal{D} = -\frac{\partial \Psi}{\partial T} \dot{T} - \frac{\partial \Psi}{\partial \mathbf{\Omega}} \cdot \dot{\mathbf{\Omega}} - \rho J S \dot{T} + \left(\mathbf{P} - \frac{\partial \Psi}{\partial \mathbf{F}} \right) : \dot{\mathbf{F}} \geq 0. \quad (2.56)$$

Eq. 2.56 can be further simplified for the case of isothermal process and considering a physical expression for the first Piola-Kirchhoff stress $\mathbf{P} = \frac{\partial \Psi}{\partial \mathbf{F}}$, which leads to an inequality of internal

energy dissipation \mathcal{D} as

$$-\frac{\partial \Psi}{\partial \Omega} \cdot \dot{\Omega} \geq 0. \quad (2.57)$$

This inequality must always be satisfied over the body during deformation.

2.3 Incompressible Materials

Resistance of most of elastomers to change volume known as incompressibility condition should be considered in the constitutive modelling. Therefore, the internal energy function of an incompressible material is modified by

$$\Psi = \hat{\Psi}(\mathbf{F}, T, \Omega) - p(J - 1), \quad (2.58)$$

where $J = \det \mathbf{F} = \frac{dV}{dV_0} = 1$ is the incompressibility constraint and p is a Lagrange multiplier to satisfy the boundary conditions. The rate of the strain energy function Ψ is

$$\dot{\Psi} = \left(\frac{\partial \Psi(\mathbf{F}, T, \Omega)}{\partial \mathbf{F}} - p \mathbf{F}^{-T} \right) : \dot{\mathbf{F}}, \quad (2.59)$$

where the incompressibility condition is considered as the volume remains constant, $\dot{V} = \dot{J} = 0$. Substituting Eq. 2.59 to Eq. 2.39, one has

$$\left(\int_{V_0} \mathbf{P} dV_0 - \int_{V_0} \left(\frac{\partial \hat{\Psi}(\mathbf{F}, T, \Omega)}{\partial \mathbf{F}} - p \mathbf{F}^{-T} \right) dV_0 \right) : \dot{\mathbf{F}} \geq 0. \quad (2.60)$$

Eq. 2.61 should be held for every deformation rate, $\dot{\mathbf{F}}$, which leads to

$$\mathbf{P} = \frac{\partial \hat{\Psi}(\mathbf{F}, T, \Omega)}{\partial \mathbf{F}} - p \mathbf{F}^{-T}, \quad (2.61)$$

This equation is valid for the case of

- Incompressible hyperelastic material

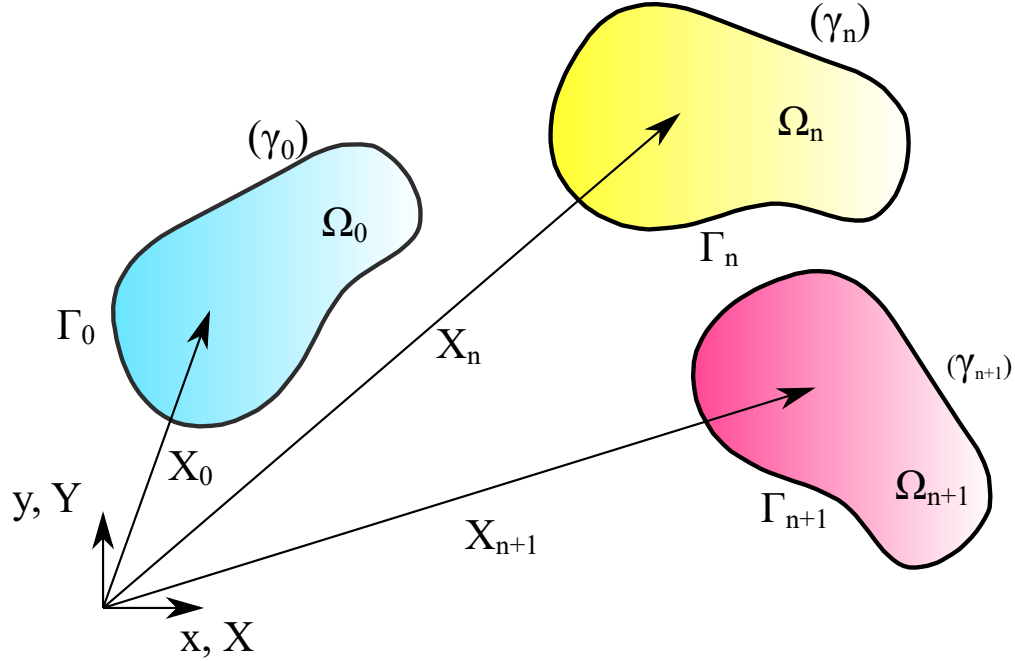


Figure 2.1: The schematic figure of continuum domain in the different configuration; initial γ_0 , current γ_n , and incremental configuration γ_{n+1} .

- Negligible contribution of internal energy in deformation
- Isothermal deformation
- Moderate and large range of deformation

2.4 Nonlinear Finite Element Analysis

The macro-scale in the multi-scale framework is assumed as a continuum body (see Fig. 2.1), which is analyzed using the nonlinear finite element method. Accordingly, by considering the reference configuration, the governing equilibrium equation of the continuum body can be expressed as

$$\nabla \cdot \mathbf{P} + \mathbf{b} = 0, \quad (2.62)$$

where the \mathbf{P} is used to denote the first Piola-Kirchhoff stress tensor, and \mathbf{b} represents the body force in the reference configuration. In this study, the following fonts are used, X for scalar, \mathbf{X} represents vector, \mathbf{X} for second-order tensor, and \mathbb{X} for fourth-order tensor.

The weak form of Eqn. 2.62 can be achieved by multiplying a virtual displacement δU to its both side and then integrating over the domain in the initial configuration Ω_0 which could be written as

$$\int_{\Omega_0} \delta U^T (\nabla \cdot \mathbf{P} + \mathbf{b}) d\Omega_0 = 0. \quad (2.63)$$

oBy applying the Divergence theorem, Eqn. 2.63 can be rewritten as

$$\int_{\Omega_0} \frac{\partial \delta U^T}{\partial \mathbf{x}_0} \mathbf{P} d\Omega_0 = \int_{\Gamma_t} \delta U^T \bar{\mathbf{t}} d\Gamma + \int_{\Omega_0} \delta U^T \mathbf{b} d\Omega_0, \quad (2.64)$$

where $\bar{\mathbf{t}}$ denotes the the applied traction on the surface Γ_t , and \mathbf{x}_0 is the displacement vector in reference configuration. Generally, the total or updated Lagrangian description can be utilized to solve the Eqn. 2.64. Defining the state variable at the known step is n , the variable at step $n + 1$ is what needed to be determined. Different from the updated Lagrangian description, where the state variable at $n + 1^{th}$ step is resolved by the previous step n , the state variable in the total Lagrangian description are obtained at step $n + 1$ with respect to the initial configuration. The schematic description of the initial configuration n , and incremental configuration of step $n + 1$ is represented in Fig. 2.1. Here, the Lagrangian description is adapted to the analysis of the macro domain. Hence, Eqn.2.64 can be expressed as

$$\int_{\Omega_n} \frac{\partial \delta U^T}{\partial \mathbf{x}_n} \mathbf{P} d\Omega_n = \int_{\Gamma_t} \delta U^T \bar{\mathbf{t}} d\Gamma + \int_{\Omega_n} \delta U^T \mathbf{b} d\Omega_n, \quad (2.65)$$

where, the term $\partial \delta U^T / \partial \mathbf{x}_n$ is the deformation gradient in the updated Lagrangian description $\delta \mathbf{F}_n$. Hence, the Eqn .2.65 could be rewritten as

$$\int_{\Omega_n} \delta \mathbf{F}_n : \mathbf{P} d\Omega_n = \int_{\Gamma_t} \delta U^T \bar{\mathbf{t}} d\Gamma + \int_{\Omega_n} \delta U^T \mathbf{b} d\Omega_n. \quad (2.66)$$

Due to the non-symmetric nature of first PK stress \mathbf{P} , the nodal forces are generally expressed in terms of second PK stress $\mathbf{S} = \mathbf{F}_n^{-1} \mathbf{P}$. Having the second PK stress, and its work conjugate strain

$\mathbf{E} = \frac{1}{2}(\mathbf{F}_n^T \mathbf{F}_n - 1)$, one can rewrite Eqn. 2.66 as

$$\int_{\Omega_n} \delta \mathbf{E}_n : \mathbf{S} d\Omega_n = \int_{\Gamma_t} \delta \mathbf{U}^T \bar{\mathbf{t}} d\Gamma + \int_{\Omega_n} \delta \mathbf{U}^T \bar{\mathbf{b}} d\Omega_n. \quad (2.67)$$

Furthermore, it should be noted that the Green strain tensor \mathbf{E} is the summation of linear and nonlinear terms, which can be written as

$$\mathbf{E} = \mathbf{E}_L + \mathbf{E}_{NL} = \mathbf{E}_L + \frac{1}{2} \mathbf{A}_\theta \cdot \theta, \quad (2.68)$$

where \mathbf{E}_L and \mathbf{E}_{NL} are used to define two-dimensional plane stress/strain problems as

$$\mathbf{E}_L = \begin{bmatrix} \frac{\partial u}{\partial x_n} \\ \frac{\partial v}{\partial y_n} \\ \frac{\partial u}{\partial y_n} + \frac{\partial v}{\partial x_n} \end{bmatrix},$$

$$\mathbf{E}_{NL} = \begin{bmatrix} \frac{1}{2} \left(\frac{\partial u}{\partial x_n} \right)^2 + \frac{1}{2} \left(\frac{\partial v}{\partial x_n} \right)^2 \\ \frac{1}{2} \left(\frac{\partial u}{\partial y_n} \right)^2 + \frac{1}{2} \left(\frac{\partial v}{\partial y_n} \right)^2 \\ \frac{\partial u}{\partial x_n} \frac{\partial u}{\partial y_n} + \frac{\partial v}{\partial x_n} \frac{\partial v}{\partial y_n} \end{bmatrix} = \frac{1}{2} \begin{bmatrix} \frac{\partial u}{\partial x_n} & \frac{\partial v}{\partial x_n} & 0 & 0 \\ 0 & 0 & \frac{\partial u}{\partial y_n} & \frac{\partial v}{\partial y_n} \\ \frac{\partial u}{\partial y_n} & \frac{\partial v}{\partial y_n} & \frac{\partial u}{\partial x_n} & \frac{\partial v}{\partial x_n} \end{bmatrix} \begin{bmatrix} \frac{\partial u}{\partial x_n} \\ \frac{\partial v}{\partial x_n} \\ \frac{\partial u}{\partial y_n} \\ \frac{\partial v}{\partial y_n} \end{bmatrix} \equiv \frac{1}{2} \mathbf{A}_\theta \cdot \theta \quad (2.69)$$

Implementing the standard finite element method in line with the Galerkin discretization approach, the shape functions N can be applied to approximate the displacement field within each element as $\mathbf{U} = N \bar{\mathbf{U}}$. Taking variation from Eqn. 2.68 results in

$$\delta \mathbf{E} = \mathbf{B}_L \delta \bar{\mathbf{U}} + \mathbf{A}_\theta \mathbf{G} \delta \bar{\mathbf{U}} = (\mathbf{B}_L + \mathbf{B}_{NL}) \delta \bar{\mathbf{U}} \equiv \mathbf{B} \delta \bar{\mathbf{U}}, \quad (2.70)$$

where \mathbf{B}_L and \mathbf{G} are matrices that contain the derivatives of shape functions which can be written

in terms of the node j as

$$\mathbf{B}_L^j = \begin{bmatrix} \frac{\partial N_j}{\partial x_n} & 0 \\ 0 & \frac{\partial N_j}{\partial y_n} \\ \frac{\partial N_j}{\partial y_n} & \frac{\partial N_j}{\partial x_n} \end{bmatrix} \quad \text{and} \quad \mathbf{G}^j = \begin{bmatrix} \frac{\partial N_j}{\partial x_n} & 0 \\ 0 & \frac{\partial N_j}{\partial x_n} \\ \frac{\partial N_j}{\partial y_n} & 0 \\ 0 & \frac{\partial N_j}{\partial y_n} \end{bmatrix} \quad (2.71)$$

Substituting Eqn. 2.70 into Eqn. 2.67, one can obtain the governing equation of the finite element analysis by

$$\boldsymbol{\Psi}(\bar{\mathbf{U}}) = \mathbf{f}_{int} - \mathbf{f}_{ext} = \int_{\Omega_n} \mathbf{B}^T \mathbf{S} d\Omega - \left(\int_{\Gamma_t} \mathbf{N}^T \bar{\mathbf{t}} d\Gamma + \int_{\Omega} \mathbf{N}^T \mathbf{b} d\Omega \right) = 0, \quad (2.72)$$

where the term $\boldsymbol{\Psi}(\bar{\mathbf{U}})$ is the residual force vector which can be divided into two parts namely; the internal force \mathbf{f}_{int} and external force \mathbf{f}_{ext} . Besides, due to the nonlinear nature of Eqn. 2.72, it should be solved iteratively. Hence, the Newton-Raphson scheme is utilized as

$$\boldsymbol{\Psi}_{n+1}^{i+1}(\bar{\mathbf{U}}) = \boldsymbol{\Psi}_{n+1}^i(\bar{\mathbf{U}}) + d\boldsymbol{\Psi} \simeq 0, \quad (2.73)$$

where, the i^{th} iteration of Newton-Raphson method is denoted using the superscript i , and the subscript n represents the n^{th} step of simulation process. Besides, the residual force term $d\boldsymbol{\Psi}$ can be delivered with

$$d\boldsymbol{\Psi} = \int_{\Omega_n} \mathbf{B}^T \mathbf{S} d\Omega + \int_{\Omega_n} \mathbf{B}^T d\mathbf{S} d\Omega. \quad (2.74)$$

Having the material property tensor \mathbb{C}_{SE} aligned with the 2^{nd} Piola-Kirchhoff stress and Green strain and constitutive relation as $d\mathbf{S} = \mathbb{C}_{SE} : d\mathbf{E}$, one can rewrite the residual force term $d\boldsymbol{\Psi}$ in terms of nodal displacement. Accordingly, by substituting Eqn. 2.70 into Eqn. 2.74, and having \mathbb{C}_{SE} in plane stress/strain condition as C , $d\boldsymbol{\Psi}$ can be written as

$$d\boldsymbol{\Psi} = \left(\int_{\Omega_n} \mathbf{G}^T \mathbf{M}_S \mathbf{G} d\Omega + \int_{\Omega_n} \mathbf{B}^T C \mathbf{B} d\Omega \right) d\bar{\mathbf{U}} = (\mathbf{K}_{geo} + \mathbf{K}_{mat}) d\bar{\mathbf{U}} \equiv \mathbf{K}_T d\bar{\mathbf{U}}, \quad (2.75)$$

where \mathbf{K}_T is the tangential stiffness matrix which can be decomposed into two distinct matrices namely; the geometric stiffness matrix \mathbf{K}_{geo} and the material stiffness matrix \mathbf{K}_{mat} . The symmetric matrix \mathbf{M}_S comprising the 2^{nd} PK stresses in Eqn. 2.75 can be composed as

$$\mathbf{M}_S = \begin{bmatrix} \mathbf{S}_{11}\mathbf{I}_{2 \times 2} & \mathbf{S}_{12}\mathbf{I}_{2 \times 2} \\ \mathbf{S}_{21}\mathbf{I}_{2 \times 2} & \mathbf{S}_{22}\mathbf{I}_{2 \times 2} \end{bmatrix}, \quad (2.76)$$

where \mathbf{I} is the identity matrix. The linearized system of equations can be achieved by substituting Eqn.2.75 into Eqn.2.73 which results in

$$\mathbf{K}_T d\bar{\mathbf{U}} = -\Psi_{n+1}^i(\bar{\mathbf{U}}). \quad (2.77)$$

It should be noted that the tangential stiffness matrix is a function of the 2^{nd} PK stress tensor and material property matrix C , which is obtained by a multi-scale approach from the statistical mechanics of polymer chains.

CHAPTER 3

A Multi physics Constitutive Model to Predict Hydrolytic Aging in Quasi static Behaviour of Thin Cross linked Polymers

3.1 Introduction

In view of the high resistance to abrasion, corrosion, and chemical degradation, elastomers are widely used in many sensitive applications to transfer load in high deformation regimes or to dissipate kinetic energy in high frequency. In many industrial applications, it is necessary to provide a realistic approximation of the nominal service life of a sample subjected to a specific loading profile. In many cases, elastomers are expected to sustain millions of load cycles or sustain extreme environmental loads for years, if not decades. However, environmental factors along with the mechanical loads will contribute to chemo-physical damages that will eventually lead to material failure [21]. Understanding the relation between chemical damages and decay in mechanical performance is critical for the prediction of elastomer failure in extreme applications, such as offshore platforms. Such decay can be formed due to an individual or combined effects of different degradation processes [22]. Those mechanisms can be categorized into those with the major impacts such as thermo-oxidation [23, 24], hygro-thermal [25], hydrolysis [26, 27], deformation-induced aging [28, 29, 30] , and those with the less severe impact such as chemical corrosion [13], and ozone cracking [14]. While each of those mechanisms can significantly reduce the life of elastomeric material in a certain condition, the latter group is not as prevalent in nature as those of the first group are. The aging process can be formed due to an individual or combined effects of different degradation processes such as thermos-oxidation, photo-oxidation, and hydrolysis [31]. While predicting the individual contribution of those mechanisms has been the center of attention in the last few years, there is still a long way to go in modeling the damage accumulation in materials

exposed to multiple damages simultaneously.

Elastomeric systems are used in a variety of applications ranging from tires to adhesives, sealants, and thin films [32]. In view of their excellent properties, e.g. abrasion resistance and durability, elastomeric components can be reliably designed to be subjected to a high number of cyclic loading in harsh environments. However, their reliability considerably decreases over time due to the so-called aging process. The aging process, often described by a gradual decay of the mechanical performance, is a menace to the polymeric components such as joints, adhesives, sealant,s and fillers that are used in different components in multiple applications.

In the last 15 years, our predictive abilities have been significantly improved, and many theories have been developed to describe different aging mechanisms, most of which were focused on thermo-oxidative aging. To this end, Loeffel and Anand [33] investigated a multi-physics model for the thermal oxidation aging of coatings in severe operating conditions. Some approaches described the thermo-oxidative aging of a polymer matrix with respect to the chemical reactions, diffusion and mechanical coupling [34, 35, 36], and some described it using the mechanism of curing [37, 38]. In all the aforementioned studies, the damage has been micro-mechanically modeled by a coupled approach to link chemical/physical aging to the thermo-mechanical state of the network [39, 40].

The effect of time on the constitutive behaviour of elastomers is often described by visco-elastic behavior, which is more of the short-term effects of time [41, 42, 43]. Visco-elastic properties have been studied extensively both theoretically [44, 45, 46] and experimentally [47]. Ayoub et al. [48] proposed a constitutive model using a Zener-type framework. Their model predicts the behavior by integrating the physics of polymer chains and their alteration under cyclic loading. Furthermore, Khan et al. [49] proposed a phenomenological model to characterize the thermo-mechanical behavior of visco-elastic polymers.

Here, we mainly focus on the Quasi-static behaviour of samples submerged in water for a long time (hydrolytic aging) [50], e.g. those used in off-shore plants, biological systems or within the cooling systems [51]. At this stage, the model cannot take into account the effects of loading

frequency as well as visco-elastic effects. In such applications, the predictive models can prevent catastrophic failure of the systems due to the aging of components. To this end, a model for hydrolytic aging and its effect on the mechanical properties of rubber-like material can be subject to broader interest in our community. Hydrolytic aging can be described in two categories: physical or chemical [52]. Physical aging has no effect on the chemical structure and is a result of the movement of polymer chains. Chemical aging, on the other hand, is an irreversible process that changes the morphology of the matrix and directly affects the mechanical performance of the sample and the probability of premature failure.

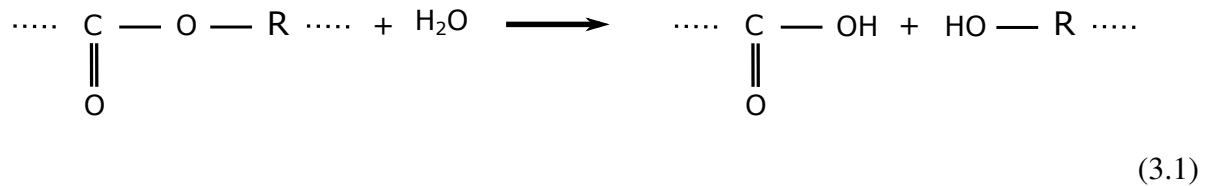
Hydrolytic aging has been mostly studied through experimental studies. So far, only a few phenomenological models, and no micro-mechanical model, are available that can successfully take into account the effect of hydrolytic aging on the behavior of elastomeric materials. Vieira et al. [53] proposed a model for hydrolytic aging of PLA-PCL fibers used in surgeries, and Breche et al. [54] who used a non-linear visco-elastic model to predict the response of biodegradable materials throughout hydrolytic aging. From the experimental side, several studies were conducted to explore the relation between hydrolytic aging and loss of mechanical performance in different materials, such as polyester urethane [55], and thermoplastic polyurethanes [56]. On another approach, many studies were focused on describing the correlation between aging and changes of the matrix morphology, such as molecular weight [57], cross-link density [58] and formation/detachment of cross-links [59].

In this work, a new micro-mechanical model is developed to predict the non-linear behavior of rubber-like materials such as the Mullins effect and Permanent set during hydrolytic aging. "Mullins effect" refers specifically to the softening observed between the first loading and the subsequent reloadings. However, for the sake of simplicity, many models [60, 61, 62] exclude the difference between unload and reload, and thus come up with a stabilized stress-strain curve that has considerably less noise for fitting. The stabilized softening is often referred to as the Idealized Mullins effect [63], and our model is also developed to predict this behaviour. The fundamentals of hydrolysis kinetics and assumptions are first discussed in Section 3.2. Then, the experimental

study is presented in Section 5.2. Next, in section 5.3, the constitutive model is presented. After a parameter study in section 3.5, an evaluation of the proposed model in comparison to our experimental data and other sets available in the literature is presented (section 6.4). Finally, the summary and discussion are provided in section 3.7.

3.2 Hydrolysis Kinetics and Assumptions

Hydrolytic aging results from the interaction of elastomer matrix with the hydroxyl(OH⁻) or hydrogen(H⁺) ions in water [64]. In general, this process can occur in any media with OH⁻ or H⁺ e.g. acids or alkaline, while the hydrolysis reaction rate is influenced mainly by ions concentration. Esters, amide, imide, and carbonates are particularly vulnerable to hydrolysis which occurs during water attack. Regardless of the location of those groups in macro-molecules, hydrolytic attack of water molecules to those groups can cause chain scission which consequently leads to the production of carboxylic and alcohol end-groups (see Eq.3.1). Thus aging results in increased concentration of carboxylic end-groups. On the other hand, hydrolytic attack reduces the molecular weight of the matrix, which consequently, influences the mechanical behaviour.



Kinetic equations are mathematical models to predict and describe a chemical reaction. In this respect, the hydrolysis process can be best modeled via a first-order kinetic equation with respect to the carboxylic end groups' formation rate[57]

$$\frac{d[\text{COOH}]}{dt} = \zeta[\text{Ester}][\text{Water}][\text{COOH}] = \mathcal{K}[\text{COOH}], \quad (3.2)$$

where $[\text{COOH}] = [\text{COOH}]_0 \exp(\mathcal{K}t)$. Here, the [Ester],[Water], and [COOH] are the concentrations of ester, diffused water, and carboxyl end-groups in the polymer matrix, respectively. The

parameter ζ is the hydrolysis constant which defines the rate of hydrolytic attack \mathcal{K} . Here, t is the time variable, and subsequently, we define the subscript \bullet_0 to represent the magnitude of a non-kinematic parameter at $t = 0$, e.g. $[COOH]_0$ represents the initial concentration of carboxylic group. Since carboxyl end group concentration is inversely related to number-average molecular weight M_n , one can determine \mathcal{K} by measuring M_n during hydrolytic aging using

$$[COOH] = \frac{1}{M_n} \Rightarrow M_n = M_{n,0} \exp(-\mathcal{K}t). \quad (3.3)$$

In view of Eq.3.3, the factors that influence the hydrolysis rate \mathcal{K} are the [Ester], [Water], [COOH] and the hydrolysis constant ζ which itself is a function of temperature, and media's pH, where

- temperature increases the polymer chain mobility and thus increases the ζ [53]
- PH of the degradation environment affects reaction rates through catalysis. and thus increases the ζ [65, 66, 67]

In this study, ζ is assumed to be constant since the temperature, and the PH were kept constant. Accordingly, the proposed model in this work is based on the following assumptions

- The process of water diffusion into the sample is considered to be complete and thus $\frac{d[Water]}{dt} = 0$. In fact, the proposed model is based on the assumption that the water diffusion time t_{diff} inside the sample is significantly smaller than the hydrolytic aging time t_{aging} (i.e. $t_{diff} \ll t_{aging}$) [68]. The proposed model is mainly relevant for super-thin samples where the assumption of homogeneous diffusion is relevant. Here, we will not investigate inhomogeneous water diffusion due to the sample thickness. Accordingly, all experiments used for validation were performed on super-thin samples (thickness $< 2mm$) that are stored for a duration much longer than a few minutes [69].
- Following completion of water diffusion, the water concentration all over the sample is identical and equal to the maximum saturation level possible $[Water]_{S \in V} =$ where V represents the sample volume.

- The model is not valid for short time intervals or ultra thick samples in which $\nabla[Water] \neq 0$ [70].
- Likewise, the concentration of the ester groups $[Ester]$ located at the backbone chains are considered to be almost constant, despite their random scission during the early stages of the aging process [71].

Satisfying the conditions used for the assumption of constant ζ , $[Ester]$ and $[water]$, one can derive the setting at which we can assume \mathcal{K} to be constant. Obviously, this assumption is not relevant in cases where ζ , $[Ester]$ and $[water]$ are non-constant, such as non-uniform water diffusion or varying temperature, and those conditions are not the subject of interest in this work.

3.3 Experiment

Material: Styrene-butadiene rubber (SBR) procured in rectangular sheets of 24" \times 12" \times 0.125" were used for validation of the model. The SBR sheets were processed from one batch and provided by one supplier. Standardized dumbbell shape samples were cut from the sheets with a punch die (Die C from the ASTM-D412).

Accelerated aging: Samples were fully immersed in several sealed containers filled with distilled water at temperatures 60°C and 80°C under constant pressure. After a specific aging time, samples were removed and dried at room temperature (i.e. 23°C) for ten days before characterization.

Gravimetric measurement: To measure water uptake, each sample was individually weighed before and after aging/drying with an accuracy of 0.01mg. Samples were aged in two individual ovens (i.e. 60°C & 80°C) for 1, 10, and 30 days each. Immediately after aging, the samples were carefully dried with tissue paper and weighed on the same electronic balance. In this respect, the percentage of the water uptake W_C can be written as

$$W_c = \frac{W_t - W_0}{W_0} \times 100 \quad , \quad (3.4)$$

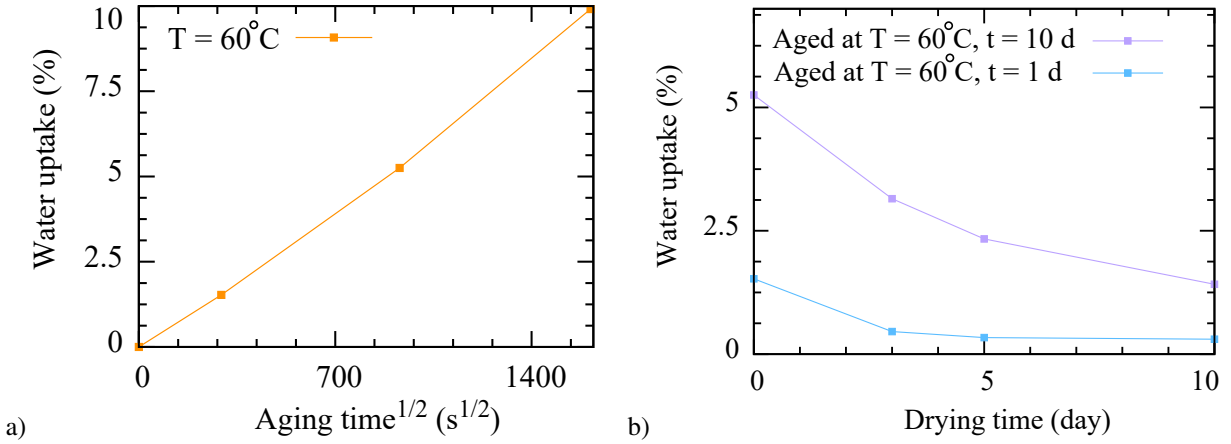


Figure 3.1: Water content of samples (a) extent of water absorption versus the square root of hydrolytic aging time for 60°C aging temperature, and (b) the loss of absorbed water versus drying time for aged samples.

where W_t and W_0 are the sample weights at time t and virgin state, respectively. Fig. 3.1a is the plot of the water absorption content versus the square root of hydrolytic aging time for the aging temperature of 60°C. Our data shows that the water uptake is linearly correlated with the square root of aging time (i.e. $W_c \propto \sqrt{t}$), representing that it follows Fick's second law [72].

In order to investigate the efficacy of the drying process, the aged samples were kept at ambient temperature (i.e. 23°C) and their weights W_{t^*} were recorded at three different drying times t^* (i.e. 3, 5, and 10 days). For each case, all the weights were then compared with the weight of the virgin sample by substituting W_t with W_{t^*} in Eq.3.4. Fig. 3.1b shows the loss of absorbed water along the drying period for two different accelerated aging conditions. The water maintained in the sample reduced exponentially with time and after 10 days, the water content nearly reached its equilibrium value.

Mechanical test: United testing machine SFM-20 with a load cell of 1000 lb. was used for quasi-static tensile tests. All tests were displacement controlled with the strain rates of 43.29 $\frac{\%}{min}$. The distance between the machine grips was set to 2.71 inches and all the experiments were performed at room temperature. In monotonic failure tests, the samples were stretched until breakage while in the cyclic test, the samples were stretched to preset amplitudes of 1.3, 1.6, 1.9, and 2.1. Each sample is subjected to a non-relaxing cyclic test with increasing amplitude, where

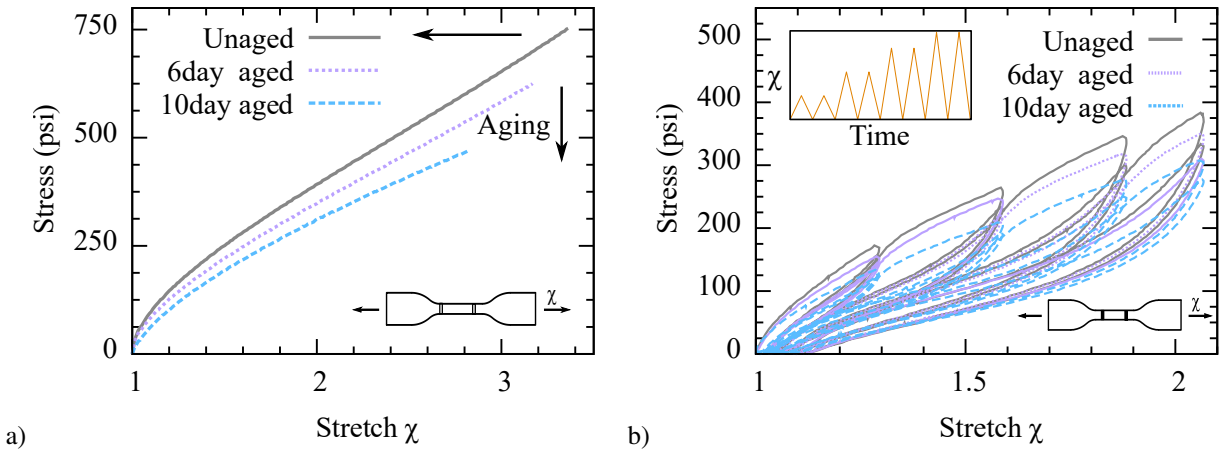


Figure 3.2: Constitutive behaviour of the dog-bone SBR sample at various aging times shown in (a) failure, and (b) cyclic tests that were performed at 60°C.

the samples are loaded two times at each amplitude. In the course of deformation, the elongation of the central zone has been measured by an external extensometer (see Fig. 3.2). The cyclic experiment is designed to illustrate the evolution of the permanent set and stress softening during the primary loading for both unaged and aged samples.

Data treatment: The aim of the present work is the modeling of the nonlinear inelastic phenomena such as *permanent set*, *idealized Mullins effect* during hydrolytic aging. To this end, the experimental data must be treated to highlight the characteristics of these inelastic features. To derive the idealized Mullins effect, the following data treatment will be applied to the experimental data

- The difference between the reloading and unloading curves will be skipped (see Fig. 3.3a).
- The unloading responses are extended to meet the primary loading that is obtained from the monotonic tensile test. The maximum stress is set to that of the maximum stretch in loading history.

The modified experimental results for unaged and aged SBR at 60°C are presented in Fig. 3.3b. In this figure, the dashed lines refer to the result of monotonic tensile tests and are considered as the primary loading curves. The solid lines are referred to as the secondary curves which correspond to the unloading curves. Each sample experiences a continuous cyclic test regime with increasing

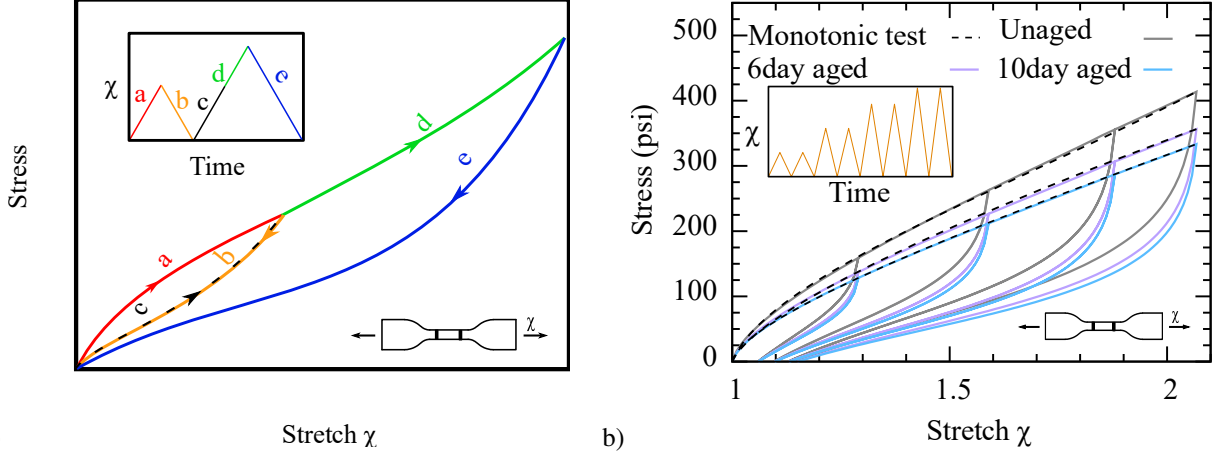


Figure 3.3: (A) a schematic diagram of idealized Mullins effect, and (b) the treated experimental results of SBR at 60°C for modeling purposes. dashed lines refer to the result of the monotonic tensile tests, while solid lines refer to the result of cyclic tests.

stretches in each cycle. The experimental data after the above-mentioned treatment will be used as the basis for the discussion on the modeling of inelastic phenomena such as *idealized Mullins effect and permanent set* in rubber-like material during hydrolytic aging.

3.4 Constitutive Model

Damage in the polymer matrix should be described with respect to three independent variables temperature T , time t , and deformation which is given by deformation gradient tensor \mathbf{F} . To describe the state of damage with respect to time, one can use the status of the matrix at time 0 and ∞ as the reference points and then define a shape function to interpolate the damage status at time t . Representing the energy of the matrix in the virgin state by Ψ_0 and after indefinite aging time by Ψ_∞ , one can approximate the strain energy of the matrix Ψ_M at time t as

$$\Psi_M(t, T, \mathbf{F}) = N(t, T)\Psi_0(\mathbf{F}) + N'(t, T)\Psi_\infty(\mathbf{F}), \quad (3.5)$$

where $N(t, T)$ and $N'(t, T) = 1 - N(t, T)$ represent the weight of each state. To define the changes of the matrix in the course of hydrolytic aging, one needs to describe the matrix degradation with respect to the shape function N and the energy states Ψ_0 , and Ψ_∞ . By representing the evolution

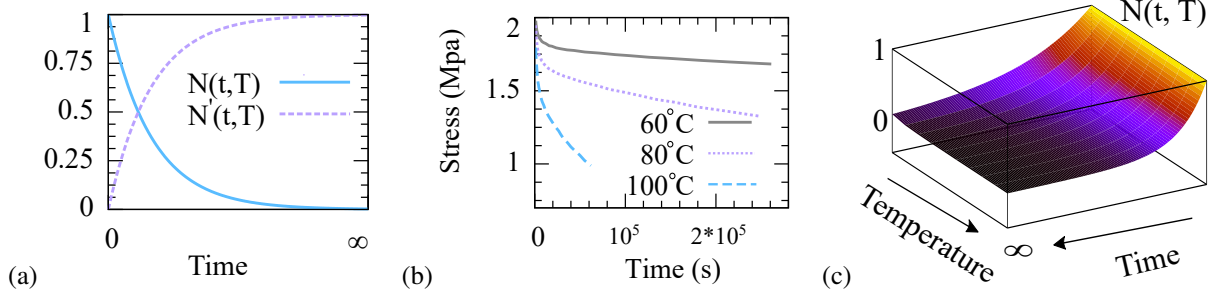


Figure 3.4: (a) Shape functions in one dimension using Arrhenius function, and (b) Relaxation tests designed to capture the changes in the stress during a deformation controlled aging scenario [24] , and (c) the reconstructed surface of $N(t, T)$.

of the shape function by the Arrhenius function [73], one can write $N(t, T)$

$$N(t, T) = \exp \left(-\gamma \exp \left(-\frac{E_a}{\mathcal{R}T} \right) t \right), \quad (3.6)$$

where γ is the degradation constant that defines the rate of hydrolytic aging, E_a the activation energy, and $\mathcal{R} = 8.314 [J]/[mol][K]$ the gas constant (see Fig. 3.4a).

Experimental Derivation of $N(t, T)$ can be carried out through specific relaxation tests, in which samples were aged at constant stretch amplitude for an indefinite time. The changes of the mechanical response from time 0 to ∞ can be associated with the energy states of the material, namely Ψ_0 and Ψ_∞ . Having the test results at multiple temperatures, the resulting curves can be used to derive the 3D surface of the $N(t, T)$ directly from the experimental data. *Similar approach can be used in other types of aging including, thermo-oxidative or photo-oxidative.* For example, by considering similar tests that were performed by Johlitz et al [24] on thermo-oxidative aging (see Fig. 3.4b), one can derive the 3D surface of $N(t, T)$ directly from the experiments (see Fig. 3.4c). However, in view of the excessive costs associated with relaxation tests, especially in hydrolysis conditions, we introduced another approach to approximate $N(t, T)$ based on simpler experiments and a fitting procedure.

In the matrix of rubber-like materials, the polymer macro-molecules are often cross-linked or bonded to aggregate surfaces at many points along their length. Thus, each macro-molecule

has been often bonded at many locations and forms multiple polymer strands which are named "chains" throughout this manuscript [74]. Here, the definition of a chain is considered as the whole or a part of a polymer molecule restricted between two constrained segments, which are either cross-linked or entangled with other chains or alternatively bonded to the aggregate surface. Considering that the length of an active chain is measured between two cross-linked regions along a polymer molecule, the less the cross-link density within a polymeric material, the lengthier the active chains will be. Accordingly, once water attacks the matrix, two parallel phenomena occur [58] (i) reduction of the cross-links which increases the average chain length in the matrix, and (ii) Energy dissipation due to the reduction of polymer active agents (see Fig. 3.5). To this end, a fully attacked matrix Ψ_∞ can be decomposed into two independent networks, namely a newly morphed network Ψ_m and a deactivated network Ψ_d as given below

$$\Psi_\infty = \alpha\Psi_m + (1 - \alpha)\Psi_d, \quad (3.7)$$

where Ψ_m and Ψ_d represent the energies of the morphed and deactivated networks, respectively. The morphed network results from the reduction of the unattacked network cross-links, and consequently, it has chains that are longer than those of the virgin matrix. Moreover, the deactivated network results from a water attack on polymer chains. Hence, in this network, the chain length distribution is similar to that of the original polymer matrix. The parameter α defines the contribution of each network. Substituting Eq.5.6 into Eq.5.3, one gets the total strain energy of the polymer matrix as

$$\Psi_M = N(t, T)\Psi_0 + \alpha N'(t, T)\Psi_m + (1 - \alpha)N'(t, T)\Psi_d. \quad (3.8)$$

Fig. 3.6 shows the evolution of the polymer matrix with respect to time. At time $t = 0$, the polymer matrix can be represented by Ψ_0 state only. As time passes, the contribution of Ψ_∞ grows which itself can be decomposed into two networks, m and d . This process continues until the contribution of Ψ_0 becomes negligible and $\Psi_M \approx \Psi_\infty$.

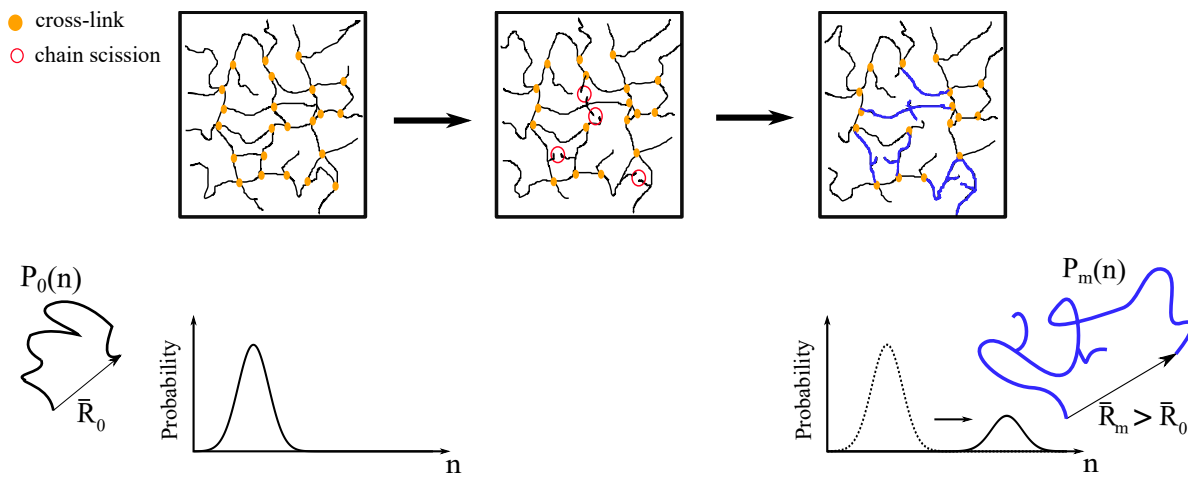


Figure 3.5: Development of longer chains due to chain scission.

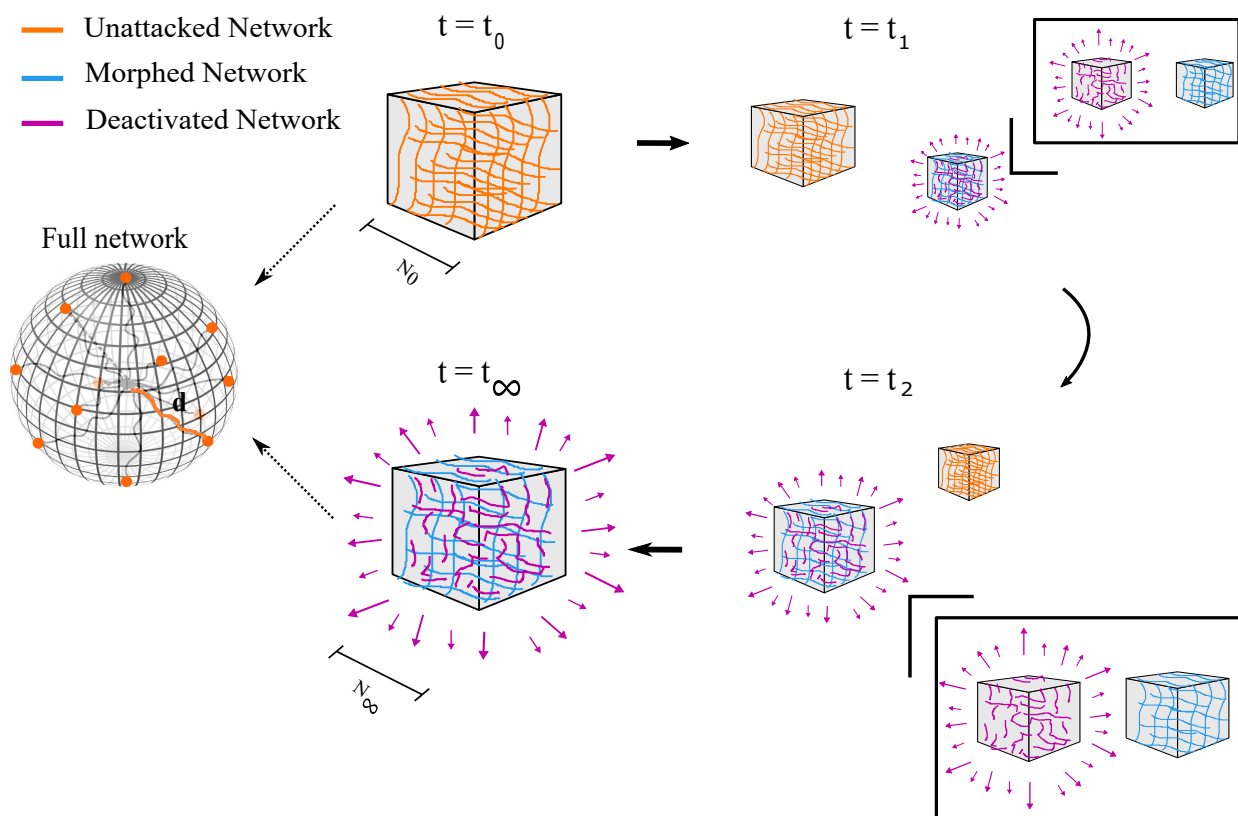


Figure 3.6: Evolution of the networks throughout hydrolytic aging (cube dimensions represent the number of their chains).

We assume that all chains that are exposed to water attack within the deactivated network will form free-end chains with no contribution to entropic energy, so $\Psi_d = 0$. So in Eq.3.8, Ψ_M is mainly determined by the energies of the other two networks, namely Ψ_0 and Ψ_m .

Networks and Sub-networks Each network is considered to have a unique composition and describes a specific energy-dissipating damage mechanism. Using the concept of micro-sphere,[75, 76] each network is considered as a 3D composition of infinite 1D sub-networks that are distributed in all spatial directions. Sub-networks can only be subjected to uni-axial deformation λ , and thus will experience different deformations based on their directions (see Fig. 3.6)[77, 78]. To develop a model for the sub-network in direction \mathbf{d} , only a simplified form of entropic energy is needed, with respect to uni-axial deformation, $\lambda^{\mathbf{d}}$. The parameter $\psi^{\mathbf{d}}$ represents the energy of the sub-network in an arbitrary direction, \mathbf{d} . Integrating a sub-network in all directions, the consequent network is a representation of that concept in a 3D configuration. Here, by assuming the isotropic spatial distribution of the polymer matrix in reference configuration, the macroscopic energy of an arbitrary network, Ψ_{\bullet} , can be written as

$$\Psi_{\bullet} = \frac{1}{A_s} \int_S \psi_{\bullet}^{\mathbf{d}} d\mathbf{u}^{\mathbf{d}} \cong \sum_{i=1}^k \psi_{\bullet}^{\mathbf{d}_i} w_i, \quad \Rightarrow \quad \psi_M^{\mathbf{d}} = N(t, T) \psi_0^{\mathbf{d}} + \alpha N'(t, T) \psi_m^{\mathbf{d}}, \quad (3.9)$$

where A_s is the surface area of a micro-sphere S , and $u^{\mathbf{d}}$ the unit area of the surface with the normal direction \mathbf{d} . The parameters w_i are weight factors corresponding to the collocation directions \mathbf{d}_i ($i = 1, 2, \dots, k$). A set of $k = 45$ integration points on the half sphere was found to yield the best optimization between computational expenses and the resulting error [79, 80]. Fig. 3.6 depicts the composition of the polymer matrix into the three networks 0 , m and d to describe hydrolysis-induced damages.

Probability Distribution Function of a Polymer Chain Assuming all sub-networks of each network to have the same composition of chains, one can derive a Gaussian probability function like $\mathcal{P}_{\bullet}(L|\sigma, \mu_{\bullet}, R_{\bullet})$ which holds for both network [81]. Here, $L = nl$ and R_{\bullet} represent the contour

length and the end-to-end distance of a polymer chain, while μ_{\bullet} and σ denote the mean and the standard deviation. Considering n to be the number and l to be the length of the segments, one can normalize L and R by segment length to achieve normalized length $n = \frac{L}{l}$, and $\bar{R}_{\bullet} = \frac{R_{\bullet}}{l}$. Moreover, considering \bar{R}_{\bullet} to be constant in each sub-network, the distribution function can be abstractly written as $\mathcal{P}_{\bullet}(n) := \mathcal{P}_{\bullet}(L|\sigma, \mu_{\bullet}, R_{\bullet})$ where

$$\mathcal{P}_{\bullet}(n) = \frac{1}{2\sqrt{\pi\sigma^2}} \exp\left(\frac{(n - \mu_{\bullet})^2}{-2\sigma^2}\right), \quad (3.10)$$

where the subscript X_{\bullet} represents the network the parameter X is associated with.

Strain energy of a single chain at networks θ , and m Based on the non-Gaussian theory of rubber elasticity and its approximation through Kuhn-Grün (KG) model, the entropic energy of a single freely jointed chain is given by

$$\begin{aligned} \psi_c(n, \bar{r}_{\bullet}) &= nK_bT \left(\varphi\beta + \ln \frac{\beta}{\sinh \beta} \right) = nK_bT \int_0^{\varphi} \beta d\varphi, \\ \beta &= \mathcal{L}^{-1}(\varphi) \quad \text{where} \quad \coth(\beta) - \frac{1}{\beta} = \mathcal{L}(\varphi), \end{aligned} \quad (3.11)$$

where $\beta = \mathcal{L}^{-1}(\varphi)$ is the inverse Langevin function, $\varphi = \frac{r_{\bullet}}{L} = \frac{\bar{r}_{\bullet}}{n}$ the extensibility ratio ($\frac{\bar{r}_{\bullet}}{n}$), and \bar{r}_{\bullet} is end-to-end distance of the chain in the deformed configuration. Recent studies show that the relative error of Kuhn-Grün is significantly large in shorter length ($n < 40$) [82], and can cause significant overs estimation of force in highly cross-linked materials. Therefore, the KG is not a proper option for estimating the entropic energy of a matrix with short chains. To this end, an enhanced version of the non-Gaussian distribution function of short chains will be used, namely

$$\hat{\psi}_c(n, \bar{r}_{\bullet}) = nK_bT \int_0^{\varphi} \hat{\beta} d\varphi, \quad \hat{\beta} = \left[1 - \frac{1 + \varphi^2}{n} \right] \beta. \quad (3.12)$$

Having the same computational cost as the KG model, the enhanced model can provide us with a significantly more accurate description of force in shorter chains.

ILF Approximation The majority of the micromechanical models either calculate the ILF implicitly or approximate it with rational functions, as it cannot be explicitly derived. In the whole range of extensibility of polymer chains, it is preferable to approximate the ILF with a highly accurate simple approximation. Thus, a first-order fractional approximation with two polynomial terms (relative error of 1.0%), is used to approximate ILF [83, 84]

$$\mathcal{L}^{-1}(x) \cong \frac{x}{1-x} + 2x - \frac{8}{9}x^2. \quad (3.13)$$

3.4.1 Damage

Damage in the polymer matrix will take place with respect to two main factors: time t and deformation \mathbf{F} . Here, we consider temperature to only maximize the rate of damage rather than being an initiating factor in the damage. The time and deformation-induced damages are considered to have taken place in the following forms in networks 0 and m

- Time-induced damage is mainly associated with the dissolution of the cross-links in the course of aging which results in homogeneous detachment of polymer chains regardless of their length (random chain scission). Such damage can be best modeled by the changes in the end-to-end distance \bar{R}_\bullet of a polymer chain (see Fig. 3.7) and the peak location of the distribution function $\mathcal{P}_\bullet(n)$ (see Fig. 3.5).
- Deformation-induced damage is mainly associated with the detachment of shorter chains due to entropic force that exceeds the strength of the weakest link of the chain F^{fb} . Such damage results in the deactivation of shorter polymer chains and does not have any effects on other longer chains and thus does not change the distribution profile (see Fig. 3.8).

Hence, the shortest available chain in an arbitrary direction of a deformed network is given by

$$F\left(\frac{\bar{r}_\bullet}{n}\right) \leq F^{fb} \quad \longrightarrow \quad n_{\bullet min} = \nu \lambda_M^d \bar{R}_\bullet, \quad (3.14)$$

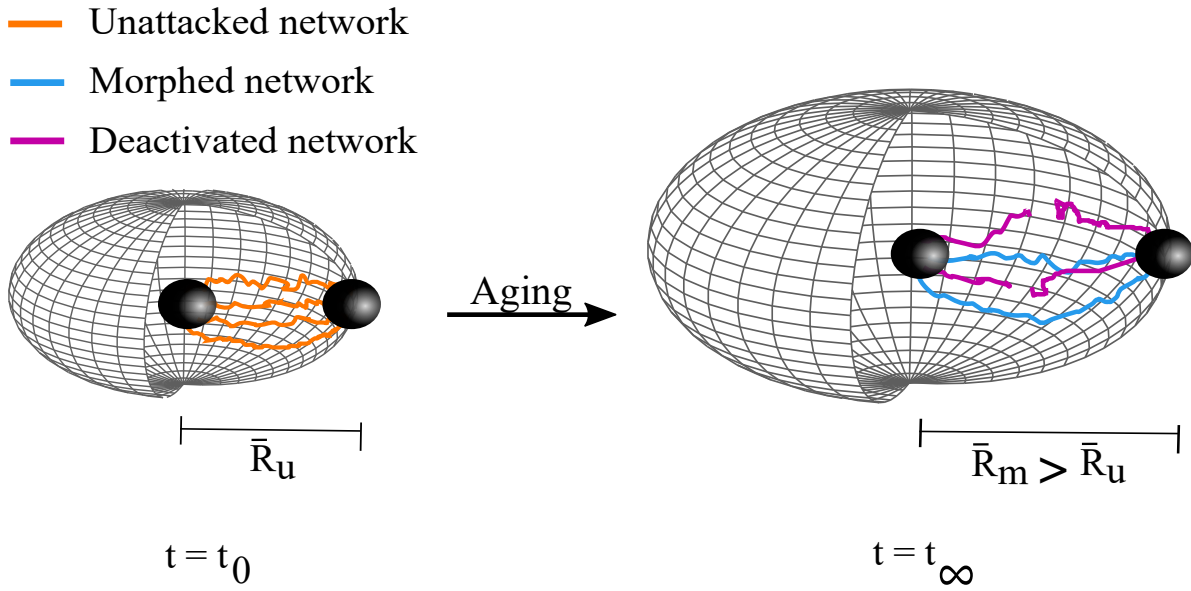


Figure 3.7: Illustration of time-induced damage due to change of the network morphology.

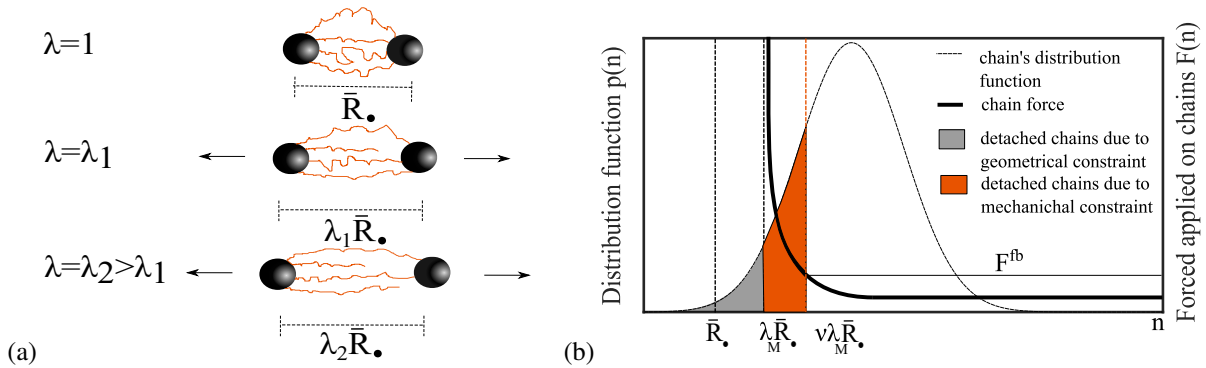


Figure 3.8: Illustration of deformation-induced Damage. (a) Detachment of shorter chains during primary loading, and (b) Distribution function and the force developed by chains with an equal initial relative end-to-end distance \bar{R}_\bullet and pre-stretched by λ_M .

where λ_M^d is the maximal micro-stretch previously reached in the loading history, while $\nu = \mathcal{L}(\frac{Ffb}{K_bT})^{-1} > 1$ refers to a material parameter representing the sliding ratio of a polymer chain (see [85] for details). Considering $n_{\bullet M} = \mu_{\bullet} + 5\sigma$ to be the length of the longest available chain in each network and use it as a cut-off length of $\mathcal{P}_{\bullet}(n)$, can significantly reduce the computational cost of the model and eliminate the negligible contribution of super-long chains. Consequently, the length of available chains in the direction \mathbf{d} of an arbitrary network is given through the following set

$$D_{\bullet} \left(\frac{\mathbf{d}}{\lambda_M} \right) = \left\{ n \mid n_{\bullet \min} \left(\frac{\mathbf{d}}{\lambda_M} \right) \leq n \leq n_{\bullet M} \right\}. \quad (3.15)$$

3.4.2 Network Rearrangement

Time-induced Rearrangement The chain length distribution function $\mathcal{P}_{\bullet}(n)$ in each network is not a function of time and only its multiplicative amplitude, $N(t, T)$ is evolving over time. Thus, one can show that the total number of bonds at time 0 and ∞ are identical as a result of the conservation of the number of active chains in the matrix. However, the chains of virgin network transformed into the new chains of attacked networks, which can be summarized as follows

$$\begin{aligned} N(0, T)\mathcal{N}_0 \int_{D_0(1)} \mathcal{P}_0(n) ndn &= N'(\infty, T)\alpha\mathcal{N}_m \int_{D_m(1)} \mathcal{P}_m(n) ndn \\ &+ N'(\infty, T)(1 - \alpha)\mathcal{N}_d \int_{D_d(1)} \mathcal{P}_d(n) ndn, \end{aligned} \quad (3.16)$$

where \mathcal{N}_{\bullet} represents the number of chains in an arbitrary network. Here, one should note that the process of hydrolysis can be defined as the conversion of chains of the virgin network \mathcal{N}_0 to the chains of the deactivated and morphed networks $\alpha\mathcal{N}_m + (1 - \alpha)\mathcal{N}_d$. In other words, initial polymer chains transform into two states in the course of hydrolytic aging; (i) longer chains formed by the merger of original detached chains and (ii) detached chains that could not stay active in the system. Here, we assumed water attacked the part of chains in the virgin network and deactivated them.

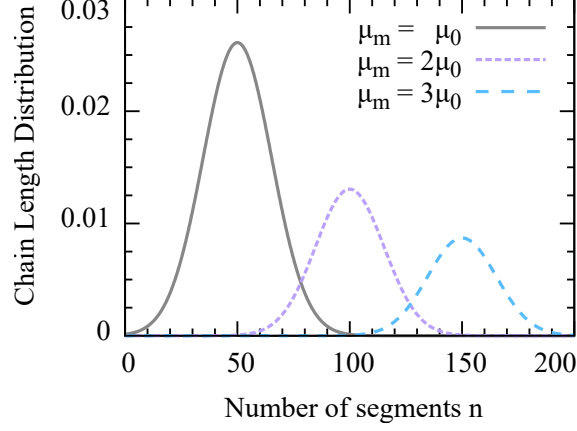


Figure 3.9: Alteration of the morphed network chain length distribution with respect to the μ_m .

Thus, the chain length distribution, $\mathcal{P}_d(n)$ and number of chains, \mathcal{N}_d , in the deactivated networks are considered to be the same as the ones of the virgin network, $\mathcal{P}_d(n) \approx \mathcal{P}_0(n)$ and $\mathcal{N}_d = \mathcal{N}_0$. Thus, Eq.3.16 can be rewritten as

$$\begin{aligned} \mathcal{N}_0 \int_{D_0(1)} \mathcal{P}_0(n) n dn &= \mathcal{N}_m \int_{D_0(1)} \mathcal{P}_m(n) n dn & (3.17) \\ \Rightarrow \hat{\mathcal{N}} &= \frac{\mathcal{N}_m}{\mathcal{N}_0} = \frac{\int_{D_0(1)} \mathcal{P}_0(n) n dn}{\int_{D_m(1)} \mathcal{P}_m(n) n dn}, \end{aligned}$$

where $\hat{\mathcal{N}}$ is a normalization constant, which satisfies the mass conservation in the networks during aging time.

In this respect, Fig. 3.9 shows the alteration of the chain distribution function due to the change of \mathcal{N}_m with respect to μ_m in the morphed network. By increasing μ_m , \mathcal{N}_m decreases and moves the distribution function to the right and down (See Fig. 3.9).

Deformation-induced Rearrangement Considering that the detached chains still remain part of longer macro-molecules, two presumptive conclusions can be made; (i) the detachment of the chains does not lead to full dissipation of their energy, and (ii) the number of active segments within a network remains constant in the course of deformation (see e.g. To implement this assumption,

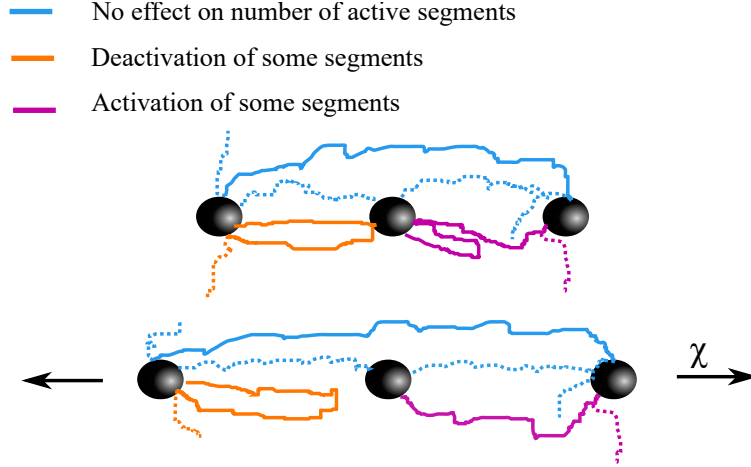


Figure 3.10: Effect of chain detachment on the number of active segments.

we consider the detached chains to be evenly distributed among available chains and thus increase the number of active chains, though with the same probability function $\mathcal{P}_\bullet(n)$. Accordingly, in the course of primary loading shorter chains detach and become part of the longer chains (see Fig. 3.10). In the unloading and reloading, no further damage occurs, as long as λ_M remains the same. [85, 86] for details). The network rearrangement can be best quantified through an amplification factor $\Phi_\bullet(\lambda_M)$ which amplifies the distribution profiles $\mathcal{P}_\bullet(n)$ as more chains are detached from the matrix [87]. This process can take place in m or 0 networks depending on the λ_M on that direction. Assuming the number of segments to be identical before and after deformation, one can write

$$\mathcal{N}_\bullet \Phi_\bullet(1) \int_{D_\bullet(1)} \mathcal{P}_\bullet(n) n dn = \mathcal{N}_\bullet \Phi_\bullet(\lambda_M) \int_{D_\bullet(\lambda_M)} \mathcal{P}_\bullet(n) n dn. \quad (3.18)$$

The detachment process is irreversible; we consider no new bonds to be formed during reloading and unloading, and thus one can rewrite Eq. 5.14 by considering $\Phi_\bullet(1) = 1$ as

$$\Phi_\bullet(\lambda_M) = \frac{\int_{D_\bullet(1)} \mathcal{P}_\bullet(n) n dn}{\int_{D_\bullet(\lambda_M)} \mathcal{P}_\bullet(n) n dn}. \quad (3.19)$$

3.4.3 Strain Energy of Networks

The free energy of networks 0 and m in an arbitrary direction d can be written with respect to Eqs. 5.10, 3.17, and 5.15

$$\psi_{\bullet}^d = \int_{D_{\bullet}(\lambda_M^d)} \Phi_{\bullet}(\lambda_M^d) \psi_c(n, \bar{r}_{\bullet}) \mathcal{P}_{\bullet}(n) dn, \quad (3.20)$$

where D_{\bullet} represents the available chains' length in \bullet^{th} network.

Micro-Macro Scale Transition is used to define the relationship between the micro and macro deformation within the polymer matrix. Here, *the non-affine directional model* is used to relate the macro-stretch χ , and the micro-stretch λ . Based on this concept, a non-homogeneous distribution of the stretch within the network domain is assumed. Here, a classical strain amplification function which is often used in rubber-like materials [88] is used, however the model can be changed for polymers with more elaborate behaviour.

$$\frac{d}{\lambda} = \frac{\chi^d - C^p}{1 - C^p} \quad (3.21)$$

where $C \in [0, 1]$ is the volume fraction of hard segments per unit volume of the rubber matrix, and p depends on the structure of the network ($p \approx 1/3$ for details see [89]).

3.4.4 Constitutive formulation

For an incompressible polymer matrix

$$\det \mathbf{F} = 1 \quad (3.22)$$

where \mathbf{F} stands for the macro-scale deformation gradient. The first Piola-Kirchhoff stress tensor \mathbf{P} can be written as

$$\mathbf{P} = \frac{\partial \Psi_M}{\partial \mathbf{F}} - p \mathbf{F}^{-T} = \frac{\partial \Psi_0}{\partial \mathbf{F}} + \frac{\partial \Psi_m}{\partial \mathbf{F}} - p \mathbf{F}^{-T}, \quad (3.23)$$

where p denotes an arbitrary scalar parameter that can be defined to assure incompressibility, and

Table 3.1: The reference set of parameters of the proposed model.

| $\mathcal{N}_0 k_b T [Mpa]$ | \bar{R}_0 | \bar{R}_m | μ_0 | μ_m | σ | ν | α | $\gamma \exp(-\frac{E_a}{RT})$ |
|-----------------------------|-------------|-------------|---------|---------|----------|--------|----------|--------------------------------|
| 40 | 3 | 18 | 13 | 15 | 4.5 | 1.0065 | 0.02 | 0.1 |

$$\begin{aligned} \frac{\partial \Psi_0}{\partial \mathbf{F}} &= N(t, T) \sum_{j=1}^k w_j \frac{\partial \psi_0}{\partial \lambda} \frac{\partial \lambda}{\partial \chi} \frac{1}{2 \chi} \frac{\partial \mathbf{d}_j \bar{\mathbf{C}} \mathbf{d}_j}{\partial \bar{\mathbf{F}}} : \frac{\partial \bar{\mathbf{F}}}{\partial \mathbf{F}}, \\ \frac{\partial \Psi_m}{\partial \mathbf{F}} &= \alpha N'(t, T) \sum_{j=1}^k w_j \frac{\partial \psi_m}{\partial \lambda} \frac{\partial \lambda}{\partial \chi} \frac{1}{2 \chi} \frac{\partial \mathbf{d}_j \bar{\mathbf{C}} \mathbf{d}_j}{\partial \bar{\mathbf{F}}} : \frac{\partial \bar{\mathbf{F}}}{\partial \mathbf{F}}, \end{aligned} \quad (3.24)$$

where \mathbf{C} denotes the right Cauchy–Green tensor, $J^2 = \det \mathbf{C}$, and $\bar{\mathbf{C}} = J^{-2/3} \mathbf{C}$. Detailed description of the derivation procedure of each of the terms of Eq. 5.3.4 has been provided in Appendix A.

3.5 Parameters Study

Parameter study is carried out to evaluate the contribution of the physical parameters and validate the properties associated with them. First, a reference set of values is selected for all parameters which is given in Table 3.1. The values are specifically chosen to provide high resolution in material behavior during the aging time (See Fig. 3.11). To investigate the effects of each parameter on model predictions, we investigate the increased and decreased values of that parameter while all others are kept constant. In view of different effects of parameters at different aging times, we investigated each parameter at three different times, namely $t = 0$, $t = t_1$, and $t = \infty$.

The proposed model has ten material parameters, four represents the behaviour of unchanged network (\bar{R}_0 , μ_0 , σ , and ν), five those of morphed network (\bar{R}_m , μ_m , α , E and γ), and one parameter namely \mathcal{N}_0 just serves as a multiplication factor to describe the response of the polymer

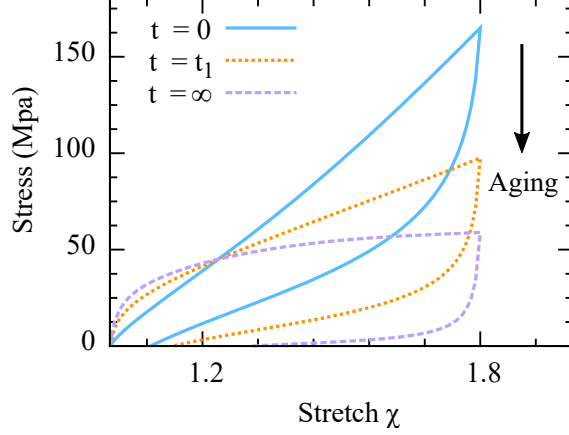


Figure 3.11: Model prediction with the selected material parameters during the aging time.

matrix. Due to similarity of the effect of $\frac{E_a}{RT}$ and γ on the response of the material in a constant aging temperature, here, we only investigate the variation of $\gamma \exp(-\frac{E_a}{RT})$ as a rate of aging. In order to analyze the parameters, first, the effect of unchanged network parameters are investigated along the aging trajectory. Fig. 3.12 shows a summary of the parametric analysis of $(\bar{R}_0, \mu_0, \sigma, \nu, \alpha, \text{ and } \gamma \exp(-\frac{E_a}{RT}))$ during aging time.

- **Parameter** \bar{R}_0 , which represents the end-to-end distance of unchanged network, governs the minimum available chain length ($n_{0_{min}} = \nu \lambda_M \bar{R}_0$) in the unattached network in any arbitrary direction. Thus by increasing \bar{R}_0 , $n_{0_{min}}$ increases while the mean length of polymer chains in the network, which is governed by μ_0 , remains constant. As shown in Fig. 3.12a, decreasing \bar{R}_0 decreases the inelastic effects such as the hysteresis ratio. As expected, the effects of \bar{R}_0 on material response diminishes along aging time since contribution of Ψ_0 becomes negligible .
- **Parameter** μ_0 defines the peak of chain distribution, $P_0(n)$, and can be represented as a multiplicative factor of \bar{R}_0 . In virgin material, μ_0 plays a significant role in defining the evolution of damage. Accordingly, the damage will increase when \bar{R}_0 reaches the peak of probability, μ_0 (see Fig. 3.12b) as the network loses more chain due to deformation. In addition, this parameter control the number of chain in the morphed network through the normalization constant, \mathcal{N}_m . Thus, response of the material will change along the aging

time. It is shown (Fig. 3.12b) that by increasing the μ_0 the softening of material response decreases at $t = 0$ and increases at $t = \infty$.

- **Parameters** σ defines the variance of of chain distribution, $P_{\bullet}(n)$, and thus have a direct effect on the amount of damage the material experience during deformation. Regardless of aging time, higher values of σ represents wider distribution and consequently lower damage as shown in figures see Fig. 3.12c.
- **Parameter** v governs the magnitude of energy dissipation in detachment of a chain, and thus the hysteresis ratio and also the profile of the unloading curves. Regardless of aging time, lower values of v represents higher energy dissipation per chain and consequently results in stronger and yet more damageable networks as shown in Figures 3.12d.
- **Parameter** α defines the composition of the transformed matrix, in particular it is correlated with the percentage of the polymers that transform into m and inversely correlated with those that transform into d networks. Considering the zero contribution of the d network in energy of the matrix, parameter α can be considered as a multiplicative scaling factor for Ψ_m that can linearly scale the contribution of morphed network. As expected, the contribution of α in the final response increases over time as Ψ_m grows with aging as shown in Fig. 3.12e.
- **Parameter** $\gamma \exp(-\frac{E_a}{RT})$, or the hydrolysis constant, mainly governs the decay rate of the 0 network and formation rate of the m network. Higher values of $\gamma \exp(-\frac{E_a}{RT})$, thus, represents a faster transformation from 0 to m networks (See Fig. 3.12f).

3.6 Validation and Results

To validate the proposed model, its predictions were bench-marked against a set of new experimental data specifically designed to capture the effects of **(1) deformation** χ , **(2) deformation history** χ_M , **(3) aging time** t and **(4) aging temperature** T . Hereafter, t refer to the time that

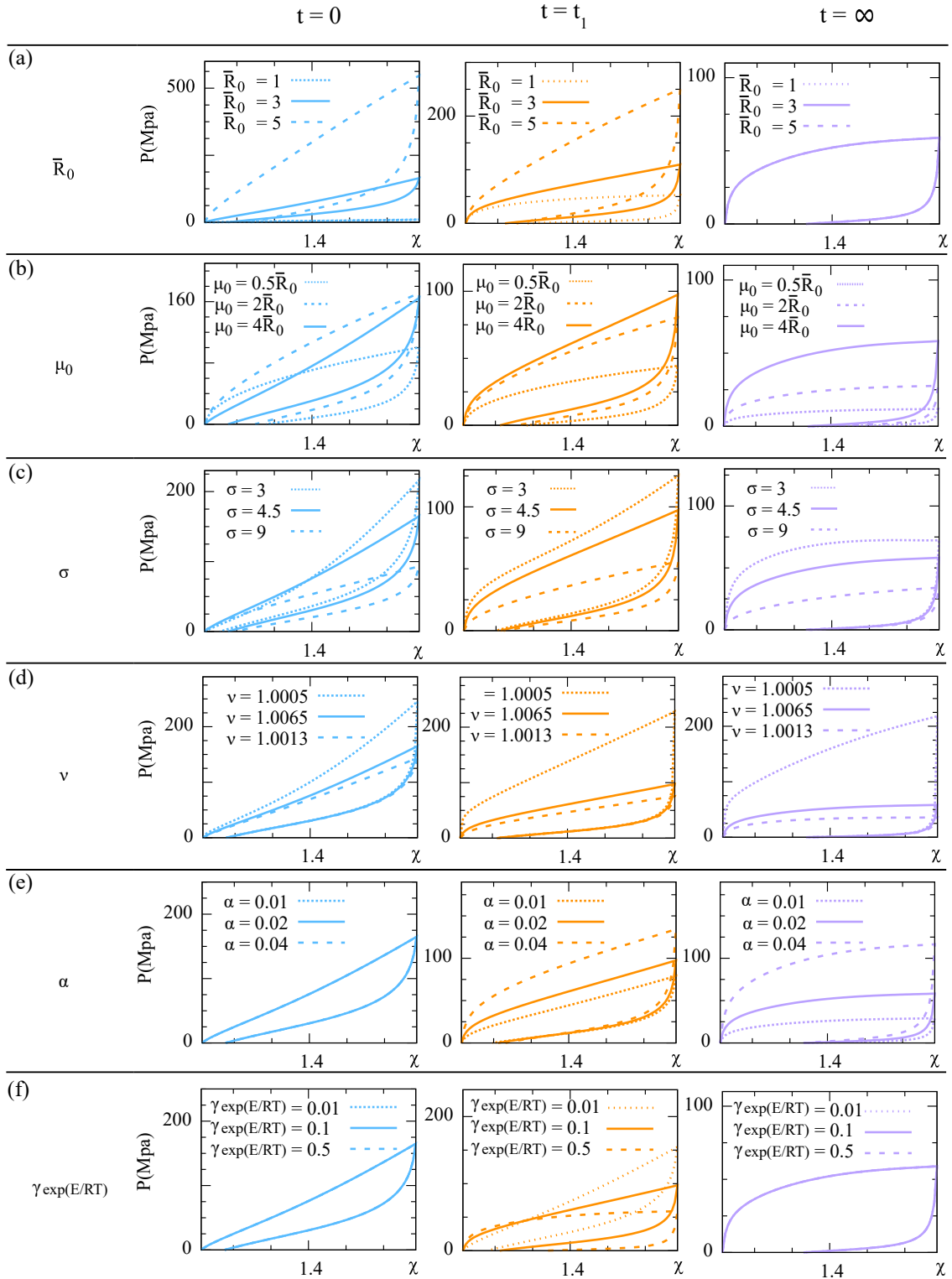


Figure 3.12: Sensitivity analysis of the material parameters included in the model. Each plot consists of three independent lines. Solid lines represent the reference curve, and dashed lines depict model predictions due to the variation of the control parameters. In some cases, all three lines are on top of each other.

Table 3.2: Material parameters of the proposed model for SBR.

| $\mathcal{N}_0 k_b T [psi]$ | \bar{R}_0 | \bar{R}_m | μ_0 | μ_m | σ | ν | α | $\gamma [1/day]$ | $\frac{E_a}{R} [K]$ |
|-----------------------------|-------------|-------------|---------|---------|----------|--------|----------|------------------|---------------------|
| 95.4 | 3.0547 | 3.3849 | 7.04 | 7.24 | 7.28 | 1.0055 | 0.001 | 1459 | 3700 |

samples were aged before inducing the deformation χ . The model was optimized by fitting the aforementioned ten material parameters to the following set of load-unload curves

- Primary loading curve of the unaged sample, to study χ
- One unload cycle of the 1.3 stretch amplitude of the unaged sample, to study χ_M
- Only loading curve of 10 days aged sample at 80°C, to study χ , χ_M , and t
- One point: stress at 1.5 stretch for 6 days aged sample 60°C, to study t , and T

To this end, the least square error function was minimized with the aid of the Levenberg–Marquardt algorithm. Once the material parameters are obtained, the model can predict the other loading-unloading curves of materials for a different amount of aging times and strains. In this regard, the model predictions are validated against our own experimental tests for different aging times and temperatures in Fig. 3.13, while the obtained values of the material parameters are given in Table 6.2.

Here, we validate the model predictions on different types of damages as given below

- Fig. 3.13a: Damages induced by deformation, and deformation history in multiple cycles
- Fig. 3.13b: Damages induced by time and temperature in one cycle
- Fig. 3.13c and d: Effect of time on damages induced by deformation, and deformation history in multiple cycles
- Fig. 3.13e and f: Effect of temperature on damages induced by deformation, and deformation history in multiple cycles

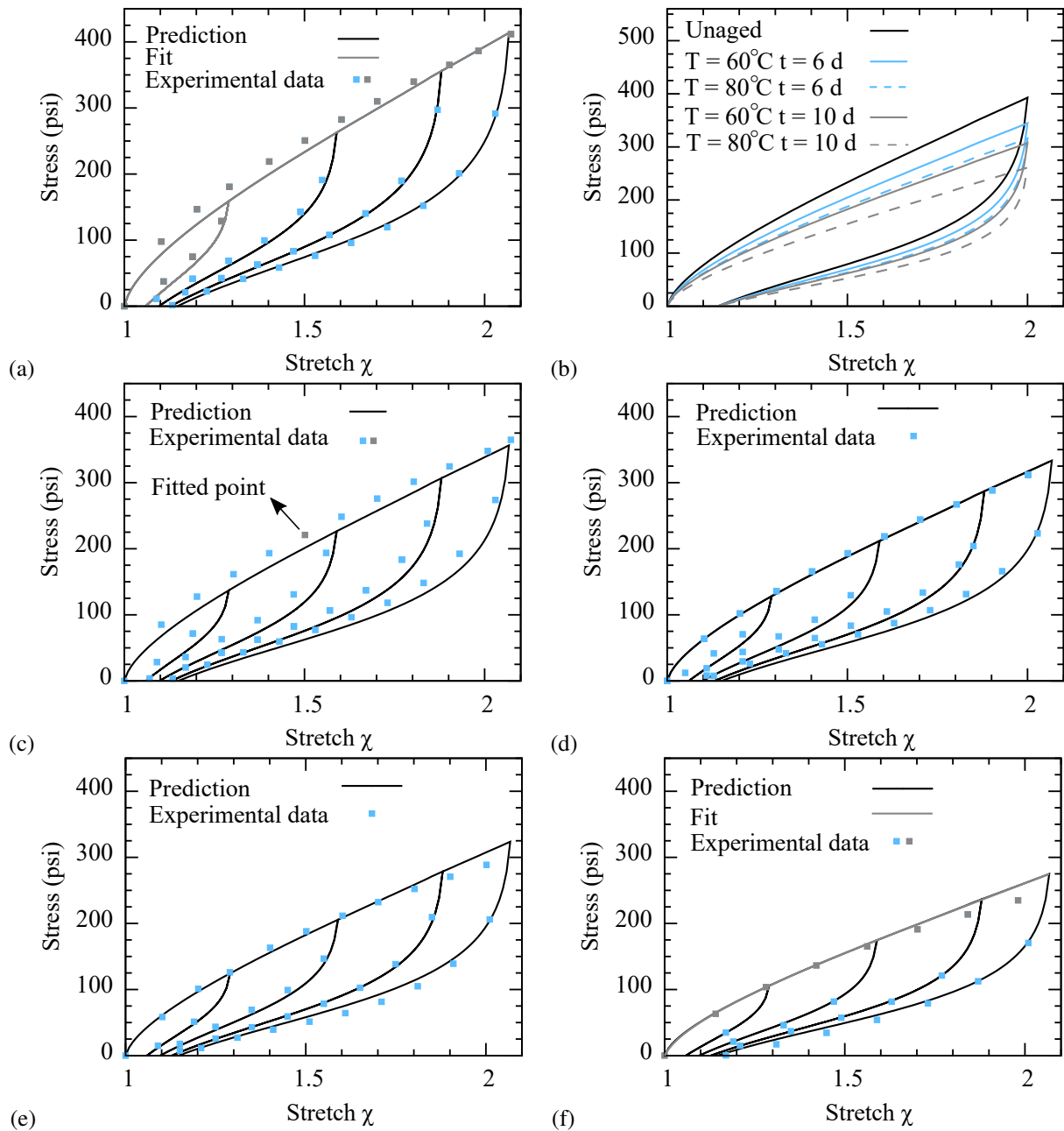


Figure 3.13: Validation of model predictions for SBR in multiple conditions; (a) unaged, (b) Comparison of one cycle load on samples stored at 60°C and 80°C for 6 and 10 days, (c) constitutive behaviour for 6 days aged sample at temperature 60°C, (d) constitutive behaviour for 10 days aged sample at temperature 60°C, (e) constitutive behaviour for 6 days aged sample at temperature 80°C, (f) constitutive behaviour for 10 days aged sample at temperature 80°C.

Moreover, to quantify the deformation-induced damages of polymers in the course of hydrolytic aging, the dissipated energy in each cycle in the model is predicted and compared to those of the experimental data. Throughout this contribution, the term "Hysteresis" will be used to refer to "quasi-static" energy dissipation observed in one load-unload cycle in uni-axial tensile tests. In elastomers, while hysteresis is strongly dependent on deformation rate, even at close to zero rates, certain hysteresis can be observed which is referred to as rate-independent or "quasi-static" hysteresis. We generally refer to the hysteresis of the first cycle as idealized Mullins effect, while those of the second and next cycles are referred to as hysteresis. Please note that this "Hysteresis" is different than frequency dependent visco-elastic hysteresis since this one is resulted by a combination of reversible and irreversible energies observed in quasi-static loading as the result of sub-structural damages such as bond detachments. At any aging time t and temperature T , the dissipated energy per unit of volume during the first cycle can be calculated from the experiments as follows

$$U_{hys}^{t,T} = \int_{loading} \mathbf{P}^{t,T} \mathbf{X} \otimes \mathbf{X} d\chi - \int_{unloading} \mathbf{P}^{t,T} \mathbf{X} \otimes \mathbf{X} d\chi, \quad (3.25)$$

where \mathbf{X} is the deformation vector applied on the matrix. Fig. 3.14 show the evolution of dissipated energy against χ_M for different aging times at 60°C, and 80°C, respectively. As expected, the dissipated energy increases exponentially with χ_M while the growth rate is being inversely correlated to aging time t .

Considering the micro-mechanical nature of the mode, the concept can be further generalized and implemented for other types of cross-linked polymers with *complex inelastic patterns such as hardening behavior and alteration of curvature*. Here, we generalized the model to predict the hydrolytic aging behavior of three other compounds form experimental data that are available in literature

- Polyurethane [90]
- Suture fibers of PLA–PCL[53]
- Natural rubber[91]

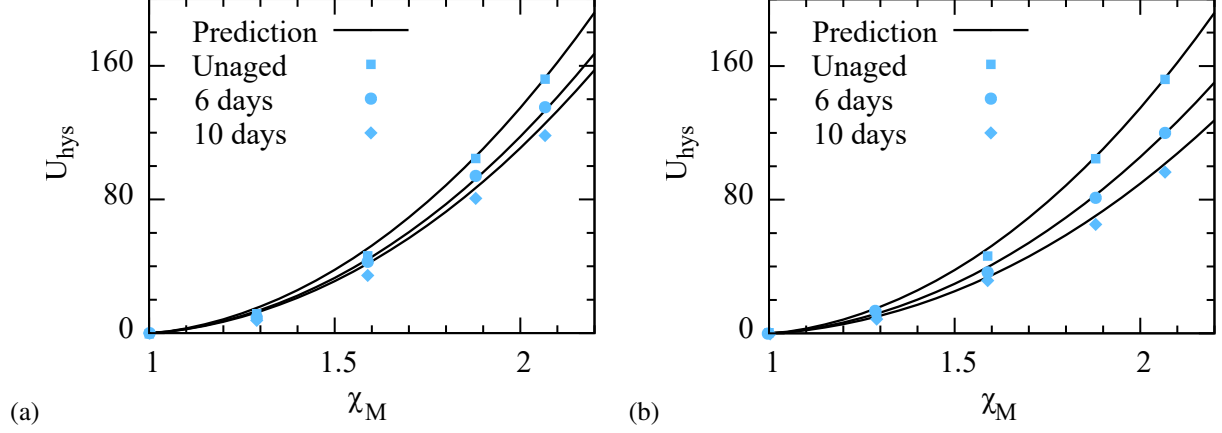


Figure 3.14: Evolution of dissipated energy during aging at different temperatures; (a) 60°C, (b) 80°C.

Table 3.3: Material parameters of the proposed model for different Set of rubber-like materials.

| Ref. | $\mathcal{N}_0 k_b T$ [Mpa] | \bar{R}_0 | \bar{R}_m | μ_0 | μ_m | σ | ν | α | $\gamma \exp(-\frac{E_a}{RT})$ [1/day] |
|-------------------|--------------------------------|-------------|-------------|---------|---------|----------|-------|----------|---|
| Gac et al.[90] | 0.32 | 13.374 | 17.535 | 5.5 | 7.5 | 5.1 | 1.005 | 0.3 | 0.0209 |
| Vieira et al.[53] | 4.88 | 10.567 | 21.795 | 13.04 | 15.5 | 4.28 | 1.01 | 0.128 | 0.0443 |
| Stevenson.[91] | 0.13 | 6.027 | 12.582 | 17.04 | 19.04 | 8.28 | 1.055 | 0.36 | 0.001 |

To fit the parameters for each material, two loading curves of unaged and aged samples, as well as one point of an additional loading curve from another sample with a different aging period were considered for fitting. The parameters for each of the above mentioned materials are derived and summarized in Table 3.3. In this table, the decay constant $\gamma \exp(-\frac{E_a}{RT})$ presented as single parameter as material responses captured only in one temperature. Fig. 3.15 shows the predictive capabilities of the presented model against the experiments for all three materials, and the good agreement for rest of curves were obtained automatically.

Depending on the polymer matrix, we assume that **all chains** which are exposed to water attack within the **deactivated network** will form free-end chains, which will have no further contribution to entropic energy. Accordingly, the ratio of morphed network to deactivated network α describes how the matrix elasticity is perceived at time ∞ . In this work, we assume that α has been inversely correlated to Ψ_{∞} , so for $\alpha = 0$ we expect the material to show no retention force at time ∞ , and

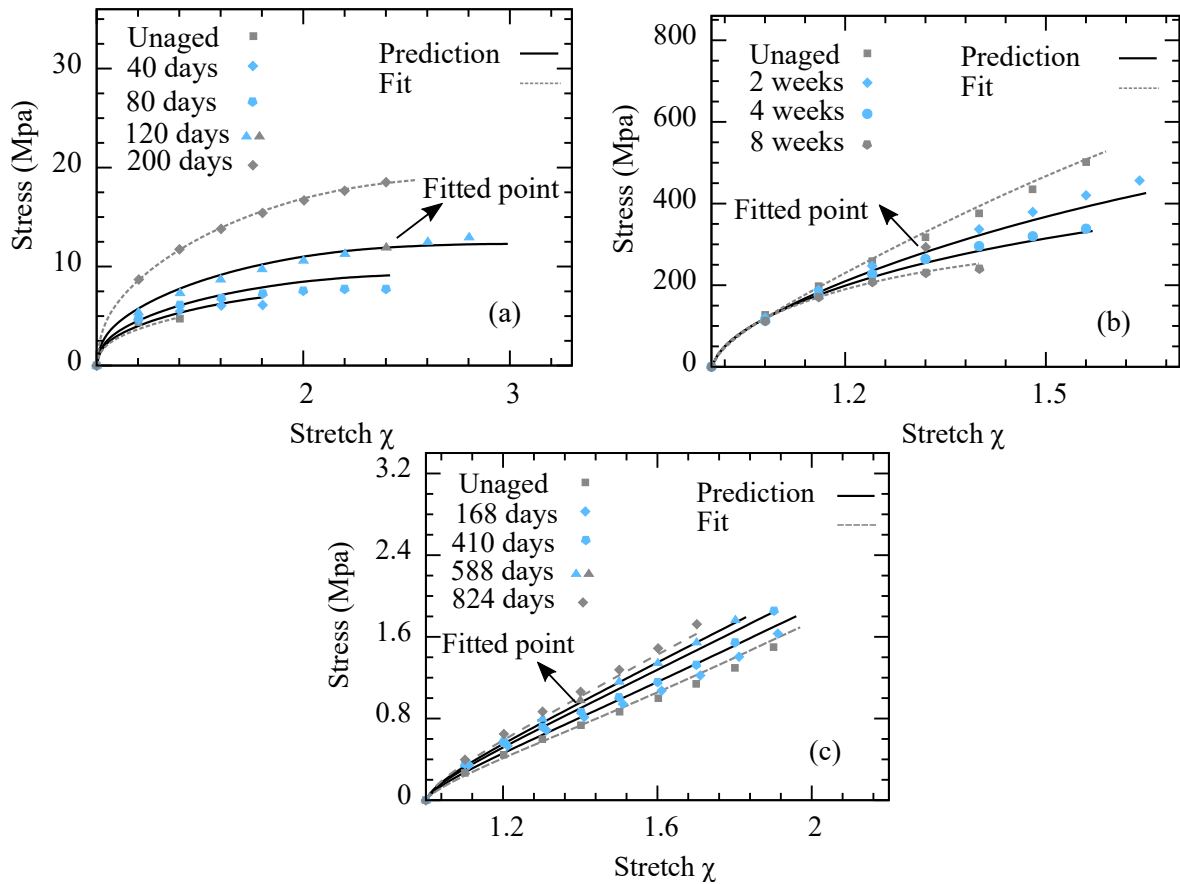


Figure 3.15: Validation of model predictions against aging of three different materials; (a) PolyUrethane (PU) submerged in seawater at 100°C[90], (b) PLA-PCL fiber submerged in phosphate buffer solution at 37°C[53], (c) Natural rubber (vulcanized A) submerged in seawater at 40°C [91].

for $\alpha = 1$ we expect the system to remain fully elastic. Since SBR loses most of its elasticity due to hydrolysis, the response can be simply described by transformation of the virgin network to the deactivated network with almost negligible contribution of morphed network $\alpha \approx 0$. Hence, the energy at infinity state can be considered zero (i.e. $\Psi_\infty = 0$) which shows that the material will be annihilated through aging. However, for other type of the material such as polyurethane which retain elasticity at time ∞ , α will remain relatively high and $\Psi_\infty = \alpha\Psi_m$.

Using micro-sphere as the basis of deactivated and morphed networks in our model, the proposed model can be independently used to predict aging in different mechanical loading scenarios. Once the model has been fitted to uni-axial data, its predictions were validated against shear and uni-axial tensile loads in virgin-state (see Fig. 3.16). While we did not find data on the multi-axial performance of elastomeric samples under hydrolytic aging, model predictions on the aging of samples under different loading were predicted but only validated with respect to uni-axial loading. Using the data of [92] on uni-axial and pure shear of filled silicone rubber, the proposed model validated for different loading scenarios in Fig.3.16. For the fitting, we used one loading-unloading cycle of the 1.413 stretch amplitude in the uni-axial tensile direction. The good agreement with all loading-unloading curves in pure shear, as well as other loading-unloading curves of uni-axial tensile, was attained automatically. The obtained values of the material parameters are given in Table 3.4.

Table 3.4: Material parameters of the proposed model for filled silicone rubber.

| Ref. | $\mathcal{N}_0 k_b T$ [Mpa] | \bar{R}_0 | \bar{R}_m | μ_0 | μ_m | σ | ν | α | γ [1/day] | $\frac{E_a}{\mathcal{R}}$ [K] |
|--------------------|--------------------------------|-------------|-------------|---------|---------|----------|-------|----------|---------------------|----------------------------------|
| Machado et al.[92] | 0.2858 | 2.0640 | 4.25 | 13.04 | 15.04 | 6.28 | 1.004 | 0.04 | 1759 | 3700 |

3.7 Summary and Discussion

We have developed a large strain three-dimensional micro-mechanical constitutive model to describe the hydrolytic aging of a cross-linked polymers matrix with permanent chemical cross-links

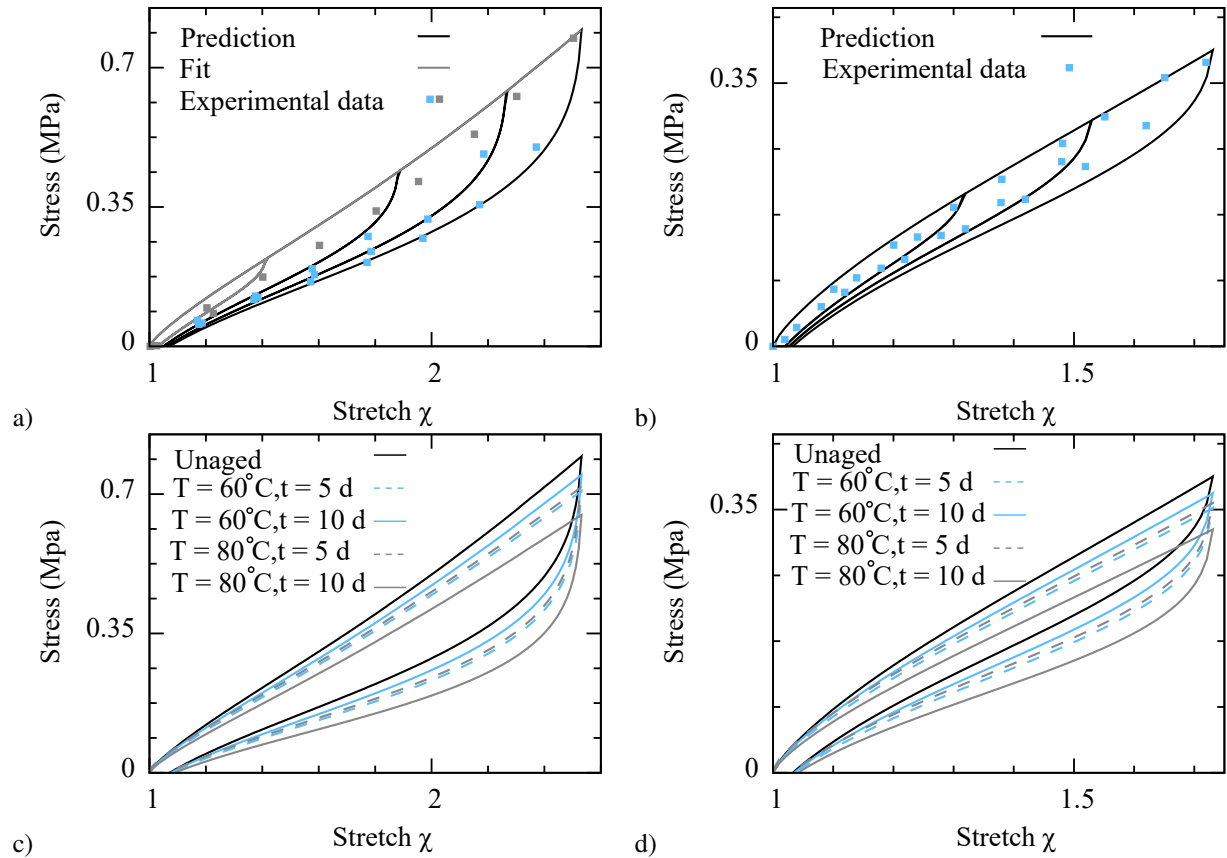


Figure 3.16: Validation of model predictions for silicone rubber under different loading scenarios against experimental data from [92]; (a) unaged sample under uni-axial tension, (b) unaged sample under pure shear, (c) Comparison of one cycle of uni-axial tension load on samples stored at 60°C and 80°C for 5 and 10 days, (d) Comparison of one cycle of pure shear load on samples stored at 60°C and 80°C for 5 and 10 days.

that can break and reform the matrix with respect to four external load factors of (i) deformation, (ii) deformation history, (iii) aging time and (iv) aging temperature. Our model show excellent agreements with the experimental data on five different types of loading and on four different materials. To the best of our knowledge, this is the first micro-mechanical model of hydrolytic aging.

The model has been based on the concept that the chemical cross-links can break, can consequently transform the network in the course of aging. We hypothesized two different types of network transformation depending on the source of cross-link breakage, namely time or deformation. During a test with continuous loading, the deformation-induced damage will lead to detachment

of shorter chains and thus results in a rearranged network with slightly longer polymer chains. In the course of aging and in the absence of deformation, we assume that the chain detachment due to water attack on polymer active agents occurs randomly and thus the reformed network will have a different composition from the original network with fewer chains. Rearrangement of the chains contributes significantly to the overall stress of the cross-linked polymer matrix and was accurately represented by our model. Although our model has ten independent parameters, two of them can be immediately eliminated if deformation controlled relaxation aging tests are available. Here, Our formulation neglects rate dependency and visco-elasticity while the major focus of this work is on relatively long aging times and low deformation rates where the effects of visco-elasticity is assumed to disappear. Thus, if the deformation rate is sufficiently low one can assume the tests, pre- and post-aging, as quasi-static tests which makes the unloading curves insensitive to the loading rate and mainly a function of deformation history.

The proposed model captures the basic physical laws governing the hydrolytic aging of cross-linked polymers as frequently encountered in nature and thus is relevant to two other types of chemically cross-linked polymers such as rubber-like materials, adhesives and sealants. For polymeric systems with more complex morphology, e.g. those with two or more types of cross-links or polymers, while the proposed concepts are still relevant, the models describing the dynamics of breaking of cross-links and network rearrangement should be updated and probably, would be way more complex than those used in this work. The proposed model has ten material parameters, all of which have a clear physical meaning. The excellent performance of the proposed method was proven by validating against different experimental data on different materials that are particularly selected to reveal the evolution of inelastic behaviour during hydrolytic aging. The model predictions was further validated by comparing the evolution of hysteresis against experiments. Our model and experiments illustrate how polymer networks with their mechanical behaviour dominated by entropic chains, can respond to time, temperature and deformation at the micro-structural level and further explore the relation to describe macroscopic response with respect to micro-structural changes.

CHAPTER 4

A Physically Based Model for Thermo-Oxidative and Hydrolytic Aging of Elastomers

4.1 Introduction

There is a high demand for using cross-linked polymers in demanding applications due to their excellent properties, such as high extensibility, strength, abrasion and chemical resistance, and durability [32, 21, 93, 94, 95]. They are extensively used in a wide range of industrial applications, such as automotive, transportation, power distribution, and aerospace. Due to their usage in sensitive applications, they are constantly exposed to high numbers of cyclic loading in unfavorable environments. However, these extreme environmental conditions can severely degrade their mechanical performance and hence their reliability [96]. In the literature, this process is often known as *aging*. Individual or combined environmental factors such as high temperature, radiation, and humidity can cause the aging process [5]. These environmental factors facilitate degradation mechanisms. Based on the prevalence of their environmental factors, aging mechanism can be categorized as ones with severe impact such as hygro-thermal [97, 98], hydrolysis [99, 58], thermo-oxidation [100, 101, 102, 103], photo-oxidation [104, 105, 106] and those that are not that prevalent in nature such as ozone cracking [14], and chemical corrosion [13]. Although there is a vast literature on proposed aging constitutive models to predict the material behavior in one aging scenario, there is still a long way to go for simple and efficient models that can be used alternately for different aging scenarios at the same time. Therefore, in this research, we focused on proposing a computationally simple model that can be used for thermo-oxidative aging or hydrolysis separately. Regarding thermo-oxidative aging, there are extensive experimental studies on cross-linked polymers using accelerated testing. Celina et al. [107, 108] thoroughly reviewed such studies. Several

potential problems of accelerated testing methods were discussed in detail in [109, 110, 111, 112]. Moreover, Shaw et al. [113] investigated the effects of thermo-oxidative aging on oxidative scission, viscoelastic relaxation, and thermal expansion of elastomers. Rabanizada et al. [114] used air, distilled water, seawater, and freshwater as different mediums to perform accelerated aging tests on natural rubber. Furthermore, they studied the changes in visco-elastic behavior through dynamic mechanical analysis (DMA) tests. In a similar fashion, the thermal aging of peroxide-cured nitrile butadiene rubber (NBR) has been examined by Pazur et al. [115]. Then, they used their experimental results to study the effect of thermal aging on the bulk properties of the rubber. They suggested that to understand the decay of material one should study the cross-link distribution within the bulk specimen in detail. The experimental approaches to understanding hydrolysis are not as detailed as thermo-oxidative aging, but there is still a rich literature on this subject. In this regard, experimental research on the mechanical properties of thermoplastic polyurethanes in various thermal, mechanical, and humidity conditions has been conducted by Slater et al. [56]. The results revealed that the water acts as a plasticizer and produces a greater magnitude of compression set. A series of experiments on polyglyconate B for distinct initial polymer molecular weights have been done by Farrar and Gillson [57] to show that the degradation rate depends on polymer morphology. Besides, they suggest an empirical relation between tensile strength and molecular weight. Later on, similar decreasing trends for tensile strength and molecular weight were found experimentally by Vieira et al. [116], during hydrolytic aging. Compared to the experimental efforts in this field, there are fewer theoretical approaches in the literature. These theoretical efforts can be mainly categorized into two groups of phenomenological and micro-mechanical models. Phenomenological approaches describe the degradation of elastomers based on a thermodynamic framework, along with a mathematical model without a physical meaning [15, 16]. On the other hand, micro-mechanical models are based on the statistical mechanics of polymer structure. Therefore, their parameters do have physical meaning [117, 17]. Recently, with the growth of machine learning techniques in engineering fields, a new data-driven approach to model behavior is coming into the picture as well. In this regard, Ghaderi et al. [118, 119] proposed infusing machine learn-

ing algorithms and polymer physics to model inelastic behavior of rubber-like materials and their degradation. Phenomenological models are more prevalent than the micro-mechanical ones. In thermo-oxidative aging, Ha-Anh and Vu-Khanh [120] used the Mooney-Rivlin model along with an Arrhenius decay to analyze hyperelastic behavior of polychloprene during aging. Furthermore, Lion and Johlitz [121] introduced a 3-D phenomenological model for the chemical behavior of rubbers. Helmholtz free energy has been differentiated into three parts, temperature-dependent hyper-elasticity, volumetric material behavior, and a function of deformation history. Then, these parts are added to the decomposition of the deformation gradient. Their model was successful in simulating the experimental data. In addition, Johlitz [122] proposed a phenomenological model which was rheologically motivated. Later on, he used finite strain theory and simulated the behavior of aged automobile bearings [24]. In order to study the aging behavior of an adhesive, Dipple et al. [123] used a coupled chemo-mechanical modeling approach. Using finite element simulation, they investigated the dependency of aging to the geometry between substrate and adhesive. Recently, Konica and Sain [124, 125] numerically studied the coupled mechanical behavior and diffusion-reaction of polymers during aging. Thermal aging can also be modeled using molecular dynamics simulations [126], although it requires higher computational costs, implementation of coarse-graining methods could accelerate these simulations [127]. For hydrolysis, so far, aside from our previous model, only a few phenomenological models have been proposed [26]. To model the constitutive behavior of PLA-PCL fibers during hydrolysis, Vieira et al. [53] developed a phenomenological model and validated it with their experimental data. To this end, they used Bergström and Boyce's constitutive model, which decomposes the mechanical behavior into two separate parts; i) time-independent and ii) time-dependent response. Recently, Breche et al. [54] predicted the response of biodegradable materials throughout hydrolytic aging by using a linear-quasi viscoelastic model. Recently, the demand for physically-based models is increasing. Schlomka et al. [128] used the Neo-Hookean model to model the polymer's stiffness during aging. They used the same staggered solution presented in [129] to solve the problem of the time scale difference between chemical reactions and mechanical deformations. Beurle et al. [130] proposed

a micro-mechanical model that uses a network dynamics model to capture the changes in polymer network topology due to cross-link formation and chain scission. Mohammadi et al. [131, 12] predicted the constitutive behavior of elastomers during thermo-oxidative aging. Their model used the dual network hypothesis of Tobolsky for decay modeling alongside the network evolution model for deformation-induced damage. Their model has the ability to model idealized Mullins effect as well as follow complex loading, aging, and unloading profiles. In a similar fashion, Bahrololoumi et al. [9, 132] proposed a physically-based model for polymer behavior undergoing hydrolytic aging. Although this model is pretty accurate and versatile in predicting different inelastic features, it is computationally expensive. The main objective of this work is to provide a generalized method to reduce complexity and computational cost associated with training of our recent aging models [9, 133, 12]. The proposed model will use a generic description of two competing phenomena that are generally observed in aging, namely the formation and dissolution of cross-links, which results in varying densities of active chains throughout the process. The model simplifies the aging by assuming the mechanical and environmental damages to be independent and thus can be modeled as multiplicative damage components. Here, we validate the model with respect to two aging processes, namely hydrolysis, and thermo-oxidation, and we show that it can capture both mechanisms with relatively good accuracy.

4.2 Kinetics and Assumptions

In order to develop a micro-mechanical model, one should first understand the kinetics of chemical reactions during thermal and hydrolytic degradation.

4.2.1 Thermo-Oxidative Kinetics

The rate of chemical oxidation during thermo-oxidative aging can be defined as [134]

$$-\frac{d[P]}{dt} = k [P]^q, \quad (4.1)$$

where $[P]$ is the chemical compound concentration of P , k the coefficient of reaction rate, and q the reaction order. Note that Eq. (4.1) is only meaningful when q has a discrete value [135]. First-order kinetic equations ($q = 1$) are usually used for describing the chemical reaction governing a degradation process[136]. Moreover, in the presence of homogeneous conditions, low stretches during aging, and assuming there is no diffusion-limited oxidation in place, k would follow the famous Arrhenius function and therefore is only a function of temperature.

$$k = \tau_0 \exp\left(-\frac{E_a}{RT}\right), \quad (4.2)$$

where $R = 8.314[JK^{-1}mol^{-1}]$ is the ideal gas constant, $E_a[Jmol^{-1}]$ the activation energy of the chemical reaction, and $\tau_0[s^{-1}]$ a pre-exponential factor. By solving Eq.(4.1) when $q = 1$ and substituting it into Eq.(4.2), following equation for describing $[P]$ can be derived

$$[P] = A_0 \exp\left(-\tau_0 \exp\left(-\frac{E_a}{RT}\right)t\right). \quad (4.3)$$

Where A_0 and τ_0 , in general, are functions of temperature to satisfy Eq. (4.1).

Now, that we understand the kinetics of reactions, we can further expand it to derive our micro-mechanical model foundations. Chemical reactions between the polymer backbone and oxygen during thermo-oxidative aging are the main reason for changes in polymer matrix [137]. Two types of chemical reactions occur which have been represented in Fig. 4.1 ; (1) cross-linking, which often leads to material embrittlement [138], and (2) polymer scission. Therefore, in view of Eq. (4.3), one can define the new peroxide cross-link density during thermo-oxidative aging as

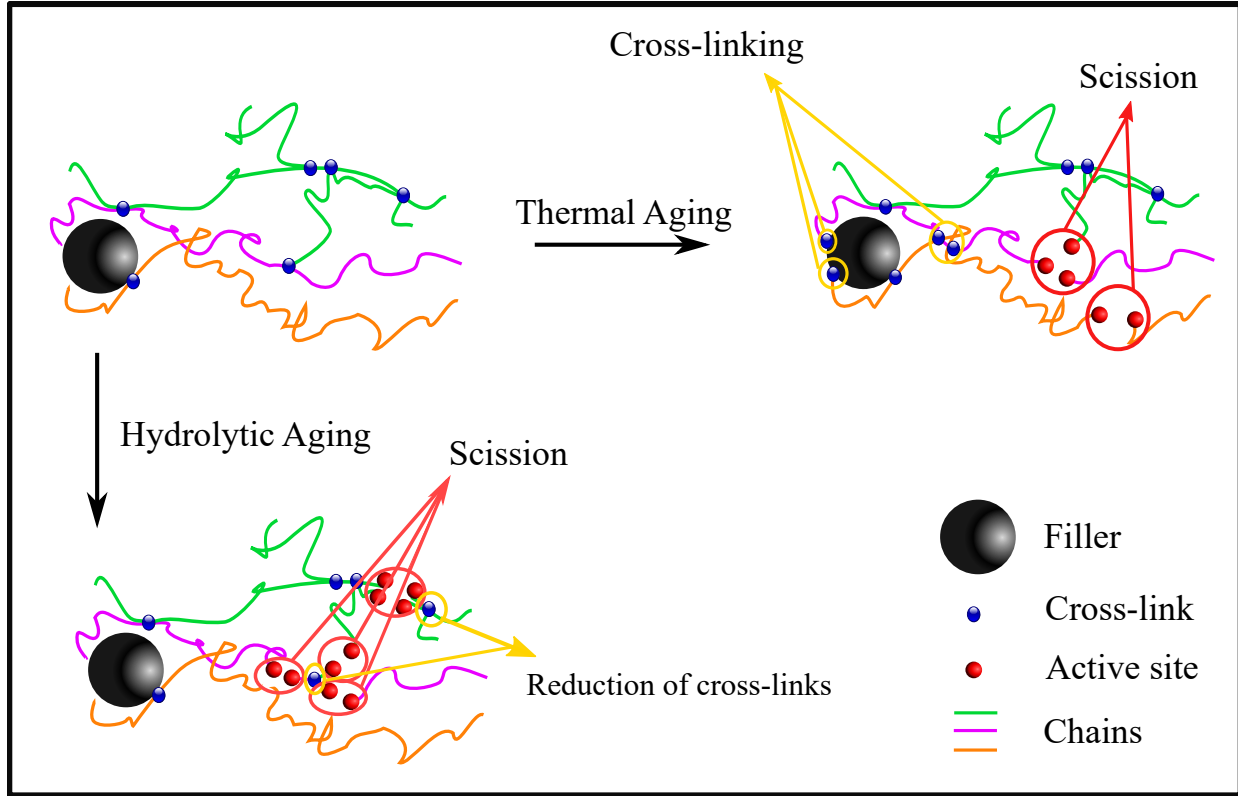


Figure 4.1: A schematic diagram of chemical aging (i.e. thermal and hydrolytic aging). Thermal aging results from two simultaneous phenomena; cross-linking, and chain scission while hydrolytic aging is due to the reduction of cross-links and chain scission.

$$[CR_P] = CR_{P_\infty} - CR_{P_1} \exp\left(-\tau_0 \exp\left(-\frac{E_a}{RT}\right)t\right). \quad (4.4)$$

Where $[CR_P]$ is the peroxide cross-link concentration, CR_{P_∞} is its concentration in a totally aged stage and CR_{P_1} is the difference between the initial and final concentration of cross-links.

4.2.2 Hydrolysis Kinetics

Similar to thermo-oxidative aging, hydrolysis is generally modeled via first-order kinetics equations, but with respect to the carboxylic end groups' formation rate

$$\frac{d[C]}{dt} = \zeta[C], \quad (4.5)$$

where $[C]$ is the concentration of carboxyl end groups in the polymer matrix. The parameter ζ is the hydrolytic degradation rate, which mainly defines the speed of aging. In this respect, mechanical stress, the ester group condensation, polymer structure, water diffusion, temperature, and the degradation environment's pH are several factors that affect the degradation rate. Accordingly, implementing mechanical stress during hydrolytic degradation can raise the probability of chain cleavage and subsequently increase the hydrolysis rate constant ζ . Moreover, temperature escalates the ζ as it increases the polymer chain mobility. Similarly, the degradation environment's pH can affect the hydrolysis rate constant through catalysis. In this study, the hydrolysis rate ζ remains constant during the degradation process due to the absence of mechanical loading, constant temperature, and constant domain pH. Besides, the time for diffusing the water into the sample's volume is negligible in comparison to the hydrolytic aging. In fact, the water spread out in the sample's volume homogeneously. Hence, the concentration of the water molecules is assumed to be constant over the degradation time. In this work, to simplify the formulation, the degradation rate is assumed to be constant in the course of aging for a specified temperature T . Hence the hydrolytic degradation rate can be rewritten as

$$\zeta = \gamma \exp\left(-\frac{E_a}{\mathcal{R}T}\right), \quad (4.6)$$

where γ is the aging constant that describes the rate of hydrolytic aging. Since carboxyl end groups' concentration is inversely related to number-average molecular weight M_n , one can write the evaluation of the molecular weight along the hydrolytic aging trajectory as

$$M_n = M_{n_0} \exp\left(-\gamma \exp\left(-\frac{E_a}{\mathcal{R}T}\right)t\right) + M_{n_\infty}, \quad (4.7)$$

where M_{n_0} is the initial value of the number-average molecular weight and M_{n_∞} is its final value.

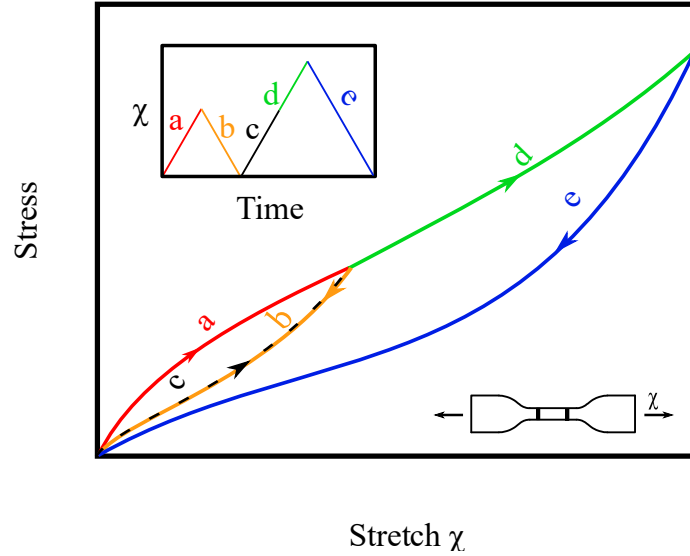


Figure 4.2: A schematic diagram of idealized Mullins effect (considerable softening between first loading and unloading). The idealized Mullins effect, which is generally regarded as stabilized softening, excludes the difference between unloading and reloading.

4.3 Constitutive Model

Generally, constitutive models of rubber-like materials are divided into two groups, namely phenomenological and micro-mechanical. The difference between these two groups lies in the source of construction of their strain energy function $W(\mathbf{F})$. Regarding the phenomenological models, $W(\mathbf{F})$ is often expressed as a function of strain invariant terms (i.e. I_1 , and I_2). On the other hand, the micro-mechanical models developed constitutive behavior of the material based on the polymer physics [74, 139]. The aim of this section is to build a physically-based constitutive model for cross-linked polymers, which is able to take into account the nonlinear inelastic mechanical behavior such as *idealized Mullins effect* along with each type of chemical aging (i.e. thermo-oxidative, and hydrolytic aging). The idealized Mullins effect, which is often referred to as stabilized softening, neglects the difference between unloading and reloading (see Fig. 4.2).

4.3.1 Statistical mechanics of polymers

Experimental observations revealed that elastomers constructed out of the long polymer chains which are randomly scattered in different directions [140, 141]. A single polymer chain consists of

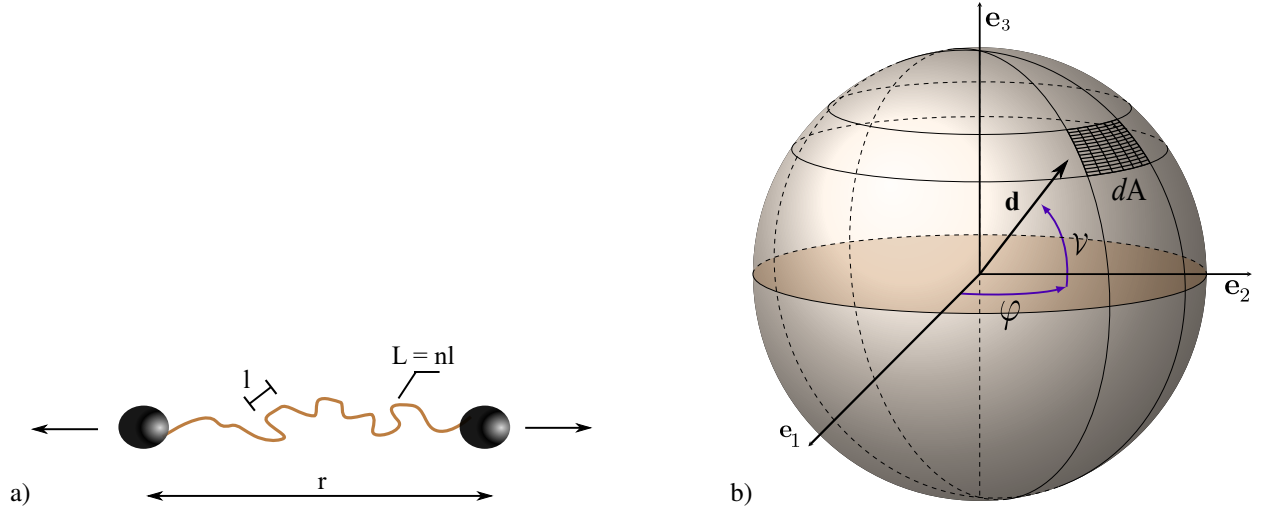


Figure 4.3: Schematic figures of a) a single polymer chain consisting of n segments with length l , and contour length nl and b) the unit micro-sphere with the orientation vector $\mathbf{d} = d_1 \mathbf{e}_1 + d_2 \mathbf{e}_2 + d_3 \mathbf{e}_3$.

several monomers which are constrained by two linkages at the end (see Fig. 6.6a) each of which might be resulted either from chemical or physical cross-linking. In order to duplicate mathematically, the morphology of the polymer network is assumed as a 3D composition of unlimited 1D chains that are distributed in all available spatial directions (for details, see [117]). As a result, the macroscopic free energy of polymer network $W(\mathbf{F})$ is expressed as the sum of microscopic strain energies of all active chains available within the network, which can be numerically calculated by integration over the unit sphere (see Fig. 6.6b). Within this concept, a freely rotating chain (FRC) consists of a certain number n , and length l of Kuhn segments with an end-to-end distance of \sqrt{nl} and a density of ρ_r^d . Due to the one-dimensional nature of sub-networks, they can only experience uni-axial stretches $\lambda^d = \sqrt{\mathbf{d}^T \mathbf{F}^T \mathbf{F} \mathbf{d}}$ and accordingly, they will be subjected to unique deformations due to their different directions [77]. Hereafter, the following font styles are used: for a scalar X , a vector \mathbf{X} , a second-order tensor \mathbf{X} , and a fourth-order tensor \mathbb{X} . Moreover, the bar sign over the parameters $\bar{X} = \frac{\bar{X}}{l}$ refers to their normalized value with respect to the Kuhn length l .

3-D generalization Integrating the entropic energy of a sub-network in all directions, the macroscopic energy of an arbitrary three-dimensional matrix can be written as

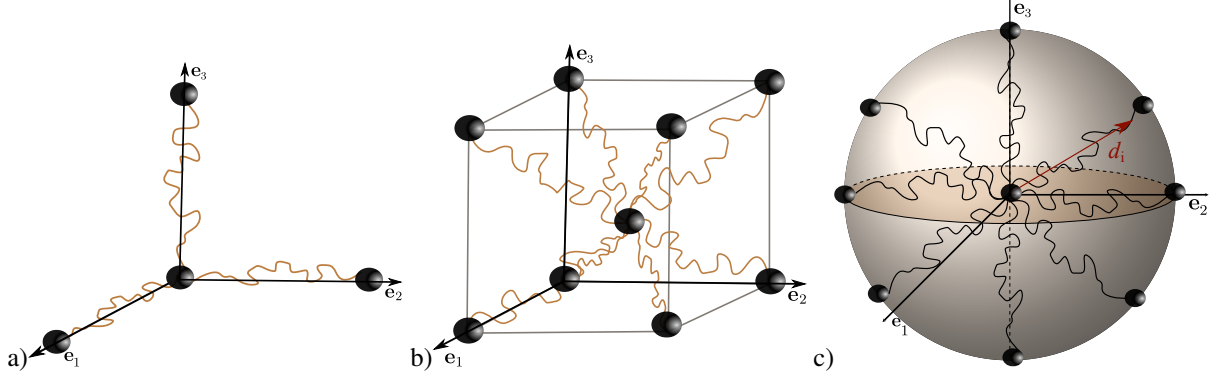


Figure 4.4: Polymer network models employed for modeling the chemical aging. a) the three-chain model, b) the eight-chain model, and c) the micro-sphere model.

$$W(\mathbf{F}) = \frac{1}{4\pi} \int_S \rho_r^d \psi^d dA \cong \sum_{i=1}^k \rho_r^d w_i \psi^d, \quad (4.8)$$

where the parameter ψ^d serves as the entropic energy of a single chain in an optional direction, \mathbf{d} . The parameter A is the unit area of the surface, normal to the direction \mathbf{d} . The parameters w_i are weight factors corresponding to the collocation directions \mathbf{d}_i ($i = 1, 2, \dots, k$). A different number of integration points on the half sphere yields different polymer network models with distinct properties. By choosing three points on the half sphere, the resulted network will be a three-chain model (see Fig. 4.4a) while by integrating on a four-point, the eight-chain model will be produced (see Fig. 4.4b). The eight and three-chain models can only model the idealized Mullins effect among all the inelastic phenomena. However, a set of $k = 21$ integration points on the half sphere can be used to capture more complex inelastic phenomena such as *deformation induced anisotropy* (see Fig. 4.4c).

Energy of a single chain Based on an enhanced version of non-Gaussian statistics (see [142] for details), the strain energy density of a freely rotating chain is written as

$$\hat{\psi}_c(\bar{n}) = \bar{n} K_b T \int_0^{\mathcal{T}} \hat{\beta} d\hat{\mathcal{T}} + \psi_0, \quad \hat{\beta} = \left[1 - \frac{1 + \mathcal{T}^2}{\bar{n}} \right] \beta. \quad (4.9)$$

where $\beta = \mathcal{L}^{-1}(\mathcal{T})$ is the inverse Langevin function, $\mathcal{T} = \frac{\lambda^d}{\sqrt{\bar{n}}}$ the extensibility ratio in the deformed configuration, K_b and T denote Boltzmann's constant and the absolute temperature, and ψ_0 is the entropy of the chain in reference state. An appropriate approximation approach for the inverse Langevin function can be selected depending on the elongation range of polymer chains. Here, a simple and accurate approximation with first-order rational function (relative error of 0.9%) is used (see [84] for details)

$$\mathcal{L}^{-1}(x) \cong \frac{x}{1-x} + 2x - \frac{8}{9}x^2. \quad (4.10)$$

4.3.2 Damage

The main sources of damage in the polymer matrix are, namely: i) mechanical, and ii) environmental. Here the main assumption of our recent model is that the nature of these two phenomena is independent of each other, and as a result, their effects on polymer matrix can superpose on top of each other. Hence, in order to take into account the chemical degradation along with mechanical loading, the deterioration of the polymer matrix should be characterized by three external variables; (i) storage temperature T , (ii) storage time t , and (iii) deformation \mathbf{F} . All the aforementioned parameters are similar for thermo-oxidative and hydrolytic aging.

- In the course of mechanical, the induced damage results from the debonding of shorter chains from cross-links or aggregates surface during the primary loading. By stretching the material, the junction between cross-links and polymer chains will be broken. Accordingly, the Mullins effect can be regarded as the evolution of the polymer macro-molecules through the maximum micro-stretch in an arbitrary direction \mathbf{d} previously reached in the loading history $\lambda_m^d = \max_{\tau \in (-\infty, t]} \lambda^d(\tau)$. In this respect, Marckmann et al.[143] considered the evolution of the polymer chains as a result of two phenomena; (i) active chains' length \bar{n}^d increase which are involved in polymer network elasticity, and (ii) number of active chains per unit of volume ρ_r^d decrease. Moreover, in the course of deformation-induced matrix transition, they assumed that the number of active polymer monomers per unit of volume would remain almost constant throughout the deformation. Based on the network alteration theory, the

mechanical damage in each direction d can be best modeled via an exponential function of the maximum deformation endured previously by the material λ_m^d :

$$\bar{n}^d = n_0 \exp(\mu \lambda_m^d) \quad \text{and} \quad \rho_r^d = \rho_{r_0} \exp(-\mu \lambda_m^d), \quad (4.11)$$

where n_0 , ρ_{r_0} , and μ are the material parameters that will be determined through the fitting process. Due to the assumption that the number of active segments remains constant during the deformation, the rate of the exponential functions μ in both of the equations represented in Eq.4.11 are equal.

- During the chemical aging without the presence of mechanical loading, damage is mainly related to the alteration of the number of active polymer chains resulting in a change in the morphology of the polymer matrix. Accordingly, in order to see the effects of the storage time and temperature on the number of available active chains in each direction ρ_r^d , one can assume that the alteration of the chain density along the aging trajectory is equal to the peroxide cross-link density for thermo-oxidation and the change of the average molecular weight M_n for hydrolysis. Hence, the modified chain density function in the case of hydrolytic or thermal oxidation aging is given by

$$\rho_r^d = \rho_{r_\infty} \exp(-\mu \lambda_m^d) + \begin{cases} \rho_{r_0} \exp(-\exp(-\frac{E_a}{RT})t - \mu \lambda_m^d), & \rho_{r_0} > \rho_{r_\infty} & \text{if hydrolytic Aging} \\ -\rho_{r_0} \exp(-\exp(-\frac{E_a}{RT})t - \mu \lambda_m^d), & \rho_{r_0} < \rho_{r_\infty} & \text{if thermo-oxidative Aging} \end{cases} \quad (4.12)$$

In view of the reduced computational cost of the proposed model in comparison to [9, 133, 12], the proposed model has certain limitations

- Model needs to be fitted to multiple loading types; otherwise the predictions obtained by fitting to uni-axial tension only, may not be accurate for bi-axial loading.

- The model is relevant only for compounds in which mechanical and environmental damages are entirely independent of each other.
- Model is built on the presumption of homogeneous and consistent oxygen/water absorption throughout the material, which is only the case in thin samples that are aged for a sufficiently long time.

4.3.3 Constitutive formulation

For an incompressible polymer matrix

$$\det \mathbf{F} = 1 \quad (4.13)$$

where \mathbf{F} stands for the macro-scale deformation gradient. The first Piola-Kirchhoff stress tensor \mathbf{P} can be written as

$$\mathbf{P} = \frac{\partial W(\mathbf{F})}{\partial \mathbf{F}} - p\mathbf{F}^{-T}, \quad \frac{\partial W(\mathbf{F})}{\partial \mathbf{F}} = \sum_{j=1}^k w_j \rho_r^{d_j} \frac{\partial \psi_c^{d_j}}{\partial \lambda} \frac{1}{2} \frac{\partial \mathbf{d}_j \bar{\mathbf{C}} \mathbf{d}_j}{\partial \mathbf{F}} : \frac{\partial \bar{\mathbf{F}}}{\partial \mathbf{F}} \quad (4.14)$$

where parameter p guarantees the incompressibility, \mathbf{C} stand for the right Cauchy–Green tensor, $J^2 = \det \mathbf{C}$, and $\bar{\mathbf{C}} = J^{-2/3} \mathbf{C}$. The Eq.4.14 can be even more simplified by using the following procedure

$$\frac{\partial \psi_c(\bar{n}, \lambda^d)}{\partial \lambda^d} = \sqrt{\bar{n}} K_B T \hat{\beta} \left(\frac{\lambda^d}{\sqrt{\bar{n}}}, \bar{n} \right), \quad \frac{\partial \mathbf{d} \bar{\mathbf{C}} \mathbf{d}}{\partial \mathbf{F}} : \frac{\partial \bar{\mathbf{F}}}{\partial \mathbf{F}} = 2\bar{\mathbf{F}}(\mathbf{d} \otimes \mathbf{d}) : J^{-\frac{1}{3}} \mathbb{I} = 2J^{-\frac{1}{3}} \bar{\mathbf{F}}(\mathbf{d} \otimes \mathbf{d}). \quad (4.15)$$

In the Eq. 4.15, $\hat{\beta}$ is the modified version of nonlinear Langevin force which is suitable for

polymers including short chains. Thus, Eq.4.14 yields

$$\mathbf{P} = K_B T \sum_{i=1}^k \rho_r^{d_i} \sqrt{\bar{n}^{d_i}} \mathcal{L}^{-1} \left(\frac{d_i}{\sqrt{\bar{n}^{d_i}}} \right) \frac{w_i}{d_i} J^{-\frac{1}{3}} \bar{\mathbf{F}}(\mathbf{d}_i \otimes \mathbf{d}_i) - p \mathbf{F}^{-T}. \quad (4.16)$$

4.4 Finite Element Linearization

In what follows, the algorithmic framework of the devised model which is suitable for an FE implementation is presented. To this end, first, the second Piola-Kirchhoff stress \mathbf{S} and consistent tangent modulus \mathbb{C} are derived. Then, The in-compressible plane stress condition in total Lagrangian finite strain is formulated. Since the system of the equations is nonlinear, the Newton-Raphson method is utilized to iteratively solve the problem [144]. Hence, the second Piola-Kirchhoff stress should be linearized, and it could be written as

$$\delta \mathbf{S} = \mathbb{C} : \delta \mathbf{E}, \quad (4.17)$$

where \mathbf{E} is the Green-Lagrange strain tensor (i.e. $\mathbf{E} = \frac{1}{2}(\mathbf{C} - \mathbf{I})$). The second Piola-Kirchhoff stress \mathbf{S} is the first derivatives of the strain energy $W(\mathbf{F})$ with respect to Green-Lagrange strain tensor \mathbf{E} . By considering incompressibility condition, the second Piola-Kirchhoff stress \mathbf{S} could be written as

$$\mathbf{S} = \frac{\partial W(\mathbf{F})}{\partial \mathbf{E}} - p J \mathbf{C}^{-1} = 2 \frac{\partial W(\mathbf{F})}{\partial \bar{\mathbf{C}}} : \frac{\partial \bar{\mathbf{C}}}{\partial \mathbf{C}} - p J \mathbf{C}^{-1}, \quad (4.18)$$

where $\frac{\partial \bar{\mathbf{C}}}{\partial \mathbf{C}}$ is a fourth order deviatoric projection tensor in Lagrangian description and could be written as

$$\frac{\partial \bar{\mathbf{C}}}{\partial \mathbf{C}} = J^{-\frac{2}{3}} \left(\mathbb{I} - \frac{1}{3} \mathbf{C} \otimes \mathbf{C}^{-1} \right), \quad (4.19)$$

where \mathbb{I} is the fourth order identity tensor. By substituting Eq. 4.19 in Eq. 4.18, one can rewrite

the second Piola-Kirchhoff stress as

$$\mathbf{S} = 2J^{\frac{-2}{3}} \frac{\partial W(\mathbf{F})}{\partial \bar{\mathbf{C}}} - \frac{2}{3} J^{\frac{-2}{3}} \frac{\partial W(\mathbf{F})}{\partial \bar{\mathbf{C}}} : (\mathbf{C} \otimes \mathbf{C}^{-1}) - pJ\mathbf{C}^{-1}. \quad (4.20)$$

Here, *the plane stress* assumption is used to determine Lagrangian multiplier. In this respect, the Cauchy stress σ in the out-of-plane direction is set to zero. Accordingly, by defining $\mathbf{S}^n = 2 \frac{\partial W(\mathbf{F})}{\partial \bar{\mathbf{C}}}$, the hydrostatic pressure p can be obtained as

$$p = J^{\frac{-5}{3}} \mathbf{S}_{33}^n \mathbf{F}_{33}^2 - \frac{1}{3} J^{\frac{-5}{3}} \mathbf{S}^n : \mathbf{C}. \quad (4.21)$$

By substituting hydrostatic pressure p in the Eq. 4.21, one can write the second Piola-Kirchhoff stress tensor in the case of plane stress as

$$\mathbf{S} = J^{\frac{-2}{3}} (\mathbf{S}^n - \mathbf{S}_{33}^n \mathbf{F}_{33}^2 \mathbf{C}^{-1}). \quad (4.22)$$

The Lagrangian elasticity tensor \mathbb{C} is derived thanks to the differentiation of the second Piola-Kirchhoff stress tensor \mathbf{S} with respect to the Green-Lagrange strain tensor \mathbf{E} :

$$\mathbb{C} = \frac{\partial \mathbf{S}}{\partial \mathbf{E}} = 2 \frac{\partial \mathbf{S}}{\partial \bar{\mathbf{C}}} = 2 \frac{\partial \mathbf{S}}{\partial \bar{\mathbf{C}}} : \frac{\partial \bar{\mathbf{C}}}{\partial \mathbf{E}}. \quad (4.23)$$

By defining $\mathbb{C}^n = 4 \frac{\partial^2 W(\mathbf{F})}{\partial \bar{\mathbf{C}}^2}$, $\mathbf{Z} = \begin{Bmatrix} 0 & 0 & 0 \\ 0 & 0 & 0 \\ 0 & 0 & \mathbf{F}_{33}^2 \end{Bmatrix}$, and $\mathbf{Z}' = \begin{Bmatrix} 0 & 0 & 0 \\ 0 & 0 & 0 \\ 0 & 0 & 2\mathbf{F}_{33} \end{Bmatrix}$ the Lagrangian tangent modulus is calculated:

$$\begin{aligned}
\mathbb{C} = & \frac{-2}{3} J^{\frac{-2}{3}} (\mathbf{S}^n - \mathbf{S}_{33}^n \mathbf{F}_{33}^2 \mathbf{C}^{-1}) \otimes \mathbf{C}^{-1} \\
& + J^{\frac{-4}{3}} \left(\mathbb{C}^n - \frac{1}{3} \mathbb{C}^n : \mathbf{C} \otimes \mathbf{C}^{-1} - \mathbf{C}^{-1} \otimes \mathbb{C}^n : \mathbf{Z} + \frac{1}{3} (\mathbf{C} : \mathbb{C}^n : \mathbf{Z}) \mathbf{C}^{-1} \otimes \mathbf{C}^{-1} \right) \\
& - J^{\frac{-2}{3}} \left(2\mathbf{S}^n : \mathbf{Z}' \mathbf{C}^{-1} \otimes \frac{\partial \mathbf{F}_{33}}{\partial \mathbf{C}} - 2\mathbf{S}^n : \mathbf{Z} \mathbf{C}^{-1} \otimes \mathbf{C}^{-1} \right), \tag{4.24}
\end{aligned}$$

where

$$\frac{\partial \mathbf{F}_{33}}{\partial \mathbf{C}} = \frac{\partial \mathbf{F}_{33}}{\partial \mathbf{F}} \frac{\partial \mathbf{F}}{\partial \mathbf{C}} = \frac{1}{2} \mathbf{F}^{-1} \mathbf{F}', \quad \text{where} \quad \mathbf{F}' = \frac{\partial \mathbf{F}_{33}}{\partial \mathbf{F}} = \mathbf{F}_{33}^2 \begin{Bmatrix} -\mathbf{F}_{22} & \mathbf{F}_{21} & 0 \\ \mathbf{F}_{12} & -\mathbf{F}_{11} & 0 \\ 0 & 0 & 0 \end{Bmatrix}. \tag{4.25}$$

4.4.1 The Plane-Stress Condition

The general 3-D incremental stress-strain relation in Eq. 4.17 can be simplified for a certain special case, namely plane stress. In the plane stress case, all stresses are parallel to the xy-plane and normal to the z-axis and therefore all the out of plane shear component of the stress tensor are equal to zero (i.e. $\delta \mathbf{S}_{13} = \delta \mathbf{S}_{31} = \delta \mathbf{S}_{23} = \delta \mathbf{S}_{32} = 0$). By using Voigt-Mandel notation Eq. 4.17 can be rewritten as

$$\begin{Bmatrix} \delta \mathbf{S}_{11} \\ \delta \mathbf{S}_{22} \\ \delta \mathbf{S}_{12} \\ \delta \mathbf{S}_{33} \end{Bmatrix} = \begin{Bmatrix} \mathbb{C}_{1111} & \mathbb{C}_{1122} & \mathbb{C}_{1112} & \mathbb{C}_{1133} \\ \mathbb{C}_{2211} & \mathbb{C}_{2222} & \mathbb{C}_{2212} & \mathbb{C}_{2233} \\ \mathbb{C}_{1211} & \mathbb{C}_{1222} & \mathbb{C}_{1212} & \mathbb{C}_{1233} \\ \mathbb{C}_{3311} & \mathbb{C}_{3322} & \mathbb{C}_{3312} & \mathbb{C}_{3333} \end{Bmatrix} \begin{Bmatrix} \delta \mathbf{E}_{11} \\ \delta \mathbf{E}_{22} \\ 2\delta \mathbf{E}_{12} \\ \delta \mathbf{E}_{33} \end{Bmatrix}. \tag{4.26}$$

In Eq. 4.26, the strain in the out-of-plane direction $\delta \mathbf{E}_{33}$ is not an independent variable. As $\delta \mathbf{S}_{33} = 0$ and $\mathbb{C}_{3333} = 0$, the static condensation cannot be applied. Hence in order to remove $\delta \mathbf{E}_{33}$ from the system of equation, it should be written in terms of in-plane strains (i.e. $\delta \mathbf{E}_{11}$, $\delta \mathbf{E}_{22}$, and

$\delta \mathbf{E}_{12}$). By knowing

$$\mathbf{E}_{33} = \frac{1}{2} (\mathbf{C}_{33} - 1) = \frac{1}{2} (\mathbf{F}_{33}^2 - 1), \quad (4.27)$$

$\delta \mathbf{E}_{33}$ could be written as

$$\delta \mathbf{E}_{33} = \frac{\delta \mathbf{E}_{33}}{\delta \mathbf{E}} : \delta \mathbf{E} = \frac{\delta \mathbf{E}_{33}}{\delta \mathbf{F}_{33}} \frac{\delta \mathbf{F}_{33}}{\delta \mathbf{C}} \frac{\delta \mathbf{C}}{\delta \mathbf{E}} : \delta \mathbf{E} = \frac{1}{2} \mathbf{F}_{33} \mathbf{F}^{-1} \mathbf{F}' : \delta \mathbf{E}. \quad (4.28)$$

By defining $\mathbf{A} = \frac{1}{2} \mathbf{F}_{33} \mathbf{F}^{-1} \mathbf{F}$, the plane stress Lagrangian elasticity tensor \mathcal{C} could be written as

$$\mathcal{C} = \left\{ \begin{array}{ccc} \mathbf{C}_{1111} & \mathbf{C}_{1122} & \mathbf{C}_{1112} \\ \mathbf{C}_{2211} & \mathbf{C}_{2222} & \mathbf{C}_{2212} \\ \mathbf{C}_{1211} & \mathbf{C}_{1222} & \mathbf{C}_{1212} \end{array} \right\} + \left\{ \begin{array}{ccc} \mathbf{A}_{11} \mathbf{C}_{1133} & \mathbf{A}_{22} \mathbf{C}_{1133} & 2\mathbf{A}_{12} \mathbf{C}_{1133} \\ \mathbf{A}_{11} \mathbf{C}_{2233} & \mathbf{A}_{22} \mathbf{C}_{2233} & 2\mathbf{A}_{12} \mathbf{C}_{2233} \\ \mathbf{A}_{11} \mathbf{C}_{1233} & \mathbf{A}_{22} \mathbf{C}_{1233} & 2\mathbf{A}_{12} \mathbf{C}_{1233} \end{array} \right\}. \quad (4.29)$$

Finally, the detailed derivation of \mathcal{C}^n and \mathbf{S}^n are given in the appendix.

4.5 Validation and Results

4.5.1 Comparisons with our experimental data

In order to evaluate the capability of the devised model, its predictions were bench-marked against our experimental results, which particularly designed to show the effect of chemical aging on the constitutive response of polymers. In this respect, a universal testing machine (*TestResources 311 Series Frame*) was utilized for uni-axial tensile tests. All the experiments were displacement controlled under the quasi-static condition with a cross-head speed of $50 \frac{mm}{min}$. The vertical gap between the extensometer grips was fixed to 25.4 mm and, all the tests were operated at room conditions (i.e. $22 \pm 2^\circ\text{C}$, $50 \pm 3\%$ RH). Each sample was stretched until breakage, and all the aging condition has been repeated with five samples for reliability control. In this study, two different cross-linked polymers, namely PDMS (Polydimethylsiloxane)-based adhesives, and Styrene-butadiene rubber (SBR) was used to evaluate the generality of the model for different polymer types. Hence, in the

case of the hydrolytic aging, the PDMS was used due to its high sensitivity to the water attack while in the thermo-oxidative aging, the SBR was used owing to its susceptibility to the thermal degradation. The experimental procedure was as follows. First, all the samples were matched the standard dimensions mentioned in ASTM D412 (Die C). Next, in the case of hydrolytic aging, all the samples were entirely submerged in several closed buckets filled with de-ionized water at temperatures 60°C, 80°C, and 95°C, while in the thermo-oxidative aging samples were put in the ovens with the relative humidity of zero (i.e. RH= 0%) at temperatures 45°C, 60°C, and 80°C. All the specimens were aged with a constant pressure, and after a certain amount of aging time, specimens were removed from containers and immediately dried with tissue paper. Using the six material parameters, the model was fitted for the following three cases:

- The primary loading curve of the virgin specimen to investigate the effects of λ and λ_m
- one point of loading curve of 10 days aged specimen to study the effects of λ_m , and t
- one point of loading curve of 30 days aged specimen to investigate the effects of t , and T

To this end, Levenberg–Marquardt algorithm was used to minimize the least square error function. The so-obtained parameters of the devised model for silicon adhesive during hydrolytic aging are given in Table 4.2 while the material parameters of SBR during the thermo-oxidative aging are given in Table 4.1. The predictions of the proposed model against the experimental data for different types of aging and different amounts of aging times, temperatures, and deformations are plotted in Figs. 5.15a-e and Figs. 4.6a-e. It should be noted that for the case of unloading experiments, we used the concept of data treatment (see [61] for details). Moreover, the changes in the loading-unloading response of the silicon adhesive aged at 80°C along with the hydrolytic aging are compared in Fig. 5.15f, while the alteration of the cyclic response of the SBR during thermal degradation at 60°C is plotted in Fig. 4.6f. Due to the simplicity of the current model, it cannot capture complex behaviors such as curvature change, so this is the best fit that can be achieved. In fact, it is a trade-off between the accuracy and simplicity of the model. Furthermore, during aging experiments, there are different sources of error, such as diffusion-limited oxidation

Table 4.1: Material parameters of the proposed model for SBR subjected to the thermo-oxidative aging.

| $\rho_{r_0} K_b T [Mpa]$ | $\rho_{r_\infty} K_b T [Mpa]$ | n_0 | μ | $\gamma [1/d]$ | $\frac{E_a}{R} [K]$ |
|--------------------------|-------------------------------|-------|-------|----------------|---------------------|
| 1.4416 | 2.2072 | 2.497 | 0.52 | 4.09875e+18 | 1.6148e+04 |

Table 4.2: Material parameters of the proposed model for silicon adhesive subjected to the hydrolytic aging.

| $\rho_{r_0} K_b T [Mpa]$ | $\rho_{r_\infty} K_b T [Mpa]$ | n_0 | μ | $\gamma [1/d]$ | $\frac{E_a}{R} [K]$ |
|--------------------------|-------------------------------|-------|-------|----------------|---------------------|
| 0.1594 | 0.0106 | 2.497 | 0.52 | 4.387e+14 | 1.323e+04 |

(DLO), incomplete water diffusion, and over-curing. Since considering all of these phenomena in the model will result in a more complicated model, which would not be computationally efficient, we neglect their effects in our model. Therefore, facing errors as high as 10% (for instance in the case of 10 days at $95^\circ C$) is still acceptable.

Compared with our previous models, our recent model reduces the number of parameters significantly which is mainly due to the change of the model's kernel and the correlation of mechanical and environmental damages. In our previous models, the *network evolution model* was utilized as the kernel of the models while in this paper, the *network alteration model* is used to model the rubber inelasticity. In addition, here we assumed that the mechanical and environmental damages are independent while in our previous models, these damages were coupled to each other. To demonstrate this reduction quantitatively, four material parameters were reduced in the case of our hydrolytic aging model while four and six material parameters were reduced for our first and second models in the thermo-oxidative aging, respectively.

To demonstrate quantitatively the computational efficiency of the proposed model, its performance was compared to our recent models. In this respect, Table 4.3 shows the computational cost of each model for calculating the second Piola-Kirchhoff stress during one loading-unloading cycle. The computational cost of our devised model generally depends on the number of integration points on the micro-sphere. By choosing the four-point on the half-sphere, the model can

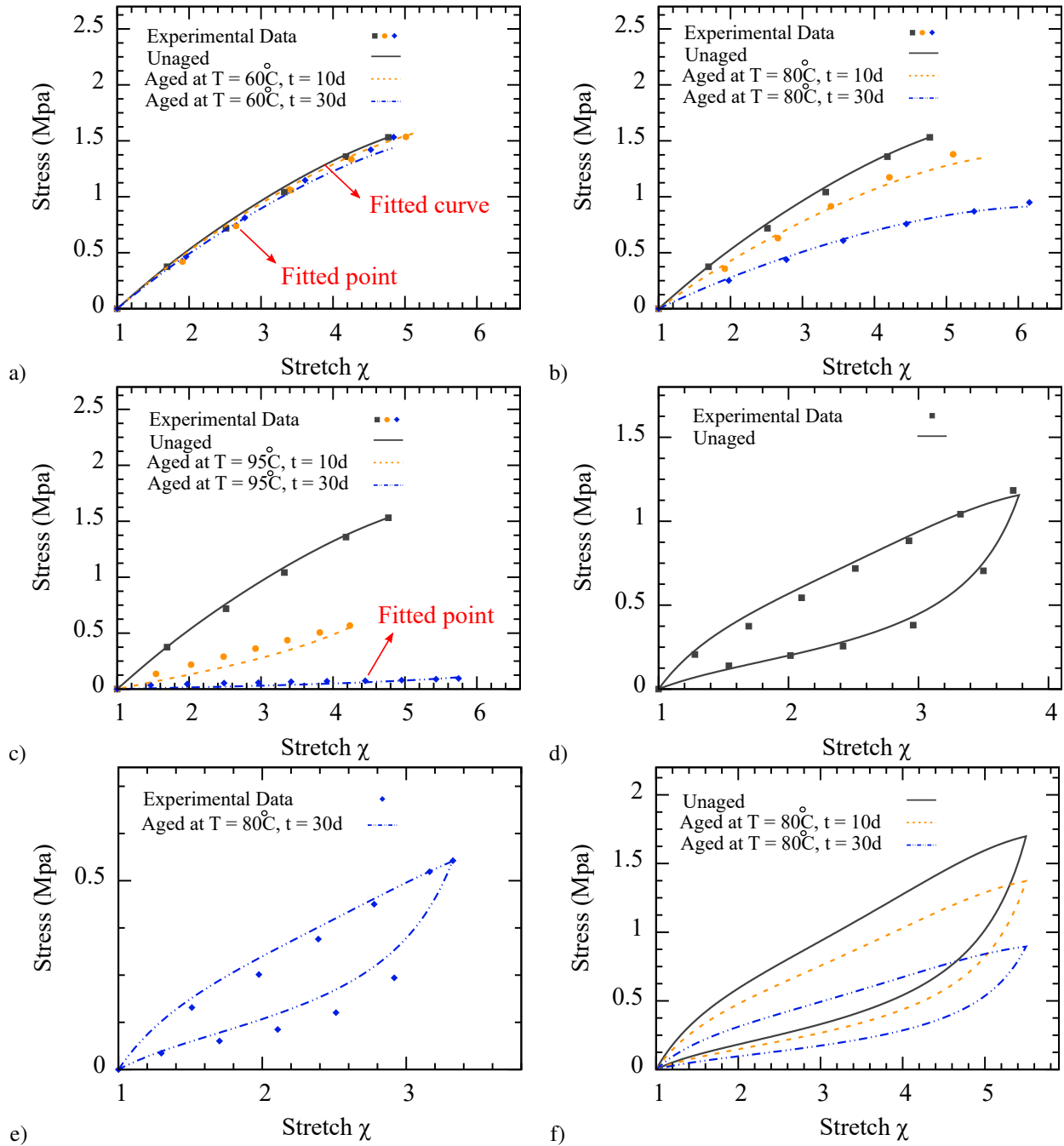


Figure 4.5: Validation of model predictions against experimental results for silicon adhesive in unaged state, and submerged in distilled water for 10 and 30 days in multiple temperature conditions; (a) 60°C , (b) 80°C , (c) 95°C , (d) constitutive behavior for unaged sample, (e) constitutive behavior for 30 days aged sample at temperature 80°C , and (f) Comparison of one cycle of loading-unloading on samples stored at 80°C for 10 and 30 days. As it can be seen, the devised constitutive model is able to predict the softening caused by hydrolytic aging. Solid lines represent model predictions while dot points depict the experimental data. The arrows demonstrate the curves and the points which are used for fitting.

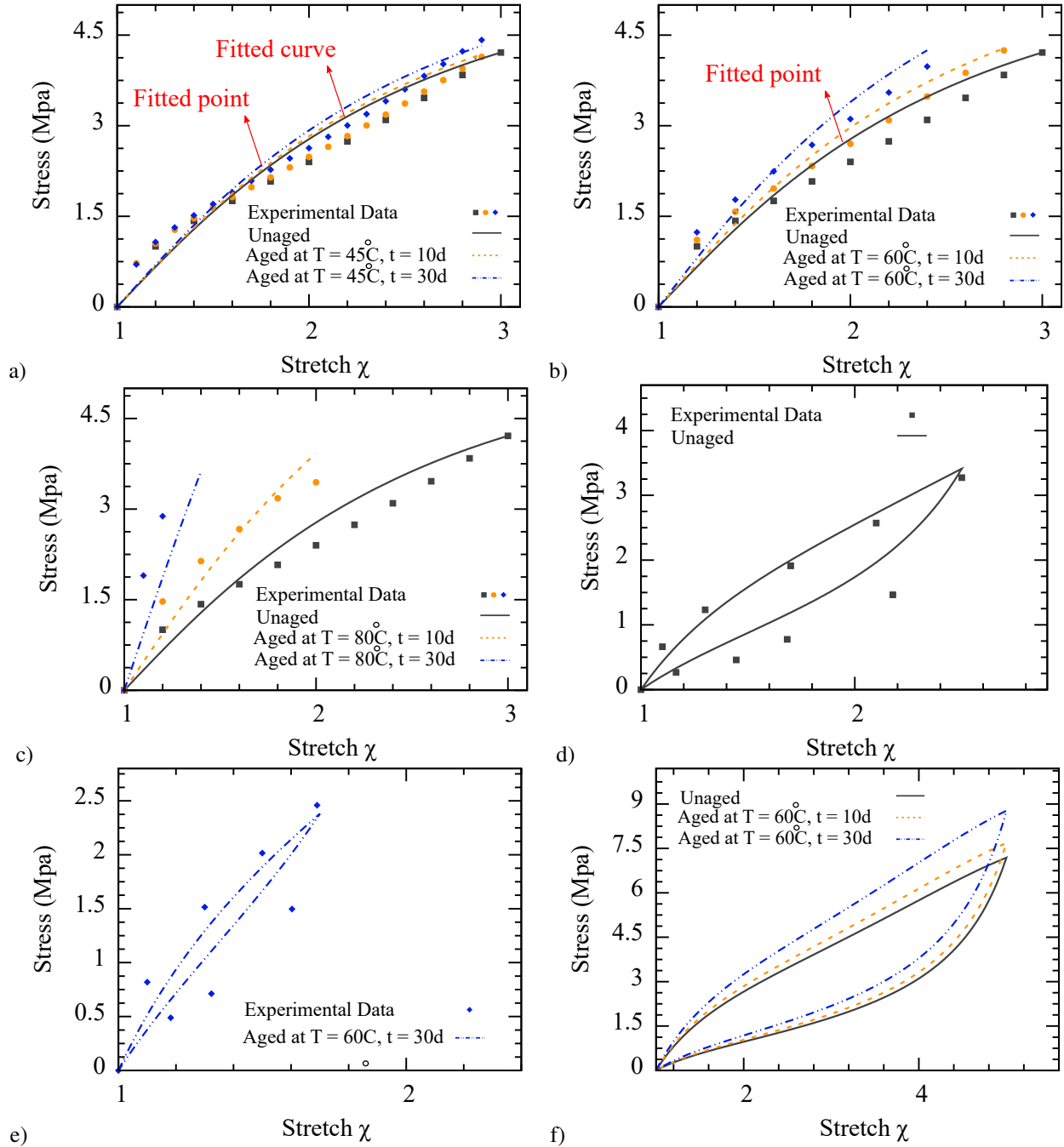


Figure 4.6: Validation of model predictions against our experimental data for SBR in unaged state and during thermo-oxidative aging for 10 and 30 days in multiple temperature conditions; (a) 45°C , (b) 60°C , (c) 80°C , (d) constitutive behavior for unaged sample, (e) constitutive behavior for 30 days aged sample at temperature 60°C , and (f) Comparison of one cycle of loading-unloading on samples stored at 60°C for 10 and 30 days. As it can be seen the devised constitutive model can predict the hardening effect caused by thermo-oxidation. Solid lines represent model predictions while dot points depict the experimental data. The arrows demonstrate the curves and the points which are used for fitting.

reduce the run time of simulation by almost 400 times in the case of hydrolytic aging and 600 times in thermo-oxidative aging.

Table 4.3: Comparison of computational costs of our recent models. In the table below, characters PM4, PM21, and PM45 represent the proposed model with 4, 21, and 45 Gaussian points on the half sphere respectively. Moreover, the character HM stands for our hydrolytic aging model [9] while TM1 and TM2 depict our first [133], and second [12] models for thermo-oxidative aging respectively.

| Hydrolytic aging | | | | | |
|-------------------------------|-------|-------|-------|---------|---------|
| Model | PM4 | PM21 | PM45 | HM | |
| Run time (sec) | 0.209 | 0.262 | 0.287 | 84.87 | |
| Thermo-Oxidative aging | | | | | |
| Model | PM4 | PM21 | PM45 | TM1 | TM2 |
| Run time (sec) | 0.209 | 0.262 | 0.287 | 121.834 | 236.401 |

4.5.2 Numerical simulation results

In order to demonstrate the capability of the proposed method in modeling the mechanical response of cross-linked polymers in large deformation along with aging, two numerical examples are presented. Indeed, the objective of this simulation is to assess the accuracy of the proposed model in predicting complex strain fields combined with either hydrolytic or thermo-oxidative aging. In both examples, the parameter values of the previous section are utilized.

- In the first example, a classical dog-bone specimen is modeled under prescribed displacements along the direction. Its length is equal to 115 mm, thickness is 3.75 mm, and the extensometer’s gauge length is 25.4 mm (see Fig. 4.7a for details). It is meshed with linear elements in displacement. Due to its thickness, the plane stress assumption is adopted. The strain–stress response predicted by the simulation in the central section is identical to the analytical response for the different amounts of deformations, aging times, and temperatures. Next, in order to see the effects of aging on the 3D state of stress, the contours of the second-Piola Kirchhoff stress S_{11} are plotted. In hydrolysis, the second-Piola Kirchhoff stress is

reduced by the aging time (see Fig. 4.9) while in thermal degradation, it is vice-versa (see Fig. 4.8). However, in both aging mechanisms, the induced deformation (i.e. mechanical damage) causes increases in the stress.

- In the last example, the capability of the proposed constitutive model is presented by modeling of a polymer sheet with large in-homogeneous deformations. A polymer sheet with the dimensions $62 \times 82.5 \times 1.75$ mm and five 20 mm diameter holes C1, C2, C3, C4, and C5 is modeled under prescribed displacements along-y direction. The detailed positions of the holes on the sheet are given in Fig. 4.7b. Here, the eight-chain model is utilized to plot the contour of chain density ρ_r^d . In fact, due to the symmetry of the eight-chain model, all the directions \mathbf{d} experience the same deformation (i.e. $\lambda^d = \sqrt{\frac{I_1}{3}}$), and as a result, the directional chain density ρ_r^d is the same for all directions and it can be a plottable quantity. Fig.4.10 shows the evolution of chain density, which is proportional to the number of active monomers during the hydrolytic and thermo-oxidative aging. Accordingly, the smaller the chain density in the network, the greater the stress-softening effect. Here, the chain density is a function of the first invariant of the deformation and aging time. Accordingly, due to the homogeneous aging assumption, the chain density will be the same over the entire sheet due to the effects of aging time while deformation causes the in-homogeneous distribution of chain density especially near the edges of the holes in the rubber sheet.

These two numerical results validate the implementation of the presented constitutive model and illustrate the independency of mechanical and environmental damage. Such simulations are crucial to show the capacities of structures in which the level of stress-softening through environmental and mechanical damages is noticeable.

4.6 Conclusion

The focus of this study was to reduce the number of model parameters without sacrificing the precision of the model to remedy the complexity of previous models. Here, a large strain three-

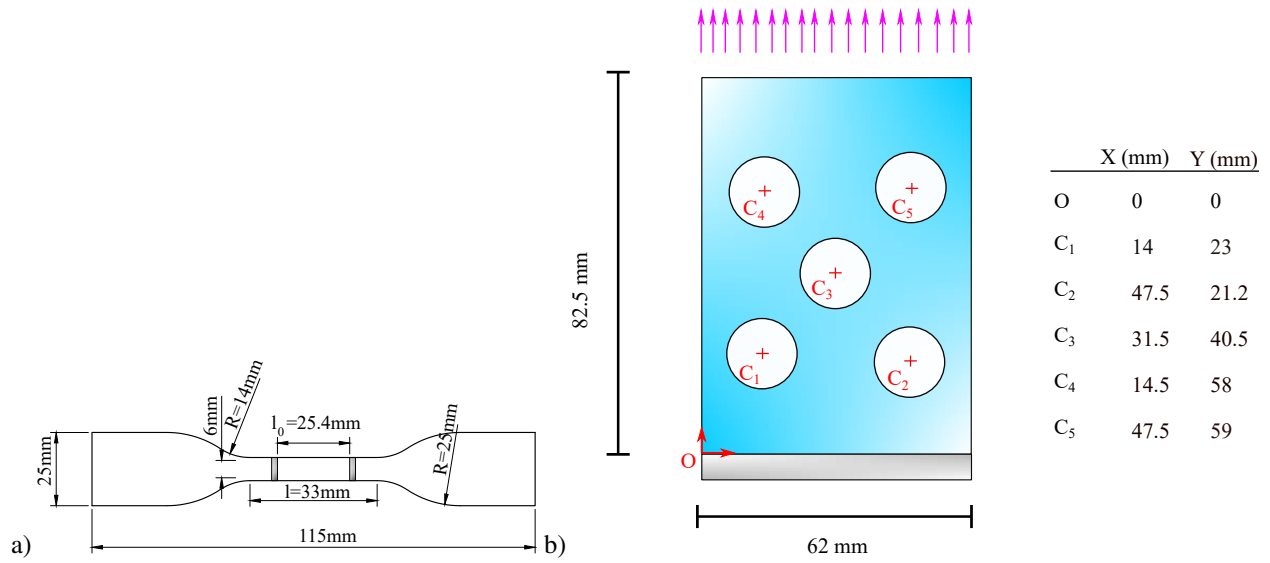


Figure 4.7: Detailed geometry of the samples used for FE (a) dog-bone sample and (b) rubber sheet with appropriate coordinates for its holes position.

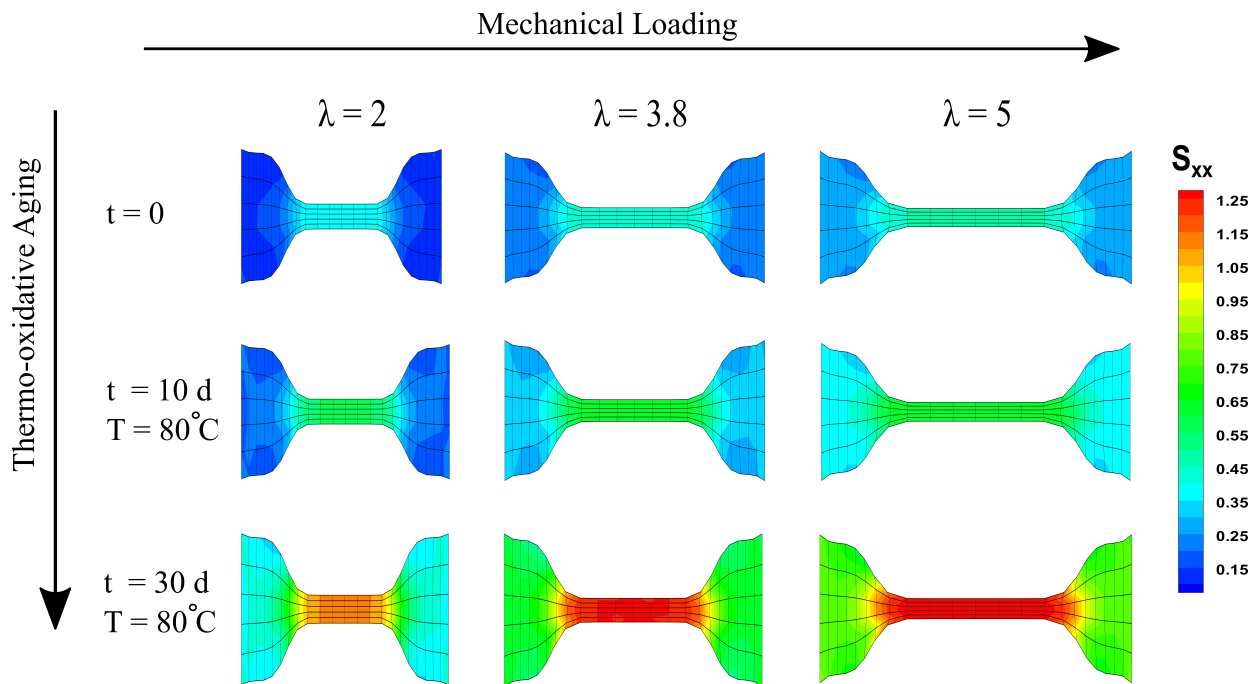


Figure 4.8: Evolution of the second-Piola Kirchhoff stress S_{11} of the SBR through thermo-oxidative aging and mechanical loading. As it can be seen, higher aging durations caused higher stress values due to hardening effect of thermo-oxidative aging.

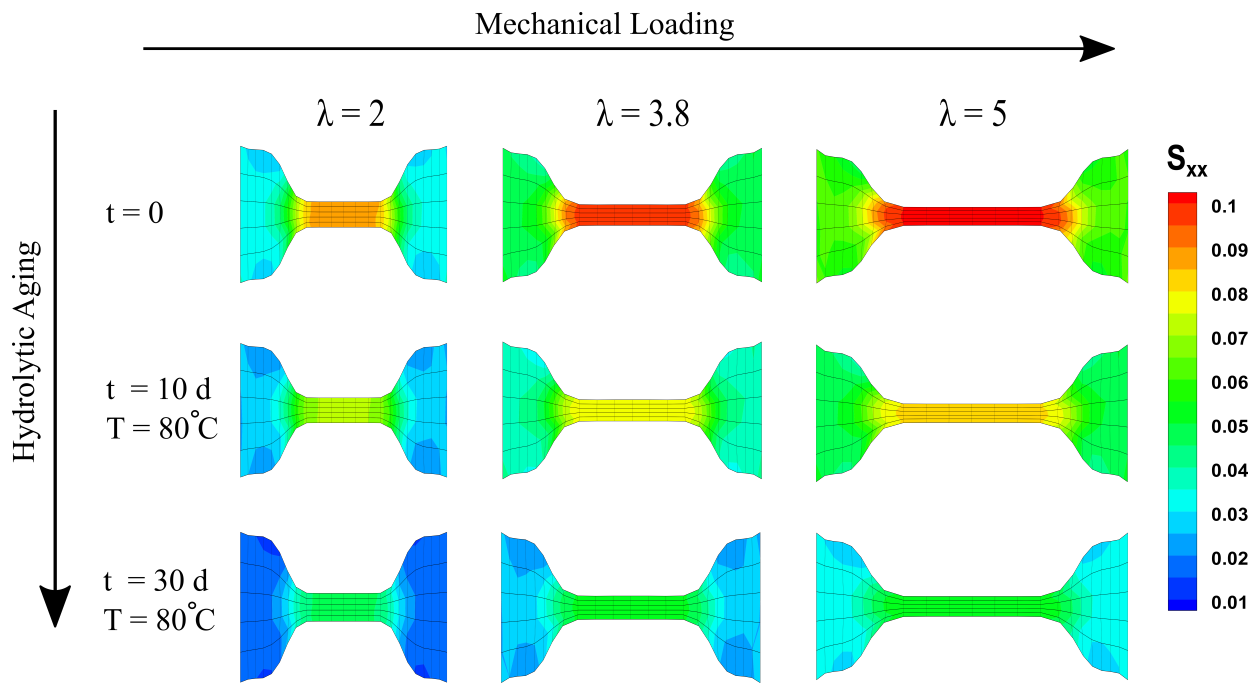


Figure 4.9: Evolution of the second-Piola Kirchhoff stress S_{11} of the silicon adhesive through hydrolytic aging and mechanical loading. As it can be seen, higher aging durations caused lower stress values due to softening effect of hydrolytic aging.

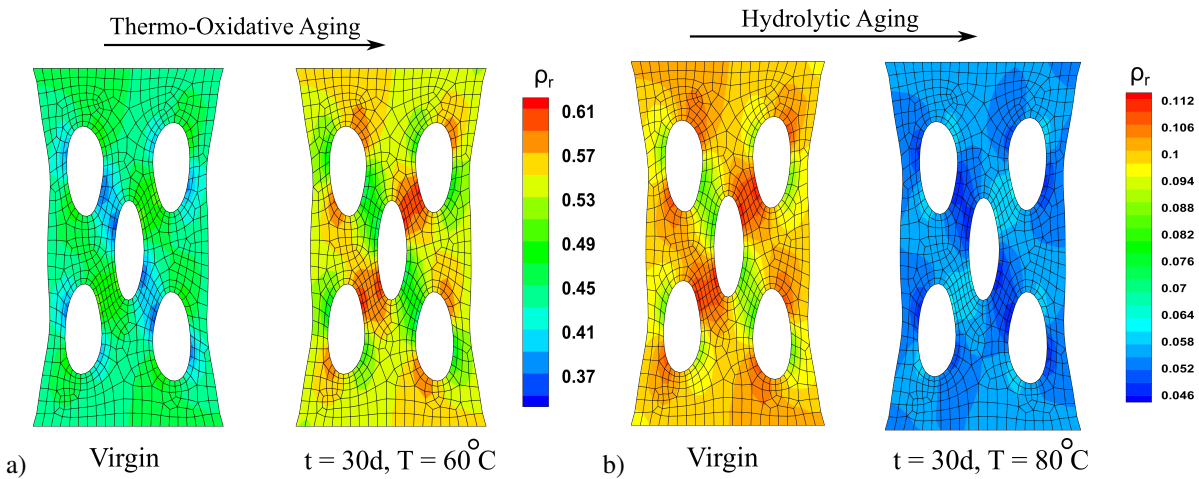


Figure 4.10: Evolution of the chain density ρ_r of (a) SBR during thermo-oxidative and (b) silicon adhesive during hydrolytic aging. Based on stress evolution, we expected that chain density increase during thermo-oxidation due to cross-linking phenomenon and the opposite for hydrolysis which both can be seen here.

dimensional network alteration theory was adapted to understand and predict the inelastic behavior of elastomers during hydrolytic and thermo-oxidative aging. Despite significant efforts in modeling the aging and its influence on the mechanical performance of cross-linked matrix materials, there have been very few models that can reliably predict the aging with reasonable computational efforts. Assuming the alteration of the chain density along the aging trajectory is identical to the peroxide cross-link density for thermo-oxidation, and the change of the average molecular weight for hydrolysis, the strain energy of polymer matrix can be modified to predict chemical aging. The proposed model includes only six physically inspired material parameters. Thus, while it is computationally efficient, it shows good agreement with the experimental data. The proposed model breaks the polymer matrix corresponding to four external load scenarios of (i) deformation, (ii) deformation history, (iii) storage time, and (iv) aging temperature. In this respect, in the course of deformation-induced damage, the continuous loading can detach chains from either cross-linked or aggregate surfaces and reform the composition of the polymer matrix with longer chains. However, during the immersion of polymer matrix in the water and the absence of the induced deformation, the aging can reduce the polymer active agents, which are involved in the rubber elasticity. In contrast, in thermal degradation, the aging mechanism is vice versa and increases polymer chains' density. The excellent performance of the proposed method was proven by validating against a new set of own experimental data, particularly designed to reveal the evolution of constitutive behavior during hydrolytic and thermo-oxidative aging. Moreover, the proposed model implemented for FE simulation and the tangent moduli for large deformation regimes is formulated in terms of internal variables. The model also suffers from some limitations such as inability to predict inhomogeneous aging, which could be addressed in the near future. Here, our formulation neglects the rate dependency so-called visco-elastic behavior of the polymer matrix, while the primary focus of this work is on the quasi-static behavior. With respect to its computational efficiency, simplicity, accuracy, and interpret-ability, the model is the right choice for advanced implementations in FE programs.

CHAPTER 5

A Multi Physics Approach on Modeling of Hygrothermal Aging and its Effects on Constitutive Behavior of Cross linked Polymers

5.1 Introduction

Due to the unique features such as high stretchability, chemical toleration, wear resistance, anti-slipping, and durability; industrial applications of the cross-linked polymers have been growing through past decades [93]. Their practical function can cover a broad range of applications from insensitive to sensitive industries such as automotive, medical, mining, petroleum, and energy storage [145, 146]. In most such cases, the polymeric components are simultaneously exposed to mechanical loads as well as environmental elements like humidity and oxygen. This affair can considerably reduce the nominal service life of the polymers and cause irreversible damage to their functionality [96, 147, 148]. In the literature, this phenomenon is generally regarded as the *aging* mechanism, which is classified into different subcategories based on the chemical source of aging.

Thermo-oxidation [101, 102, 103, 149], hydrolysis [99, 58], hygrothermal [97, 98] and photo-oxidation [104, 105, 106] are some of the main types of aging in which oxygen, water, and UV play major roles in polymer degradation, respectively (see Fig. 5.1). Such classes can be either the result of individual aging elements or due to combined synergized effects of the above-mentioned environmental factors [5]. For instance, hygrothermal aging is one of the combined mechanisms in which oxygen and water molecules both are the leading actors in polymer deterioration. Generally, since these factors coexist in nature, natural aging is seen as a combined effect of all conditions together. Lately, solo environmental damage models have been of significant interest in the literary and research communities. However, there are still wide gaps in the modeling of coupled-aging phenomena since finding the mutual effect and correlation of each environmental element is chal-

lenging and needs a huge set of experimental observations. Accordingly, realizing the correlation of the mechanical and coupled-environmental elements (damage accumulation) is crucial for providing a realistic prediction of such materials' behaviour. *There currently exists no constitutive model of polymeric materials that can simultaneously consider two damage mechanisms.* Therefore, in this paper, we mainly focus on providing a multi-Physic model to predict the constitutive response of cross-linked polymers along with hygrothermal aging, which is a coupled concurrent effect of thermo-oxidative and hydrolysis aging.

So far, we have studied the individual effect of hydrolytic [9, 132] and thermo-oxidative aging [11] and the contribution of their decay functions on the constitutive behavior of cross-linked polymers in our recent works. Following the fundamental formulations presented in those studies, our goal here is to provide a newly physically-based model to predict the constitutive behavior of cross-linked polymers exposed to hygrothermal aging which is assumed as the combination of thermal and hydrolytic aging. Due to the synergistic effects of combined hydrolytic, thermo-oxidative, and hygrothermal aging, the devised model should be able to capture the constitutive behavior of polymers in all three mentioned aging scenarios simultaneously.

Moreover, our model also should be able to predict the inelastic properties of cross-linked polymers as well, in particular, the idealized Mullins effect (stress softening after the first loading cycle) and permanent set (time-independent residual strain) which are necessary to be considered for reliable prediction of material response. Many of these inelastic features have been modeled so far in the context of micro-mechanical and phenomenological approaches [150? , 151]. While micro-mechanical approaches are based on the physically inspired models developed from statistical mechanics of polymer structure and physics of polymer chain network [152, 153, 154, 155], the phenomenological ones use a mathematical model, usually without physical meaning [156]. Subsequently, a growing interest in micro-mechanical models is developing recently. For instance, Guo and Zaïri [157] developed a micro-mechanical model to predict failure in elastomers while Ben Hassine et al. combined the fracture mechanics and the intrinsic defect concept to establish a failure criterion accounting for elastomers during thermal aging [158]. Accordingly, we chose

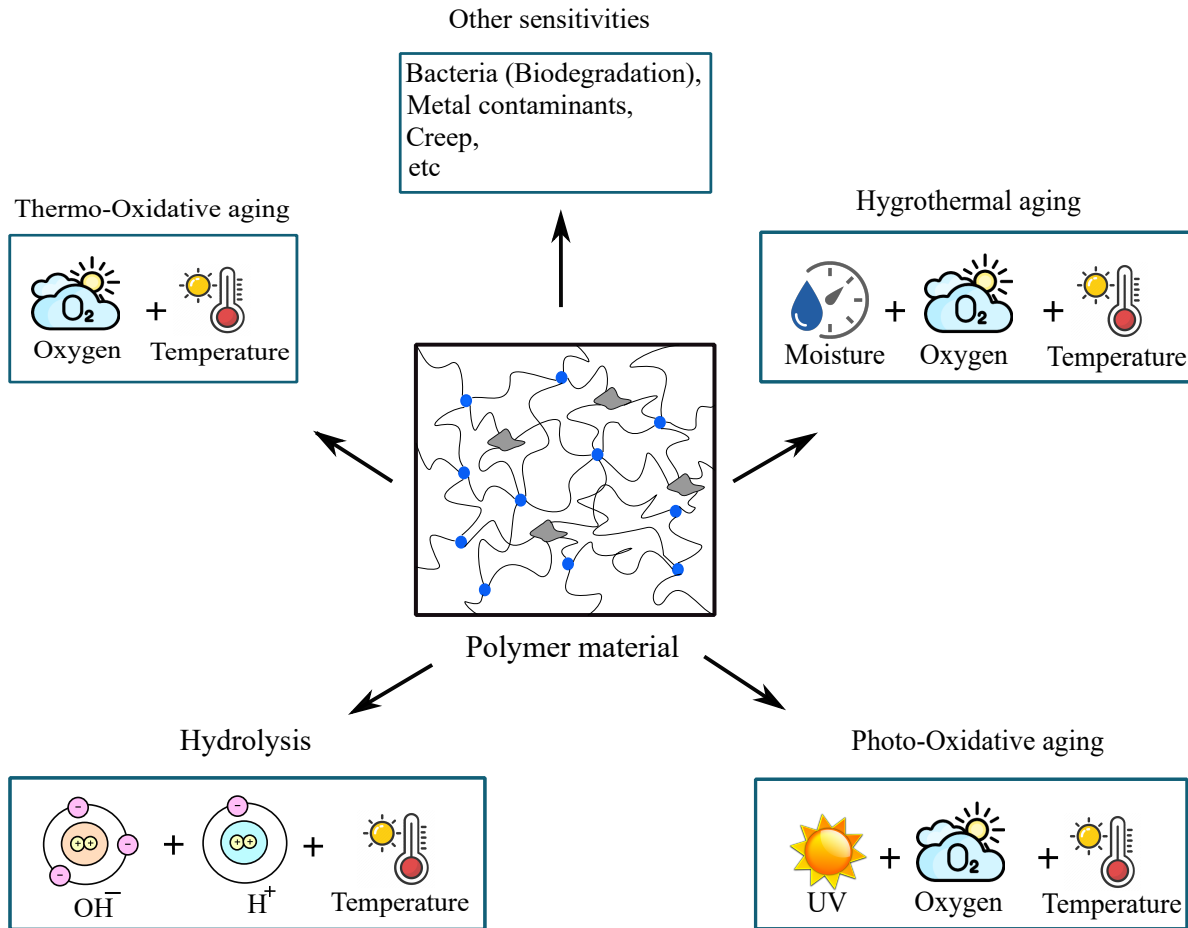


Figure 5.1: Different categories of aging.

micro-mechanical approaches for this study.

Aging is a complex continuous phenomenon that involves several chemo-mechanical aspects of the material [?]. While testing in the real-time aging trajectory can be expensive and challenging, the experimental investigation of this phenomenon is among key interests of the mechanical engineering community. Therefore, several experimental studies were conducted to investigate the behavior of the polymeric components along with the solo chemical aging mechanisms [159, 160, 161]. In this respect, some of them used the concept of accelerated aging to keep the practical relevance of experiments alive besides reducing the experimental costs [162]. Within this concept, the elevated temperature has been utilized to reduce the actual aging time and to perform the test at a reasonable cost. Accordingly, Celina's [107, 108] literature review on this concept shed light on its various related aspects. Although this approach significantly cuts down the test

expenses, it is not always the best scenario for the investigation of aging phenomena [109, 110]. In fact, it can impose some additional chemical anomalies, such as diffusion-limited oxygen (DLO) on the material. DLO, generally, causes heterogeneous aging and occurs when the rate of input oxygen is lower than oxygen consumption in the polymer matrix [163]. These potential problems are widely investigated by several researchers [111, 112]. The accelerated aging method can also be conducted using various mediums such as air, distilled water, and salinated water [164]. Accordingly, Rabanizada et al. [114] investigated the effects of different aging media on the natural rubber (NR). They performed DMA tests to investigate the change in the viscoelastic behavior of NR due to aging. Moreover, thermo-oxidative aging has effects on viscoelastic relaxation and thermal expansion of elastomers, which is shown by Shaw et al. [113]. Similarly, Pazur et al. [115] studied the bulk properties of rubber during thermal degradation.

In comparison to thermal degradation, the experimental efforts for hydrolytic aging are not as abounding. However, there are still some extensive studies that exclusively investigate the effects of water aging on the elastomers. In this respect, Slater et al. [56] conducted experimental research to find the effects of different conditions (i.e. thermal, mechanical, and humidity) on the mechanical performance of thermoplastic polyurethanes. They observed that the presence of water causes plasticizing of the polymer matrix and results in a greater amount of compression set. Ensuing similar trend, Farrar and Gillson [57] performed a series of experiments on polyglyconate-B to find the relation between polymer morphology and degradation rate. Later on, Vieira et al. [116] showed that during hydrolysis, the alteration of molecular weight average has a similar trend with the change of tensile strength.

From the modeling side, so far, aside from our recent models [9, 11, 12], both phenomenological and micro-mechanical models are presented to describe the constitutive behavior of the polymer matrix for solo chemical aging. In the case of thermo-oxidative aging, Ha-Anh and Vu-Khanh [120] established a phenomenological model based on the Arrhenius function to predict the behavior of polychloroprene rubber during thermo-oxidative aging. Moreover, Johlitz et al. [24] presented a physically-based model to simulate the mechanical response of automobile bear-

ings during thermo-oxidative aging. In addition, Dippel et al. [123] introduced a material model that describes material aging as a function of position from the surface to the center of the joints. Recently, Konica and Sain [124] established a chemo-physical model that can predict the heterogeneous oxidation profile in the polymeric material due to high temperature. However, only a few studies were conducted on the modeling of hydrolytic aging. In this regard, Vieira et al.[53] adapted the Bergström and Boyce model in a way that it can predict the mechanical response of biodegradable polymers during the aging trajectory. Later on, they presented a four-dimensional computation approach to modeling biodegradable fibrous material during hydrolysis [26]. Besides, the aging phenomenon can also be modeled using molecular dynamics simulations, although it requires higher computational costs, implementation of either coarse-graining schemes [127?] or multi-scaling approaches [144] could accelerate these simulations.

The main objective of this work is to provide a physically-inspired constitutive model to predict the inelastic response of cross-linked polymers during hygrothermal aging. The proposed model is developed based on the concepts of network evolution [85] and network decomposition [17]. The devised model takes into account the damage accumulation of coupled-aging phenomena by using a generic description of two competing solo-aging phenomena, namely thermo-oxidative, and hydrolytic aging. The model is based on the assumption that each of the aging phenomena works independently, and as a result, they can superpose each other. The model includes relatively fewer material parameters and is validated with respect to new sets of our experimental data. The paper is outlined as follows. The experimental study is first discussed in section 5.2. Then, the devised constitutive model is presented in section 5.3, while the sensitivity analysis of model parameters is discussed in section 5.4. Next, the parameter identification and model verification are presented in section 6.4 and finally, the conclusion is provided in section 5.6.

5.2 Experimental Characterization

5.2.1 Material

In order to investigate the behavior of cross-linked polymers during hygrothermal aging and demonstrate the generality of the devised model, the behavior of two different elastomers was experimentally investigated. The neoprene rubber and Ethylene Propylene Diene Monomer (EPDM) rubber in this study were procured as rectangular sheets of nearly 0.0625" thickness from one supplier. From the same batch, each sample was cut with a punch die in the form of the standardized dumb-bell shape (Die C from the ASTM-D412). These two rubbers were selected due to the fact that their constitutive response was affected by hygrothermal aging. In fact, the material was chosen in a way that all involving environmental factors (i.e. oxygen, temperature, and humidity) were able to degrade them at the same time.

5.2.2 Hydrolytic aging

To simulate the hydrolytic aging condition, samples were fully immersed in sealed containers filled with distilled water (pH = 7) under constant pressure. Grit guards were placed under the specimens to ensure that maximum surface area of samples was exposed to water (see Fig. 5.2a). Elevated temperatures of 80° C, and 95° C were utilized to simulate accelerated aging conditions. After certain amounts of storage times (i.e. 10, 20, and 30 days), samples were removed from the containers and dried at room condition (i.e. $22 \pm 2^{\circ}\text{C}$, $50 \pm 3\% \text{ RH}$).

5.2.3 Hygrothermal aging

To achieve hygrothermal aging, saturated saltwater solutions were utilized to maintain particular values of relative humidities inside sealed containers (see Fig. 5.2b). Salt solutions were replaced on a weekly basis to avoid drying-up and to maintain constant relative humidity conditions inside the containers. Two different humidities of 0%, and 80%, two temperatures 80°C, and 95°C and

three aging duration 10, 20, and 30 days were adopted for this aging experiment. In fact, the temperature setting for this experiment is kept in the range of 80°C and 95°C because further increase in the temperatures would make the materials susceptible to diffusion-limited oxidation (DLO) while lower temperatures would significantly slow down the kinetics of accelerated aging of materials under study [165, 166]. Potassium chloride KCl is utilized as a chemically pure salt to obtain the relative humidity of 80%. Whereas, for 0% RH (i.e. thermo-oxidative aging), molecular sieves were used in containers.

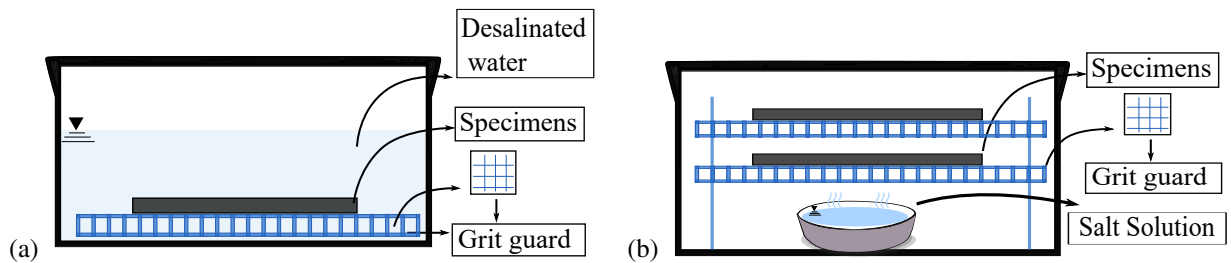


Figure 5.2: Schematic sketches of the storage conditions of specimens in a) hydrolytic, and b) hygrothermal aging.

5.2.4 Mechanical test

Mechanical tests were performed by a uni-axial universal testing machine (TestResources 311 Series Frame). Tests were done in a displacement control manner with a very slow strain rate (i.e. $43.37 \frac{\%}{min}$) to assure the quasi-static condition. The distance between the extensometer grips was set to 25.4mm and all the experiments were performed at room condition (i.e. $22 \pm 2^\circ\text{C}$, $50 \pm 3\%$ RH). Each test has been repeated with 3 samples for reliability control. The error bar is added to the experimental curves to show the variation of tests. Accordingly, sample reliability was also not increased since the variation of mechanical tests is less than 5% (see Fig 5.3). In monotonic cyclic test, the samples were stretched to preset amplitudes of 1.25, 1.5, 1.75, and 2. At each stretch amplitude, four cycles were applied. While in the failure tests, the samples were subjected to an increasing monotonic tension load until they break (see Figs. 5.3 and 5.4). In the course of deformation, elongation of the central zone of 25.4mm has been measured by an external

extensometer. The cyclic experiment is designed to illustrate the evolution of the permanent set and stress softening during the primary loading for both virgin and aged samples.

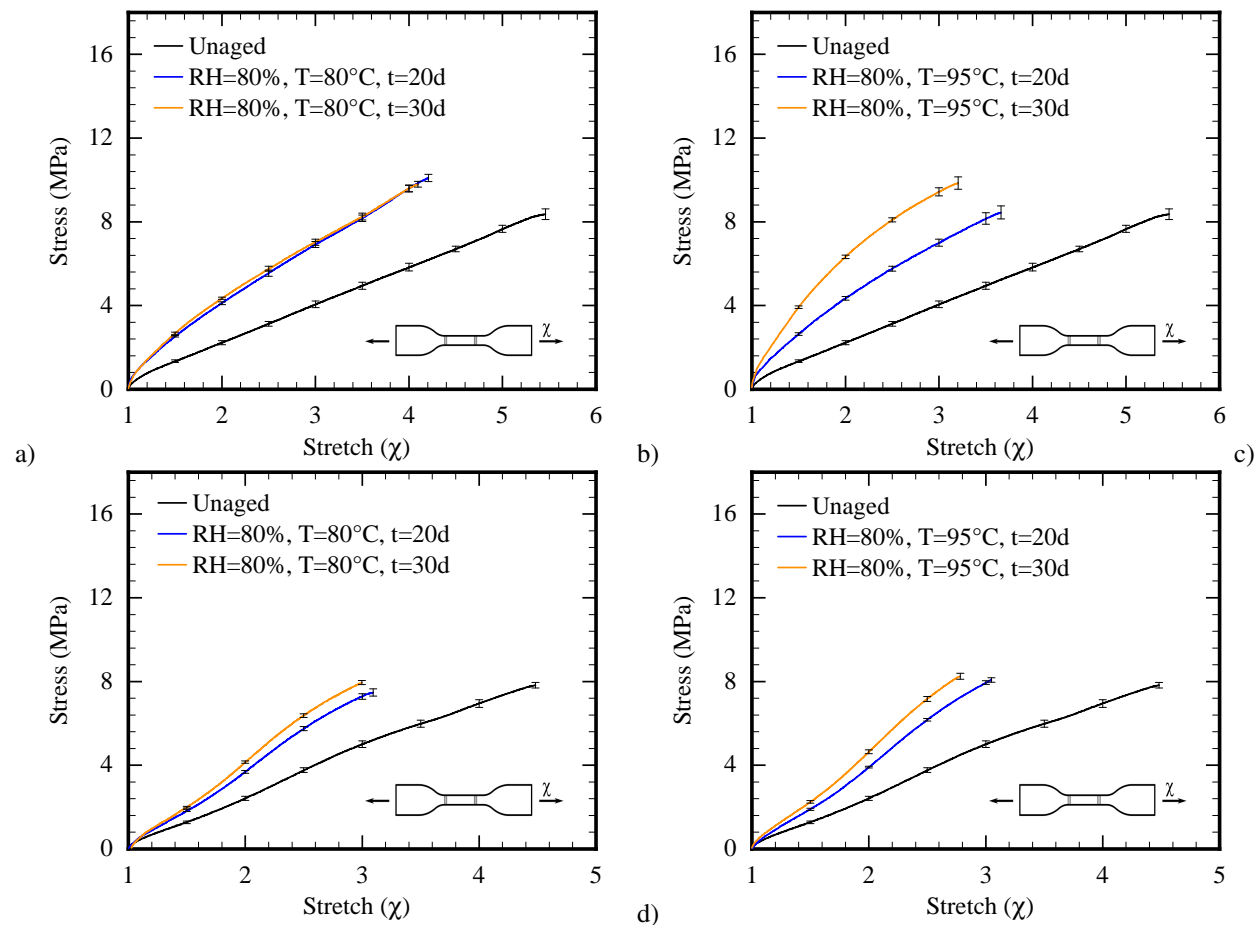


Figure 5.3: The constitutive response of rubber specimens aged at multiple conditions; (a) Neoprene at T= 80°C, RH= 80%, (b) Neoprene at T= 95°C, (c) EPDM at T= 80°C, RH= 80%, and (d) EPDM at T= 95°C, RH= 80%.

5.2.5 Water uptake

To measure water-uptake (see Fig. 5.5), unaged specimens were weighed on an electronic balance (0.01mg accuracy) before being exposed to aging conditions. Specimens were then placed in designated humidity and temperature conditions for planned aging time spans. After aging, the specimens were carefully dried with a tissue paper and weights were recorded once again. The water content W_c in the sample was measured as the % weight increase in the sample at completion

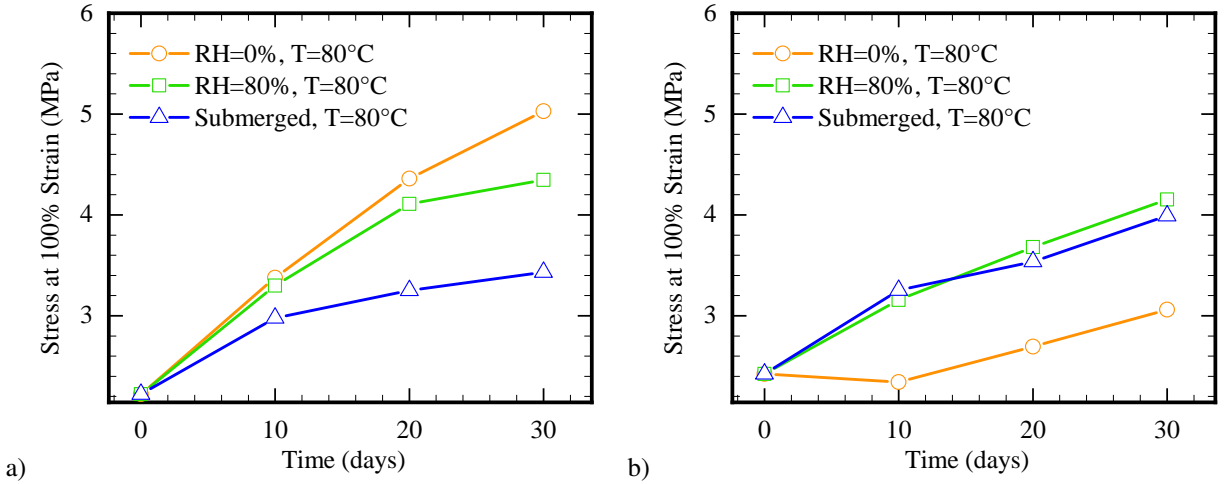


Figure 5.4: Comparison of tensile stress at 100% strain influenced by hygrothermal aging versus hydrolytic and thermo-oxidative aging at temperatures of 80°C a) Neoprene, and b) EPDM.

of aging. The water uptake percent was calculated as

$$W_c(\%) = \left[\frac{W_t - W_0}{W_0} \right] \times 100, \quad (5.1)$$

where W_t is the weight of aged sample at time t and W_0 is the weight of unaged sample.

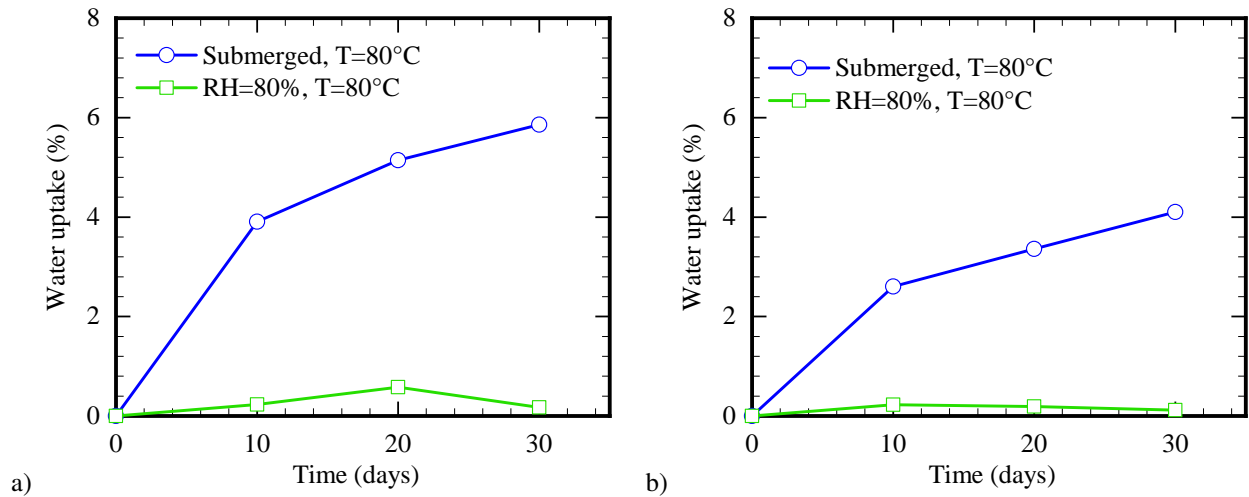


Figure 5.5: Comparison of water uptake specimens aged in submerged condition and in relative humidity of 80%; (a) Neoprene, (b) EPDM.

5.2.6 Cross-link density

The cross-link density analysis for Neoprene and EPDM rubber was done using equilibrium swelling method [167]. Both unaged and aged specimens were immersed in toluene (molar volume $106.3 \frac{mL}{mol}$) and the specimen weight changes were recorded till a constant weight signifying maximum solvent absorbance was reached. The cross-link density and average molecular weights between the chains can be calculated [168] as

$$\frac{n_e}{V_0} = \frac{\rho}{M_x} \left(1 - \frac{2M_x}{M}\right), \quad (5.2)$$

where n_e is the molar cross-linking, V_0 is the specimen volume before swelling, ρ is the density of the solvent, M_x is solvent molar mass and M is the molar volume of the polymer sample.

It is observed that cross-linking agents in Neoprene rubber are relatively more active and susceptible to temperature changes as compared to EPDM (see Fig. 5.6). Especially, this phenomenon is highlighted in environments favorable for oxidation reactions such as thermo-oxidative and hygrothermal (80%RH) aging conditions. But regardless of any behavioral variations in both materials, they responded to the aging environment in a similar fashion.

5.2.7 The competitive aging scenario

The results of cross-link density changes of samples aged in different aging environments (see Fig. 5.6), water uptake (see Fig. 5.5), and mechanical tests (see Fig. 5.4) show that the effects of hygrothermal aging are always between hydrolytic and thermo-oxidative aging. Indeed, thermo-oxidative aging is induced by two competing sub-mechanisms of cross-link formation C_f (see Fig. 5.6), and chain scission S_c which results in the variation of cross-link density CD as $\delta CD^T \propto C_f^T - S_c^T$. Hydrolytic aging is mainly induced by chain scission which results in the reduction of cross-link density $\delta CD^{Hd} \propto -S_c^{Hd}$ and massive deactivation of polymer chains. In thermo-oxidative aging, for most materials cross-link formation is prevalent thus $C_f^T > S_c^T$. Hence, hygrothermal aging has two effects: i) addition of C_f^T , and ii) reduction of S_c^{Hd} due to

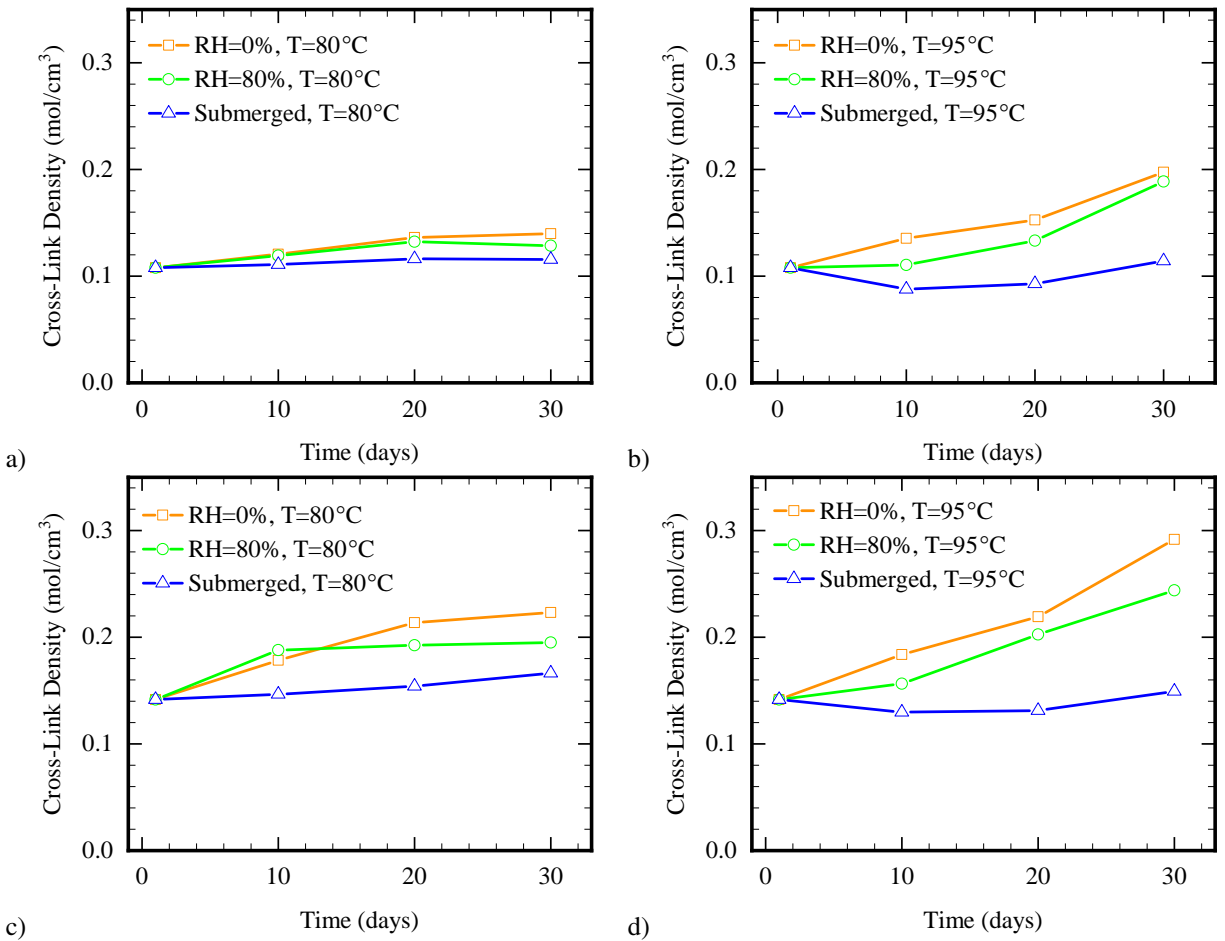


Figure 5.6: The cross-link density of rubber specimens during thermo-oxidation, hydrolytic and hydrothermal environments aged at multiple conditions; (a) EPDM at temperature 80°C, (b) EPDM at temperature 95°C, (c) Neoprene at temperature 80°C, and (d) Neoprene at temperature 95°C.

the reduced water uptake in hygro in comparison to hydro (see Fig. 5.5). Accordingly, one can conclude that hydrothermal aging is induced by competitive aging of two concurrent phenomena namely, hydrolytic and thermo-oxidative aging.

5.3 Constitutive Model

Mechanical loads and environmental conditions play critical role in the damage accumulation within the polymer matrix. Damages induced by environmental loads are often irreversible due to the chemical reaction of the polymer components with environmental factors such as oxygen and moisture. Damages induced by mechanical loads are composed of both permanent and re-

versible damages. Permanent damages are often induced by chemical changes in the network, such as detachment of cross-links, and chain scission, while reversible damages are often induced by changes in matrix topology like chain slippage, detachment of physical bonds, or chain adsorption/detachment from particles surfaces. Hygrothermal aging is a kind of environmental damage that results from two simultaneous sub-aging mechanisms, namely, thermo-oxidative and hydrolytic aging (see Fig.5.7). We consider thermo-oxidative aging to be governed by two competing micro-mechanisms [137]: chain scission and cross-link formation (see Fig. 5.9), while hydrolytic aging is considered as the result of parallel reduction in the active chains and cross-links [58] (see Fig. 5.10). Accordingly, one should separately formulate the effect of each aging mechanism and couple them to develop a combined aging constitutive model.

Hereafter, the following notations are employed: for a scalar X , a vector \mathbf{X} , a second-order tensor \mathbf{X} , and a fourth-order tensor \mathbb{X} . The subscript X_{\bullet} depicts the network which the parameter X is associated with and the bar sign over the parameters $\bar{X} = \frac{\bar{X}}{l}$ refers to their normalized value with respect to the Kuhn length l .

5.3.1 Damage Accumulation

Combining hydrolytic and thermo-oxidative in the form of hygrothermal aging leads to strain energy of the polymer matrix as a function of three parallel damage sub-mechanisms, C_f^T , S_c^T , and S_c^{Hd} . To capture the mutual effects and the correlation of thermo-oxidative and hydrolytic aging, *we assume that each of the aging phenomena works individually, and consequently, they superpose each other due to their independent relation.* Accordingly, for each damage sub-mechanism, a separate degradation rate has been considered, which eventually defines the contribution of each mechanism in the overall damage imposed on the matrix.

To characterize the effects of aging time on the constitute behavior of polymer matrix, we defined two end-states of the material as the state of polymer matrix at initial state Ψ_0 and fully aged state at time infinity Ψ_{∞} . The end-states are considered as extreme points of aging, and accordingly, strain energy of the material in all other states of aging can be calculated through

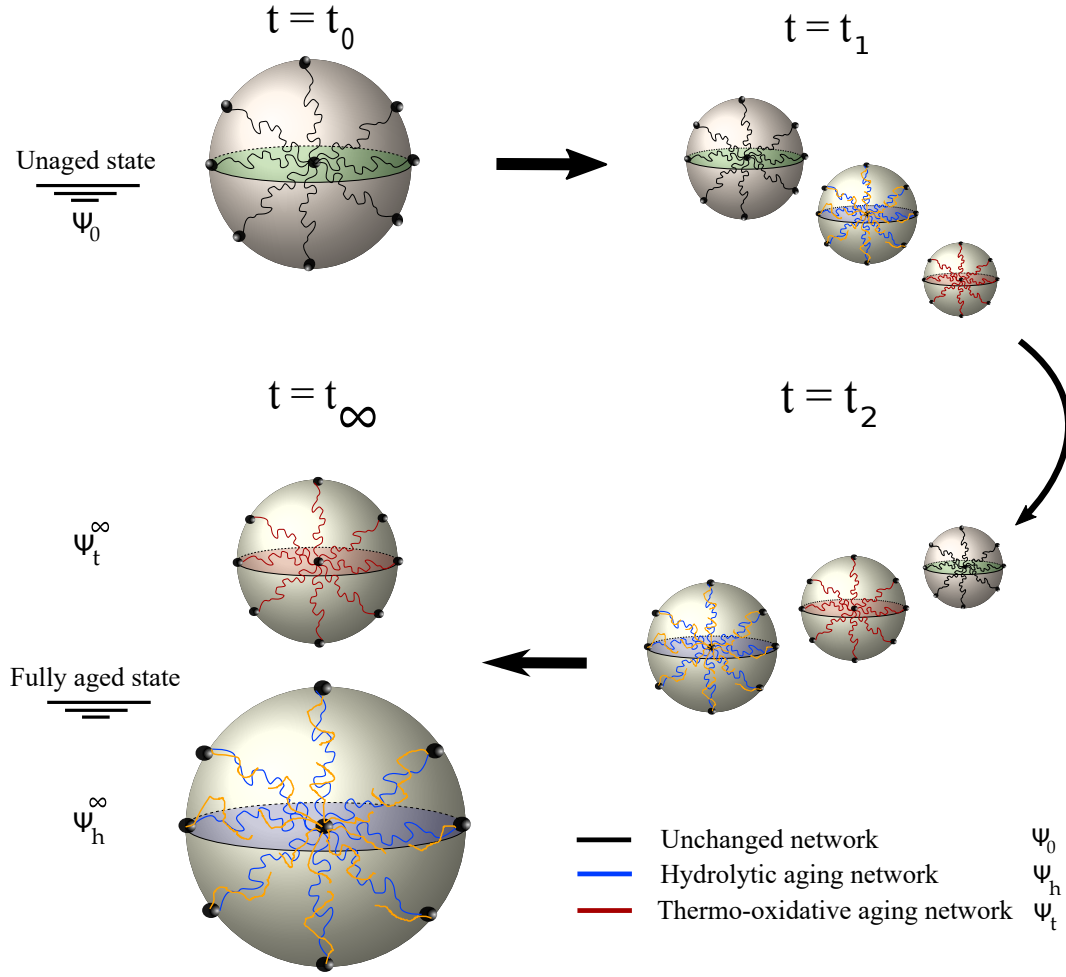


Figure 5.7: Evolution of the sub-aging networks throughout hygrothermal aging. At unaged state (i.e. $t = 0$), there is only unchanged network. As time passes, the oxygen and water molecules attack the polymer matrix and lead to two sub-aging networks namely, thermo-oxidative and hydrolytic networks. The unchanged network continues its shrinkage till it disappeared and got replaced by two new networks with different morphology at the fully aged state (i.e. $t = \infty$).

predefined shape functions, $N(t, T)$ and $N'(t, T)$, as

$$\Psi_M(t, T, RH, \mathbf{F}) = N(t, T)\Psi_0 + N'(t, T)\Psi_\infty; \quad N'(t, T) = 1 - N(t, T), \quad (5.3)$$

where $N(t, T)$ is the shape function that represents the contribution of each initial state in the current state. In most solo aging of the polymeric systems, the evolution of the shape function can

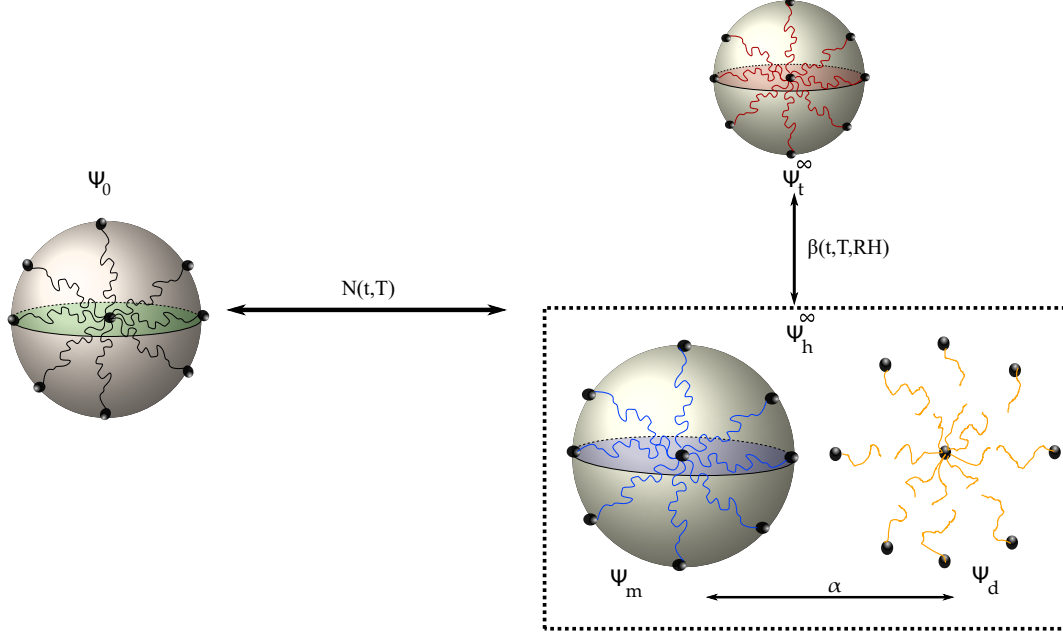


Figure 5.8: Decomposition of the hydrothermal aging into two aging networks namely, thermo-oxidative and hydrolytic networks. The hydrolytic network, itself, decomposes to the two morphed and deactivated networks.

be well captured by the Arrhenius decay function [73] as

$$N(t, T) = \exp \left(-\gamma \exp \left(-\frac{E_a}{\mathcal{R}T} \right) t \right). \quad (5.4)$$

Here, γ is the underlying degradation rate, E_a the activation energy, and $\mathcal{R} = 8.314[J]/[mol][K]$ the universal gas constant. The main challenge is to define the status of the polymer matrix at the fully aged state Ψ_∞ . Here, based on the theory of network decomposition, we assume that fully aged polymer matrix decomposes into two different networks (see Fig. 5.7); one of them resulted from the diffusion of oxygen to the polymer matrix Ψ_t^∞ , and the second one modeled the effect of water on the polymer matrix Ψ_h^∞ . Hence, the infinity state of the polymer matrix can be written as

$$\Psi_\infty = (1 - \beta)\Psi_t^\infty + \beta\Psi_h^\infty, \quad (0 \leq \beta \leq 1), \quad (5.5)$$

where $\beta(t, T, RH)$ defines the portion of each network, which contributes to the complete aging of polymer matrix for a certain amount of aging temperature and humidity (see Fig. 5.8). The

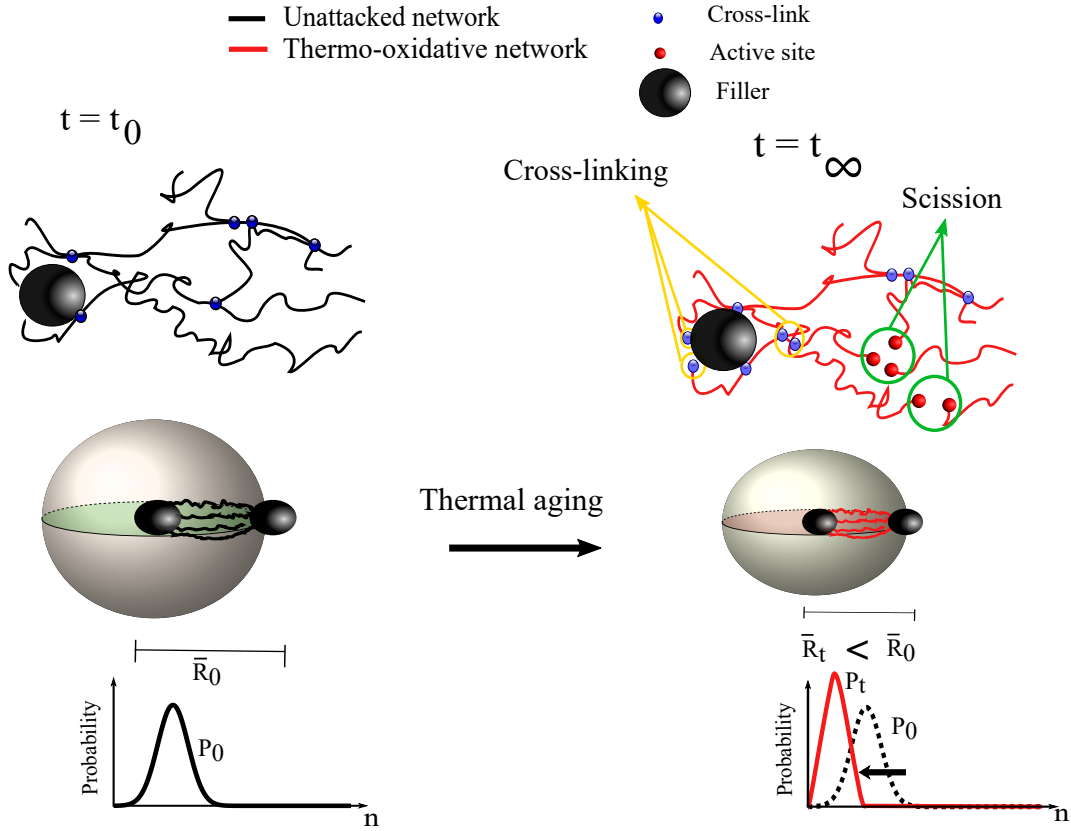


Figure 5.9: A schematic diagram of thermo-oxidative aging. Thermal aging results from two simultaneous phenomena; cross-linking, and chain scission and it can be best modeled via a new network with shorter chains [12].

hydrolysis network Ψ_h^∞ , itself, decomposes into two independent sub-networks namely morphed Ψ_m^∞ and deactivated networks Ψ_d^∞ (see [9] for details) and can be written as

$$\Psi_h^\infty = \alpha \Psi_m^\infty + (1 - \alpha) \Psi_d^\infty, \quad (0 \leq \alpha \leq 1), \quad (5.6)$$

where the parameter α depicts the contribution of each sub-microstructural phenomenon and is considered as a fitting parameter. The next step is to find the portion of each aging mechanism (i.e. the parameter β), which is involved in the construction of the polymer elasticity. In this respect, experimental studies reveal that the more water in the polymer matrix, the lower T_g it has and, as a result, the more plasticizing damage [169]. Hence, the parameter β should be a function of water absorption. Here, *the main assumption of the model is that the contribution of the water network*

in the total entropy of polymer matrix is linearly related to the amount of water in the matrix. Based on this assumption, the decay function can be assumed similar to the water uptake function. It is clear that the rate of damage in the polymer matrix is different from the rate of water uptake in the samples since the water first penetrates into the samples, then it starts imparting attrition to the polymer matrix. Within this concept, experimental observations confirm that [170] the water uptake is a nonlinear function of time t , temperature T , and humidity RH and could be best modeled via Arrhenius function [169]. Hence one can define the function $\beta(t, T, RH)$ as

$$\beta(t, T, RH) = \operatorname{erf}\left(\frac{RH}{Q}\right) \sqrt{\theta \exp\left[-\frac{E_b}{RT}\right] t}, \quad (5.7)$$

where the parameter E_b is the activation energy which is attributed to the water diffusion, and parameters Q and θ are adjusting parameters that keep the range of $\beta(t, T, RH)$ between 0, and 1 (i.e. $0 \leq \beta \leq 1$). The lower bound of the β (i.e. $\beta = 0$) indicates that there is no humidity effect on mechanical response and only thermal degradation Ψ_b causes the matrix deterioration. In contrast, the upper bound (i.e. $\beta = 1$) shows that the hydrolytic aging wins the competition between the two sub-aging phenomena, and the effects of oxygen are negligible regarding polymer degradation.

5.3.2 3D to 1D transition

Based on the experimental observation, it is assumed that the micro-structure of the polymer network is embodied by the isotropic spatial distribution of polymer chains, which are scattered in all directions (see Fig. 6.6a). Accordingly, the macroscopic energy of polymer network Ψ_M can be carried out by integrating overall available configurations at micro-scale [171, 172]. This process can be done by numerical integration scheme by utilizing the concept of the unit micro-sphere (see Fig. 6.6b, and see [85] for details). Hence, the isochoric strain energy of the polymer network can

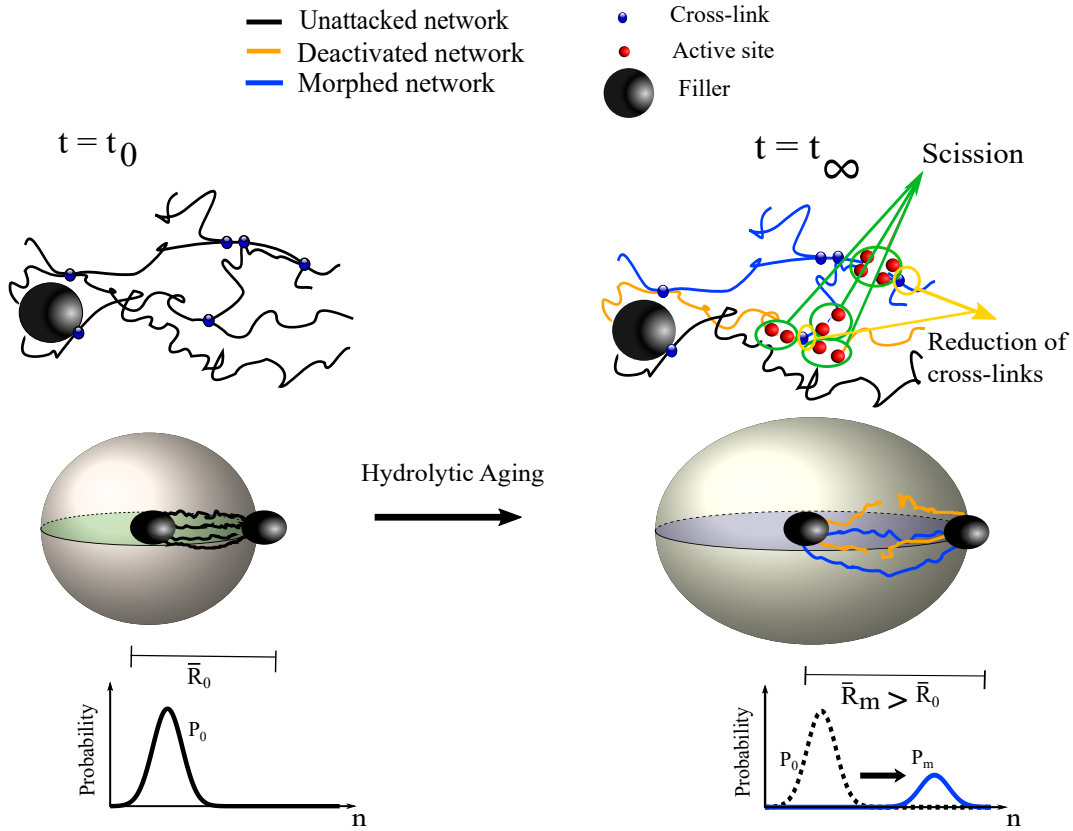


Figure 5.10: A schematic diagram of hydrolytic aging. Hydrolytic aging is due to the reduction of cross-links and chain scission and it can be modeled with a new network with longer chains [9].

be written as

$$\Psi_M = \frac{1}{A_s} \int_S \psi_M^d d\mathcal{A} \cong \sum_{i=1}^k \psi_M^{d_i} w_i \Rightarrow$$

$$\psi_M^d = N(t, T) \psi_0^d + (1 - \beta(t, T, RH)) N'(t, T) \psi_t^d + \alpha \beta(t, T, RH) N'(t, T) \psi_m^d, \quad (5.8)$$

where the parameter A_s is the surface area of unit sphere, \mathcal{A}^d the unit area normal to the direction \mathbf{d} , w_i Gaussian weight coefficients according to the direction \mathbf{d}_i ($i = 1, 2, \dots, 45$), and ψ_\bullet represents the total energy of each network in direction \mathbf{d} .

Chain length distribution function Each network is made by many sub-networks, each having the same set of chains with a different relative length (number of segments n) in an arbitrary direction \mathbf{d} . The polymer chains in each network are bonded to cross-link only at their first and

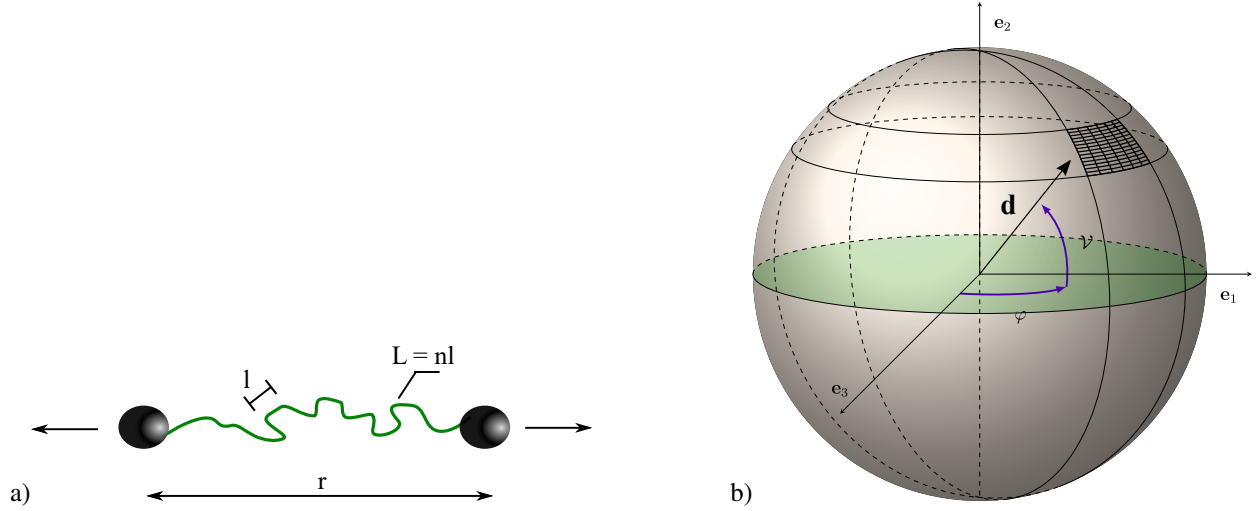


Figure 5.11: Schematic figures of a) a freely rotating chain consisting of n monomers with Kuhn length of l , and b) the unit micro-sphere representation with the unit basis vectors of e_1 , e_2 , and e_3 and normal direction $\mathbf{d} = d_1 e_1 + d_2 e_2 + d_3 e_3$.

last segments, giving specific end-to-end distances of \bar{R}_\bullet . Here, the chains' distribution function at a given distance \bar{R}_\bullet is considered as normal distribution and can be written as

$$P_\bullet(n) = \frac{1}{2\sqrt{\pi\sigma^2}} \exp\left(\frac{(n - \mu_\bullet)^2}{-2\sigma^2}\right), \quad (5.9)$$

where, σ is the standard deviation, and μ_\bullet the mean value. In order to summarize our framework, the damage accumulation is modeled according to the following functions:

- $N(t, T)$ is a temporal shape function that is mainly influenced by t .
- $\beta(t, T, RH)$ is a nonlinear function of the RH , t , and T .
- α is a compound based function and that is why it is constant for each material.
- Ψ_0 is the strain energy of the polymer matrix in the virgin state.
- Ψ_t^∞ is the strain energy of the thermo-oxidative network in the infinity state. This network is constructed with higher cross-link density and shorter chain (see [12] for details) which can be best modeled by changing the mean value of chain length distribution and end-to-end distance of chain (i.e. $\bar{R}_t < \bar{R}_o$, and $\mu_t < \mu_o$).

- Ψ_m^∞ represent the strain energy of the morphed network (see [9] for details) which consists of longer chains with respect to the virgin network (i.e. $\bar{R}_m > \bar{R}_o$, and $\mu_m > \mu_o$).

Energy of a single chain The strain energy density of a freely jointed chain (FJC) were obtained by utilizing an enhanced version of non-Gaussian statistics (see [142] for details) and can be written as

$$\hat{\psi}_c(n, \bar{r}_\bullet) = nK_bT \int_0^\Omega \hat{\beta} d\Omega, \quad \hat{\beta} = \left[1 - \frac{1 + \Omega^2}{n} \right] \beta, \quad (5.10)$$

where $\Omega = \frac{r_\bullet}{L} = \frac{\bar{r}_\bullet}{n}$ is the stretchability ratio ($\frac{\bar{r}_\bullet}{n}$) of a single polymer chain, while \bar{r}_\bullet is end-to-end distance in the deformed configuration. The parameter $\beta = \mathcal{L}^{-1}(\Omega)$ denotes the inverse Langevin function (ILF), which can not be explicitly derived and should be implicitly determined. There are several accurate rational functions that are developed in the literature [173] in which choosing the suitable approximation function generally depends on the maximum stretchability of the polymer chain. Here, a simple yet accurate (maximum error less than 1%) first-order rational function is being utilized as ILF [84], and can be written as

$$\mathcal{L}^{-1}(x) \cong \frac{x}{1-x} + 2x - \frac{8}{9}x^2. \quad (5.11)$$

Polymer chain detachment In all networks, permanent damage results from the debonding of shorter chains from cross-links or aggregates' surface during the primary loading. Detachment or sliding occurs if the chain force f_p goes beyond the finite breakage force of a polymer chain denoted by f_c . Obviously, this force approaches infinity $f_p \rightarrow \infty$ as the end to end distance of the chain \bar{r}_\bullet becomes close to its contour length $\bar{r}_\bullet \rightarrow n$. This detachment starts with the shortest chain and gradually affects the longer chains. Considering the parameter ν as the sliding ratio of a polymer chain (see [85] for details), the length of the shortest available chain in a deformed network is

$$n_{\bullet min} = \nu \lambda_{max}^d \bar{R}_\bullet, \quad (5.12)$$

while λ_{max}^d is the maximal micro-stretch previously reached in the loading history in an arbitrary direction d . On the other hand, the length of longest available chain in each network $n_{\bullet,max}$ is considered as a cut-off length of probability distribution function of polymer chains $P_{\bullet}(n)$. Accordingly, the set of available relative chain lengths in the direction d of networks are given by

$$D_{\bullet}\left(\lambda_{max}^d\right) = \left\{ n \mid n_{\bullet,min}\left(\lambda_{max}^d\right) \leq n \leq n_{\bullet,max} \right\}, \quad \text{where} \quad n_{\bullet,max} = \mu_{\bullet} + 5\sigma. \quad (5.13)$$

5.3.3 Network rearrangement

The network rearrangement is categorized into two independent groups namely mechanical-induced and environmental-induced rearrangement.

Mechanical-induced rearrangement . The main assumption here is that the detachment does not lead to the complete energy dissipation of the chains since the chains will still serve as part of a larger macro-molecule. As such, the detachment will lead to partial dissipation of the energy only, and part of it will remain as kinetic energy in the new, longer chains that are formed during this rearrangement process (see [85] for details). All in all, the number of active segments remain constant during deformation and given by the following expression

$$\int_{D_{\bullet}(1)} \mathcal{N}_{0_{\bullet}} \mathcal{P}_{\bullet}(n) ndn = \int_{D_{\bullet}(\lambda_{max})} \tilde{\mathcal{N}}_{0_{\bullet}}(\lambda_{max}) \mathcal{P}_{\bullet}(n) ndn. \quad (5.14)$$

The debonding process is irreversible; no new bonds will appear because of loading and unloading the specimen. For this reason, the number of active chains can be defined as

$$\tilde{\mathcal{N}}_{0_{\bullet}}(\lambda_{max}) = \Phi_{\bullet}(\lambda_{max}) \mathcal{N}_{0_{\bullet}}, \quad \text{where} \quad \Phi_{\bullet}(\lambda_{max}) = \frac{\int_{D_{\bullet}(1)} \mathcal{P}_{\bullet}(n) ndn}{\int_{D_{\bullet}(\lambda_{max})} \mathcal{P}_{\bullet}(n) ndn}. \quad (5.15)$$

Environmental-induced rearrangement As the probability of the chain length changes over time, conservation of active segment numbers should be considered in the number of chains in

each network (see [9, 12] for details). Accordingly, by keeping the number of segments constant at any time between zero and infinity, we have

$$\mathcal{N}_{0\bullet} = \phi_{\bullet}\mathcal{N}_0, \quad \text{where} \quad \phi_{\bullet} = \frac{\int_{D_{\bullet}(1)} \mathcal{P}_0(n) ndn}{\int_{D_{\bullet}(\infty)} \mathcal{P}_{\bullet}(n) ndn}. \quad (5.16)$$

Evolution of sub-network energy Average strain energy of an arbitrary sub-network in direction d , namely ψ^d_{\bullet} can be written with respect to chain's length distribution in that direction. Thus, considering Eqs. 5.10, 5.15, and 5.16, ψ^d_{\bullet} is given by

$$\psi^d_{\bullet} = \mathcal{N}_0 \int_{D_{\bullet}(\lambda_{max}^d)} \phi_{\bullet}\Phi_{\bullet} \left(\lambda_{max}^d \right) \hat{\psi}_c(n, \bar{r}_{\bullet}) \mathcal{P}_{\bullet}(n) dn \quad (5.17)$$

Accordingly, the strain energy for each network can be written as

$$\begin{aligned} \psi^d_0 &= \mathcal{N}_0 \int_{D_0(\lambda_{max}^d)} \Phi_0 \left(\lambda_{max}^d \right) \hat{\psi}_c(n, \bar{r}_0) \mathcal{P}_0(n) dn \\ \psi^d_t &= \mathcal{N}_0 \int_{D_t(\lambda_{max}^d)} \phi_t\Phi_t \left(\lambda_{max}^d \right) \hat{\psi}_c(n, \bar{r}_t) \mathcal{P}_t(n) dn \\ \psi^d_m &= \mathcal{N}_0 \int_{D_m(\lambda_{max}^d)} \phi_m\Phi_m \left(\lambda_{max}^d \right) \hat{\psi}_c(n, \bar{r}_m) \mathcal{P}_m(n) dn. \end{aligned} \quad (5.18)$$

5.3.4 Final formulation

The total strain energy of polymer matrix can be written in terms of deformation gradient \mathbf{F} , storing temperature T , time t , and relative humidity RH by substituting Eqs. 5.4, 5.5, 5.6, 5.7, and 5.18 in Eq. 5.3. Hereafter, \mathbf{F} stands for the deformation gradient while \mathbf{C} represents the right Cauchy–Green tensor. By assuming incompressibility condition (i.e. $J^2 = \det \mathbf{C} = 1$), the first

Piola-Kirchhoff stress tensor T can be obtained as

$$\mathbf{T} = \frac{\partial \Psi_M}{\partial \mathbf{F}} - p \mathbf{F}^{-T} = N(t, T) \frac{\partial \Psi_0}{\partial \mathbf{F}} + N'(t, T) \left[\beta(t, T, RH) \frac{\partial \Psi_t^\infty}{\partial \mathbf{F}} + (1 - \beta(t, T, RH)) \frac{\partial \Psi_h^\infty}{\partial \mathbf{F}} \right] - p \mathbf{F}^{-T}, \quad (5.19)$$

where p is a scalar parameter to guaranty the incompressibility. In view of the Eq. 5.19, the first Piola–Kirchhoff stress tensor \mathbf{T} is a nonlinear tensor valued function of the state variable \mathbf{F} . By utilizing the chain rule, it can be obtained by as

$$\begin{aligned} \frac{\partial \Psi_0}{\partial \mathbf{F}} &= \sum_{j=1}^k w_j \frac{\partial \psi_0}{\partial \lambda} \frac{1}{2} \frac{\partial \mathbf{d}_j \bar{\mathbf{C}} \mathbf{d}_j}{\partial \bar{\mathbf{F}}} : \frac{\partial \bar{\mathbf{F}}}{\partial \mathbf{F}}, \\ \frac{\partial \Psi_h^\infty}{\partial \mathbf{F}} &= \alpha \sum_{j=1}^k w_j \frac{\partial \psi_m}{\partial \lambda} \frac{1}{2} \frac{\partial \mathbf{d}_j \bar{\mathbf{C}} \mathbf{d}_j}{\partial \bar{\mathbf{F}}} : \frac{\partial \bar{\mathbf{F}}}{\partial \mathbf{F}}, \\ \frac{\partial \Psi_t^\infty}{\partial \mathbf{F}} &= \sum_{j=1}^k w_j \frac{\partial \psi_t}{\partial \lambda} \frac{1}{2} \frac{\partial \mathbf{d}_j \bar{\mathbf{C}} \mathbf{d}_j}{\partial \bar{\mathbf{F}}} : \frac{\partial \bar{\mathbf{F}}}{\partial \mathbf{F}}, \end{aligned} \quad (5.20)$$

The detailed derivation of the stress tensor is provided in appendix A.

As a summary, this model should be considered an extension of our recent models [9, 132, 11] which predict the polymer constitutive behavior during dual aging mechanisms. Similar to our recent works, network evolution theory [85] considered as a kernel of our model, which is a tool to predict deformation-induced damages. The term *deformation-induced damage* is used to refer to any types of damages which are induced by the deformation such as strain-induced anisotropy, and idealized Mullins effect. This kernel could be replaced by simpler theories such as Analytical network-averaging [174] to improve the computational efficiency of the model. However, the reason that why we choose a numerical scheme method as the kernel of our model is that it be able to model the inelastic directional-dependent phenomena such as the idealized Mullins effect. In fact, it is a trade-off between the accuracy and simplicity of the model. In order to simplify our model kernel, we assumed the homogeneous distribution of the micro-stretch λ^d within the network. Accordingly, the relationship between the micro-stretch λ^d and macro-stretch χ^d in the

direction d is assumed as $\chi^d = \lambda^d$. Here, the main novelty of our current model lies in the extension in modeling of environmental damages (see Fig. 5.12). Our recent works can only consider one type of single aging mechanism such as hydrolytic or thermo-oxidative aging. In this paper, we offered a new generic model to predict the behavior of cross-linked polymers during hygro-thermal aging which is a dual aging mechanism. Hence, hydrolytic and thermo-oxidative aging considered as subsets of hygro-thermal aging since it is due to the synergized effects of oxygen, water, and temperature. From the mathematical point of view, with one set of material parameters, our generic model is able to cover these two types of single aging mechanisms as well as their nonlinear interaction.

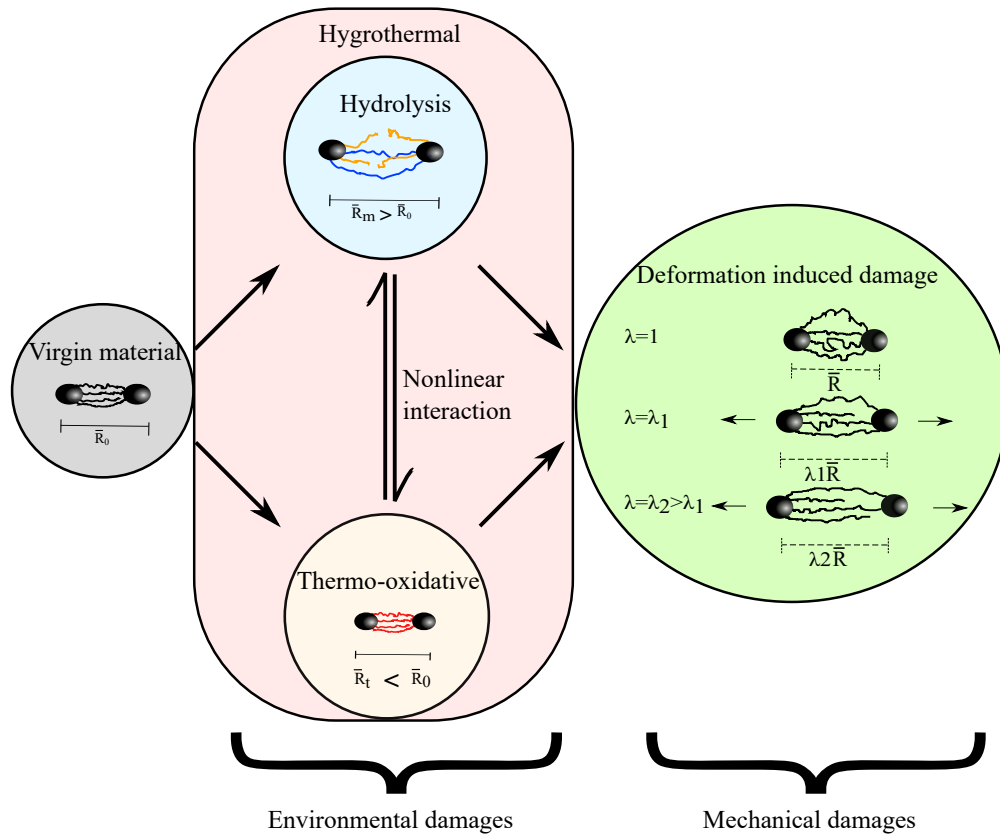


Figure 5.12: Schematic figure of different damage mechanisms' modeling.

Table 5.1: Summary of material parameters.

| Material Parameter | Description |
|--------------------|--|
| \mathcal{N}_0 | The number of chains of virgin network per unit volume |
| \bar{R}_0 | Normalized end-to-end distance of the chains in the unchanged network |
| μ_0 | Mean value of unchanged network chain length distribution |
| σ | Standard deviation of chain length distribution in all networks |
| ν | Sliding ratio denoting the strength of bonds |
| \bar{R}_m | The normalized end-to-end distance of chains in the morphed network which is bigger than the unchanged one ($\bar{R}_m > \bar{R}_o$) |
| μ_m | The mean value of morphed network chain length distribution which is bigger than the unchanged one ($\mu_m > \mu_o$) |
| α | The percentage of active chains in the hydrolytic network after aging |
| \bar{R}_t | The normalized end-to-end distance of chains in the thermo network which is smaller than the unchanged one ($\bar{R}_t < \bar{R}_o$) |
| μ_t | The mean value of thermo network chain length distribution which is smaller than the unchanged one ($\mu_t < \mu_o$) |
| γ | Arrhenius rate factor |
| Q, θ | Adjusting parameters to keep β between zero and one |
| E_a, E_b | Activation energies |

5.4 Parameter sensitivity analysis

The developed model has fifteen material parameters, five of which belong to the unchanged network (\mathcal{N}_0 , \bar{R}_0 , μ_0 , σ , and ν), three to the morphed (\bar{R}_m , μ_m , and α), two to the thermo-oxidative network (\bar{R}_t , and μ_t), and the rest are for the decaying functions (γ , Q , θ , E_a , and E_b). The material parameters for the unchanged, morphed, and thermo-oxidative networks along the aging trajectory are comprehensively studied in our previous work (for detail see [9, 12]). As a summary, each of these material parameters is described in Table 5.1.

In order to better understand the effect of the damage accumulation parameters (Q , θ and E_b) on the inelastic response of the material, a parametric sensitivity analysis is utilized to capture the variation of each of these parameters. The reference sets of material parameters are presented in Table 5.2. To highlight the interaction of the deformation-induced damage and aging degradation, the analysis of the parameters is carried out in two different aging times of 10, and 100 days.

Table 5.2: The model's reference material parameters for parametric analysis.

| $\mathcal{N}_0 k_b T$ | \bar{R}_0 | \bar{R}_m | \bar{R}_T | μ_0 | μ_m | μ_T | σ | ν | α | Q | γ | θ | $\frac{E_a}{\mathcal{R}}$ | $\frac{E_b}{\mathcal{R}}$ |
|-----------------------|-------------|-------------|-------------|---------|---------|---------|----------|-------|----------|-----|----------|----------|---------------------------|---------------------------|
| [MPa] | | | | | | | | | | | [1/day] | [1/day] | [K] | [K] |
| 3 | 5 | 7 | 2 | 10 | 15 | 5 | 4 | 1.01 | 0.1 | 100 | 5.42e+12 | 1e+9 | 1.17e+04 | 0.965e+04 |

In fact, the parameter $\frac{E_a}{\mathcal{R}}$ and γ are calibrated in a way that temporal shape function $N'(t, T)$ is approached to its upper limit at aging time 100 days and temperature 95°C (i.e. $N'(t, T) \xrightarrow[T=95^\circ C]{t=100d} 1$) to represent the infinity state of the material. Accordingly, the effect of material parameters involved in $\beta(t, T, RH)$ function on the inelastic response of the reference sample is investigated and described below.

- Parameter Q , controls the effect of humidity on the response of the material. Indeed, for a certain value of humidity, having the higher value of Q , means the contribution of the hydrolytic network in the infinity state of the material is lower, and as a result thermo network will be dominant (see Fig. 5.13a).
- Parameter θ , the water uptake rate factor, controls the effect of aging time t on the contribution of the hydrolytic network in the infinity state. Here, the aging time is involved in $N(t, T)$, and $B(t, T, RH)$ functions and as a result, it is a very complex variable. Indeed, aging time t can decrease the contribution of the unchanged network as well as increase the role of the hydro network in the response of the material. Hence, a higher value of the θ results in a higher effect of water on the response of the material (see Fig. 5.13b).
- Parameter $\frac{E_b}{\mathcal{R}}$, the water uptake activation energy, control the effect of aging temperature T on the contribution of the hydro network. Similar to the aging time t , aging temperature T is playing role in both temporal and humidity functions. Accordingly, the higher value of $\frac{E_b}{\mathcal{R}}$, the less contribution of water in the response of material (see Fig. 5.13c).

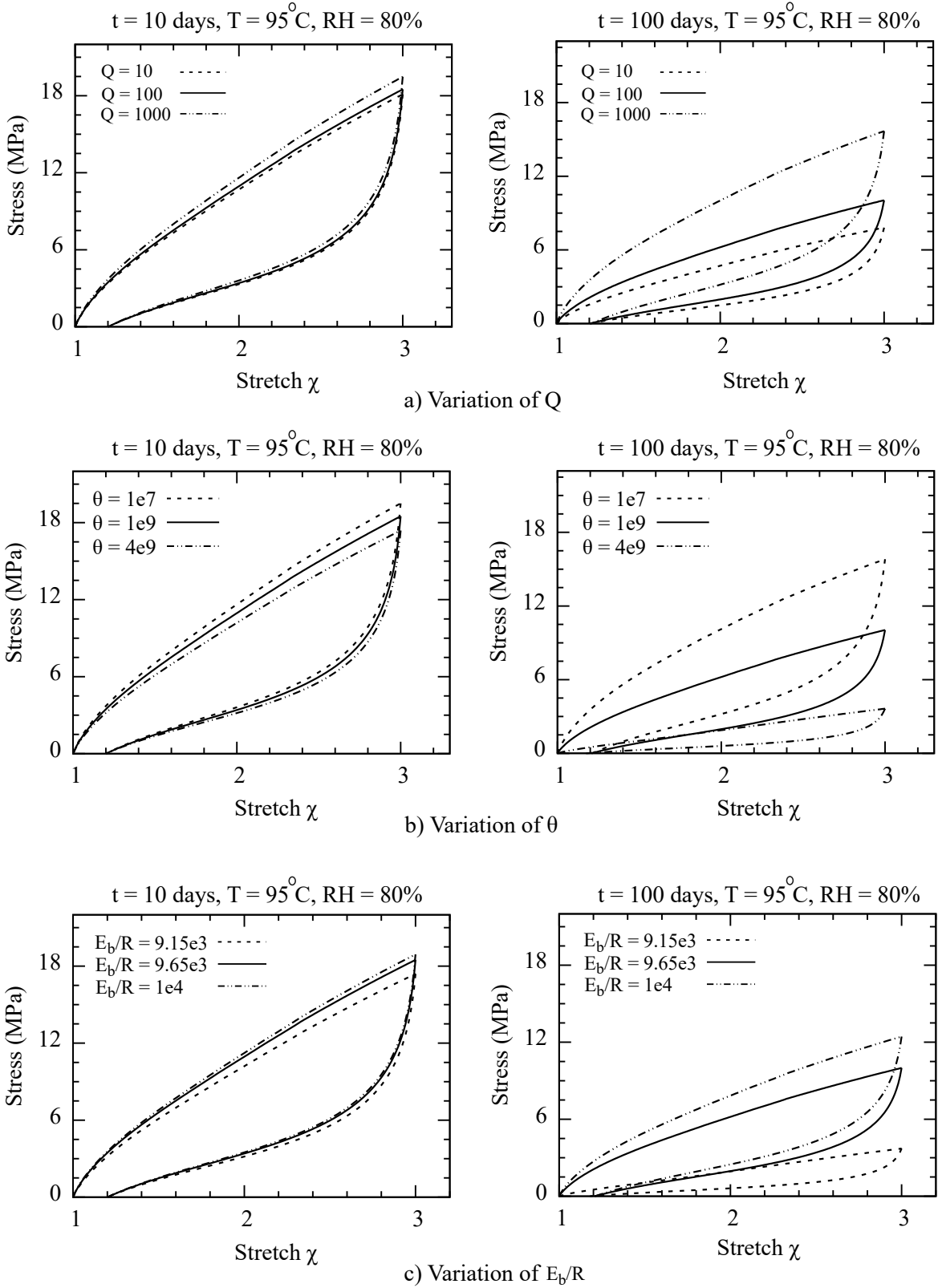


Figure 5.13: Sensitivity analysis of aging trajectory material parameters in the proposed model.

5.5 Parameter identification and model verification

5.5.1 Parameter identification

To validate the proposed constitutive model, its responses were compared to our experimental data. Depending on the specific aging phenomena to be modeled, different portions of the strain energy function can be employed, as depicted in Fig. 5.14. The model is a kind of modular

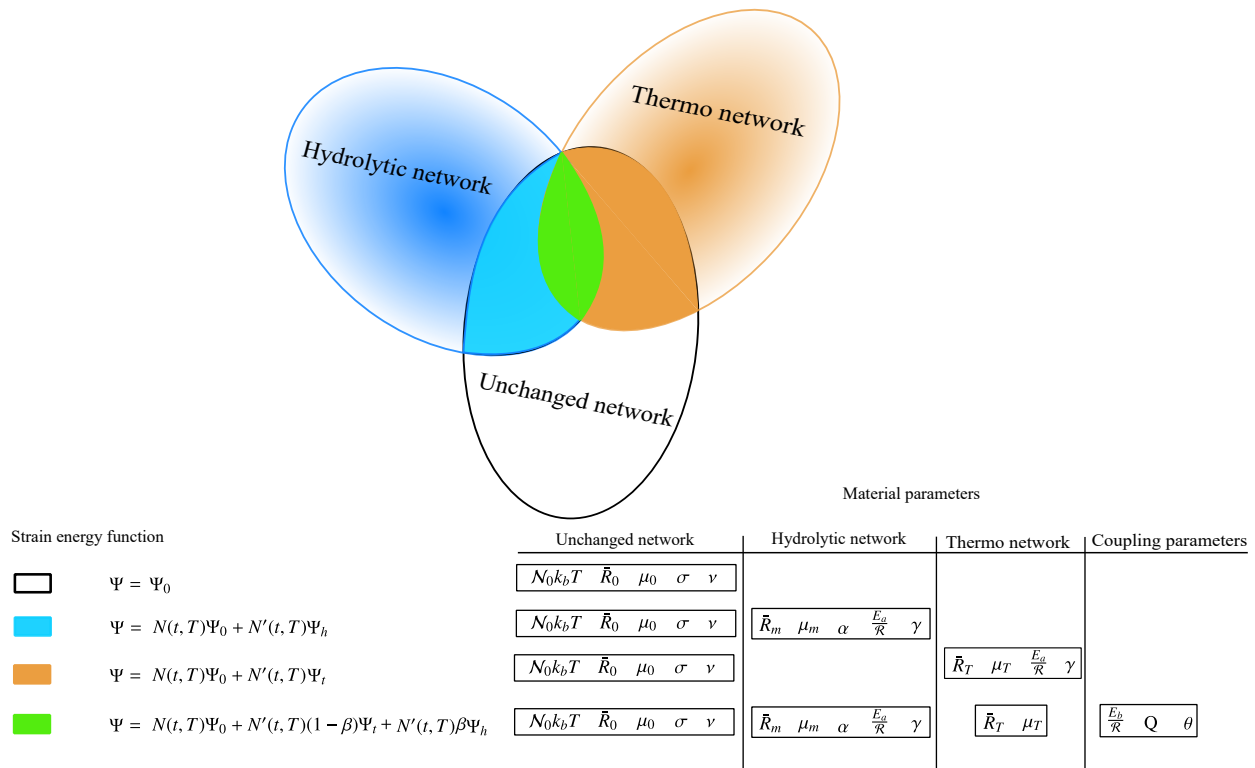


Figure 5.14: Aging phenomena to be modeled and the corresponding network decompositions.

platform to describe damage accumulation in the course of hygrothermal corrosion. Each network is responsible to model the energy reduction of sub-aging mechanisms, i.e. i) hydrolytic, and ii) thermo-oxidative. The correlation between these two independent aging mechanisms is held by a nonlinear function of time, temperature, and relative humidity. Therefore, each network should be fitted to the experiments separately. Accordingly, by setting β to its upper limit (i.e. $\beta = 1$), the thermo-oxidative network will be eliminated and therefore the three material parameters of the morphed network, as well as the unchanged one, can be achieved by fitting to the following three

cases;

- One loading-unloading cycle of the virgin sample to find the effects of λ and λ_m
- Only, one point of loading curve of 20 days hydrolytically aged sample at 80°C (i.e. submerged condition) to find the effects of t , and T
- The primary loading curve of 30 days hydrolytically aged sample at 95°C (i.e. submerged condition) to find the effects of λ , t , and T

On the other hand, the material parameters related to the thermo-oxidative network can be obtained by adjusting $B = 0$ and fitting them to the following cases:

- The primary loading curve of 30 days thermally aged sample at 95°C (i.e. $RH = 0$) to find the effects of λ , t , and T
- Only one point of loading curve of 20 days thermally aged sample at 80°C (i.e. $RH = 0$) to find the effects of t , and T

Lastly, the parameters in function $\beta(t, T, RH)$ can be obtained by fitting to the one point of loading curve of 20 days hygrothermally aged sample at 80°C (i.e. $RH \neq 0$) to find the effects of RH . Once all the material parameters are achieved, the model can predict other loading-unloading curves for the two thermo-oxidative and hydrolytic aging and their collaborative damages.

5.5.2 Model verification

Figs. 5.15, 5.16, 5.17, and 5.18 shows the prediction of the devised model which were benchmarked against our experimental results, while the Tables 6.2, and 5.4 depicts the so-obtained material parameters. In these figures, solid lines represent model predictions while dot points depict the experimental data. The arrows demonstrate the curves and the points which are used for fitting.

To assess the goodness of fit and robustness of the model, the coefficient of determination R^2 is calculated in each aging temperature (See Figs. 5.15, 5.16, 5.17, 5.18). In this respect, the

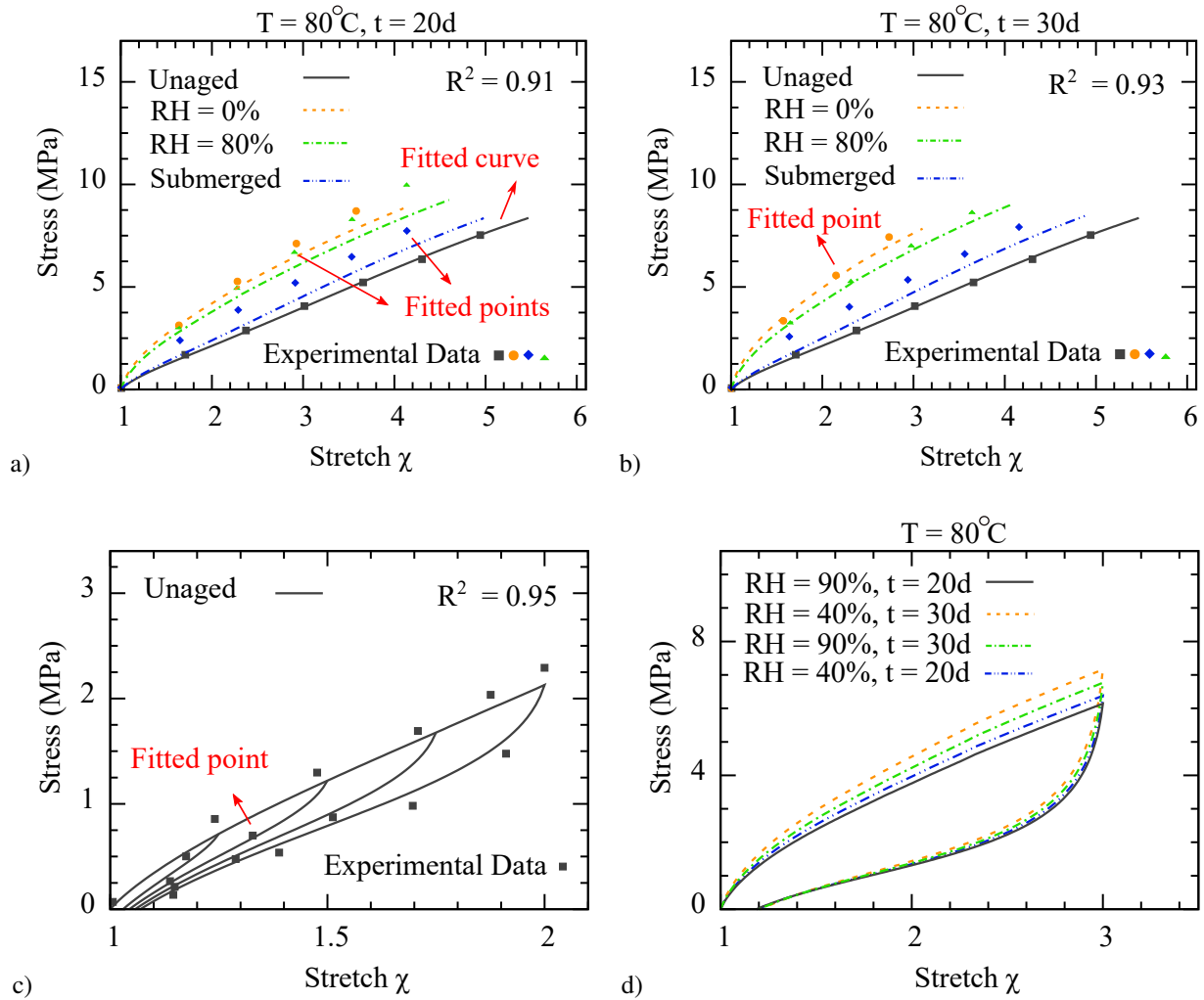


Figure 5.15: Validation of the proposed model for neoprene rubber in the unaged state, thermo-oxidative (i.e. RH = 0%), hydrothermal (i.e. RH = 80%), and hydrolytic aging at $T = 80^{\circ}\text{C}$, in multiple aging conditions; (a) $t = 20\text{d}$, (b) $t = 30\text{d}$, (c) constitutive behavior of virgin sample, (d) Comparison of one cycle load on samples aged at different relative humidities and aging times.

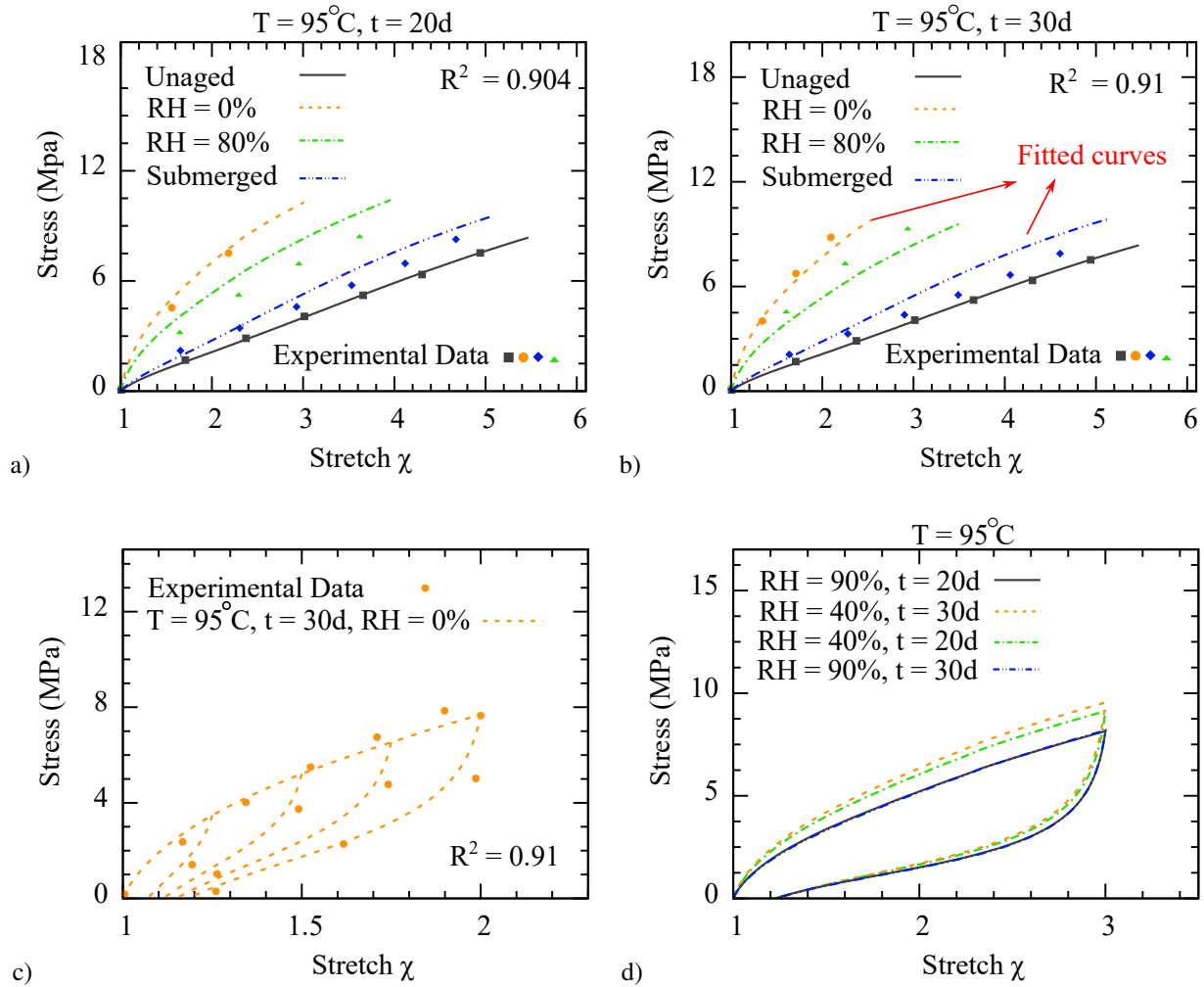


Figure 5.16: Validation of the proposed model for neoprene rubber in the unaged state, thermo-oxidative (i.e. RH = 0%), hydrothermal (i.e. RH = 80%), and hydrolytic aging at $T = 95^\circ\text{C}$, in multiple aging conditions; (a) $t = 20\text{d}$, (b) $t = 30\text{d}$, (c) constitutive behavior of aged sample at $t = 30\text{d}$, $\text{RH} = 0\%$, (d) Comparison of one cycle load on samples aged at different relative humidities and aging times.

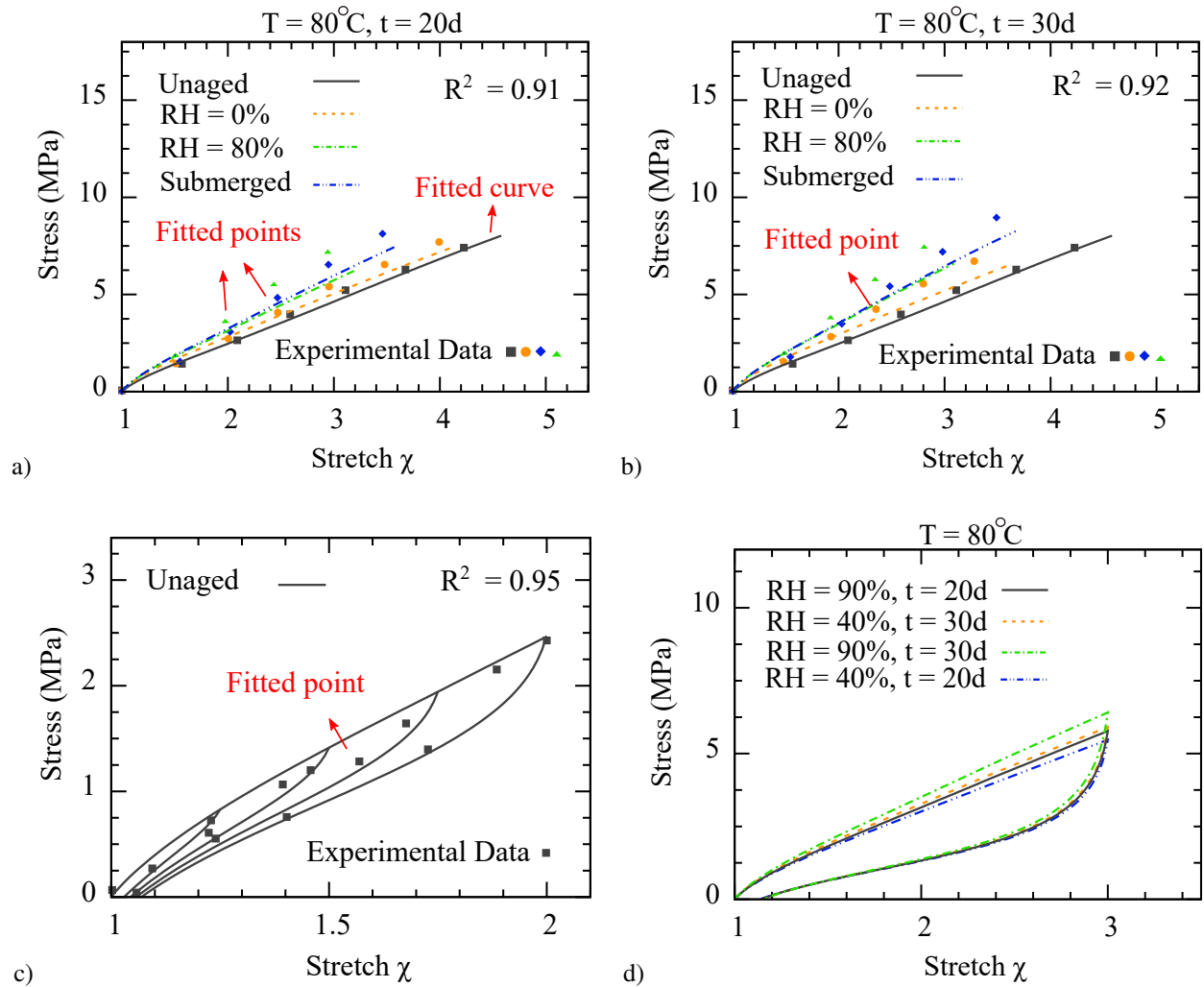


Figure 5.17: Validation of the proposed model for EPDM rubber in the unaged state, thermo-oxidative (i.e. RH = 0%), hydrothermal (i.e. RH = 80%), and hydrolytic aging at $T = 80^\circ\text{C}$, in multiple aging conditions; (a) $t = 20\text{d}$, (b) $t = 30\text{d}$, (c) constitutive behavior of virgin sample, (d) Comparison of one cycle load on samples aged at different relative humidities and aging times.

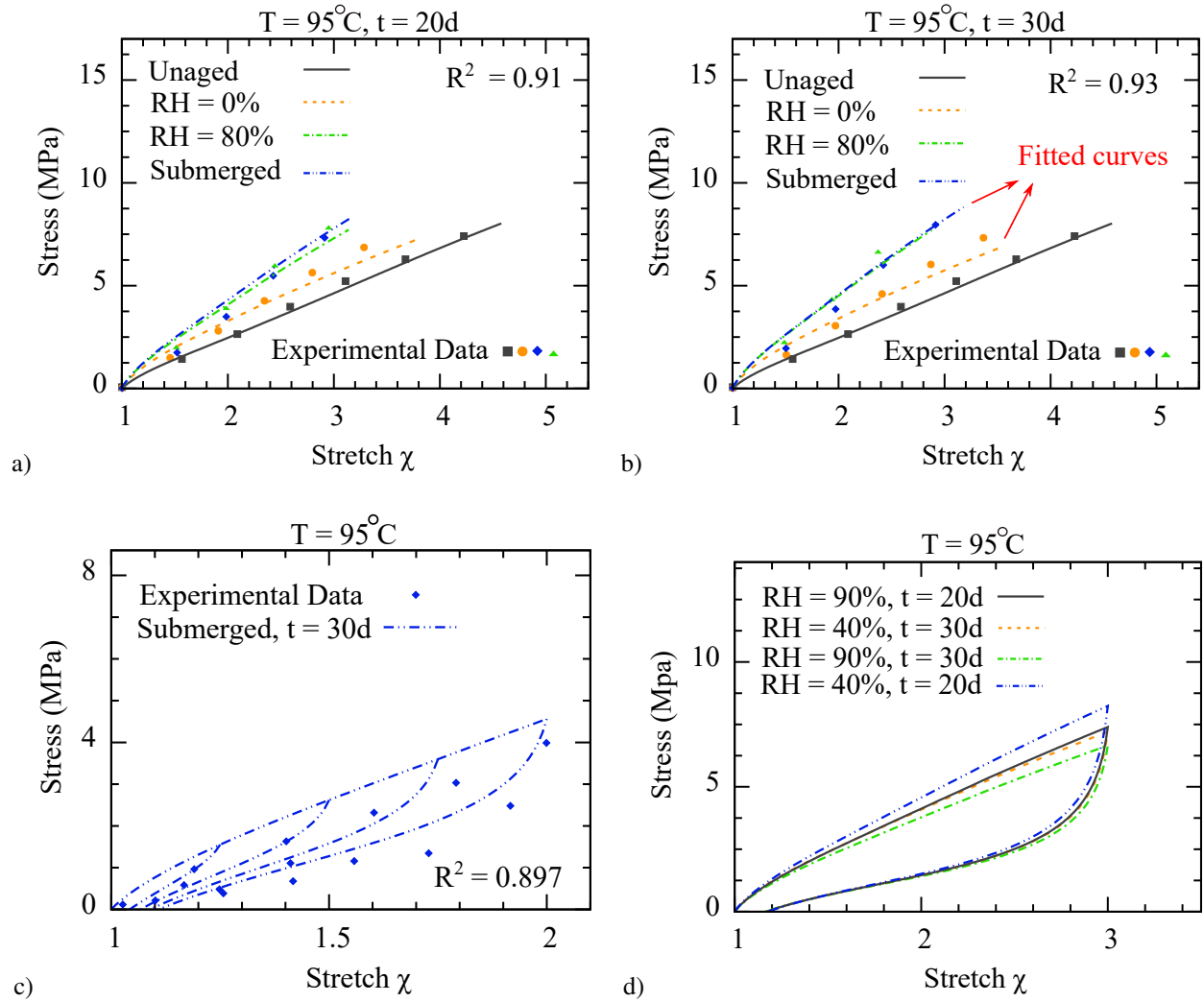


Figure 5.18: Validation of the proposed model for EPDM rubber in the unaged state, thermo-oxidative (i.e. $RH = 0\%$), hydrothermal (i.e. $RH = 80\%$), and hydrolytic aging at $T = 95^{\circ}\text{C}$, in multiple aging conditions; (a) $t = 20\text{d}$, (b) $t = 30\text{d}$, (c) constitutive behavior of aged sample at $t = 30\text{d}$ and submerged condition, (d) Comparison of one cycle load on samples aged at different relative humidities and aging times.

Table 5.3: Material parameters of the devised model for neoprene rubber.

| $\mathcal{N}_0 k_b T$ | \bar{R}_0 | \bar{R}_m | \bar{R}_T | μ_0 | μ_m | μ_T | σ | ν | α | Q | γ | θ | $\frac{E_a}{\mathcal{R}}$ | $\frac{E_b}{\mathcal{R}}$ |
|-----------------------|-------------|-------------|-------------|---------|---------|---------|----------|-------|----------|-----|----------|----------|---------------------------|---------------------------|
| [MPa] | | | | | | | | | | | [1/day] | [1/day] | [K] | [K] |
| 1.663 | 2.65 | 3.88 | 2.54 | 8.04 | 9.06 | 1.9 | 3.28 | 1.01 | 0.685 | 100 | 5.42e+12 | 3.50e+9 | 1.17e+04 | 0.965e+04 |

Table 5.4: Material parameters of the devised model for EPDM rubber.

| $\mathcal{N}_0 k_b T$ | \bar{R}_0 | \bar{R}_m | \bar{R}_T | μ_0 | μ_m | μ_T | σ | ν | α | Q | γ | θ | $\frac{E_a}{\mathcal{R}}$ | $\frac{E_b}{\mathcal{R}}$ |
|-----------------------|-------------|-------------|-------------|---------|---------|---------|----------|-------|----------|-----|----------|----------|---------------------------|---------------------------|
| [MPa] | | | | | | | | | | | [1/day] | [1/day] | [K] | [K] |
| 1.927 | 2.65 | 3.86 | 2.34 | 8.04 | 8.06 | 5.63 | 3.27 | 1.009 | 0.7639 | 80 | 5.42e+12 | 3.2e-1 | 1.17e+04 | 0.74e+03 |

devised model is capable of predicting the constitutive behavior of aged samples With a marginal error. The major source of error, here, is ignoring the effects of nonhomogenous aging. In fact, hygrothermal aging (i.e. water penetration) starts from the surface and is highly dependent on diffusion factors that have not been considered in our recent model. The model is then used to describe different cross-linked polymer damage behaviors as they age once it has been validated. To this end, the changes in the loading-unloading response of the material aged at various aging temperatures and humidity levels are compared (See Figs. 5.15d, 5.16d, 5.17d, 5.18d). Finally, it should be noted that the model can be used for any loading scenario; all that needs to be done is to change the deformation gradient \mathbf{F} to match the desired loading. Accordingly, we mainly focused on uni-axial tensile loading due to the ease of experiments.

5.6 Conclusion

We propose the first physically based model to account for multi-factor damage accumulation of hygrothermal aging. Our model can take into account three damage mechanisms namely hydrolytic aging, thermo-oxidative aging, and deformation-induced damage at the same time. Each of those damage mechanism is induced by sub-mechanisms that are extensively studied before but

has not been modeled in parallel so far. We modeled each sub-mechanism through a linear kinetic equation which is then coupled into the modular network concept to allow calculation of synergies and parallel damage accumulation through multiple sources. In this respect, hydrolytic aging is considered to be induced by chain scission and reduction of the cross-link, while thermo-oxidative aging is considered as a superposition of two competing effects of cross-link formation and chain scission as previously discussed in our recent models [9, 11, 12]. Deformation-induced damage is modeled by implementing the concept of network evolution [85]. Combining these three damage mechanisms can define the damage accumulation in the case of hygrothermal aging. In order to capture the mutual effects of thermo-oxidative and hydrolytic aging, the assumption has been made that each of the aging phenomena can be superposed upon each other. From the micro-mechanical perspective, hygrothermal damage can be regarded as a race among three micro-structural phenomena; i) chain scission due to the presence of temperature, ii) reduction of cross-links attributed to the attendance of water and iii) formation of cross-links as a consequence of oxygen reactions. Utilizing the theory of network decomposition, all phenomena and their correlation were modeled. The proposed model is micro-mechanically based and is mainly relevant on thin samples due to our underlying assumption of homogeneous diffusion of oxygen and water throughout the matrix. The model has been validated against extensive data-sets obtained from experiments we specifically designed for concept validation. In view of its interpretation, precision, and deep insight, it provides an insight into the nature of damage accumulation. The model is a good choice for advance implementation in FE applications.

CHAPTER 6

Thermal Aging Coupled with Cyclic Fatigue in Cross-linked Polymers: Constitutive Modeling & FE Implementation

6.1 Introduction

In view of polymeric materials' prevalence in a myriad number of industries such as aerospace where a component failure could potentially lead to disastrous outcomes; having a reliable model that can predict their mechanical properties degradation induced by different aging conditions is a necessary process [7, 11, 175, 9, 176, 177, 176]. The resistance of polymeric materials against external factors such as mechanical fatigue and environmental elements is the center of attention for decades [178, 179, 180, 181, 182, 149, 145]. These external factors induce irreversible damages to the polymer matrix, resulting in reduction of material's nominal service life [183, 184, 147]. Accordingly, damage accumulation in the polymeric matrix is mostly due to two sources; mechanical damages and environmental aging.

- *Environmental aging*: Environmental aging is an irreversible process that occurs due to changes in the molecular structure of the polymer matrix [185, 186, 103, 157]. Environmental aging can be induced either by a single environmental element such as oxygen [187, 8], water [188, 189], UV [190, 191] or a synergized effect of multi-factor environmental elements such as hygrothermal which is due to mutual effects of oxygen and water. Extensive efforts have been made to describe the effects of environmental aging on the mechanical behaviour of polymers, and many successful models were developed [114, 113]. However, when it comes to synergized effects of chemical and physical aging [192], there is still a large gap in our understanding. Although the popularity of the models to predict the behavior of materials during aging is increasing, aside from our previous models [11, 7, 9], the theoretical efforts for that are limited. In this respect, Konica

and Sain [124] developed a 3D large deformation model for polymers that simultaneously considers the diffusion of chemical reaction to the material during high deformation regime. Besides, they implemented their model in commercial finite-element software to numerically investigate the coupled diffusion-reaction and constitutive response of polymers during oxidation aging. In a similar fashion, Dippel et al. [193] provided a constitutive model to predict the behavior of adhesives in the joints during chemical aging. Their model can consider the internal structure of an adhesive by introducing an interface zone where the material properties alter from the surface to the center of the joint. Moreover, in the same direction, Lamnii et al. [194] investigated the effects of photo-oxidation on the fatigue life of low-density polyethylene. They used dissipated energy in each cycle as a damage indicator and tried to model the evolution of damage with respect to physical and chemical aging.

- *Mechanical damages*: Generally, mechanical damages retain the morphology of the polymer matrix intact, and the decay is mainly attributed to the movement of polymer chains. Due to the high cost of in-situ testing of elastomers, a reliable predicting tool becomes a dire need. In this respect, mechanical damage models are mostly focused on fatigue analysis and there are very few that describe the gradual loss of performance of the material in multi-cycle loading [195, 196]. In this regard, recently, we developed a 3D micro-mechanical model for elastomers Shakedown where the samples are subjected to a high number of cyclic deformations [175]. Moreover, Wang et al. [197] developed a phenomenological model to predict the shakedown of tough hydrogels under cyclic loading. Accordingly, they provide a new evolution of damage variables for multiple cycles, which is achieved by the experimental observations.

The concurrent exposure of rubber to fatigue and environmental aging has been mostly studied through experimental efforts [198, 199, 200, 201, 202, 203, 204, 205]. So far, only a few phenomenological models, and no micro-mechanical models, are available. In this respect, Moon et al. [206] predicted the changes in the fatigue life of tires with respect to aging by implementing the Arrhenius equation. Moreover, Neuhaus et al. [207] investigated the direct and indirect effects of temperature on the response of the rubber-like material. They also proposed a new model which

can take into account the effects of thermal aging as well as the instantaneous effects of temperature on the material lifetime. Jouan and Constantinescu [208] conducted an experimental study to investigate the effects of thermal aging on the fatigue life of silicone adhesive joints. Accordingly, they proposed a law based on two mechanical predictors including the dissipated energy for adhesive joints exposed to thermal aging. Besides, Wang et al. [209] proposed a relationship between thermal aging conditions and the aging lifetime of carbon-black-filled styrene-isoprene-butadiene rubber (SIBR-CB). To the best of the authors' knowledge, currently, there are no physically based models that can predict synergized effects of mechanical and environmental damages on the constitutive response of polymeric matrix. Despite few successful models that can predict the constitutive behavior of polymeric components exposed to either mechanical or environmental damages, describing the material behavior in coupled aging conditions remains to be understood. Here, We first formulate the constitutive behavior of virgin material using the network alteration concept and then couple it with environmental aging and mechanical damages which are thermal aging and low cycle fatigue. This paper is outlined as follows, first, the experimental characterization and observations are discussed in section 6.2. Then the constitutive model is presented in 6.3. Finally, validation and results are presented in section 6.4.

6.2 Experimental observations

6.2.1 Material and procedure

For this study, we used sulfur-vulcanized SBR sheets supplied by a local retailer. The SBR specimens were cut into dog-bone samples using ASTM D412-C size die with its geometry given in Fig. 6.1a. The experimental characterizations are briefly summarized here. In this respect, a uniaxial universal testing machine (Test Resources 311 series frame) was used for quasi-static tensile tests. All tests were displacement controlled and the extensometer grips holding each specimen were 25.4 mm apart and all the experiments were performed at normal room temperature. *To induce thermal aging damage:* Thermal aging progressively alters the rubber materials' chemi-

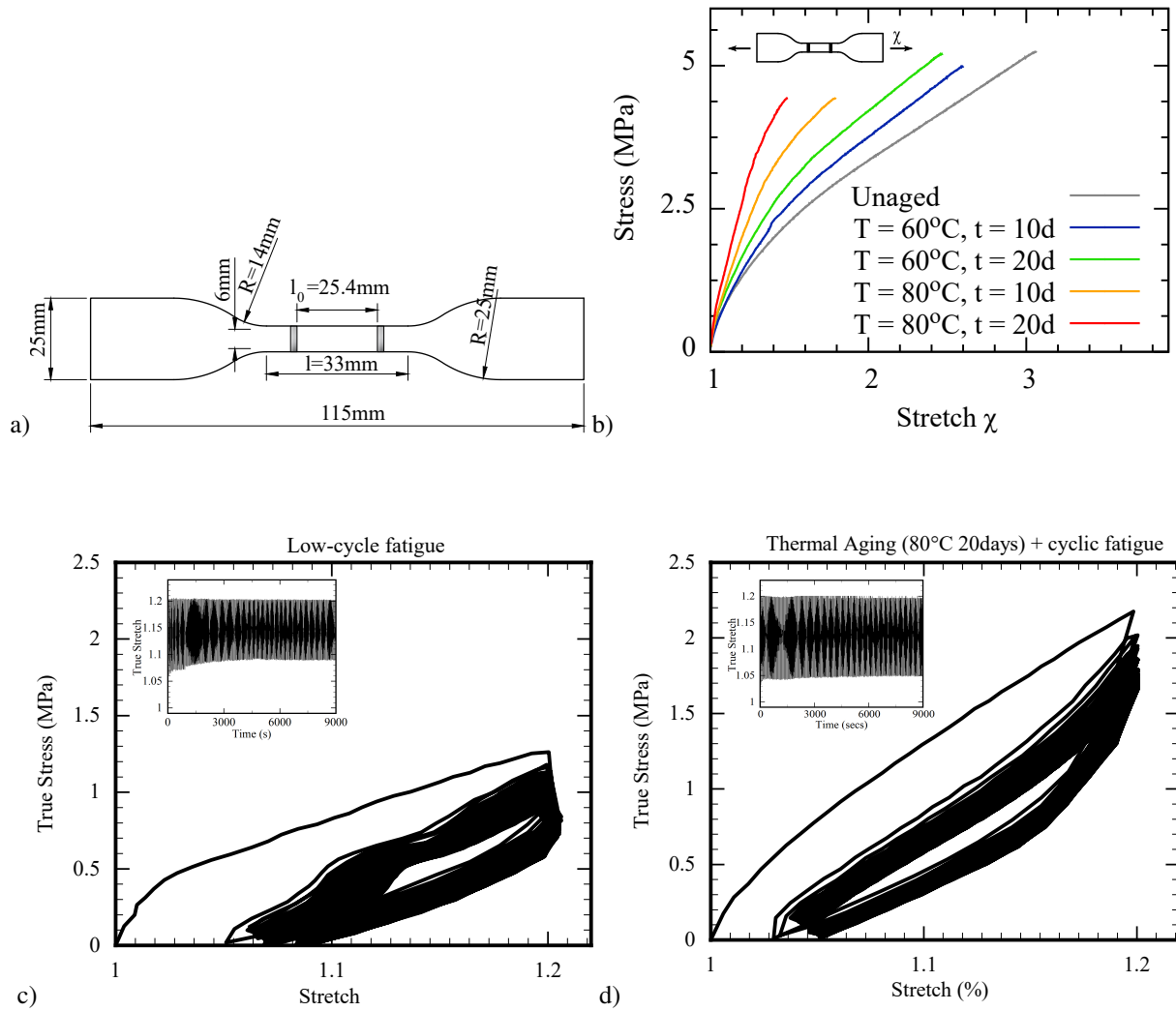


Figure 6.1: (a) Detailed geometry of dog-bone sample. Constitutive behavior of a dog-bone SBR sample damaged by exposure to (b) only thermal aging, (c) only low cycle fatigue, and (d) fatigue-induced damage on thermally aged specimen stored at 80°C for 20 days.

cal composition, which subsequently modifies the structure of their macro-molecular network. In the last decade, a number of investigations worked on identifying the different aging mechanisms induced by thermo-oxidation [210, 103, 211, 212, 213, 214]. In contrast with the thermal treatment (which usually should be done in an oxygen-free environment), thermal aging involves the creation of free radicals P° . The free radicals P° are extremely reactive with oxygen and consequently favor a chain reaction of chemical processes in the polymer, denoted as propagation. Mechanical characterization of material during aging could be categorized into intermittent and contentious investigations. In intermittent tests for thermal aging, material samples are kept in an air convection oven for several weeks or months at a constant temperature and with ambient oxygen [192, 24, 215]. The aged samples are removed from the medium at predefined intervals and submitted to a short-term test at room temperature [183]. Here, the intermittent test was utilized. Accordingly, the aged samples are removed from the medium at predefined intervals and submitted to a short-term test at room temperature [183]. The specimens were stored in stress-free state at 60°C or 80°C with 0%RH for 10 or 20 days (see Fig. 6.1b).

To induce low cycle fatigue damage: Aged and virgin samples were exposed to uni-axial tensile cycles under displacement control settings, with a certain amplitude. In this respect, low cycle fatigue is induced by non-relaxing cyclic loads with different amplitudes of 10% or 20% with a cross-head speed of 50 mm/min. Here, we characterized accumulated damage after a certain number of cycles namely 5, 50, 100, and 500 cycles by measuring the changes in constitutive behavior under uni-axial loading (see Figs. 6.1c and 6.1d).

Table 6.1 shows the summary of all test conditions.

Table 6.1: Summary of coupled fatigue+thermal aging tests performed on SBR specimens, and the changes in their constitutive behaviour.

| Strain(%) | Number of cycles (j) | Aging time (days) | Aging temperature (°C) |
|------------------|-----------------------------|--------------------------|-------------------------------|
| 10% | 5, 50, 100, 500 | Unaged, 10, 20 | 60, 80 |
| 20% | 5, 50, 100, 500 | Unaged, 10, 20 | 60, 80 |

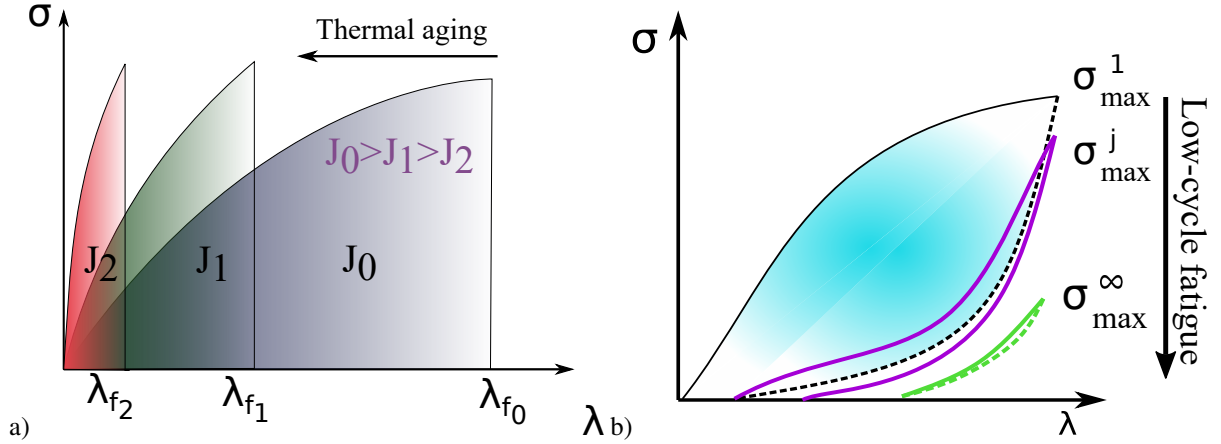


Figure 6.2: Schematic diagrams of evolution of constitutive response of elastomers during (a) thermal aging, and (b) low cycle fatigue.

6.2.2 Accumulative damage

- **Thermal damage:** In view of thermal aging, two sub-structural phenomena namely chain scission and cross-link formation occur that make the material more brittle and reduce its toughness (see Fig. 6.2a). In most elastomers, this phenomenon can be simply modeled via first-order kinetics and it can be best approximated by the famous Arrhenius function [11].
- **Fatigue damage:** Due to fatigue-induced damage, the stress–stretch curves of elastomers soften in each cycle toward a steady-state value often known as fatigue limit. As shown in Fig. 6.2b, the peak stress level σ_{max}^1 is at its maximum in the first cycle, and continuously decrease with number of cycles toward a steady-state σ_{max}^∞ . Since experimental characterization of σ_{max}^∞ is extremely costly, many studies are focused on derivation of σ_{max}^∞ through a limited number of cycles. By normalizing the peak stress value to that of the first cycle σ_{max}^1 , one can define a dimensionless, strain independent function

$$\hat{\sigma}^j = \frac{\sigma_{max}^j(\lambda_i)}{\sigma_{max}^1(\lambda_i)} \approx j^{-\zeta}. \quad \forall j, \quad (6.1)$$

where ζ is a material constant. In fact, this is an important function for the concept of intrinsic fracture toughness, which defines the minimum energy required for a crack to propagate.

Interestingly, experimental data show that $\hat{\sigma}^j$ is independent of the stretch amplitudes and is an ever-decreasing function that depends only on j (see Fig. 6.3). It should be noted that the extent of the normalized softening (beginning of the softening until reaching the steady zone) depends on how far is this zone from the fracture. Accordingly, the normalized softening plots till fracture have three-zone [216] :

- i) In the first zone, commencing with the second cycle, a stress softening occurs until the steady zone is reached.
- ii) In the second zone, there is a minor fluctuation of the normalized maximum stress lying up to achieve the critical damage amount.
- iii) The third and final zone corresponds to a rapid decline in the normalized maximum stress until the sample fails.

Here, since we mostly focused on the synergized effect of thermal aging and fatigue we narrowed our model to the first zone and for that reason we choose a relatively small fatigue amplitude. While the fatigue of metals has been extensively studied, there are very few studies capable of describing fatigue phenomena in soft materials, especially with respect to mechanical modeling [175, 197].

- **Thermal + fatigue damage:** Different sub-structural phenomena such as chain scission, or cross-link formation are responsible for the damage accumulation in various conditions of mechanical (chain breakage) and environmental degradation (chain scission + cross-link formation). Thermal aging results in two sub-structural phenomena namely chain scission and cross-link formation which made the material more brittle[217]. Accordingly, an increase in apparent modulus during thermal aging is mainly attributed to the cross-link formation, while the physical explanations for stress softening in cyclic fatigue could be bond rupture [218], molecules slipping [219], filler rupture [220], and disentanglement [221, 63]. Summarizing our experimental results in Fig.6.4, data suggests that the evolution of σ_{max}^j , in quasi-static cyclic tests, depends mainly on the number of cycles j and status of thermal

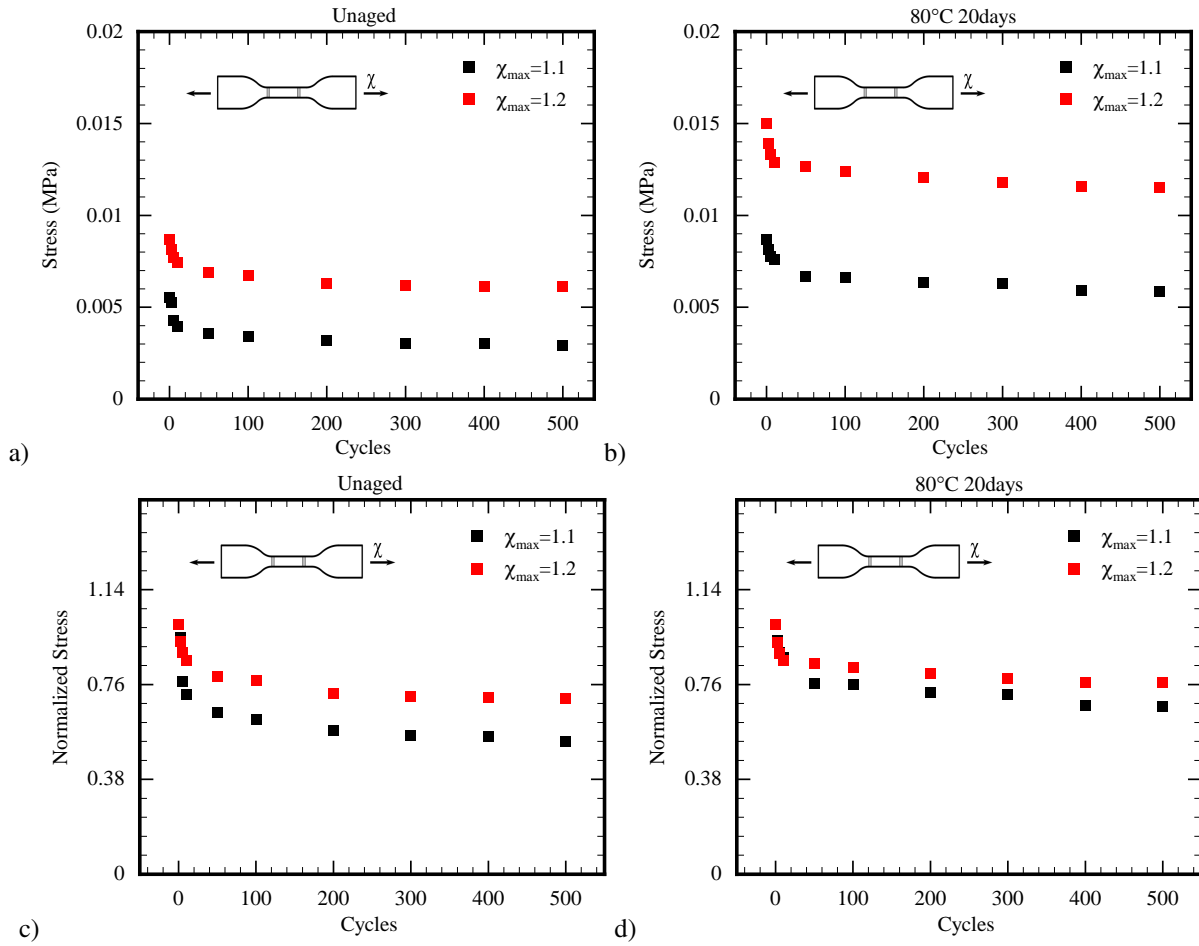


Figure 6.3: Maximum Stress against number of cycles for different stretch amplitude: (a) $\sigma_{max}^j(\lambda_i)$ versus cycle number j for unaged material, (b) σ_{max}^j versus cycle number j for material aged at 80 °C for 20 days, (c) $\hat{\sigma}_{max}^j$ normalized maximum stress versus cycle number j for unaged material, and (d) $\hat{\sigma}_{max}^j$ normalized maximum stress versus cycle number j for for material aged at 80 °C for 20 days.

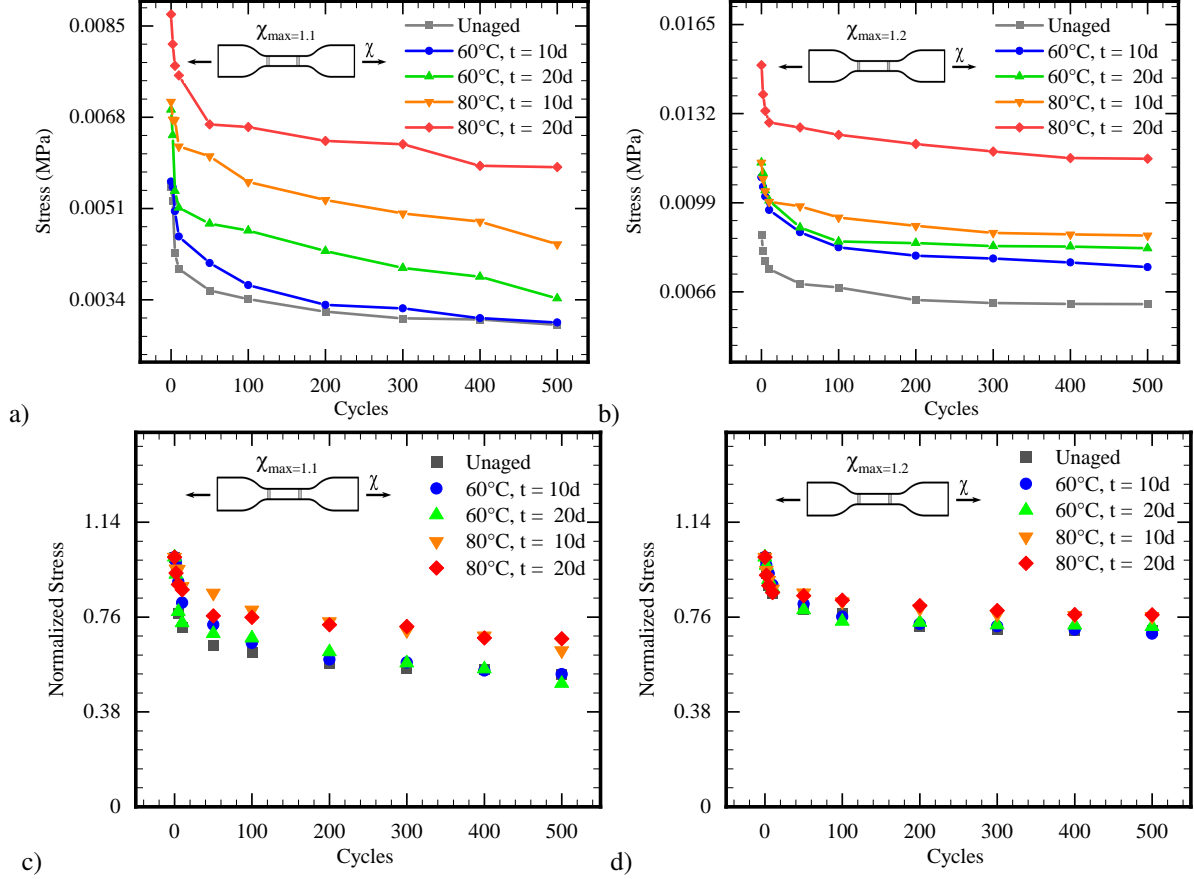


Figure 6.4: Maximum Stress against number of cycles for different aging conditions: (a) σ_{max}^j versus cycle number j for $\lambda = 1.1$, (b) σ_{max}^j versus cycle number j for $\lambda = 1.2$, (c) $\hat{\sigma}_{max}^j$ normalized maximum stress versus cycle number j for $\lambda = 1.1$, and (d) $\hat{\sigma}_{max}^j$ normalized maximum stress versus cycle number j for $\lambda = 1.2$.

damage (aging time and temperature). Normalizing the peak stress value to that of the first cycle σ_{max}^1 for each aging condition, suggests that we can decouple thermal and fatigue damage and represent fatigue damage as a function of the number of cycles (see Figs. 6.4c and 6.4d).

Following such experimental conclusion, our goal here is to predict the constitutive response of material that are concurrently exposed to fatigue and thermal aging for different amount of time.

6.3 Constitutive model

The experimental results confirm that the behavior of an elastomeric sample exposed to concurrent damage can be described as a hyper-elastic behavior with superimposed mechanical and environmental damages. Accordingly, the damage accumulation in the elastomers is a contribution of two phenomena; (i) environmental damage, and (ii) mechanical damage which is induced by fatigue. The proposed approach allows us to integrate damage within any constitutive law that is based on chain density N . Here for the sake of simplicity, we choose the full-network model to describe the mechanical behavior of the SBR network [222], while other models like network alteration [223, 224], or network evolution can be also used [7]. As shown in Fig. 6.5, the modular nature of the proposed model can be best described by the decomposition of the behavior into three parts

1. *Full-network model* to describe the constitutive behaviour of unaged matrix [224].
2. *Thermal aging model* to describe the damage induced by thermal oxidation [11].
3. *Fatigue model* to describe the damage induced by fatigue during multiple cyclic loading [197].

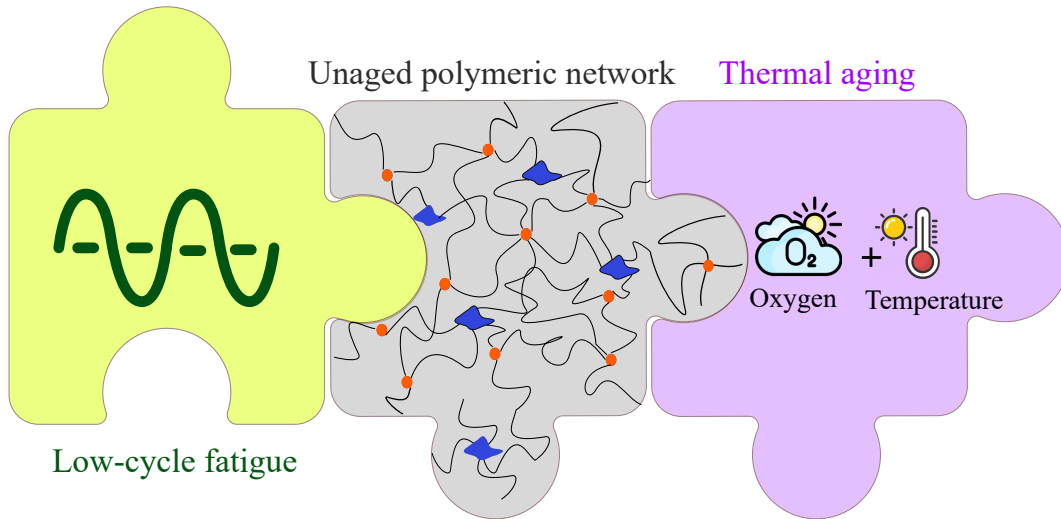


Figure 6.5: Schematic figure of modular nature of the proposed model.

Hereafter, the following notations are utilized: y as a scalar, \mathbf{y} as a vector, \mathbf{Y} as a second-order tensor, and \mathbb{Y} as a fourth-order tensor. Furthermore, we use the overhead index $\overset{d_i}{X}$ to describe

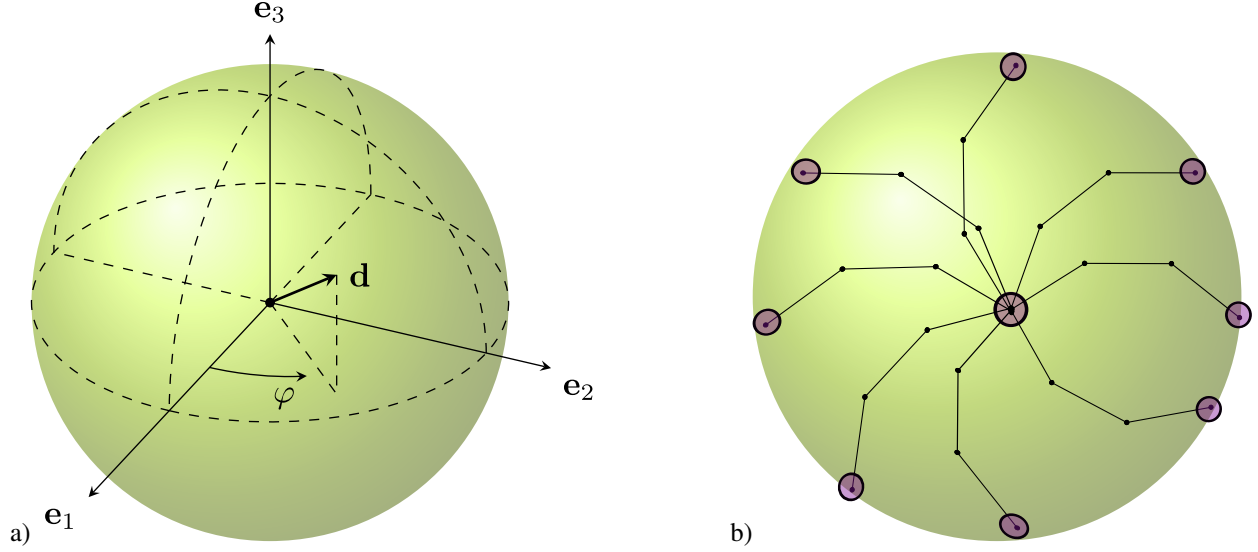


Figure 6.6: Schematic figures of a) the unit micro-sphere having an orientation vector $\mathbf{d} = d_1 \mathbf{e}_1 + d_2 \mathbf{e}_2 + d_3 \mathbf{e}_3$, and b) the schematic representation of polymer network system.

certain entity X along direction \mathbf{d}_i . Note that we have reserved the superscript indices for power-law relations and subscript indices for the state of the networks/matrix.

6.3.1 Full-network model

Assuming the elastomers to be isotropic and in-compressible, a representative volume element (RVE) can be represented by a micro-sphere made by polymer chains homogeneously and equivalently distributed in all spatial directions within the sphere. In each direction, one can assume a similar set of chains with density per direction given as $\frac{d}{N}$. Integrating the energy of chains in all directions (see Fig. 6.6), one can write the volumetric strain energy of the RVE as

$$\Psi(\mathbf{F}) = \frac{1}{4\pi} \int_S \frac{d}{N} \psi dA \cong \frac{1}{4\pi} \sum_{i=1}^k \frac{d_i}{N} w_i \psi, \quad (6.2)$$

where ψ is the strain energy of a single polymer chain in direction \mathbf{d} , and \mathbf{F} stands for the macro-scale deformation gradient. This integration could be numerically achieved by the Gaussian integration scheme [145, 225, 226] (see Fig. 6.6b). Here, w_i is the weight factor corresponding to each integration directions \mathbf{d}_i ($i = 1, 2, \dots, k$). Since chains in different directions are subjected to dif-

ferent micro-stretches $\overset{d}{\lambda} = \sqrt{\mathbf{d}^T \mathbf{F}^T \mathbf{F} \mathbf{d}}$, it is important to rewrite the energy of a single polymer chain with respect to $\overset{d}{\lambda}$ as

$$\begin{aligned} \overset{d}{\psi} &:= \psi \left(\overset{d}{\lambda}, \overset{d}{n} \right), & \text{where} & \quad \psi(\lambda, n) = nK_bT \left(\frac{\lambda}{\sqrt{n}}\beta + \ln \frac{\beta}{\sinh \beta} \right) + c_0, \\ \overset{d}{n} &= n_0 \exp \left(\mu \overset{d}{\lambda}_m \right) & \text{and} & \quad \overset{d}{N} = N_0 \exp \left(-\mu \overset{d}{\lambda}_m \right) \end{aligned} \quad (6.3)$$

where K_b is Boltzmann's constant, T temperature, and c_0 the entropy of a chain in the reference state. Here, $n = L/l$ represents the normalized chain of the length with respect to the segment Kuhn length l . It should be noted that, for the sake of simplicity, we assumed the homogeneous distribution of the micro-stretch $\overset{d}{\lambda}$ within the network. Accordingly, the relationship between the micro-stretch $\overset{d}{\lambda}$ and macro-stretch $\overset{d}{\chi}$ in the direction \mathbf{d} is assumed as $\overset{d}{\chi} = \overset{d}{\lambda}$. The evolution of damage in matrix can be considered to be a function of maximum stretches in each direction, e.g. $\overset{d}{\lambda}_m = \max_{\tau \in (-\infty, t]} \overset{d}{\lambda}(\tau)$. Deformation-induced irreversible damage appears only when the material is stretched to a level never experience before, or in other words when $\overset{d}{\lambda}_m = \overset{d}{\lambda}$. During unloading and reloading, irreversible damage does not appear anymore and we have $\overset{d}{\lambda}_m = \text{Const}$. Thus, the evolution of matrix can be best modeled by representing parameters n and N as exponential functions of $\overset{d}{\lambda}_m$. Moreover n_0 , and μ are material parameters that will be determined through the fitting procedure. Using the concept of Network alteration theory [224, 216], the full network model can further be advanced to include the irreversible deformation-induced damage, by assuming the total number of active polymer segments remain unchanged. To this end, one has

$$\overset{d}{n} \overset{d}{N} = n_0 N_0 = \text{Const}. \quad (6.4)$$

where n_0 and N_0 are both material parameters. Considering chains to have an original end-to-end distance of $R_0 = \sqrt{n}l$, and maximum end-to-end distance equal to the chain contour length

$R_{max} = L = nl$, one can write

$$R = \overset{d}{\lambda} \sqrt{\overset{d}{n}l} \quad \text{where} \quad R \leq R_{max} \quad \text{and} \quad \overset{d}{\lambda} \leq \sqrt{\overset{d}{n}} \quad (6.5)$$

The parameter $\beta = \mathcal{L}^{-1}\left(\overset{d}{\mathcal{A}}\right)$ stands for inverse Langevin function, while $\overset{d}{\mathcal{A}} = \frac{\overset{d}{\lambda}R_0}{nl} = \frac{\overset{d}{\lambda}}{\sqrt{\overset{d}{n}}}$ denotes the extensibility ratio in direction \mathbf{d} . The inverse Langevin function $\mathcal{L}^{-1}(x)$ could not be explicitly derived and it should be approximated by a rational function. Here, a simple yet accurate approximation is utilized [11] and it could be written as

$$\mathcal{L}^{-1}(x) \cong \frac{x}{1-x} + 2x - \frac{8}{9}x^2. \quad (6.6)$$

6.3.2 Thermal model

In the course of thermal aging, we assumed that the changes in the chain density N_{ev} follow the same trend as the alteration of peroxide cross-link density (see [11] for details). Hence, in the absence of mechanical damages, the Ψ_{aged} can be written as

$$\Psi_{aged} = \frac{1}{4\pi} \int_S \overset{d}{N}_{ev} \overset{d}{\psi} \overset{d}{d}A \quad \text{where} \quad \overset{d}{N}_{ev} = \rho_{\infty} - \rho_0 \exp\left(-\gamma \exp\left(-\frac{E_a}{\mathcal{R}T}\right)t\right), \quad \rho_0 < \rho_{\infty} \quad (6.7)$$

where ρ_0 , and ρ_{∞} are material parameters which describe the concentration of polymer chains in two states of virgin and infinity aged matrix. Moreover, $\mathcal{R} = 8.314 [J.K^{-1}.mol^{-1}]$ is the ideal gas constant, $E_a [J.mol^{-1}]$ the activation energy of the chemical reaction, and $\gamma [(day)^{-1}]$ a degradation constant which is considered as a material constant. Figure 6.7a shows the evolution of the normalized value of N_{ev} through aging time and temperatures.

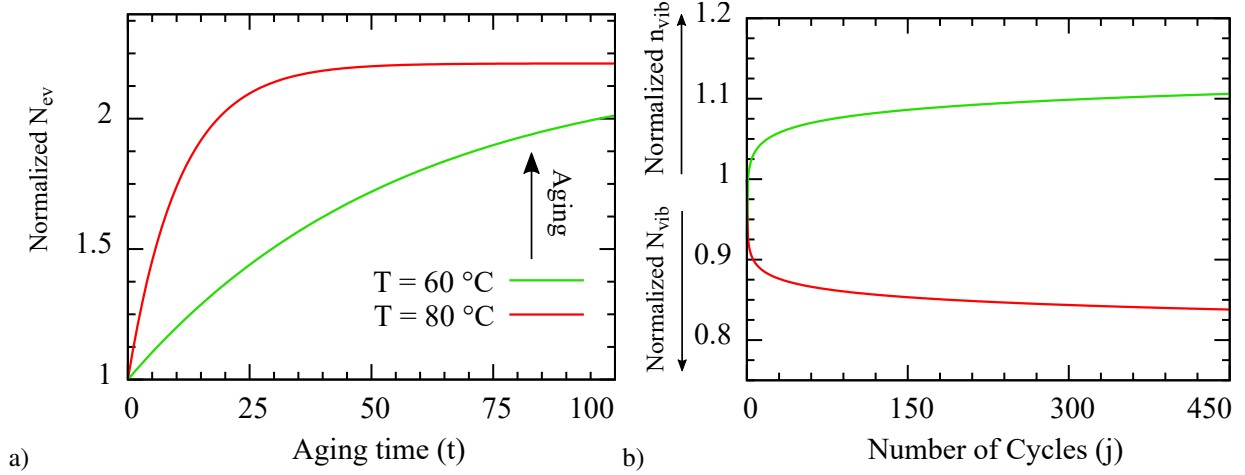


Figure 6.7: Evolution of the model parameters for multiple conditions; (a) N_{ev} for a different aging times, and (b) N_{vib} , n_{vib} for a different number of cycles.

6.3.3 Fatigue model

In fatigue-induced damage, the irreversible damage sustained by matrix is mainly associated to detachments/re-attachments of the physical bonds, the total number of which reduces over time [227]. Gradual reduction of physical cross-links leads to increase of the average length of polymer chain n and consequently decrease in the number of polymer chains N , since $n \cdot N = \text{Const}$. After the irreversible damage occurred in the first cycle, the evolution of the macro-molecular network is mainly governed by the gradual loss of physical bonds which is also irreversible and its associated changes in number N and length of polymer chains n . It is important to note that this assumption is valid as long as experimental data confirms that the evolution of irreversible damage which is governed through n and N , is fully independent of the fatigue stretch amplitude λ_i (see Figs. 6.3c and 6.3d).

To describe the contribution of the irreversible damage in the j th cycle, we represent the composition of the damaged matrix through n_{vib} and N_{vib} using power-law functions [197] as

$$\frac{N_{vib}}{N} = j^{-\zeta} \quad \text{considering} \quad n \cdot N = n_{vib} \cdot N_{vib} \quad \Rightarrow \quad \frac{n_{vib}}{n} = j^{\zeta}. \quad (6.8)$$

It should be noted that the parameter ζ in Eqs. 6.8 and 6.1 are the same. Figure 6.7b depicts the

evolution of the normalized values of N_{vib} , and n_{vib} through fatigue loading. Note that here, the total number of segments is altered during thermal aging while the length of the chains remain unchanged. In fact, keeping the chains length unchanged during thermal aging is a simplification assumption to keep the number of material parameters low. In cyclic fatigue, the length of the polymer chain N increases while the number of the active chain n decreases which makes the total number of segments remain unchanged. This means that during mechanical loading conservation of the total number of segments is held while along the aging trajectory the total number of segments is altered due to the change of the polymer matrix [59].

6.3.4 Damage superposition

The main assumption here, is that mechanical and environmental aging collaboratively induce damage and thus, they can be modeled as two parallel damage mechanisms. Here, damage accumulation is given in terms of multiplicative decomposition of damages induced by thermal aging and fatigue-induced damages (see Fig. 6.5). Accordingly, accumulated damage within the matrix can be described by inserting Eqs. 6.3, 6.7, and Eq. 6.8 into 6.2 which yields

$$\Psi_D = \frac{1}{4\pi} \sum_{i=1}^k w_i \tilde{N} \psi \left(\frac{d_i}{\lambda}, n_0 j^\zeta \exp \left(\mu \lambda_m \right) \right), \quad \text{where}$$

$$\tilde{N} = \frac{1}{j^\zeta \exp \left(\mu \lambda_m \right)} \left(\tilde{N}_\infty - \tilde{N}_0 \exp \left(-\gamma \exp \left(-\frac{E_a}{\mathcal{R}T} \right) t \right) \right). \quad (6.9)$$

where the two material parameters \tilde{N}_∞ and \tilde{N}_0 are defined by multiplication of other constants, namely

$$\tilde{N}_\infty = \rho_\infty N_0 \quad \tilde{N}_0 = \rho_0 N_0,$$

and thus both can be directly derived from fitting.

6.3.5 Constitutive formulation

To derive a constitutive equation for an in-compressible polymer matrix (i.e. $J = \det \mathbf{F} = 1$), the strain energy function can be postulated by

$$\Psi_M = \Psi_D - p(J - 1), \quad (6.10)$$

where the scalar p can be regarded as an indeterminate Lagrange multiplier, which is generally known as hydro-static pressure and it can be determined from boundary conditions (detailed derivation of p for the plane stress condition is discussed in [11]). The first Piola-Kirchhoff tensor \mathbf{P} can be achieved by differentiating the Eq. 6.10 with respect to the deformation gradient \mathbf{F} [228, 229, 230] and using the identity of $\frac{\partial J}{\partial \mathbf{F}} = J\mathbf{F}^{-T}$. Hence, \mathbf{P} can be written as

$$\mathbf{P} = \frac{\partial \Psi_M(\mathbf{F})}{\partial \mathbf{F}} - p\mathbf{F}^{-T}, \quad \frac{\partial \Psi_M(\mathbf{F})}{\partial \mathbf{F}} = \sum_{i=1}^k w_i \bar{N} \frac{d_i}{\partial \lambda} \frac{\partial \psi}{\partial \lambda} \frac{1}{2} \frac{\partial d_i \bar{\mathbf{C}} d_i}{\partial \bar{\mathbf{F}}} : \frac{\partial \bar{\mathbf{F}}}{\partial \mathbf{F}}, \quad (6.11)$$

where \mathbf{C} denotes for the right Cauchy–Green tensor, $\bar{\mathbf{F}} = J^{-1/3}\mathbf{F}$, and $\bar{\mathbf{C}} = J^{-2/3}\mathbf{C}$. Besides, the Eq. 6.11 could be even more simplified by using the following identities

$$\frac{\partial \psi \left(n, \lambda \right)}{\partial \lambda} = \sqrt{n} K_b T \beta \left(\frac{\lambda}{\sqrt{n}}, n \right),$$

$$\frac{\partial d \bar{\mathbf{C}} d}{\partial \bar{\mathbf{F}}} : \frac{\partial \bar{\mathbf{F}}}{\partial \mathbf{F}} = 2\bar{\mathbf{F}}(\mathbf{d} \otimes \mathbf{d}) : J^{-\frac{1}{3}} \mathbb{I} = 2J^{-\frac{1}{3}} \bar{\mathbf{F}}(\mathbf{d} \otimes \mathbf{d}),$$

$$\mathbf{P} = K_b T \sum_{i=1}^k \bar{N} \sqrt{n^{d_i}} \mathcal{L}^{-1} \left(\frac{\lambda}{\sqrt{n^{d_i}}} \right) \frac{w_i}{d_i} J^{-\frac{1}{3}} \bar{\mathbf{F}}(\mathbf{d}_i \otimes \mathbf{d}_i) - p\mathbf{F}^{-T}. \quad (6.12)$$

6.3.6 FE linearization

To analyze a boundary value problem with the proposed model, the macro-scale domain is assumed as a homogeneous continua body analyzed in the framework of the nonlinear finite element

method [231], as shown in Fig. 6.8. In what follows, we present the consistent tangent modu-

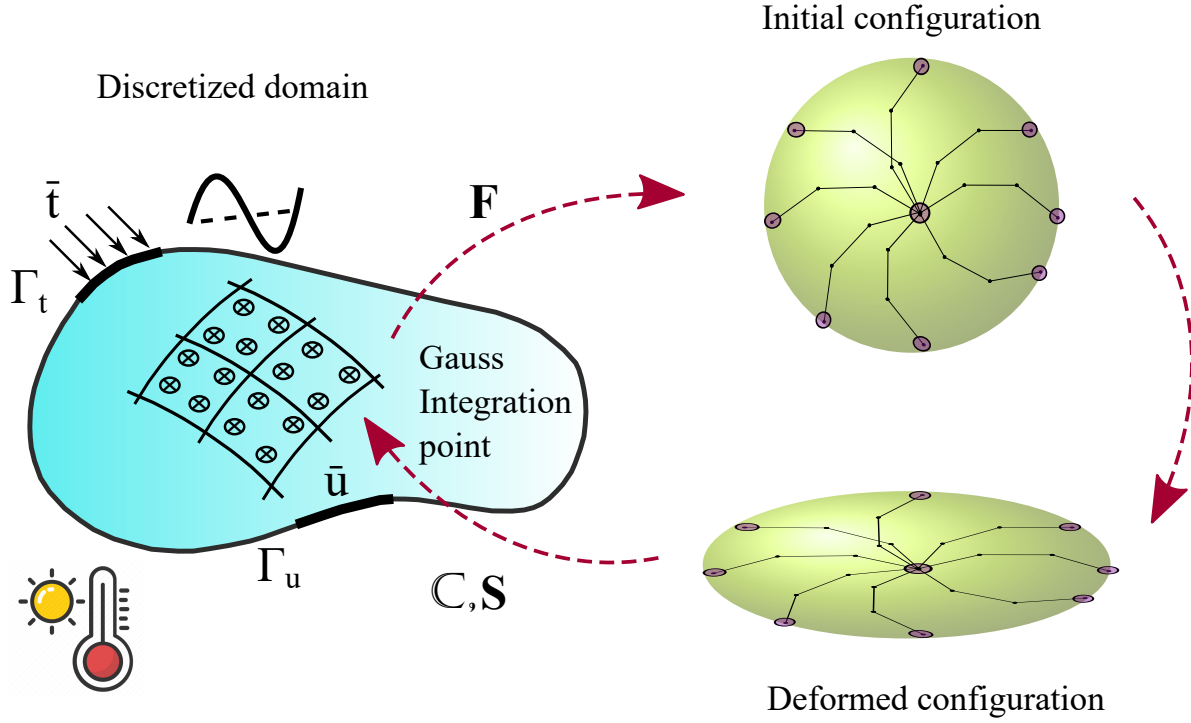


Figure 6.8: A schematic figure of the hierarchical micro-macro multi-scale nature of the model.

lus \mathbb{C} of the proposed constitutive model for an FE implementation. Accordingly, one can derive the Lagrangian elasticity tensor \mathbb{C} by differentiation of the second Piola–Kirchhoff stress tensor $\mathbf{S} = \mathbf{F}^{-1}\mathbf{P}$ with respect to the Green-Lagrange strain tensor $\mathbf{E} = \frac{1}{2}(\mathbf{F}^T\mathbf{F} - \mathbf{I})$ (see [11] for details

). Having the plane stress condition and defining $2\frac{\partial\Psi(\mathbf{F})}{\partial\mathbf{C}}$, $\mathbb{C}^n = 4\frac{\partial^2 W(\mathbf{F})}{\partial\mathbf{C}^2}$, $\mathbf{A} = \begin{Bmatrix} 0 & 0 & 0 \\ 0 & 0 & 0 \\ 0 & 0 & \mathbf{F}_{33}^2 \end{Bmatrix}$,

$$\mathbf{B} = \left\{ \begin{array}{ccc} 0 & 0 & 0 \\ 0 & 0 & 0 \\ 0 & 0 & 2\mathbf{F}_{33} \end{array} \right\}, \text{ one can derive the Lagrangian tangent modulus as:}$$

$$\begin{aligned} \mathbb{C} &= \frac{-2}{3} J^{\frac{-2}{3}} (\mathbf{S}^n - \mathbf{S}_{33}^n \mathbf{F}_{33}^2 \mathbf{C}^{-1}) \otimes \mathbf{C}^{-1} \\ &+ J^{\frac{-4}{3}} \left(\mathbb{C}^n - \frac{1}{3} \mathbb{C}^n : \mathbf{C} \otimes \mathbf{C}^{-1} - \mathbf{C}^{-1} \otimes \mathbb{C}^n : \mathbf{A} + \frac{1}{3} (\mathbf{C} : \mathbb{C}^n : \mathbf{A}) \mathbf{C}^{-1} \otimes \mathbf{C}^{-1} \right) \\ &- J^{\frac{-2}{3}} \left(2\mathbf{S}^n : \mathbf{B} \mathbf{C}^{-1} \otimes \frac{\partial \mathbf{F}_{33}}{\partial \mathbf{C}} - 2\mathbf{S}^n : \mathbf{A} \mathbf{C}^{-1} \otimes \mathbf{C}^{-1} \right), \end{aligned} \quad (6.13)$$

where

$$\frac{\partial \mathbf{F}_{33}}{\partial \mathbf{C}} = \frac{\partial \mathbf{F}_{33}}{\partial \mathbf{F}} \frac{\partial \mathbf{F}}{\partial \mathbf{C}} = \frac{1}{2} \mathbf{F}^{-1} \mathbf{F}', \quad \text{where} \quad \mathbf{F}' = \frac{\partial \mathbf{F}_{33}}{\partial \mathbf{F}} = \mathbf{F}_{33}^2 \left\{ \begin{array}{ccc} -\mathbf{F}_{22} & \mathbf{F}_{21} & 0 \\ \mathbf{F}_{12} & -\mathbf{F}_{11} & 0 \\ 0 & 0 & 0 \end{array} \right\}. \quad (6.14)$$

In order to determine \mathbb{C}^n and \mathbf{S}^n , we have

$$\begin{aligned} \mathbf{S}^n \mathbf{d} \otimes \mathbf{d} &= 2 \frac{\partial \Psi(\mathbf{F})}{\partial \mathbf{C}} \cong 2 \sum_{i=1}^k \frac{d_i}{N} w_i \frac{\partial \psi(\lambda)}{\partial \mathbf{C}}. \\ \mathbb{C}^n \mathbf{d} \otimes \mathbf{d} \otimes \mathbf{d} \otimes \mathbf{d} &= 4 \frac{\partial^2 \Psi(\mathbf{F})}{\partial \mathbf{C}^2} \cong 4 \sum_{i=1}^k \frac{d_i}{N} w_i \frac{\partial^2 \psi(\lambda)}{\partial \mathbf{C}^2}. \end{aligned} \quad (6.15)$$

The derivatives used in the above equations, could be derived as follows

$$\frac{\partial \psi \left(\frac{d_i}{\lambda} \right)}{\partial \mathbf{C}} = K_b T \left(\frac{\sqrt{n}}{2\lambda} \beta \right) \mathbf{d} \otimes \mathbf{d}. \quad (6.16)$$

$$\frac{\partial^2 \psi \left(\frac{d_i}{\lambda} \right)}{\partial \mathbf{C}^2} = K_b T \frac{\sqrt{n}}{4\lambda} \left(\frac{\partial \beta}{\partial \lambda} - \frac{\beta}{\lambda} \right) \mathbf{d} \otimes \mathbf{d} \otimes \mathbf{d} \otimes \mathbf{d}. \quad (6.17)$$

Table 6.2: Material parameters of the proposed model for SBR.

| $\tilde{N}_0[MPa]$ | $\tilde{N}_\infty[MPa]$ | n | μ | ζ | $\gamma[day]^{-1}$ | $E_a[j][mol]^{-1}$ |
|--------------------|-------------------------|-------|-------|---------|--------------------|--------------------|
| 1.3700 | 2.5007 | 2.687 | 0.52 | 0.06218 | 8.5860e+10 | 9.7207e+03 |

$$\frac{\partial \beta}{\partial \lambda^{d_i}} = \frac{-16\mathcal{A}^3 + 50\mathcal{A}^2 - 52\mathcal{A} + 27}{9\sqrt{n}(\mathcal{A} - 1)^2} \quad \text{where} \quad \mathcal{A} = \frac{d_i \lambda}{\sqrt{n}}. \quad (6.18)$$

6.4 Validation and results

To assess the proposed model's capability, we compared its predictions to our experimental results, which were specifically designed to demonstrate the negative impact of chemical and physical aging on the constitutive response and energy absorption of polymer matrix. The model was fitted for the following three cases using the 7 material parameters:

- The loading-unloading curve of the virgin specimen to investigate the effects of λ and λ_m .
- Two points of loading curves of 10 days chemically aged specimens at temperatures 60°C, and 80°C to study the effects of T , and t
- One points of loading curve of physically aged specimen at cycles $j = 200$ to study the effects of fatigue.

The least square error function was minimized using the Levenberg–Marquardt algorithm. Accordingly, Table 6.2 lists the so-obtained material parameters of the proposed model for the SBR. Besides, Figs. 6.9, and 6.10 show the prediction of the devised model against experimental results for various aging times, and the number of cycles for temperatures 60 and 80 °C, respectively. The devised model can predict the hardening response of material due to thermal aging as well as softening due to fatigue damage. Besides, it can also predict the behavior when both damage mechanisms are accumulated on top of each other. One should notice that the current terminology used to associate the damage to the alteration of chain density and chain length is based on

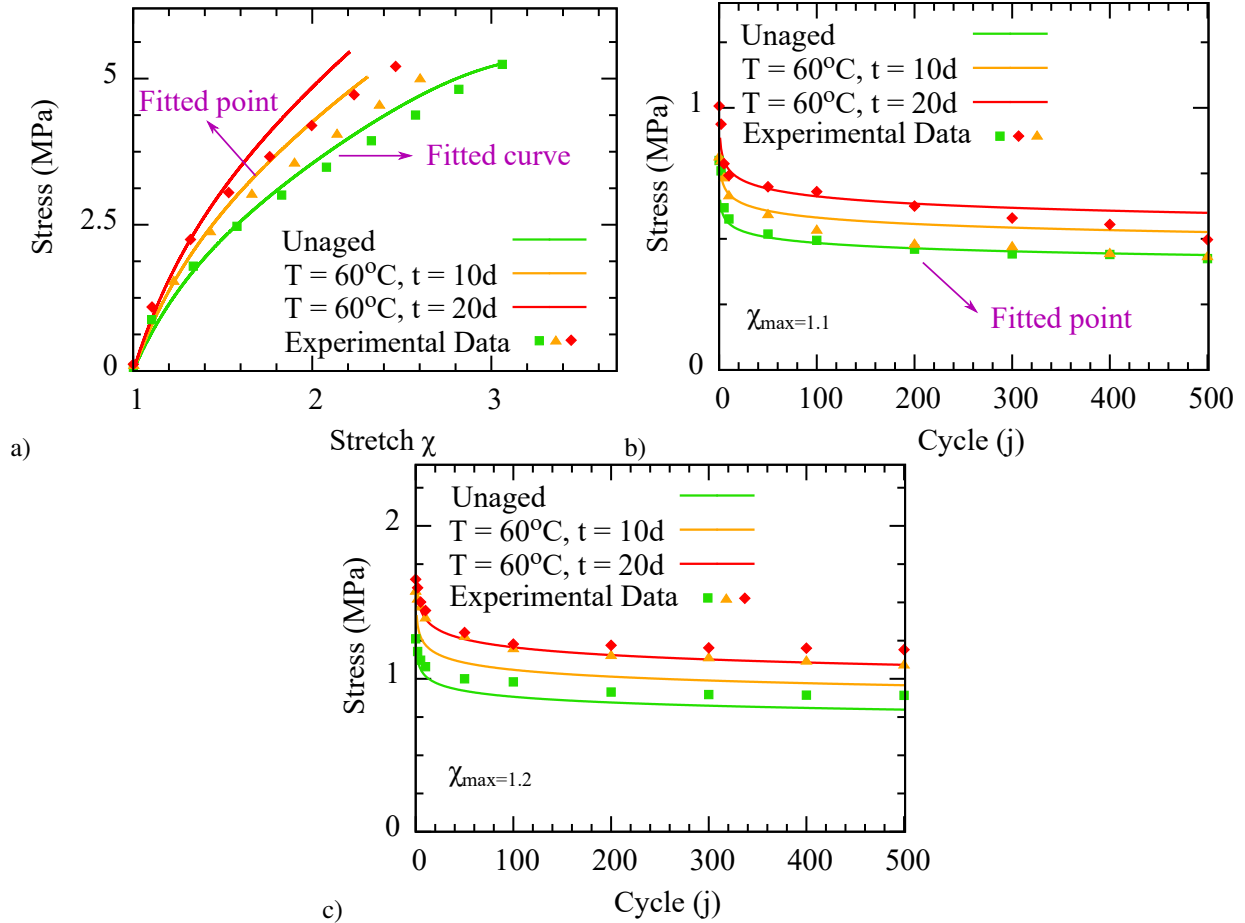


Figure 6.9: Validation of the model predictions against our experimental data for SBR in the unaged state, and during thermal aging for 10, and 20 days in the temperature 60°C in multiple conditions; (a) the constitutive response of samples including their corresponding failure points, (b) maximum stress versus the number of cycles with maximum stretch of $\chi_{max} = 1.1$, and (c) maximum stress as versus the number of cycles with a maximum stretch of $\chi_{max} = 1.2$.

a statistical representation of the matrix and has not been experimentally validated. In this study, the proposed evolution describing the alteration of the macro-molecular network through n and N are mainly derived based on our macro-scale observations of the mechanical behavior and our familiarity with the aging mechanisms.

To illustrate the performance and applicability of the derived model in modeling the mechanical behavior of polymers during concurrent exposure to thermal aging and fatigue, a numerical example is solved and presented here. The elasticity tensor, which is generated from the strain energy function mentioned in previous sections, is used to model the materials' nonlinear behavior.

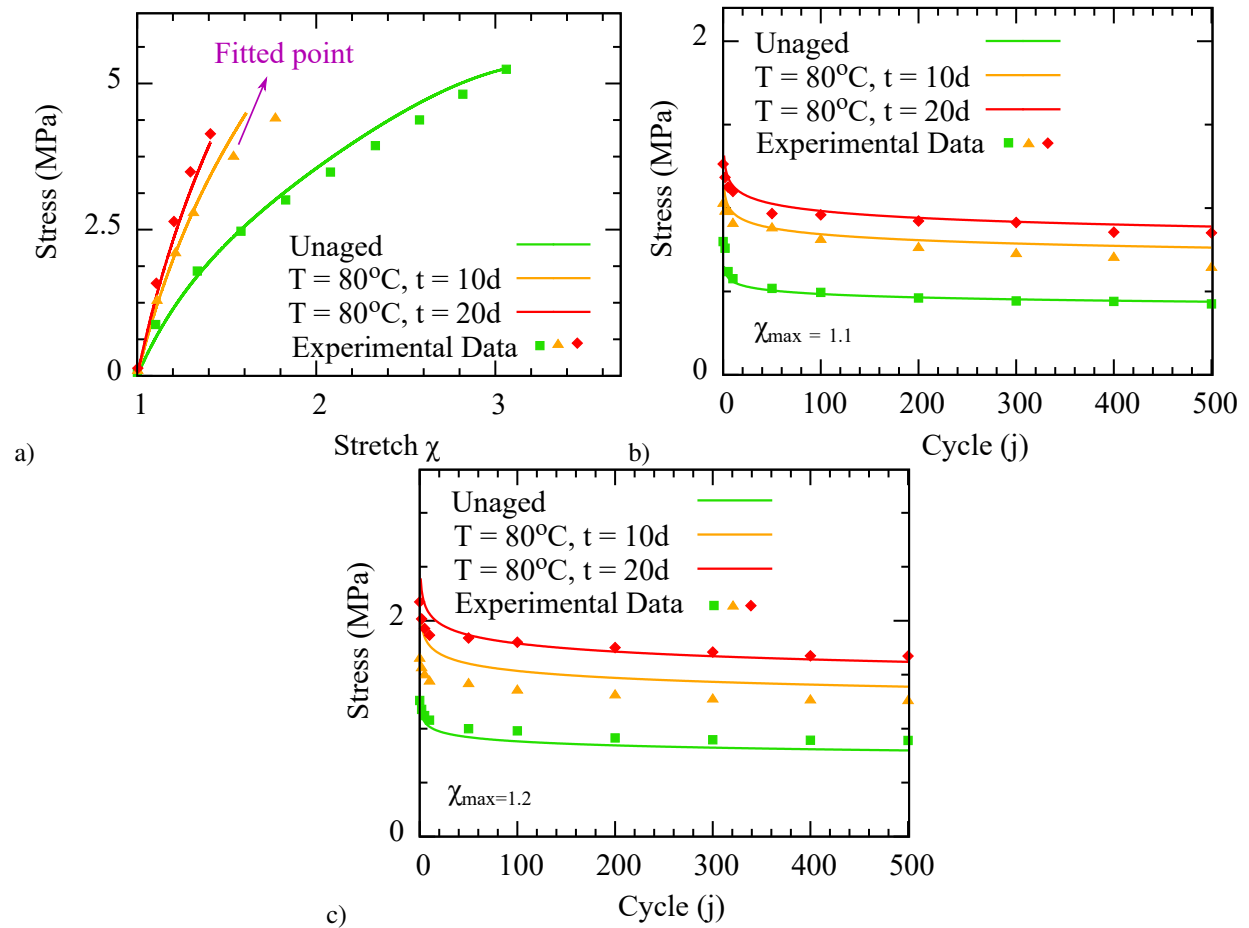


Figure 6.10: Validation of the model predictions against our experimental data for SBR in the unaged state, and during thermal aging for 10, and 20 days in the temperature 80°C in multiple conditions; (a) the constitutive response of samples including their corresponding failure points, (b) maximum stress versus the number of cycles with maximum stretch of $\chi_{\max} = 1.1$, and (c) maximum stress as versus the number of cycles with a maximum stretch of $\chi_{\max} = 1.2$.

Accordingly, the free edge of a perforated square plate with a length of 50 mm is subjected to a uni-axial deformation. Three evenly spaced holes with radii of 5, 6, and 8 mm are included on the plate (the detailed geometry is provided in Fig. 6.11a). Plane stress conditions are assumed, and quadratic elements with four Gauss points are used (see Fig. 6.11b). The right edge of the plate

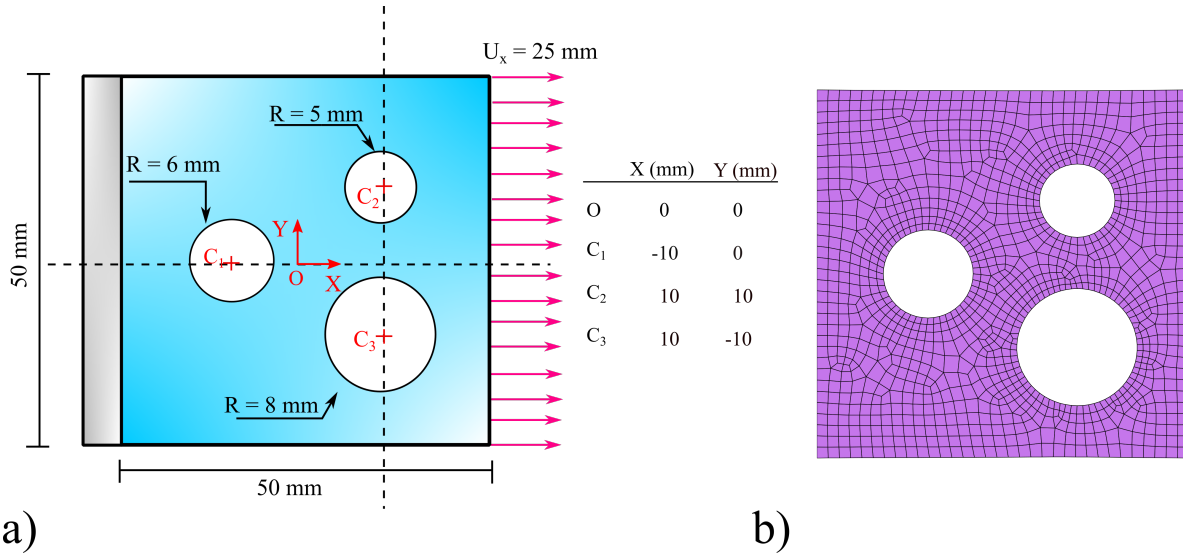


Figure 6.11: Finite element simulation of a perforated plate under uni-axial deformation: a) detailed geometry and boundary conditions; b) finite-element discretization.

is subjected to tensile deformation of 25 mm over 50 load stages, while the left edge remains stationary. The boundary value problem was solved with the different numbers of elements (i.e. $N_e = 292, 891, 1195, \text{ and } 1796$). As can be seen in Fig. 6.12, the the maximum von Mises stress of the boundary value problem converged at a reasonable limit. Accordingly, for optimal computational efficiency, we solved our boundary value problem with 1195 elements.

Figures 6.13, 6.14, and 6.15 illustrate the evolution of second-Piola Kirchhoff stress \mathbf{S} contours of the perforated plate under uni-axial deformation during thermal aging and fatigue using the suggested model. The results show that increasing the number of cycles reduces stress in the specimen while increasing the aging period makes the material stiffer. Accordingly, the largest value of S_{xx} occurs at the top and bottom margins of circles, particularly the bigger circle for the environmentally aged specimen. Similarly, the S_{xx} takes its minimum at the right and bottom edges of circles for the mechanically damaged sample.

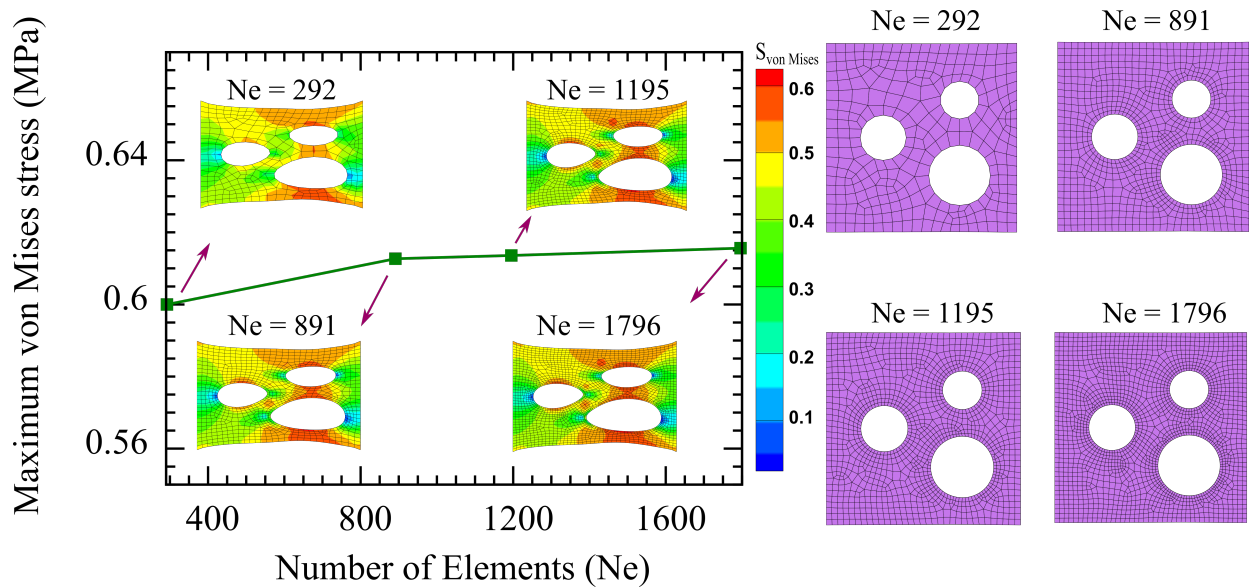


Figure 6.12: Number of elements versus the maximum von Mises stress of the boundary value problem.

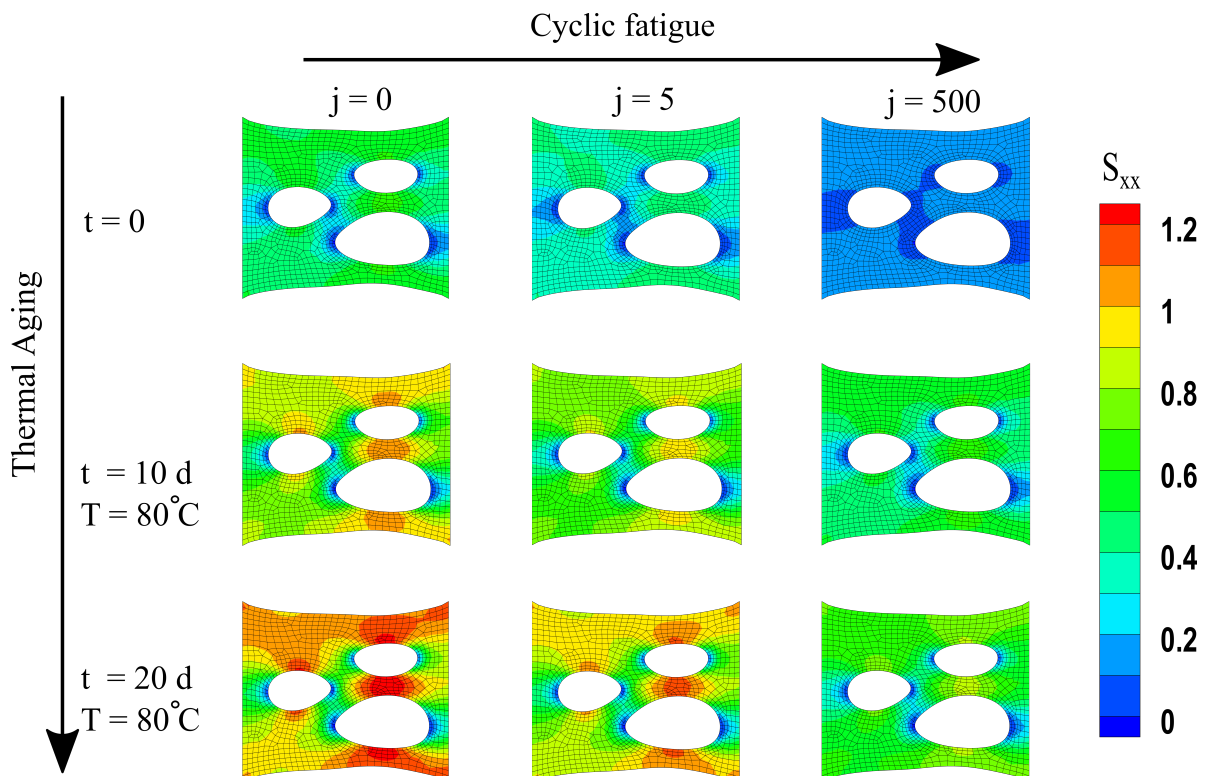


Figure 6.13: Evolution of the second-Piola Kirchhoff stress S_{xx} of the SBR through thermal aging and fatigue. As it can be seen, higher aging duration caused higher stress values due to the hardening effect of thermal aging while more number of cycles cause the stress softening.

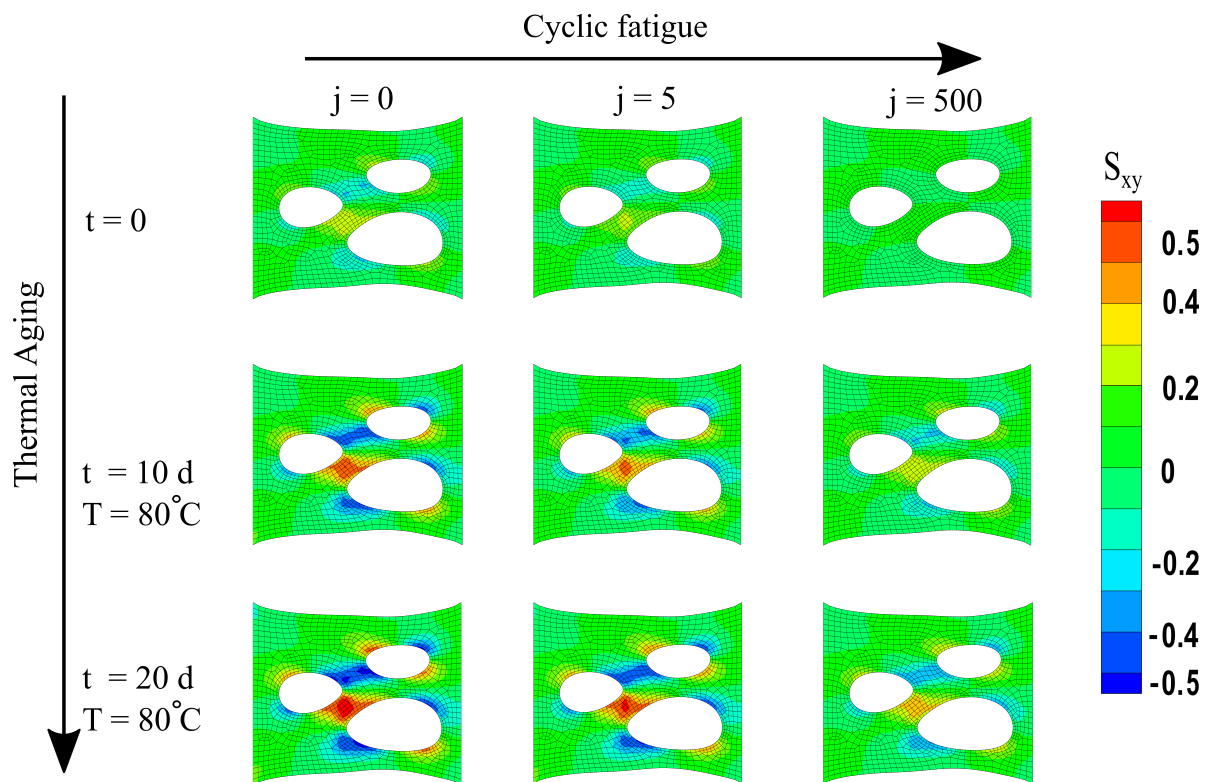


Figure 6.14: Evolution of the second-Piola Kirchhoff stress S_{xy} of the SBR through thermal aging and fatigue. As it can be seen, higher aging duration caused higher stress values due to the hardening effect of thermal aging while more number of cycles cause the stress softening.

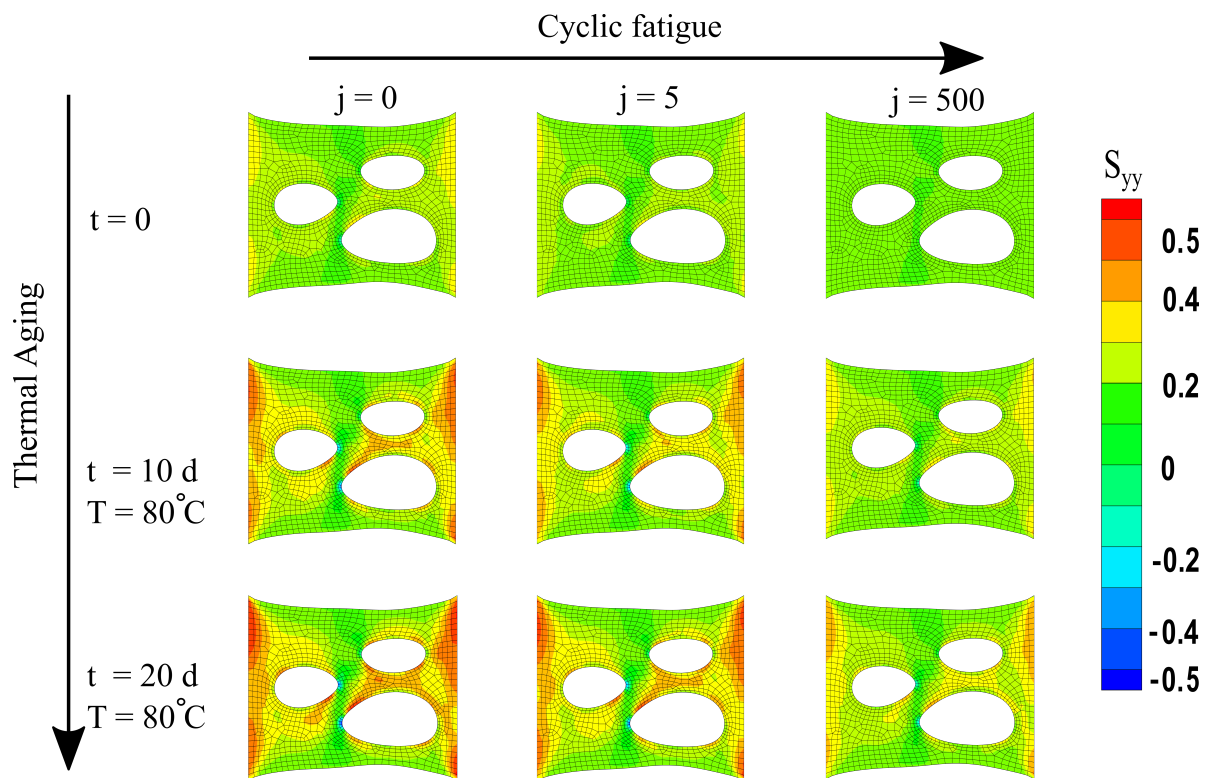


Figure 6.15: Evolution of the second-Piola Kirchhoff stress S_{yy} of the SBR through thermal aging and fatigue. As it can be seen, higher aging duration caused higher stress values due to the hardening effect of thermal aging while more number of cycles cause the stress softening.

6.5 Conclusion

In this paper, we proposed a micro-mechanical constitutive model based on the concepts of damage accumulation to describe the damage induced by temperature and low cycle fatigue on the constitutive response of cross-linked polymers. Each of those damage mechanisms is induced by mechanisms that have been extensively studied before but have not been modeled in parallel so far. We modeled each sub-mechanism through a linear kinetic equation which is then coupled into the modular network concept to allow calculation of synergies and parallel damage accumulation through multiple sources. This model could be regarded as an extension of our recent models [7, 11, 175]. Furthermore, the devised model is applied for FE simulation and the tangent modulus for large deformation regimes are expressed in terms of internal variables. A full set of experimental data was carried out to validate the model. With reasonable accuracy, the proposed model shows promising results. In addition, with meaningful parameters, the model is relatively simple.

CHAPTER 7

Summary and Future Works

The main goal of this research was to create a constitutive model for cross-linked polymers under various aging scenarios. Each section of the dissertation is briefly summarized in this chapter. An introduction to cross-linked polymers and their applications was presented in the first part of this dissertation.

7.1 General Remarks

- In chapter 3, effects of Hydrolytic aging on cross-linked polymer behavior were investigated. Following that, a comprehensive study of hydrolysis kinetics was presented. A micro-mechanical model to accurately predict the inelastic behavior of elastomers during aging has been presented later, combining the concepts of network evolution and the dual network hypothesis. Finally, the model's capabilities were tested by comparing model predictions to our experimental data.
- In chapter 4, a computationally efficient model is proposed to capture the loss of mechanical performance due to chemical aging that is formed as the competition of chain scission and cross-link formation/dissolution, such as thermo-oxidative aging or hydrolytic aging. Later on, the model is linearized for implementation into Finite Element (FE) simulations. The proposed model includes only six physically inspired material parameters. Thus, while it is computationally efficient, it shows good agreement with its own experimental data, which was performed on various ranges of accelerated aging temperatures and times.
- In chapter 5, a multi-physics model is proposed to predict the changes in the constitutive

behavior of cross-linked polymeric systems due to damages induced by deformation, oxidation, moisture, and temperature. Coupling the concept of network evolution, hydrolysis, and thermo-oxidation aging, we hypothesize that the synergized effects of deformation-induced damage, as well as different environmental factors such as humidity, temperature, and oxygen, can be taken into account through a generic model. Finally, the model is validated with respect to extensive sets of our experimental data. In view of its interoperability, precision, and deep insight it provides into the nature of the aging phenomenon, the model is a good choice for advanced implementation in FE applications.

- In chapter 6, a micro-mechanical constitutive model is presented to predict the concurrent effects of thermal aging and cyclic fatigue on the constitutive behavior of cross-linked polymers. The damage associated with each of those aging conditions is induced by mechanisms that have been extensively studied individually. Here, the main goal was to model the damage accumulated when those mechanisms work in parallel. Later on, the model is implemented into finite element simulations. For validation, the devised model is bench-marked against a comprehensive set of experimental data. The proposed model shows promising results with reasonable precision.

7.2 Future Research

Aging can be either the result of individual aging elements or due to combined synergized effects of the different environmental factors. Since these factors coexist in nature, natural aging is seen as a combined effect of all conditions together. Lately, solo environmental damage models have been of significant interest in the literary and research communities. However, there are still wide gaps in the modeling of coupled-aging phenomena since finding the mutual effect and correlation of each environmental element is challenging and needs a huge set of experimental observations. Accordingly, realizing the correlation of the mechanical and coupled-environmental elements (damage accumulation) is crucial for providing a realistic prediction of such materials' behavior.

BIBLIOGRAPHY

- [1] Lallit Anand and Sanjay Govindjee. *Continuum mechanics of solids*. Oxford University Press, 2020.
- [2] Gerhard A. Holzapfel. *Nonlinear Solid Mechanics: A Continuum Approach for Engineering*. John Wiley & Sons, 2005.
- [3] Scott W Case, Arit Das, Michael J Bortner, David A Dillard, and Christopher C White. Durability and accelerated characterization of adhesive bonds. In *Advances in Structural Adhesive Bonding*, pages 675–710. Elsevier, 2023.
- [4] Amir Bahrololoumi, Mamoon Shaafaey, Georges Ayoub, and Roozbeh Dargazany. A failure model for damage accumulation of cross-linked polymers during parallel exposure to thermal aging & fatigue. *International Journal of Non-Linear Mechanics*, 146:104142, 2022.
- [5] Rod Martin. *Ageing of composites*. Elsevier, 2008.
- [6] Amir Bahrololoumi, Mamoon Shaafaey, Georges Ayoub, and Roozbeh Dargazany. Thermal aging coupled with cyclic fatigue in cross-linked polymers: Constitutive modeling & implementation. *International Journal of Solids and Structures*, 252:111800, 2022.
- [7] Amir Bahrololoumi, Vahid Morovati, Mamoon Shaafaey, and Roozbeh Dargazany. A multi-physics approach on modeling of hygrothermal aging and its effects on constitutive behavior of cross-linked polymers. *Journal of the Mechanics and Physics of Solids*, page 104614, 2021.
- [8] Mamoon Shaafaey, Amir Bahrololoumi, Hamid Mohammadi, Sharif Alazhary, and Roozbeh Dargazany. Investigation of hygrothermal aging on the polyurethane-based (pub) adhesive: substantiating competition scenario between sub-aging thermo-oxidation and hydrolytic phenomena. *Journal of Polymer Research*, 28(12):1–25, 2021.
- [9] Amir Bahrololoumi, Vahid Morovati, Emad A Poshtan, and Roozbeh Dargazany. A multi-physics constitutive model to predict quasi-static behaviour: Hydrolytic aging in thin cross-linked polymers. *International Journal of Plasticity*, page 102676, 2020.
- [10] Wanru Miao, Amir Bahrololoumi, Shaafaey Mamoon, Mohammadi Hamid, Omid Nabinejad, and Roozbeh Dargazany. Effects of hydrolytic aging on constitutive behavior of silicone adhesives in saline and desalinated water. *Submitted to Polymer Degradation and Stability*, 2020.
- [11] Amir Bahrololoumi, Hamid Mohammadi, Vahid Morovati, and Roozbeh Dargazany. A physically-based model for thermo-oxidative and hydrolytic aging of elastomers. *International Journal of Mechanical Sciences*, 194:106193, 2021.
- [12] Hamid Mohammadi, Vahid Morovati, Emad Poshtan, and Roozbeh Dargazany. Understanding decay functions and their contribution in modeling of thermal-induced aging of cross-linked polymers. *Polymer Degradation and Stability*, page 109108, 2020.

- [13] Philip A Schweitzer et al. *Fundamentals of corrosion: mechanisms, causes, and preventative methods*. CRC press, 2009.
- [14] Ján Kruželák, Ivan Hudec, and Rastislav Dosoudil. Influence of thermo-oxidative and ozone ageing on the properties of elastomeric magnetic composites. *Polymer degradation and stability*, 97(6):921–928, 2012.
- [15] M. Gigliotti, M. Minervino, M.C. Lafarie-Frenot, and J.C. Grandidier. Effect of thermo-oxidation on the local mechanical behaviour of epoxy polymer materials for high temperature applications. *Mechanics of Materials*, 101:118 – 135, 2016.
- [16] R. Behnke and M. Kaliske. Numerical modeling of thermal ageing in steady state rolling tires. *International Journal of Non-Linear Mechanics*, 2018.
- [17] Roozbeh Dargazany, Vu Ngoc Khiêm, and Mikhail Itskov. A generalized network decomposition model for the quasi-static inelastic behavior of filled elastomers. *International Journal of Plasticity*, 63:94, 2015.
- [18] LR G Treloar. *The physics of rubber elasticity*. 1975.
- [19] B. D. Coleman and W. Noll. The thermodynamics of elastic materials with heat conduction and viscosity. *Archive for Rational Mechanics and Analysis*, 13:167, 1963.
- [20] B. Coleman and M. E. Gurtin. Thermodynamics with internal state variables. *The Journal of Chemical Physics*, 47:593, 1967.
- [21] Sima Kashi, Russell Varley, Mandy De Souza, Salwan Al-Assafi, Adriano Di Pietro, Christelle de Lavigne, and Bronwyn Fox. Mechanical, thermal, and morphological behavior of silicone rubber during accelerated aging. *Polymer-Plastics Technology and Engineering*, 2018.
- [22] Michael Johlitz. On the representation of ageing phenomena. *The Journal of Adhesion*, 88(7):620–648, 2012.
- [23] Tianying Chang, Xiansheng Zhang, and Hong-Liang Cui. Evolution of terahertz dielectric permittivity of rubber during thermo-oxidative aging. *Microwave and Optical Technology Letters*, 60, 12 2017.
- [24] Michael Johlitz, Nico Diercks, and Alexander Lion. Thermo-oxidative ageing of elastomers: A modelling approach based on a finite strain theory. *International Journal of Plasticity*, 63:138–151, 2014.
- [25] Chao Yu, Guozheng Kang, and Kaijuan Chen. A hygro-thermo-mechanical coupled cyclic constitutive model for polymers with considering glass transition. *International Journal of Plasticity*, 89:29–65, 2017.
- [26] André C Vieira, Rui M Guedes, and Volnei Tita. Damage-induced hydrolyses modelling of biodegradable polymers for tendons and ligaments repair. *Journal of biomechanics*, 48(12):3478–3485, 2015.

- [27] Amir Bahrololoumi and Roozbeh Dargazany. Hydrolytic aging in rubber-like materials: a micro-mechanical approach to modeling. In *American Society of Mechanical Engineers (ASME) 2019 International Mechanical Engineering Congress and Exposition*, 2019.
- [28] Marcos Lugo, Jason E Fountain, Justin M. Hughes, Jean-Luc Bouvard, and Mark F Horstemeyer. Microstructure-based fatigue modeling of an acrylonitrile butadiene styrene (abs) copolymer. *Journal of Applied Polymer Science*, 131(20), 2014.
- [29] Antoine Launay, Yann Marco, MH Maitournam, Ida Raoult, and Fabien Szymtka. Cyclic behavior of short glass fiber reinforced polyamide for fatigue life prediction of automotive components. *Procedia Engineering*, 2(1):901–910, 2010.
- [30] Amir K Shojaei and Pieter Volgers. Fatigue damage assessment of unfilled polymers including self-heating effects. *International Journal of Fatigue*, 100:367–376, 2017.
- [31] Wulff Possart and Markus Brede. *Adhesive Joints: Ageing and Durability of Epoxies and Polyurethanes*. John Wiley & Sons, 2019.
- [32] Mayank Sinha, Alborz Izadi, Rebecca Anthony, and Sara Roccabianca. A novel approach to finding mechanical properties of nanocrystal layers. *Nanoscale*, 11(15):7520–7526, 2019.
- [33] Kaspar Loeffel and Lallit Anand. A chemo-thermo-mechanically coupled theory for elastic–viscoplastic deformation, diffusion, and volumetric swelling due to a chemical reaction. *International Journal of Plasticity*, 27(9):1409–1431, 2011.
- [34] Marco Gigliotti and Jean-Claude Grandidier. Chemo-mechanics couplings in polymer matrix materials exposed to thermo-oxidative environments. *Comptes Rendus Mécanique*, 338(3):164–175, 2010.
- [35] Marco Gigliotti, Jean-Claude Grandidier, and Marie Christine Lafarie-Frenot. Assessment of chemo-mechanical couplings in polymer matrix materials exposed to thermo-oxidative environments at high temperatures and under tensile loadings. *Mechanics of Materials*, 43(8):431–443, 2011.
- [36] Michael Johlitz and Alexander Lion. Chemo-thermomechanical ageing of elastomers based on multiphase continuum mechanics. *Continuum Mechanics and Thermodynamics*, 25(5):605–624, 2013.
- [37] Alexander Lion and PHILIPP Höfer. On the phenomenological representation of curing phenomena in continuum mechanics. *Archives of Mechanics*, 59(1):59–89, 2007.
- [38] K Kannan and KR Rajagopal. A thermodynamical framework for chemically reacting systems. *Zeitschrift für angewandte Mathematik und Physik*, 62(2):331–363, 2011.
- [39] Hamid Mohammadi and Roozbeh Dargazany. A micro-mechanical approach to model thermal induced aging in elastomers. *International Journal of Plasticity*, 118:1–16, 2019.

- [40] H Mohammadi, A Bahrololoumi, Y Chen, and R Dargazany. A micro-mechanical model for constitutive behavior of elastomers during thermo-oxidative aging. In *Constitutive Models for Rubber XI: Proceedings of the 11th European Conference on Constitutive Models for Rubber (ECCMR 2019), June 25-27, 2019, Nantes, France*, page 542. CRC Press, 2019.
- [41] Prashant Saxena, Mokarram Hossain, and Paul Steinmann. A theory of finite deformation magneto-viscoelasticity. *International Journal of Solids and Structures*, 50(24):3886–3897, 2013.
- [42] Jianyou Zhou, Liying Jiang, and Roger E Khayat. A micro–macro constitutive model for finite-deformation viscoelasticity of elastomers with nonlinear viscosity. *Journal of the Mechanics and Physics of Solids*, 110:137–154, 2018.
- [43] GP Potirniche, A Pascu, N Shoemaker, PT Wang, MF Horstemeyer, D Stillman, and T-L Lin. A visco-hyperelastic model for the thermo-mechanical behavior of polymer fibers. *International Journal of Damage Mechanics*, 20(7):1002–1020, 2011.
- [44] Aref Ghaderi and Roozbeh Dargazany. A data-driven model to predict constitutive and failure behavior of elastomers considering the strain rate, temperature, and filler ratio. *Journal of Applied Mechanics*, 90(5):051010, 2023.
- [45] H Khajehsaeid, M Baghani, and R Naghdabadi. Finite strain numerical analysis of elastomeric bushings under multi-axial loadings: a compressible visco-hyperelastic approach. *International Journal of Mechanics and Materials in Design*, 9(4):385–399, 2013.
- [46] Aurelien Maurel-Pantel, Erwan Baquet, Jérôme Bikard, Jean-Luc Bouvard, and Noelle Bilon. A thermo-mechanical large deformation constitutive model for polymers based on material network description: Application to a semi-crystalline polyamide 66. *International Journal of Plasticity*, 67:102–126, 2015.
- [47] Babak Farrokh and Akhtar S Khan. A strain rate dependent yield criterion for isotropic polymers: low to high rates of loading. *European Journal of Mechanics-A/Solids*, 29(2):274–282, 2010.
- [48] Georges Ayoub, Fahmi Zaïri, Moussa Naït-Abdelaziz, Jean Michel Gloaguen, and G Kridli. A visco-hyperelastic damage model for cyclic stress-softening, hysteresis and permanent set in rubber using the network alteration theory. *International Journal of Plasticity*, 54:19–33, 2014.
- [49] Akhtar S Khan, Oscar Lopez-Pamies, and Rehan Kazmi. Thermo-mechanical large deformation response and constitutive modeling of viscoelastic polymers over a wide range of strain rates and temperatures. *International Journal of Plasticity*, 22(4):581–601, 2006.
- [50] Jingzhe Pan. *Modelling degradation of bioresorbable polymeric medical devices*. Elsevier, 2014.
- [51] Yanqun Yu, Zongyu Chang, Yaoguang Qi, and Dehua Feng. Research on new technology for offshore heavy oil thermal recovery with rod pumping. *Journal of Petroleum Exploration and Production Technology*, 8(3):947–955, 2018.

- [52] Leif Kari. Dynamic stiffness of chemically and physically ageing rubber vibration isolators in the audible frequency range. *Continuum Mechanics and Thermodynamics*, 29(5):1027–1046, 2017.
- [53] André C Vieira, Rui M Guedes, and Volnei Tita. Constitutive modeling of biodegradable polymers: Hydrolytic degradation and time-dependent behavior. *International Journal of Solids and Structures*, 51(5):1164–1174, 2014.
- [54] Quentin Breche, Grégory Chagnon, Guilherme Machado, Benjamin Nottelet, Xavier Garric, Edouard Girard, and Denis Favier. A non-linear viscoelastic model to describe the mechanical behavior’s evolution of biodegradable polymers during hydrolytic degradation. *Polymer degradation and stability*, 131:145–156, 2016.
- [55] Thorsten Pretsch, Ines Jakob, and Werner Müller. Hydrolytic degradation and functional stability of a segmented shape memory poly (ester urethane). *Polymer Degradation and Stability*, 94(1):61–73, 2009.
- [56] C Slater, C Davis, and M Strangwood. Compression set of thermoplastic polyurethane under different thermal–mechanical–moisture conditions. *Polymer degradation and stability*, 96(12):2139–2144, 2011.
- [57] DF Farrar and RK Gillson. Hydrolytic degradation of polyglyconate b: the relationship between degradation time, strength and molecular weight. *Biomaterials*, 23(18):3905–3912, 2002.
- [58] Emmanuel Richaud, Pierre Gilormini, Marie Coquillat, and Jacques Verdu. Crosslink density changes during the hydrolysis of tridimensional polyesters. *Macromolecular Theory and Simulations*, 23(5):320–330, 2014.
- [59] A.V. Tobolsky, I.B. Prettyman, and J.H. Dillon. Stress relaxation of natural and synthetic rubber stocks. *Journal of Applied Physics*, 15(4):380–395, 1944. cited By 87.
- [60] Sabine Cantournet, Rodrigue Desmorat, and Jacques Besson. Mullins effect and cyclic stress softening of filled elastomers by internal sliding and friction thermodynamics model. *International Journal of Solids and Structures*, 46(11-12):2255–2264, 2009.
- [61] Andri Andriyana, Mei Sze Loo, Grégory Chagnon, Erwan Verron, and Shiau Ying Ch’ng. Modeling the mullins effect in elastomers swollen by palm biodiesel. *International Journal of Engineering Science*, 95:1–22, 2015.
- [62] RW Ogden and DG Roxburgh. A pseudo–elastic model for the mullins effect in filled rubber. *Proceedings of the Royal Society of London. Series A: Mathematical, Physical and Engineering Sciences*, 455(1988):2861–2877, 1999.
- [63] Julie Diani, Bruno Fayolle, and Pierre Gilormini. A review on the mullins effect. *European Polymer Journal*, 45(3):601–612, 2009.

- [64] Morgan Deroiné, Antoine Le Duigou, Yves-Marie Corre, Pierre-Yves Le Gac, Peter Davies, Guy César, and Stéphane Bruzard. Accelerated ageing of polylactide in aqueous environments: comparative study between distilled water and seawater. *Polymer degradation and stability*, 108:319–329, 2014.
- [65] Hideto Tsuji and Yoshito Ikada. Properties and morphology of poly (l-lactide) 4. effects of structural parameters on long-term hydrolysis of poly (l-lactide) in phosphate-buffered solution. *Polymer Degradation and Stability*, 67(1):179–189, 2000.
- [66] Hideto Tsuji and Yoshito Ikada. Properties and morphology of poly (l-lactide). ii. hydrolysis in alkaline solution. *Journal of Polymer Science Part A: Polymer Chemistry*, 36(1):59–66, 1998.
- [67] Jacob Song Kiat Lim, Chee Lip Gan, and Xiao Matthew Hu. Unraveling the mechanistic origins of epoxy degradation in acids. *ACS Omega*, 4(6):10799–10808, 2019.
- [68] Suming Li. Hydrolytic degradation characteristics of aliphatic polyesters derived from lactic and glycolic acids. *Journal of Biomedical Materials Research: An Official Journal of The Society for Biomaterials, The Japanese Society for Biomaterials, and The Australian Society for Biomaterials*, 48(3):342–353, 1999.
- [69] SB Harogopad and TM Aminabhavi. Diffusion and sorption of organic liquids through polymer membranes. ii. neoprene, sbr, epdm, nbr, and natural rubber versus n-alkanes. *Journal of applied polymer science*, 42(8):2329–2336, 1991.
- [70] Suming Li. Hydrolytic degradation characteristics of aliphatic polyesters derived from lactic and glycolic acids. *Journal of Biomedical Materials Research: An Official Journal of The Society for Biomaterials, The Japanese Society for Biomaterials, and The Australian Society for Biomaterials*, 48(3):342–353, 1999.
- [71] Achim Gopferich and Robert Langer. Modeling of polymer erosion. *Macromolecules*, 26(16):4105–4112, 1993.
- [72] Man Wang, Xiaowei Xu, Jin Ji, Yang Yang, Jianfeng Shen, and Mingxin Ye. The hydrothermal aging process and mechanism of the novolac epoxy resin. *Composites Part B: Engineering*, 107:1–8, 2016.
- [73] Rong Long, H Jerry Qi, and Martin L Dunn. Modeling the mechanics of covalently adaptable polymer networks with temperature-dependent bond exchange reactions. *Soft Matter*, 9(15):4083–4096, 2013.
- [74] L.R.G. Treloar. *The Physics of Rubber Elasticity*. Oxford University Press, 2005.
- [75] C. Miehe, S. Göktepe, and F. Lulei. A micro-macro approach to rubber-like materials - part i: the non-affine micro-sphere model of rubber elasticity. *Journal of the Mechanics and Physics of Solids.*, 52:2617, 2004.

- [76] Reza Rastak and Christian Linder. A non-affine micro-macro approach to strain-crystallizing rubber-like materials. *Journal of the Mechanics and Physics of Solids*, 111:67–99, 2018.
- [77] Hüsni Dal, Christoph Zopf, and Michael Kaliske. Micro-sphere based viscoplastic constitutive model for uncured green rubber. *International Journal of Solids and Structures*, 132:201–217, 2018.
- [78] Roozbeh Dargazany and Mikhail Itskov. Constitutive modeling of the mullins effect and cyclic stress softening in filled elastomers. *Physical Review E*, 88(1):012602, 2013.
- [79] A.E. Ehret, M. Itskov, and H. Schmid. Numerical integration on the sphere and its effect on the material symmetry of constitutive equations—A comparative study. *International Journal for Numerical Methods in Engineering*, 81:189, 2010.
- [80] Erwan Verron. Questioning numerical integration methods for microsphere (and microplane) constitutive equations. *Mechanics of Materials*, 89:216–228, 2015.
- [81] Vahid Morovati and Roozbeh Dargazany. Micro-mechanical modeling of the stress softening in double-network hydrogels. *International Journal of Solids and Structures*, 164:1–11, 2019.
- [82] Vahid Morovati and Roozbeh Dargazany. Improved approximations of non-gaussian probability, force, and energy of a single polymer chain. *Physical Review E*, 99(5):052502, 2019.
- [83] Vahid Morovati, Hamid Mohammadi, and Roozbeh Dargazany. A generalized approach to improve approximation of inverse langevin function. In *ASME 2018 International Mechanical Engineering Congress and Exposition*, pages V009T12A029–V009T12A029. American Society of Mechanical Engineers, 2018.
- [84] Vahid Morovati, Hamid Mohammadi, and Roozbeh Dargazany. A generalized approach to generate optimized approximations of the inverse langevin function. *Mathematics and Mechanics of Solids*, 24(7):2047–2059, 2019.
- [85] R. Dargazany and M. Itskov. A network evolution model for the anisotropic Mullins effect in carbon black filled rubbers. *International Journal of Solids and Structures*, 46:2967, 2009.
- [86] R. Dargazany and M. Itskov. Constitutive modeling of the mullins effect and cyclic stress softening in filled elastomers. *Physical Review E*, 88(1):012602, 2013.
- [87] Vahid Morovati and Roozbeh Dargazany. Net v1. 0: A framework to simulate permanent damage in elastomers under quasi-static deformations. *SoftwareX*, 10:100229, 2019.
- [88] J.S. Bergström and M.C. Boyce. Mechanical behavior of particle filled elastomers. *Rubber Chem. Technol.*, 72:633, 1999.
- [89] R. Dargazany, V. N. Khiêm, U. Navrath, and M. Itskov. Network evolution model of anisotropic stress softening in filled rubber-like materials; parameter identification and finite element implementation. *Journal of Mechanics of Materials and Structures*, 7(8):861, 2013.

- [90] P-Y Le Gac, P Davies, and D Choqueuse. Evaluation of long term behaviour of polymers for offshore oil and gas applications. *Oil & Gas Science and Technology Revue d'IFP Energies nouvelles*, 70(2):279–289, 2015.
- [91] A Stevenson. On the durability of rubber/metal bonds in seawater. *International Journal of Adhesion and adhesives*, 5(2):81–91, 1985.
- [92] Guilherme Machado, Grégory Chagnon, and Denis Favier. Analysis of the isotropic models of the mullins effect based on filled silicone rubber experimental results. *Mechanics of Materials*, 42(9):841–851, 2010.
- [93] Yunlong Li, Quan Wang, and Shijie Wang. A review on enhancement of mechanical and tribological properties of polymer composites reinforced by carbon nanotubes and graphene sheet: molecular dynamics simulations. *Composites Part B: Engineering*, 160:348–361, 2019.
- [94] Alborz Izadi, Branton Toback, Mayank Sinha, Andrew Millar, Michael Bigelow, Sara Roccabianca, and Rebecca Anthony. Mechanical and optical properties of stretchable silicon nanocrystal/polydimethylsiloxane nanocomposites. *physica status solidi (a)*, 217(17):2000015, 2020.
- [95] Alborz Izadi, Mayank Sinha, Cameron Papson, Sara Roccabianca, and Rebecca Anthony. Mechanical behavior of sinc layers on pdms: effects of layer thickness, pdms modulus, and sinc surface functionality. *RSC Adv.*, 10:39087–39091, 2020.
- [96] Baohui Shi, Man Zhang, Shengkai Liu, Baozhong Sun, and Bohong Gu. Multi-scale ageing mechanisms of 3d four directional and five directional braided composites' impact fracture behaviors under thermo-oxidative environment. *International Journal of Mechanical Sciences*, 155:50–65, 2019.
- [97] Man Wang, Xiaowei Xu, Jin Ji, Yang Yang, Jianfeng Shen, and Mingxin Ye. The hydrothermal aging process and mechanism of the novolac epoxy resin. *Composites Part B: Engineering*, 107:1–8, 2016.
- [98] Lin Sang, Chuo Wang, Yingying Wang, and Wenbin Hou. Effects of hydrothermal aging on moisture absorption and property prediction of short carbon fiber reinforced polyamide 6 composites. *Composites Part B: Engineering*, 153:306–314, 2018.
- [99] Robert Bernstein, Dora K Derzon, and Kenneth T Gillen. Nylon 6.6 accelerated aging studies: thermal–oxidative degradation and its interaction with hydrolysis. *Polymer Degradation and Stability*, 88(3):480–488, 2005.
- [100] Bruno Musil, Michael Johlitz, and Alexander Lion. On the ageing behaviour of nbr: chemo-mechanical experiments, modelling and simulation of tension set. *Continuum Mechanics and Thermodynamics*, pages 1–17, 2018.
- [101] Adelina David, Jing Huang, Emmanuel Richaud, and Pierre Yves LE Gac. Impact of thermal oxidation on mechanical behaviour of polydicyclopentadiene: Case of non-diffusion limited oxidation. *Polymer Degradation and Stability*, page 109294, 2020.

- [102] Jing Huang, Pierre Yves LE Gac, and Emmanuel Richaud. Thermal oxidation of poly (dicyclopentadiene)-effect of phenolic and hindered amine stabilizers. *Polymer Degradation and Stability*, page 109267, 2020.
- [103] Rami Bouaziz, Komla Dela Ahose, Stéphane Lejeunes, Dominique Eyheramendy, and Franck Sosson. Characterization and modeling of filled rubber submitted to thermal aging. *International Journal of Solids and Structures*, 169:122–140, 2019.
- [104] Ricardo Baumhardt-Neto and Marco-A De Paoli. Mechanical degradation of polypropylene: effect of uv irradiation. *Polymer degradation and stability*, 40(1):59–64, 1993.
- [105] J-F Larché, P-O Bussière, and J-L Gardette. Photo-oxidation of acrylic-urethane thermoset networks. relating materials properties to changes of chemical structure. *Polymer degradation and stability*, 96(8):1438–1444, 2011.
- [106] Pierre-Olivier Bussiere, Agnes Rivaton, Sandrine Thérias, and Jean-Luc Gardette. Multi-scale investigation of the poly (n-vinylcarbazole) photoageing mechanism. *The Journal of Physical Chemistry B*, 116(2):802–812, 2012.
- [107] Mathew C Celina. Review of polymer oxidation and its relationship with materials performance and lifetime prediction. *Polymer Degradation and Stability*, 98(12):2419–2429, 2013.
- [108] Mat Celina, Kenneth T Gillen, and RA Assink. Accelerated aging and lifetime prediction: review of non-arrhenius behaviour due to two competing processes. *Polymer Degradation and stability*, 90(3):395–404, 2005.
- [109] L Steinke, U Veltin, M Flamm, A Lion, and M Celina. Numerical analysis of the heterogeneous ageing of rubber products. *Constitutive Models for Rubber*, 7:155–160, 2011.
- [110] Kenneth T Gillen, Robert Bernstein, and Mathew Celina. Non-arrhenius behavior for oxidative degradation of chlorosulfonated polyethylene materials. *Polymer degradation and stability*, 87(2):335–346, 2005.
- [111] M Celina, J Wise, DK Ottesen, KT Gillen, and RL Clough. Oxidation profiles of thermally aged nitrile rubber. *Polymer Degradation and Stability*, 60(2-3):493–504, 1998.
- [112] Kenneth T Gillen, Mathew Celina, Roger L Clough, and Jonathan Wise. Extrapolation of accelerated aging data-arrhenius or erroneous? *Trends in polymer science*, 8(5):250–257, 1997.
- [113] John A Shaw, Alan S Jones, and Alan S Wineman. Chemorheological response of elastomers at elevated temperatures: experiments and simulations. *Journal of the Mechanics and Physics of Solids*, 53(12):2758–2793, 2005.
- [114] N Rabanizada, F Lupberger, M Johlitz, and A Lion. Experimental investigation of the dynamic mechanical behaviour of chemically aged elastomers. *Archive of Applied Mechanics*, 85(8):1011–1023, 2015.

- [115] RJ Pazur, I Lopez-Carreón, CG Porter, A Herzig, and M Jöhlitz. Thermal ageing of peroxide-cured nbr, part i: Effect on bulk properties. In *Constitutive Models for Rubber XI: Proceedings of the 11th European Conference on Constitutive Models for Rubber (EC-CMR 2019), June 25-27, 2019, Nantes, France*, pages 581–586. CRC Press, 2019.
- [116] AC Vieira, JC Vieira, JM Ferra, FD Magalhães, RM Guedes, and AT Marques. Mechanical study of pla–pcl fibers during in vitro degradation. *Journal of the mechanical behavior of biomedical materials*, 4(3):451–460, 2011.
- [117] Vahid Morovati and Roozbeh Dargazany. Micro-mechanical modeling of the stress softening in double-network hydrogels. *International Journal of Solids and Structures*, 2019.
- [118] Aref Ghaderi, Vahid Morovati, and Roozbeh Dargazany. A physics-informed assembly of feed-forward neural network engines to predict inelasticity in cross-linked polymers. *arXiv preprint arXiv:2007.03067*, 2020.
- [119] Aref Ghaderi, Vahid Morovati, and Roozbeh Dargazany. A bayesian surrogate constitutive model to estimate failure probability of rubber-like materials. *arXiv preprint arXiv:2010.13241*, 2020.
- [120] T Ha-Anh and Toan Vu-Khanh. Prediction of mechanical properties of polychloroprene during thermo-oxidative aging. *Polymer testing*, 24(6):775–780, 2005.
- [121] A Lion and M Jöhlitz. On the representation of chemical ageing of rubber in continuum mechanics. *International Journal of Solids and Structures*, 49(10):1227–1240, 2012.
- [122] Michael Jöhlitz. On the representation of ageing phenomena. *The Journal of Adhesion*, 88(7):620–648, 2012.
- [123] Benedikt Dippel, Michael Jöhlitz, and Alexander Lion. Ageing of polymer bonds: a coupled chemomechanical modelling approach. *Continuum Mechanics and Thermodynamics*, 26(3):247–257, 2014.
- [124] Shabnam Konica and Trisha Sain. A thermodynamically consistent chemo-mechanically coupled large deformation model for polymer oxidation. *Journal of the Mechanics and Physics of Solids*, page 103858, 2019.
- [125] TRISHA SAIN and SHABNAM KONICA. A coupled thermo-chemo-mechanical model for high temperature oxidations in polymers and polymer composites. In *Proceedings of the American Society for Composites—Thirty-third Technical Conference*, 2018.
- [126] Yiyi Zhang, Yi Li, Hanbo Zheng, Mengzhao Zhu, Jiefeng Liu, Tao Yang, Chaohai Zhang, and Yang Li. Microscopic reaction mechanism of the production of methanol during the thermal aging of cellulosic insulating paper. *Cellulose*, 27(5):2455–2467, 2020.
- [127] Khashayar Mohammadi, Ashkan Ali Madadi, Zahra Bajalan, and Hossein Nejat Pishkenari. Analysis of mechanical and thermal properties of carbon and silicon nanomaterials using a coarse-grained molecular dynamics method. *International Journal of Mechanical Sciences*, page 106112, 2020.

- [128] C Schlomka, J Ihlemann, and C Naumann. Simulation of oxidative aging processes in elastomer components using a dynamic network model. In *Constitutive Models for Rubber X*, pages 77–82. CRC Press, 2017.
- [129] C Naumann and J Ihlemann. A dynamic network model to simulate chemical aging processes in elastomers. *Constitutive Models for Rubber IX*, 9:39, 2015.
- [130] Darcy Beurle, Markus André, Udo Nackenhorst, and Rodrigue Desmorat. Micromechanically motivated model for oxidation ageing of elastomers. In *Virtual Design and Validation*, pages 271–290. Springer, 2020.
- [131] Hamid Mohammadi and Roozbeh Dargazany. Micro-mechanical model for thermo-oxidative aging of elastomers. In *ASME 2018 International Mechanical Engineering Congress and Exposition*, pages V009T12A028–V009T12A028. American Society of Mechanical Engineers, 2018.
- [132] Amir Bahrololumi and Roozbeh Dargazany. A micro-mechanical approach to model hydrolytic aging in adhesives. In *American Society of Mechanical Engineers (ASME) 2019 International Mechanical Engineering Congress and Exposition*, 2019.
- [133] Hamid Mohammadi and Roozbeh Dargazany. A micro-mechanical approach to model thermal induced aging in elastomers. *International Journal of Plasticity*, 118:1–16, 2019.
- [134] Mariacristina Gagliardi, Pietro Lenarda, and Marco Paggi. A reaction-diffusion formulation to simulate eva polymer degradation in environmental and accelerated ageing conditions. *Solar Energy Materials and Solar Cells*, 164:93–106, 2017.
- [135] Pellegrino Musto, Giuseppe Ragosta, Mario Abbate, and Gennaro Scarinzi. Photo-oxidation of high performance epoxy networks: correlation between the molecular mechanisms of degradation and the viscoelastic and mechanical response. *Macromolecules*, 41(15):5729–5743, 2008.
- [136] Yoichi Kodera and Benjamin J McCoy. Distribution kinetics of radical mechanisms: reversible polymer decomposition. *AIChE journal*, 43(12):3205–3214, 1997.
- [137] Gottfried W Ehrenstein and Sonja Pongratz. *Beständigkeit von Kunststoffen*. Hanser München, 2007.
- [138] Jacques Verdu. *Oxydative ageing of polymers*. John Wiley & Sons, 2012.
- [139] Hesam Khajehsaeid. Mullins thresholds in context of the network alteration theories. *International Journal of Mechanical Sciences*, 123:43–53, 2017.
- [140] Yoshihiro Tomita, Keisuke Azuma, and Masato Naito. Computational evaluation of strain-rate-dependent deformation behavior of rubber and carbon-black-filled rubber under monotonic and cyclic straining. *International Journal of Mechanical Sciences*, 50(5):856–868, 2008.

- [141] Yoshihiro Tomita, Wei Lu, Masato Naito, and Yasuhiro Furutani. Numerical evaluation of micro-to macroscopic mechanical behavior of carbon-black-filled rubber. *International Journal of Mechanical Sciences*, 48(2):108–116, 2006.
- [142] Vahid Morovati and Roozbeh Dargazany. Improved non-gaussian statistical theory of polymer physics for short chains. *Physical Review E*, 2019.
- [143] G. Marckmann, E. Verron, L. Gornet, G. Chagnon, P. Charrier, and P. Fort. A theory of network alteration for the Mullins effect. *Journal of the Mechanics and Physics of Solids.*, 50:2011, 2002.
- [144] AR Khoei, A Rezaei Sameti, and Y Nikravesh Kazerooni. A continuum-atomistic multi-scale technique for nonlinear behavior of nano-materials. *International Journal of Mechanical Sciences*, 148:191–208, 2018.
- [145] Jason Mulderrig, Bin Li, and Nikolaos Bouklas. Affine and non-affine microsphere models for chain scission in polydisperse elastomer networks. *Mechanics of Materials*, 160:103857, 2021.
- [146] Shabnam Konica and Trisha Sain. A reaction-driven evolving network theory coupled with phase-field fracture to model polymer oxidative aging. *Journal of the Mechanics and Physics of Solids*, 150:104347, 2021.
- [147] Maha Zaghoudi, Anja Kömmling, Matthias Jaunich, and Dietmar Wolff. Erroneous or arrhenius: A degradation rate-based model for epdm during homogeneous ageing. *Polymers*, 12(9):2152, 2020.
- [148] Shabnam Konica and Trisha Sain. A homogenized large deformation constitutive model for high temperature oxidation in fiber-reinforced polymer composites. *Mechanics of Materials*, 160:103994, 2021.
- [149] Amina Dinari, Fahmi Zaïri, Makram Chaabane, Jewan Ismail, and Tarek Benameur. Thermo-oxidative stress relaxation in carbon-filled sbr. *Plastics, Rubber and Composites*, pages 1–16, 2021.
- [150] Makram Chaabane, Ning Ding, and Fahmi Zaïri. An approach to assess the thermal aging effects on the coupling between inelasticity and network alteration in filled rubbers. *International Journal of Non-Linear Mechanics*, page 103783, 2021.
- [151] Zisheng Liao, Mokarram Hossain, Xiaohu Yao, Markus Mehnert, and Paul Steinmann. On thermo-viscoelastic experimental characterization and numerical modelling of vhb polymer. *International Journal of Non-Linear Mechanics*, 118:103263, 2020.
- [152] Qiang Guo and Fahmi Zaïri. A physically-based thermo-mechanical model for stretch-induced crystallizable rubbers: Crystallization thermodynamics and chain-network crystallization anisotropy. *International Journal of Plasticity*, 131:102724, 2020.
- [153] Qiang Guo, Fahmi Zaïri, and Xinglin Guo. Thermodynamics and mechanics of stretch-induced crystallization in rubbers. *Physical Review E*, 97(5):052501, 2018.

- [154] Zeang Zhao, Dong Wu, Ming Lei, Qiang Zhang, Panding Wang, and Hongshuai Lei. Mechanical behaviors and the equivalent network model of self-similar multinet network elastomers. *International Journal of Solids and Structures*, page 111135, 2021.
- [155] Mahrez Saadedine, Fahmi Zaïri, Nourdine Ouali, Abderrahman Tamoud, and Amar Mesbah. A micromechanics-based model for visco-super-elastic hydrogel-based nanocomposites. *International Journal of Plasticity*, page 103042, 2021.
- [156] Mariusz Pyrz and Fahmi Zairi. Identification of viscoplastic parameters of phenomenological constitutive equations for polymers by deterministic and evolutionary approach. *Modelling and Simulation in Materials Science and Engineering*, 15(2):85, 2007.
- [157] Qiang Guo and Fahmi Zaïri. A micromechanics-based model for deformation-induced damage and failure in elastomeric media. *International Journal of Plasticity*, page 102976, 2021.
- [158] M Ben Hassine, Moussa Naït-Abdelaziz, Fahmi Zaïri, Xavier Colin, C Tourcher, and Gregory Marque. Time to failure prediction in rubber components subjected to thermal ageing: A combined approach based upon the intrinsic defect concept and the fracture mechanics. *Mechanics of Materials*, 79:15–24, 2014.
- [159] Yongqiang Du, Jian Zheng, and Guibo Yu. Influence of thermally-accelerated aging on the dynamic mechanical properties of htpb coating and crosslinking density-modified model for the payne effect. *Polymers*, 12(2):403, 2020.
- [160] Fang Xie, Liwu Liu, Xiaobo Gong, Longnan Huang, Jinsong Leng, and Yanju Liu. Effects of accelerated aging on thermal, mechanical and shape memory properties of cyanate-based shape memory polymer: I vacuum ultraviolet radiation. *Polymer Degradation and Stability*, 138:91–97, 2017.
- [161] Alok Ranjan Verma and B Subba Reddy. Accelerated aging studies of silicon-rubber based polymeric insulators used for hv transmission lines. *Polymer Testing*, 62:124–131, 2017.
- [162] Ana P Cysne Barbosa, Ana Paula P Fulco, Erick SS Guerra, Francisco K Arakaki, Márcio Tosatto, Maria Carolina B Costa, and José Daniel D Melo. Accelerated aging effects on carbon fiber/epoxy composites. *Composites Part B: Engineering*, 110:298–306, 2017.
- [163] Maha Zaghoudi, Anja Kömmling, Matthias Jaunich, and Dietmar Wolff. Erroneous or arrhenius: A degradation rate-based model for epdm during homogeneous ageing. *Polymers*, 12(9):2152, 2020.
- [164] A Simar, M Gigliotti, JC Grandidier, and I Ammar-Khodja. Evidence of thermo-oxidation phenomena occurring during hygrothermal aging of thermosetting resins for rtm composite applications. *Composites Part A: Applied Science and Manufacturing*, 66:175–182, 2014.
- [165] Adam Quintana and Mathew C Celina. Overview of dlo modeling and approaches to predict heterogeneous oxidative polymer degradation. *Polymer Degradation and Stability*, 149:173–191, 2018.

- [166] Erik Linde, Fritjof Nilsson, Matija Barrett, Mikael S Hedenqvist, and Mathew C Celina. Time- and feedback-dependent dlo phenomena in oxidative polymer aging. *Polymer Degradation and Stability*, 189:109598, 2021.
- [167] Pei Ni and Ronald W Thring. Synthesis of polyurethanes from solvolysis lignin using a polymerization catalyst: mechanical and thermal properties. *International Journal of Polymeric Materials*, 52(8):685–707, 2003.
- [168] P.J. Flory and J.R. Rehner. Statistical mechanics of cross-linked polymer networks i. rubberlike elasticity. *Journal of Chemical Physics*, 11:512, 1943.
- [169] Morgan Deroiné, Antoine Le Duigou, Yves-Marie Corre, Pierre-Yves Le Gac, Peter Davies, Guy César, and Stéphane Bruzaud. Accelerated ageing of polylactide in aqueous environments: Comparative study between distilled water and seawater. *Polymer degradation and stability*, 108:319–329, 2014.
- [170] Morgan Deroiné, Antoine Le Duigou, Yves-Marie Corre, Pierre-Yves Le Gac, Peter Davies, Guy César, and Stéphane Bruzaud. Seawater accelerated ageing of poly (3-hydroxybutyrate-co-3-hydroxyvalerate). *Polymer degradation and stability*, 105:237–247, 2014.
- [171] Hanen Mahjoubi, Fahmi Zaïri, and Zoubeir Tourki. A micro-macro constitutive model for strain-induced molecular ordering in biopolymers: application to polylactide over a wide range of temperatures. *International Journal of Plasticity*, 123:38–55, 2019.
- [172] Reza Rastak and Christian Linder. A non-affine micro-macro approach to strain-crystallizing rubber-like materials. *Journal of the Mechanics and Physics of Solids*, 111:67–99, 2018.
- [173] Benjamin C Marchi and Ellen M Arruda. Generalized error-minimizing, rational inverse langevin approximations. *Mathematics and Mechanics of Solids*, 0(0):1081286517754131, 2018.
- [174] Vu Ngoc Khiêm and Mikhail Itskov. Analytical network-averaging of the tube model:: Rubber elasticity. *Journal of the Mechanics and Physics of Solids*, 95:254–269, 2016.
- [175] Vahid Morovati, Amir Bahrololoumi, and Roozbeh Dargazany. Fatigue-induced stress-softening in cross-linked multi-network elastomers: Effect of damage accumulation. *International Journal of Plasticity*, 142:102993, 2021.
- [176] Michael R Buche and Meredith N Silberstein. Chain breaking in the statistical mechanical constitutive theory of polymer networks. *Journal of the Mechanics and Physics of Solids*, 156:104593, 2021.
- [177] Aref Ghaderi, Vahid Morovati, and Roozbeh Dargazany. A bayesian surrogate constitutive model to estimate failure probability of elastomers. *Mechanics of Materials*, 162:104044, 2021.

- [178] Ieuan Collins, Mokarram Hossain, Wulf Dettmer, and Ian Masters. Flexible membrane structures for wave energy harvesting: A review of the developments, materials and computational modelling approaches. *Renewable and Sustainable Energy Reviews*, 151:111478, 2021.
- [179] Chennakesava Kadapa, Zhanfeng Li, Mokarram Hossain, and Jiong Wang. On the advantages of mixed formulation and higher-order elements for computational morphoelasticity. *Journal of the Mechanics and Physics of Solids*, 148:104289, 2021.
- [180] Bruno Musil, Michael Johlitz, and Alexander Lion. On the ageing behaviour of nbr: chemo-mechanical experiments, modelling and simulation of tension set. *Continuum Mechanics and Thermodynamics*, 32(2):369–385, 2020.
- [181] Moussa Nait Abdelaziz, Georges Ayoub, Xavier Colin, Mouna Benhassine, and M Mouwakeh. New developments in fracture of rubbers: Predictive tools and influence of thermal aging. *International Journal of Solids and Structures*, 165:127–136, 2019.
- [182] Mariaenrica Frigione and Alvaro Rodríguez-Prieto. Can accelerated aging procedures predict the long term behavior of polymers exposed to different environments? *Polymers*, 13(16):2688, 2021.
- [183] Makram Chaabane, Ning Ding, and Fahmi Zaïri. An approach to assess the thermal aging effects on the coupling between inelasticity and network alteration in filled rubbers. *International Journal of Non-Linear Mechanics*, 136:103783, 2021.
- [184] Narueporn Payungwong, Surakit Tuampoemsab, Porntip Rojruthai, and Jitladda Sakdapanich. The role of model fatty acid and protein on thermal aging and ozone resistance of peroxide vulcanized natural rubber. *Journal of Rubber Research*, pages 1–11, 2021.
- [185] Réda Kadri, M Nait Abdelaziz, Bruno Fayolle, M Ben Hassine, and Jean-François Witz. A unified mechanical based approach to fracture properties estimates of rubbers subjected to aging. *International Journal of Solids and Structures*, 234:111305, 2022.
- [186] Rami Bouaziz, Laurianne Truffault, Rouslan Borisov, Cristian Ovalle, Lucien Laiarindrasana, Guillaume Miquelard-Garnier, and Bruno Fayolle. Elastic properties of polychloroprene rubbers in tension and compression during ageing. *Polymers*, 12(10):2354, 2020.
- [187] Maryam Shakiba and Aimane Najmeddine. Physics-based constitutive equation for thermo-chemical aging in elastomers based on crosslink density evolution. *arXiv preprint arXiv:2104.09001*, 2021.
- [188] Camille Loyer, Gilles Regnier, V Duval, and Emmanuel Richaud. Multiscale study of poly (butylene terephthalate) hydrolysis. *Polymer Degradation and Stability*, 192:109690, 2021.
- [189] Aref Ghaderi, Vahid Morovati, Yang Chen, and Roozbeh Dargazany. A physics-informed multi-agents model to predict thermo-oxidative/hydrolytic aging of elastomers. *International Journal of Mechanical Sciences*, page 107236, 2022.

- [190] Aimane Najmeddine, Zhen Xu, Guoliang Liu, Alan R Esker, and Maryam Shakiba. Physics-based constitutive modeling of photo-oxidative aging in semi-crystalline polymers based on chemical characterization techniques. *arXiv preprint arXiv:2108.07143*, 2021.
- [191] Hamid Mohammadi, Vahid Morovati, Abd-Elrahman Korayem, Emad Poshtan, and Roozbeh Dargazany. Constitutive modeling of elastomers during photo-and thermo-oxidative aging. *Polymer Degradation and Stability*, 191:109663, 2021.
- [192] Naima Rezig, Tassadit Bellahcene, Méziane Aberkane, and Moussa Nait Abdelaziz. Thermo-oxidative ageing of a sbr rubber: effects on mechanical and chemical properties. *Journal of Polymer Research*, 27(11):1–13, 2020.
- [193] Benedikt Dippel, Michael Johlitz, and Alexander Lion. Ageing of polymer bonds: a coupled chemomechanical modelling approach. *Continuum Mechanics and Thermodynamics*, 26(3):247–257, 2014.
- [194] Hamza Lamnii, M Nait Abdelaziz, Georges Ayoub, Xavier Colin, and U Maschke. Experimental investigation and modeling attempt on the effects of ultraviolet aging on the fatigue behavior of an ldpe semi-crystalline polymer. *International Journal of Fatigue*, 142:105952, 2021.
- [195] Wenbo Luo, Youjian Huang, Boyuan Yin, Xia Jiang, and Xiaoling Hu. Fatigue life assessment of filled rubber by hysteresis induced self-heating temperature. *Polymers*, 12(4):846, 2020.
- [196] Mahdi Ghazavi, Seyed Farhad Abdollahi, and M Emin Kutay. Implementation of nchrp 9-44a fatigue endurance limit prediction model in mechanistic-empirical asphalt pavement analysis web application. *Transportation Research Record*, page 03611981221076114, 2022.
- [197] Zhongtong Wang, Jingda Tang, Ruobing Bai, Wenlei Zhang, Tongda Lian, Tongqing Lu, and Tiejun Wang. A phenomenological model for shakedown of tough hydrogels under cyclic loads. *Journal of Applied Mechanics*, 85(9), 2018.
- [198] A Mousa, US Ishiaku, and ZA Mohd Ishak. Thermo-oxidative aging and fatigue behavior of dynamically vulcanized pvc/enr thermoplastic elastomers. *International Journal of Polymeric Materials*, 51(11):967–980, 2002.
- [199] Weifeng Chen, Fei Xue, Dunji Yu, Weiwei Yu, Xu Chen, et al. Effect of thermal aging on the low cycle fatigue behavior of z3cn20. 09m cast duplex stainless steel. *Materials Science and Engineering: A*, 646:263–271, 2015.
- [200] Jian Zhang, Valerian Hirschberg, and Denis Rodrigue. Mechanical fatigue of biodegradable polymers: A study on polylactic acid (pla), polybutylene succinate (pbs) and polybutylene adipate terephthalate (pbat). *International Journal of Fatigue*, 159:106798, 2022.
- [201] PYDI Hariprasadarao, H Ravisankar, and V CHITTARANJAN Das. Effect of thermal aging on mechanical properties and fatigue behavior of pp/hdpe thermoplastic polymer nanoclay composites. *Int. J. Mech. Prod. Eng. Res. Dev*, 8:349–358, 2018.

- [202] Amélie Malpot, Fabienne Touchard, and Sébastien Bergamo. Influence of moisture on the fatigue behaviour of a woven thermoplastic composite used for automotive application. *Materials & Design*, 98:12–19, 2016.
- [203] Hsoun-Wei Chou, Jong-Shin Huang, and Shih-Ting Lin. Effects of thermal aging on fatigue of carbon black–reinforced epdm rubber. *Journal of applied polymer science*, 103(2):1244–1251, 2007.
- [204] Berkan Tan and Erol Feyzullohoğlu. The investigation of effects of environmental conditions on fatigue strength and spring stiffness of rubber materials. *Journal of Elastomers & Plastics*, 53(6):632–652, 2021.
- [205] Abbas Tcharkhtchi, Sedigheh Farzaneh, Sofiane Abdallah-Elhirsiti, Bardia Esmaeillou, Fabien Nony, and A Baron. Thermal aging effect on mechanical properties of polyurethane. *International Journal of Polymer Analysis and Characterization*, 19(7):571–584, 2014.
- [206] Byungwoo Moon, Keekeun Kim, Keontae Park, Soo Park, and Chang-Sung Seok. Fatigue life prediction of tire sidewall using modified arrhenius equation. *Mechanics of Materials*, 147:103405, 2020.
- [207] Christoph Neuhaus, Alexander Lion, Michael Johlitz, Paul Heuler, Matthias Barkhoff, and Frank Duisen. Fatigue behaviour of an elastomer under consideration of ageing effects. *International Journal of Fatigue*, 104:72–80, 2017.
- [208] Alexandre Jouan and Andrei Constantinescu. A modified dissipated energy fatigue criterion to consider the thermo-oxidative ageing of electrically conductive silicone adhesive joints. *International Journal of Fatigue*, 116:68–79, 2018.
- [209] Xiaolei Wang, Kun Yang, and Ping Zhang. Evaluation of the aging coefficient and the aging lifetime of carbon black-filled styrene-isoprene-butadiene rubber after thermal-oxidative aging. *Composites Science and Technology*, page 109258, 2022.
- [210] Jieying Zhi, Qinglin Wang, Mengjie Zhang, Zhenze Zhou, Anna Liu, and Yuxi Jia. Coupled analysis on hyper-viscoelastic mechanical behavior and macromolecular network alteration of rubber during thermo-oxidative aging process. *Polymer*, 171:15–24, 2019.
- [211] Maha Zaghoudi, Anja Kömmling, Matthias Jaunich, and Dietmar Wolff. Scission, cross-linking, and physical relaxation during thermal degradation of elastomers. *Polymers*, 11(8):1280, 2019.
- [212] Tesfaldet Mengistu and Richard J Pazur. The thermal oxidation of hydrogenated acrylonitrile-co-butadiene rubber from ambient to 150° c. *Polymer Degradation and Stability*, 188:109574, 2021.
- [213] Zeng Zhang, Hui Li, Haiyue Zhou, Liying Zhao, Shikun Li, Hongzhen Wang, Zenglin Wang, and Zaifeng Li. Modification and improvement of aging resistance for hnbr/graphite composites. *Journal of Macromolecular Science, Part A*, pages 1–10, 2022.

- [214] Jannik Voges and Daniel Juhre. A phase field model for thermo-oxidative aging in cracked polymers. *PAMM*, 19(1):e201900384, 2019.
- [215] Mathew Celina, Erik Linde, Douglas Brunson, Adam Quintana, and Nicholas Giron. Overview of accelerated aging and polymer degradation kinetics for combined radiation-thermal environments. *Polymer Degradation and Stability*, 166:353–378, 2019.
- [216] G. Ayoub, F. Zaïri, M. Naït-Abdelaziz, and J.M. Gloaguen. Modeling the low-cycle fatigue behavior of visco-hyperelastic elastomeric materials using a new network alteration theory: Application to styrene-butadiene rubber. *Journal of the Mechanics and Physics of Solids*, 59(2):473–495, 2011.
- [217] Weitao Lou, Chaoyang Xie, and Xuefei Guan. Thermal-aging constitutive model for a silicone rubber foam under compression. *Polymer Degradation and Stability*, page 109873, 2022.
- [218] AF Blanchard and D Parkinson. Breakage of carbon-rubber networks by applied stress. *Rubber Chemistry and Technology*, 25(4):808–842, 1952.
- [219] Rubber Houwink. Slipping of molecules during the deformation of reinforced rubber. *Rubber Chemistry and Technology*, 29(3):888–893, 1956.
- [220] David E Hanson, Marilyn Hawley, Robert Houlton, Kiran Chitanvis, Philip Rae, E Bruce Orler, and Debra A Wroblewski. Stress softening experiments in silica-filled polydimethylsiloxane provide insight into a mechanism for the mullins effect. *Polymer*, 46(24):10989–10995, 2005.
- [221] G Kraus, CW Childers, and KW Rollmann. Stress softening in carbon black-reinforced vulcanizates. strain rate and temperature effects. *Journal of Applied Polymer Science*, 10(2):229–244, 1966.
- [222] M.F. Beatty. An average-stretch full-network model for rubber elasticity. *Journal of Elasticity*, 70:65, 2003.
- [223] Georges Ayoub, Fahmi Zaïri, Moussa Naït-Abdelaziz, Jean-Michel Gloaguen, and G Kridli. A visco-hyperelastic damage model for cyclic stress-softening, hysteresis and permanent set in rubber using the network alteration theory. *International Journal of Plasticity*, 54:19–33, 2014.
- [224] G. Chagnon, E. Verron, and L. Marckmann, G. and Gornet. Developement of new constitutive equations for the mullins effect in rubber using the network alteration theory. *International Journal of Solids and Structures*, 43:6817, 2006.
- [225] VN Khiêm, J-B Le Cam, Sylvain Charlès, and M Itskov. Thermodynamics of strain-induced crystallization in filled natural rubber under uni- and biaxial loadings, part ii: Physically-based constitutive theory. *Journal of the Mechanics and Physics of Solids*, 159:104712, 2022.

- [226] Ramin Akbari, Vahid Morovati, and Roozbeh Dargazany. Reverse physically motivated frameworks for investigation of strain energy function in rubber-like elasticity. *International Journal of Mechanical Sciences*, 221:107110, 2022.
- [227] M. Klüppel. The role of disorder in filler reinforcement of elastomers on various length scales. *Advances in Polymer Science*, 164:1, 2003.
- [228] Jaemin Kim, Erik Mailand, Ida Ang, Mahmut Selman Sakar, and Nikolaos Bouklas. A model for 3d deformation and reconstruction of contractile microtissues. *Soft Matter*, 17(45):10198–10209, 2021.
- [229] Markus Mehnert, Mokarram Hossain, and Paul Steinmann. A complete thermo-electro-viscoelastic characterization of dielectric elastomers, part ii: Continuum modeling approach. *Journal of the Mechanics and Physics of Solids*, 157:104625, 2021.
- [230] Chennakesava Kadapa and Mokarram Hossain. A unified numerical approach for soft to hard magneto-viscoelastically coupled polymers. *Mechanics of Materials*, page 104207, 2022.
- [231] Y Nikraves, A Rezaei Sameti, and AR Khoei. An atomistic–continuum multiscale analysis for heterogeneous nanomaterials and its application in nanoporous gold foams. *Applied Mathematical Modelling*, 2022.